ISBN 978-82-326-5375-1 (printed ver.)
ISBN 978-82-326-6551-8 (electronic ver.)
ISSN 1503-8181 (printed ver.)
ISSN 2703-8084 (electronic ver.)

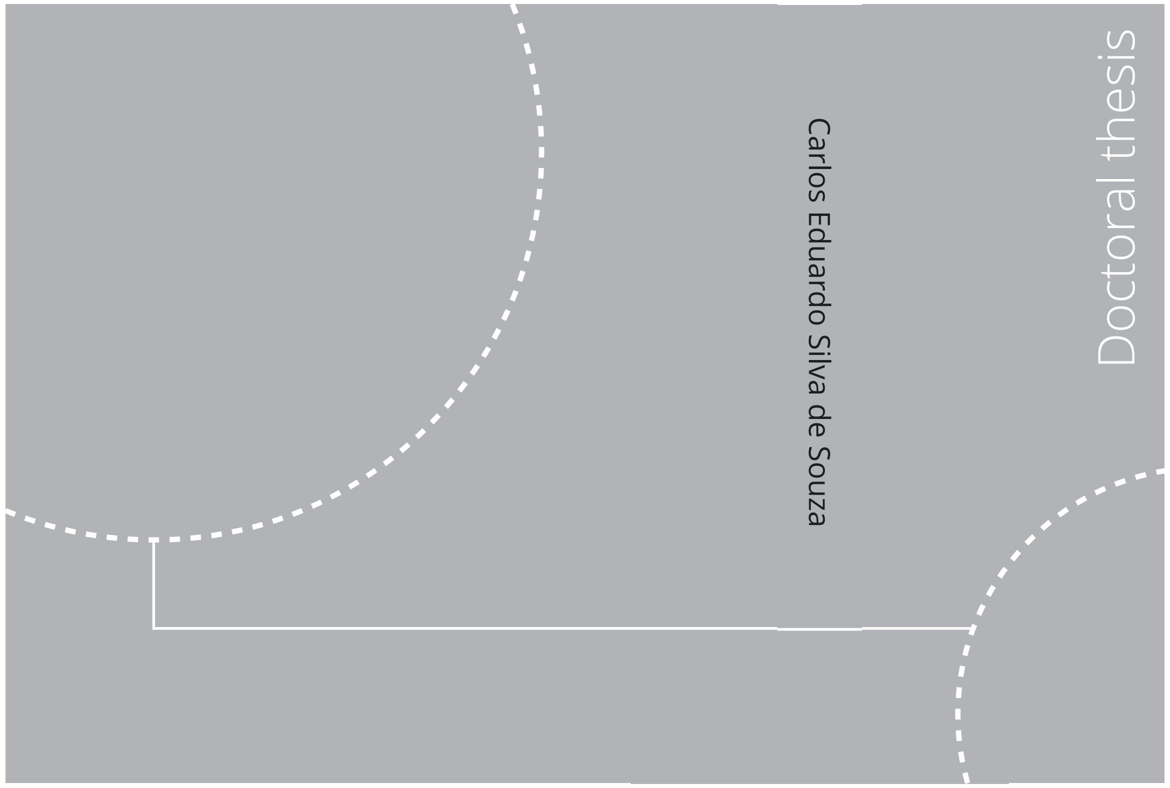

Doctoral theses at NTNU, 2022:246

NTNU
Norwegian University of
Science and Technology
Thesis for the degree of
Philosophiae Doctor
Faculty of Engineering
Department of Marine Technology

NTNU
Norwegian University of
Science and Technology

NTNU

Doctoral theses at NTNU, 2022:246

Carlos Eduardo Silva de Souza

Structural modelling, coupled dynamics, and design of large floating wind turbines

NTNU
Norwegian University of
Science and Technology

Carlos Eduardo Silva de Souza

Structural modelling, coupled dynamics, and design of large floating wind turbines

Thesis for the degree of Philosophiae Doctor

Trondheim, September 2022

Norwegian University of Science and Technology
Faculty of Engineering
Department of Marine Technology

NTNU
Norwegian University of
Science and Technology

NTNU
Norwegian University of Science and Technology

Thesis for the degree of Philosophiae Doctor

Faculty of Engineering
Department of Marine Technology

ISBN 978-82-326-5375-1 (printed ver.)
ISBN 978-82-326-6551-8 (electronic ver.)
ISSN 1503-8181 (printed ver.)
ISSN 2703-8084 (electronic ver.)

Doctoral theses at NTNU, 2022:246

PRINTED IN
NORWAY
NO - 1598

NORDIC SWAN ECOLABEL
Printed matter
2041 0731

Printed by Skipnes Kommunikasjon AS

Contents

VENTO SARDO
(Marisa Monte/Jorge Drexler)

Vento que levanta a onda
Que carrega o barco
Que ondula o mar

É o mesmo que vai dar na praia
Que levanta a saia
Rodada de oiá

Hay tiempos de andar contra el viento
Cuando el contratiempo comienza a soplar
Então o vento que é de aragem
Bate no varal pra me dar coragem

O vento que vem de longe
Quem sabe da fonte do vento solar
O vento que é o movimento do ar

Vamos levantar a vela
Abrir a janela
Ventilar a dor

Vamos a nombrar al viento
Celebrar su aliento
Purificador

Pampero, Terral, Tramontana,
Alisio, Santana, Siroco, Mistral

Levante, Minuano y Cierzo
Y mil más que el verso quisiera nombrar

Às vezes o vento muda
Sai batendo a porta faz tudo voar,
O vento é o temperamento do ar

Sopro
Sopra
Soprará

Abstract

Floating wind turbines (FWTs) are expected to contribute significantly in the transition to a low-carbon economy. In addition to their increased competitiveness for water depths higher than 50-60 m, FWTs may also benefit of the offshore wind trend of increased turbine dimensions, considering the potential improvements in the cost-effectiveness of support structures.

A better understanding of modelling approaches, coupled dynamics, design, and analysis is still needed, however, to improve their cost-effectiveness and maximize the energy produced by each unit. This thesis approaches relevant topics for the design and analysis of the next generation of FWTs, namely platform-rotor-controller coupled dynamics; modelling of flexible platforms; control strategies; and design considerations.

Changes in the surge and pitch natural periods of FWTs, operating under constant wind speed, previously reported by independent publications, were further investigated. Although well captured in fully-coupled analyses, the effect had not been explained previously, preventing its quantification at conceptual design stages. Nonlinearities in the mooring system due to the platform mean displacement are found to explain the phenomenon for the surge motions. For pitch, the effect is linked to the coupling between platform motions, rotor dynamics, and control system.

In particular, the relative phase between the nacelle motions and the ensuing fluctuations in the rotor thrust allows the dynamic thrust to be decomposed into apparent inertia and damping effects, which depend on the motion frequency, incident wind velocity, and controller configuration. The notion of a frequency-dependent aerodynamic damping coefficient is shown to be relevant in frequency-domain FWT analyses, which often assume a constant damping coefficient. The latter is demonstrated to be non-conservative in terms of pitch motions and tower loads.

Modelling of FWT platforms as flexible structures is also studied due to the expected importance for larger FWTs – both on their global dynamics and on local structural analyses of the platform. For a 5 MW tension-leg platform wind turbine (TLPWT), the platform (pontoon) elasticity significantly affects the platform global motions, as well as the 1st tower bending natural frequency. Hydroelasticity associated with the pontoons' deflections is also assessed, and found to be negligible compared with the radiation loads associated with the rigid-body modes.

Hull elasticity is also modelled for 20 MW spar-type FWTs. In this case, the focus is on the method adopted to distribute hydrodynamics loads. The adoption of potential theory results in lower fatigue damage than a formulation based on Morison's equation. A non-negligible reduction in the first tower bending frequency, due to the platform flexibility, was also observed.

Strategies to avoid instabilities associated with controller-motion interactions are also assessed. The common approach of detuning the blade-pitch controller gains is shown to be inadequate for large FWTs, which tend to have longer pitch natural periods and thus require excessive reduction of the controller frequency. Other methods, which include the nacelle velocity in the control logic, are also evaluated. Based on a coupled platform-rotor model, simple feedback of the nacelle velocity to the control law is shown to be problematic in terms of instability, especially when a low-pass filter is applied to the signal. Nacelle velocity feedforward, on the other hand, ensures stability even in the presence of the filter and when hydrodynamic damping is disregarded. A method for tuning the controller using these strategies is also provided.

Finally, design and analysis paradigms for large FWTs are evaluated through the design of three 20 MW spar-type structures, differing on the static pitch angle under rated thrust. The relative contributions of inertial, gravity, and thrust loads on global dynamics and hull/tower sectional loads are investigated. The hydrostatic restoring in pitch affects fatigue damage and extreme loads significantly. In particular, extreme sectional stresses are shown to be governed by gravity loads associated with the RNA weight, such that load cases associated with the rated wind speed may provoke the extreme loads for some sections at the platform and tower, especially for platforms with lower hydrostatic restoring in pitch.

Acknowledgements

I have had the privilege of being surrounded by extraordinary people during these PhD years. My supervisor, Prof. Erin Bachynski-Polić, is greatly acknowledged for generously dedicating her time and patience in sharing her vast knowledge. Working with her has been a once-in-a-life opportunity that shaped my way of thinking for good. Thank you, Erin.

My co-supervisor, Prof. Zhen Gao, is also acknowledged for helping me finding directions at key moments, in addition to valuable comments on my thesis. I appreciate also the careful review and relevant suggestions from the committee members, Professor Finn-Gunnar Nielsen and Professor Maurizio Collu. Professor Amir Nejad is kindly acknowledged for administrating the defense process.

I also want to thank all the employees at NTNU IMT, for keeping a smooth functioning of the department that allowed me to have minimal worries with administrative matters during my stay.

Lunch and coffee pauses were transformed in rich, multicultural events by my colleagues, each carrying a unique background. Thank you for the learning you afforded me along these years. Special thanks go to my office mate, Sangwoo Kim, for kindly tolerating my frustration during coding; and to John Marius Hegseth, for the discussions and co-authorship in a paper that granted us a memorable trip to Massachusetts.

SINTEF Ocean is kindly acknowledged for the flexibility provided during the last stage of this PhD, and not least for the opportunity to work on projects in the vanguard of floating wind technology. This experience, together with the encouragement from my colleagues, was fundamental for the completion of this thesis.

Trondheim has a great community of Brazilians, which has provided me with solid friendships. I would like to thank all of you, and in particular Marilia, Marcelo, Thiago, Itala, Vinicius, Marcela and Leonardo for the guitar afternoons, skiing tours, pub visits, cumbia concerts, cabin trips, bike rides, and not least for the support during challenging moments.

I grew up in a family that not only aroused and encouraged my curiosity since my early childhood, but also did absolutely everything to ensure that I would receive an excellent education and cultural background. This PhD actually started when my mother puzzled me with fitting the same volume of water in glasses of different height and diameter, or perhaps when I slept while solving a long list of math exercises that my father prepared for me before my first exams. Certainly also when my sister showed me that entering a top university was within our reach. Thank you for being so wonderful. It is amazing how you have always managed to be so close, despite the 11,000 km of geographic distance and the travel restrictions during some of these years. I extend my thanks to my grandparents and other members of my (huge) family, for the presence and continuous support during my growing years.

The Research Council of Norway is kindly acknowledged for funding this PhD. In addition to the position at the Department of Marine Technology, I was also associated to the Centre for Autonomous Marine Operations and Systems (AMOS).

Nomenclature

Abbreviations

BEM	Blade element momentum
DOF	Degree of freedom
FD	Frequency domain
FE	Finite element
FTF	Force transfer function
FWT	Floating wind turbine
HSS	High-speed shaft
IEA	International Energy Agency
IPC	Individual pitch control
LCOE	Levelized cost of energy
LSS	Low-speed shaft
OWT	Offshore wind turbine
PI	Proportional-integral
PSD	Power spectral density
QTF	Quadratic transfer function

RAO	Response amplitude operator
RNA	Rotor-nacelle assembly
TLP	Tension leg platform
TLPWT	Tension leg platform wind turbine
VSVP	Variable speed variable pitch

Hydrodynamic and structural modelling of FWT

a_{ij}	Added mass coefficient
$\mathbf{A}_\infty$	Matrix of asymptotic, infinite-frequency added mass coefficients
A_{wp}	Waterplane area
b_{ij}	Radiation damping coefficient
b_{ij}^v	Viscous damping coefficient
$\mathbf{B}_s$	Matrix of structural damping in FE displacement equation (Eq. 2.12)
B^v	Matrix of linear viscous damping coefficients
c_{ij}	Restoring coefficient in DOF i due to unitary motion in DOF j
C_d	Drag coefficient
$\mathbf{C}_{hs}$	Hydrostatic restoring matrix
C_m	Mass coefficient
D	Section diameter
$F_{d,i}(\omega)$	Wave excitation force/moment in DOF i
F_{hs}	Vector of restoring loads
$F_{r,i}$	Radiation force/moment in DOF i

g	Acceleration of gravity
$\mathbf{H}$	Matrix of retardation functions
h_{ij}	Retardation function in DOF i due to unitary velocity in DOF j
$\mathbf{K}_s$	Matrix of structural stiffness in FE displacement equation (Eq. 2.12)
m	Mass
$\mathbf{M}_{RB}$	Rigid-body inertia matrix
$\mathbf{M}_s$	Matrix of structural inertia in FE displacement equation (Eq. 2.12)
$\mathbf{q}$	Vector of external loads in equation of motions (Eq. 2.10)
$\mathbf{r}$	Vector of displacements in FE displacement equation (Eq. 2.12)
$\mathbf{R}^{ext}$	Vector of external loads in FE displacement equation (Eq. 2.12)
$\mathbf{v}$	Fluid velocity field
$\not{V}$	Submerged volume in equilibrium position
z_B	Vertical center of buoyancy
ξ	Vector of platform displacements around equilibrium position
ρ_w	Water density
Φ	Potential function
$\boldsymbol{\Psi}_\mathbf{i}$	Structural free-vibration eigenmode

Wind turbine aerodynamics and controls

C_P	Power coefficient
$C_{p,max}$	Maximum achievable power coefficient
C_Q	Torque coefficient

C_T	Thrust coefficient
I_d	Combined rotor and drivetrain moment of inertia about rotor shaft
k_{br}	Power maximization coefficient at region 2
K_{fb}	Nacelle velocity feedback gain
K_{ff}	Nacelle velocity feedforward gain
K_i	Controller integral gain
K_p	Controller proportional gain
L_h	Hub height from platform rotation center
N_g	Drivetrain gear ratio
P_r	Generator rated power
Q_a	Aerodynamic rotor torque
Q_g	Generator torque
$Q_{g,r}$	Rated generator torque
R	Rotor radius
T	Rotor thrust
u	Relative wind velocity through the rotor
v_f	Filtered fore-aft nacelle velocity
v_n	Fore-aft nacelle velocity
x_n	Fore-aft nacelle position
β	Blade pitch angle
ζ_{ctr}	Controller relative damping

ζ_f	Filter relative damping
λ	Tip-speed ratio
ρ_w	Air density
ϕ	Rotor azimuth
Ω	Rotor speed
Ω_0	Rated rotor speed
ω_{ctr}	Controller natural frequency
ω_f	Filter cut-off frequency
ω_g	Generator speed
Ω_r	Reference rotor speed

Floating wind turbine time-domain analysis

D	Accumulated damage
F_{var}	Varying component of rotor thrust
H_s	Significant wave height
I	Turbulence intensity
S_w	Wave spectrum
T_p	Wave peak period
u_t	Varying component of incident, turbulent wind speed
U	Incident wind velocity
U_m	Mean component of incident, turbulent wind speed
V_{hub}	Incident wind speed at hub height

z_{ref}	Reference height for incident wind speed
α	Wind shear power law exponent
α_{HU}	Shape parameter for the Weibul conditional distribution of wave significant height, for a given wind speed
α_U	Shape parameter for the Weibul marginal distribution of the wind speed
β_{HU}	Scale parameter for the Weibul conditional distribution of wave significant height, for a given wind speed
β_U	Scale parameter for the Weibul marginal distribution of the wind speed
γ	JONSWAP spectrum peak-shape parameter
μ_{TH}	Mean of log-normal conditional distribution of wave peak period and wave significant height, for a given wind speed
σ_{TH}	Standard deviation of log-normal conditional distribution of wave peak period and wave significant height, for a given wind speed
σ_x	Axial stress
ω_p	Wave peak frequency

Results and discussion

a_{aer}	Aerodynamic inertia coefficient
b_{aer}	Aerodynamic damping coefficient
f_0	Thrust amplification factor

List of Figures

List of Tables

Chapter 1

Introduction

This thesis consists of a collection of four research articles, in addition to these introductory chapters with theoretical background, discussion of research results, and conclusions.

1.1 Motivation

Floating wind turbine (FWT) design is remarkable for its multi-cross-disciplinary character. Specialists from diverse areas such as marine hydrodynamics, structural mechanics, aerodynamics, and control systems have been joining efforts to optimize these structures and make this technology more cost-effective. In this process, however, questions arise continually regarding the modelling assumptions, analysis methods, coupled dynamics, design considerations, and unexpected instabilities.

Today's floating wind technology mainly combines two branches of engineering. The accumulated experience from oil and gas floating platforms is visible on most of the FWT concepts reaching demonstration phases (Fig 1.1), such as spar (Hywind [5], TODA [6]), semi-submersible (WindFloat [7], VolturnUS [8]), tension leg platform (TLP) (PelaStar [9]), and barge (SATH [10], Floatgen [11]). Rotors and drivetrains are readily available from the offshore wind industry, which to this date announces turbines with impressive 14-16 MW nameplate rating [12–14].

At a first glance, floating wind may appear a natural outcome of two successful industries. But this has been proven not to be as simple.

The loads and vibrations associated with a wind turbine, operating at more than 100 meters above water level, differ from those associated with oil and gas platforms. Typical design considerations, including motion amplitudes, governing environmental conditions, ranges of natural frequen-

(a) Hywind Scotland spar FWT wind park [15]

(b) WindFloat semi-submersible FWT [7]

(c) Floatgen barge FWT [11]

Figure 1.1: Spar, semi-submersible, and barge FWT concepts in demonstration phases.

cies to avoid, and distribution of structural loads over the hull, have to be adapted [16].

Equivalently, towers and rotor-nacelle assemblies (RNA) designed for bottom-fixed offshore wind turbines may also require modification to operate on floating platforms. The platform motions, amplified by the tower height, impose significant inertial and gravitational loads to the RNA – which not only affects the drivetrain components [17] and rotor blades, but also impinges large moments to the tower. In addition, the interactions between the platform motions and the wind turbine control system may result in serious instabilities [18].

More than a merge of complementary expertise, floating wind technology makes a new engineering branch, to which the research community has been contributing with enhanced models for hydrodynamic and aerodynamic loads, specific design methodology, novel control approaches, and structural analysis techniques. The research carried out in this PhD is intended to improve the understanding on FWT dynamics, and discuss modelling, design, and analyses techniques for the next generation of FWTs.

1.1.1 Justification and economical viability of floating wind energy

Renewable energy is fundamental for meeting the 2015 Paris Agreement goal of limiting the global temperature increase to 1.5-2.0° C, in comparison with pre-industrial levels. The International Energy Agency (IEA) proposed a pathway to achieve zero net emissions by 2050[19], where solar and wind energy appear as the main sources of additional capacity in the next three decades. In particular, the plan expects an increase of 16 times in the annual deployment of offshore wind capacity, from the current 5 GW to 80 GW, until 2030.

This ambitious growth in the number of new offshore wind parks will meet some important limitations faced by bottom-fixed offshore wind turbines (OWT). In fact, the economic feasibility of these structures is in general reduced for increasing water depths. With time, the scarcity of suitable areas in shallow water (up to 60 m depth) may be a factor pushing the adoption of floating wind turbines [20], which also benefit from the stronger and steadier winds at sites farther from the coast [21].

As of 2021, a total of 79 MW of power capacity was available from FWTs installed around the globe, distributed among 11 demonstration projects. Although the maturity level of these projects varies, their overall performance is encouraging. For example, in 2020 the average capacity factor[1] of the Hywind Scotland park was 54%, putting it on the top of all offshore wind farms in the United Kingdom and well ahead of the 40% average [22].

The quick progress in floating wind technology is also reflected on the projections for its commercial viability. According to the 2021 Edition of the "Offshore Wind Market Report" [23], the levelized cost of energy (LCOE) for floating wind is expected to drop from 160 USD/MWh in 2020 to 60-105 USD/MWh in 2030. For sake of comparison, Jansen et al. [24] claim that currently installed bottom-fixed offshore wind parks start to become subsidy-free, with an estimated LCOE sometimes lower than €50/MWh.

Increased scale is considered one of the main reasons behind the reduction in offshore wind LCOE in the last years [25]. For floating wind turbines, increased capacity per unit can represent important savings in transportation, mooring system, installation at sea, operation/maintenance, and decommission. Floating wind farm projects to be deployed in the next few years count on 8 MW [26] and 10 MW [27] wind turbines, and at least the conceptual design of a 15 MW semi-submersible FWT has already been published [28].

1.2 Research gaps and questions, scope, and objectives

The research community has produced a large number of works regarding appropriate modelling, analysis, and design methods for FWTs in the range 5-10 MW[2]. Some remaining gaps should be assessed in the pathway to the next class concepts, supporting wind turbines of more than 10 MW, here referred to as "large FWTs".

The following research gaps were identified in the course of this PhD and are assessed in the next chapters, and mainly in the publications in Appendix A:

FWT period changes An unexpected phenomenon was observed in two independent model test campaigns, characterized by increased surge and pitch decay periods in decay tests under constant wind, and with an operating turbine. Bachynski et al [29] observed the effect for three different wind speeds, and for both surge and pitch. Goupee et al. [30] reported it for the pitch motions and one wind speed only, but

---

[1] The ratio between the energy actually produced divided by the installed capacity, over a given period of time.

[2] All the cases studied in this thesis consider horizontal-axis wind turbines (HAWT).

the effect varied with the different control strategies adopted. None of the publications provided an explanation for the effect.

Hull elasticity for a TLPWT The number of publications adopting a flexible FWT platform is scarce. When a rigid-body approach for the floater is adopted, the motions and structural loads at e.g. the tower base may be incorrect. In addition, although some works [31–33] assess hydroelasticity – i.e., the interactions between structural deformations and the surrounding flow, none of them provide a quantitative measure of this effect for typical FWT designs.

Control strategies for FWTs Controller detuning is a typical strategy for FWT control systems in academic works, consisting in reducing the controller gains to avoid interactions with the platform motions [34]. The procedure in practice reduces the controller ability to respond to wind variations with frequency above the platform pitch natural period. The literature is somewhat ambiguous regarding the consequences of this procedure to power quality, rotor speed excursions, platform motions, and structural loads. More sophisticated approaches have been proposed, for example including the nacelle velocity signal in the controller. Although easy to implement, this method is not trivial in terms of controller tuning. Very few publications [35, 36] discuss this procedure, and do not account for e,g, low-pass filter on the nacelle velocity, which is usually adopted for avoiding wave-frequency components into the control law.

Design considerations for large FWTs Large FWTs will be subjected to a different balance between inertial, gravity, and aerodynamic/hydrodynamic loads than what is observed for today's 5-10 MW FWTs. In addition, the deflections experienced by the platform tend to be larger, making the assumption of a rigid-body even more questionable. The longer pitch natural periods may have implications on the control system, making a detuned approach unrealistic. It is necessary to understand how these new characteristics affect the design of the next class of FWTs, thus helping to prevent equivocated assumptions in the modelling and analyses of these structures.

The research presented in this thesis intends to respond to the following research questions:

Q1 What are the reasons for the surge and pitch period changes under operational conditions? How are these changes affected by incoming wind speed, FWT structural properties, and the control system?

Q2 How can the platform be correctly/efficiently modelled as a flexible structure? How does platform elasticity affect the global platform dynamics? Does hydroelasticty play an important role?

Q3 What are the consequences of adopting a detuned controller for the structural loads on the FWT platform and tower? How do motion compensation strategies based on feedback and feedforward of the nacelle velocity to the blade pitch controller perform? How can one implement/tune a controller adopting such strategies?

Q4 How important it is to consider platform flexibility and advanced control strategies in early design stages of the next generation ($>$ 10 MW) units? What is the relative importance of gravity, inertia, and thrust loads in the distribution of sectional stresses along the platform and tower, as a function of the static pitch angle at rated wind speed?

1.2.1 Objectives

The topics approached in the thesis have the common target of relating structural modelling, global dynamics, and control system, to the design of large floating wind turbines. The following objectives compose the scope of this work:

O1 Better understand the interactions between FWT motions, rotor dynamics, and the control system. In particular, explain the changes in eigenperiods for a FWT subjected to wind, as well as the relation between the aerodynamic damping effect and the controller-motion interactions.

O2 Investigate the influence of the control system on FWT structural integrity, with focus on strategies to avoid controller-motion interactions.

O3 Explore aspects related to the platform flexibility, including methods for distribution of hydrodynamic loads over the hull; evaluate the influence of platform hydroelasticity on the global response of typical FWTs.

O4 Adopt hydroelastic modelling and a realistic control system in the design and analysis of a spar-type 20 MW FWT.

1.3 Background

1.3.1 FWT modelling, design, and analysis

Numerical simulations are a powerful tool in the design and analysis of floating wind turbines, due to the possibility of testing a design's performance under a large number of environmental loading conditions, at relatively low cost. Matha et al. [37] provide fundamental modelling principles for the aerodynamic and hydrodynamic effects relevant for FWTs, as well as for the structural analysis. Jonkman [38] describes the development of a time-domain aero-hydro-servo-elastic simulation tool for FWTs, and the determination of load cases. A discussion about candidate control system strategies for floating wind turbines is also provided.

A flexible model of the platform is required when internal loads are of interest. In this case, the hydrodynamic loads must be distributed over the hull. Svendsen [39] presents a flexible model of a tension leg platform wind turbine (TLPWT), with distributed radiation and diffraction loads from potential theory over the platform column and pontoons. Luan et al. [40] and Hegseth et al. [41] adopt similar approaches for semi-submersible FWTs. Engebretsen et al. [42] compare distributed potential theory against a model based on Morison's equation in the model of a flexible spar FWT, finding that the latter approach significantly overpredicts fatigue damage. Borg et al. proposed a method based in modal analysis for a spar [31] and for a "triple-spar" platform [32], where the hydrodynamic loads are evaluated with potential theory through the definition of generalized modes for representing structural flexibility. In this approach, hydroelastic effects are also accounted for.

Reference offshore wind turbine models have been fundamental in the progress of FWT research. The NREL 5 MW wind turbine by Jonkman et al. [43] provides a comprehensive description of the blades and tower, as well as an introduction to rotor dynamics and wind turbine control. The DTU 10 MW model by Bak et al. [44] has been widely adopted in current research. Ashuri et al. [4] describe a 20 MW offshore wind turbine, based on multidisciplinary design optimization. Although all these models are designed for bottom-fixed applications, they are open source and can thus be modified, allowing the user to adapt e.g. the tower and controller design for a floating substructure.

Design standards provide criteria for the load models, environmental modelling, plating scantlings, material properties, station keeping systems, stability in intact and damaged conditions, and other considerations to be adopted in the design of a structure. The IEC-61400-3 [45], the DNVGL-ST-

0119 [46], and the ABS Guide for Building and Classing of Floating Offshore Wind Turbines [47] provide specific guidelines for FWTs. Other useful references include guidelines for fatigue analysis of offshore structures [48], global analysis of floating structures [49], and modelling of environmental loads [50].

Specific design principles have also been discussed in the scientific literature. Procedures have been published for the design and modelling of TLP [51], semi-submersible [3, 52], and spar [1, 53, 54] FWT substructures.

The analysis of FWT global dynamics and structural performance also requires specific methods, in comparison with those adopted for other floating platforms and for bottom-fixed OWTs. Jonkman and Matha [55] discuss load cases for fatigue and extreme loads assessment, as well as control system particularities and other modelling details, in the analysis of three 5 MW FWT concepts. Kvittem and Moan introduced methods for fatigue analysis of semi-submersible FWTs [56, 57]. Specific procedures for the fatigue analysis of TPLWTs are provided by Bachynski [58]. Fatigue analysis of different FWT concepts accounting for wind-waves misalignment is discussed by Bachynski et al. [59]. Karimirad and Moan [60] analyze extreme loads on a fully-flexible platform. Li et al. [61] introduce a method for extreme analysis of a semi-submersible FWT, accounting for environmental contours inside the turbine operational region.

1.3.2 FWT control systems

Wind turbine control systems have the primary objectives of optimizing power production and reducing structural loads on the rotor, drivetrain, and tower [62]. Most modern wind turbines regulate the rotor dynamics through the use of two actuators: the generator, that can vary the applied torque at the shaft; and a mechanism that rotates the blades around the root axis (blade pitching), changing their angle of attack, and thus the aerodynamic torque around the rotor shaft.

In both cases, the controller uses the measured rotational speed of the generator shaft to determine the commanded torque or blade pitch angle. For the latter, a proportional-integral (PI) controller [63] on the rotor speed error is often adopted in commercial wind turbines [64].

For a floating wind turbine, the wind flow through the rotor experiences variations due to the platform motions, causing fluctuations on the rotor speed. A serious instability can occur if the controller responds to these fluctuations, leading to large platform pitch motions [18]. Controller “detuning” avoids the problem by reducing the controller natural frequency, until it becomes lower than the platform pitch natural period [34]. Although effective in preventing the instability, this method also reduces the controller performance in tracking rotor speed variations above the platform pitch natural frequency.

More sophisticated methods have been developed to avoid the instability. Some of them rely on adding the nacelle velocity to the PI control law, either by direct feedback [35, 36, 65], or via feedforward [66–68], by making the reference rotor speed a function of this new input. Alternatively, the contribution of the nacelle motions to the rotor speed fluctuations can be estimated with an observer [69, 70].

The adoption of such motion compensation strategies can reduce structural loading at the tower and substructure significantly. Lackner [71] obtained significantly lower tower damage when using the feedforward approach for a barge FWT. Fleming et al. [72] observed a similar trend when adding feedback from both the nacelle velocity and platform pitch motion to the baseline PI controller. Hegseth et al [73] compared the controller with nacelle velocity feedforward with a detuned controller, in the context of design optimization of a spar FWT, obtaining reduced tower thickness with the former approach.

1.3.3 Coupled dynamic effects of FWTs

In a review of challenges in wind energy science, Veers et al. [74] mentioned FWT coupled dynamics as a problem yet to be studied thoroughly. Some of the known issues are the above-mentioned instabilities related to control-motion interactions, as well as the changes in surge and pitch natural periods reported by Bachynski et al. [29] and Goupee et al. [30]. Other phenomena already reported in the literature include a yaw instability under fault condition, reported by Jonkman [38]; and a "roll-yaw lock" effect described by Haslum et al. [75], characterized by large-amplitude limit-cycles in both DOFs when their natural frequencies are too close.

The influence of platform flexibility on the global response may also be relevant for some FWT concepts. Zhao et al. [76] found this to be the case for a 5 MW TLPWT. Hsu [77] analyzed the effect of platform flexibility on the design of FWT towers, as well as the shift in the first tower bending frequency when it is moved from a bottom-fixed to a floating foundation.

Interactions between the platform motions and the rotor wake were analyzed by de Vaal et al. [78, 79], and found to be insignificant for typical FWT surge frequencies. An experimental study on the couplings between aerodynamic and hydrodynamic loads on FWTs is carried out by Thys et al. [80].

1.4 Contributions

The research carried out in this PhD contributes with modelling strategies for flexible FWT platforms; better understanding on the control system influence on FWT global and structural dynamics; and approaches for design and analysis of large FWTs. More specifically, the following outcomes resulted from this work:

C1 An explanation for the variation in the surge and pitch decay periods, under constant wind speed.

C2 The notion of frequency-dependent apparent inertia (or stiffness) and damping effects, resulting from the interactions between the incident wind, the control system, and the platform motions.

C3 Methods for considering the platform elasticity on time-domain coupled analyses of FWTs, in addition to the confirmation that hydroelastic effects are negligible for current FWT designs.

C4 Assessment of the benefits of adopting a blade-pitch controller with motion compensation strategies, rather than a detuned PI controller, for large FWTs.

C5 A method for tuning two control systems with motion compensation strategies, based on the low-pass filtered nacelle velocity.

C6 Modelling, design, and analysis methods for 20 MW spar FWTs, including the conclusion that detuned controllers should not be adopted even in preliminary design phases for this class of FWTs.

1.4.1 Original research articles

Publication J.1 C. E. S. Souza, E. E. Bachynski. "Changes in surge and pitch decay periods of floating wind turbines for varying wind speed". *Ocean Engineering* 180, pp. 223-237 (2019).

Description and main findings This article was motivated by the findings reported by Bachynski et al.[29] and Goupee et al.[30], regarding period changes in surge and pitch during experimental decay tests of FWTs. The phenomenon is investigated by means of time-domain simulations with three 5 MW FWT concepts. The period changes in surge are found to be caused by the variation in mooring stiffness due to the mean thrust. For the pitch motions, it is caused by interactions between the relative wind velocity through the rotor, the blade-pitch control system, and rotor dynamics. Departing from the relative phase between the rotor thrust and nacelle velocity, expressions are derived for “apparent inertia and damping” coefficients, given as a function of the incident wind speed and nacelle fore-aft motion frequency.

In addition to explaining the origin of the changes in period, the paper contributes with a better understanding of the aerodynamic damping effect in floating wind turbines. Specifically, it is shown that the aerodynamic damping depends on the control system, incident wind speed, and the platform’s own natural periods in surge and pitch.

Authorship The research work for this paper (literature review, analyses, formulations, and conclusions), as well as the writing, were mainly carried out by myself. Prof. Erin Bachynski-Polić contributed with supervision, discussions, and review of the article.

Publication J.2 C. E. S. Souza, E. E. Bachynski. “Effects of hull flexibility on the structural dynamics of a tension leg platform floating wind turbine.” *ASME Journal of Offshore Mechanics and Arctic Engineering* 142(1): 011903 (2020).

Description and main findings This paper explores the consequences of modelling the pontoons of a 5 MW TLPWT as flexible beams. Comparisons with a fully-rigid platform model are performed in terms of response amplitude operators, force transfer functions, and axial stresses and fatigue damage at the tower base and tendons. In addition, the importance of considering hydroelastic effects associated with the pontoon flexible modes is assessed, both in terms of radiation loads in the frequency domain and by means of time-domain simulations.

The fatigue damage at both the tower base and tendons was smaller for the model with flexible pontoons. Analyzing the power spectral density plots of the axial stresses at these structures, it was observed that the largest difference was beyond the wave frequency range, being more associated with the tower 1$^{\text{st}}$ bending frequency – which is lower for the flexible model. In addition, it was found that the hydroelastic effects associated with pontoon flexibility are negligible.

Authorship The research work and writing of the article were performed by myself. Prof. Erin Bachynski-Polić contributed with supervision, discussions, and review of the article.

Publication J.3 C. E. S. Souza, E. E. Bachynski-Polić. "Design, structural modeling, control, and performance of 20 MW spar floating wind turbines". *Marine Structures* 84: 103182 (2022).

Description and main findings In this paper, three 20 MW spar FWTs are obtained from a parametric design procedure, with static pitch angles under rated wind speed of 6°, 8°, and 10°. The platforms are modelled as flexible structures, with distributed hydrodynamic loads from potential theory. The wind turbine control system adopts a motion compensation strategy based on feedforward of the filtered nacelle velocity, in order to avoid resonant pitch motions. The three designs are compared by means of fatigue and extreme analyses, based on the sectional loads along the platform and tower. Additional analyses assess the controller performance, as well as the benefits of distributing potential-theory loads over the hull, rather than adopting a model based on Morison's equation.

The results show that the static pitch angle at rated wind is a design constraint that significantly affects steel/ballast mass, fatigue damage, and extreme sectional loads. For fatigue, it is found that the accumulated damage at the platform is influenced differently than for the tower, when the hydrostatic restoring varies. Extreme sectional stresses are largely influenced by gravity loads, and thus the platform with largest static pitch at rated wind presented the highest extremes. Load cases associated with the rated and 50-year wind speeds caused the extreme loads for sections at platform and tower. The controller choice has major influence on the results, and a strategy based on detuning the controller gains seems to be inappropriate for FWTs with these dimensions.

Authorship The research work and writing were performed by myself. Prof. Erin Bachynski-Polić contributed with supervision, discussions, and review of the article.

Publication C.1 C. E. S. Souza, J. M. Hegseth, E. E. Bachynski. "Frequency-dependent aerodynamic damping and inertia in linearized dynamic analysis of floating wind turbines". *Journal of Physics: Conference Series* 1452: 012040 (2020).

Description and main findings This paper complements the findings from Publication J.1, providing analytical formulations for the apparent inertia and damping coefficients in terms of the frequency and aerodynamic derivatives for a given operational point. In addition, the paper discusses the benefits of including the interaction between the blade-pitch control system and the nacelle motions in frequency-domain models of FWTs. Comparisons with time-domain simulations show that the latter approach produces more accurate results than assuming a constant aerodynamic damping coefficient, which is a common procedure when the controller is disregarded.

Authorship The research work and writing of this article were evenly distributed between myself and fellow PhD candidate John Marius Hegseth. Prof. Erin Bachynski-Polić contributed with supervision, discussions, and review of the article.

The relation between the objectives, publications, and contributions is illustrated in Fig. 1.2.

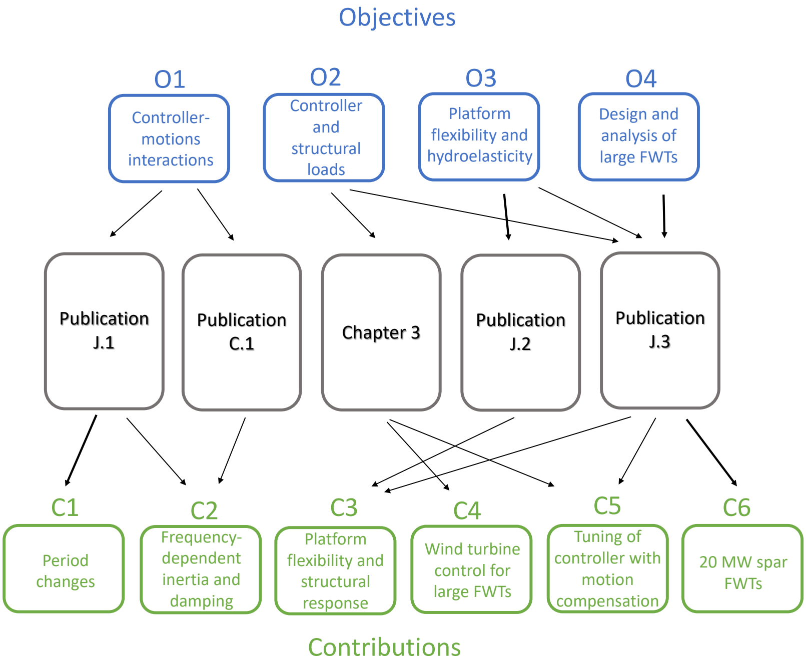

Figure 1.2: Relation between objectives, publications, and contributions.

1.5 Thesis organization

Chapter 2 provides theoretical background and practical techniques for modelling floating wind turbines. This includes a description of the main FWT components, a review of the relevant hydrodynamic models, and topics in structural and hydroelastic modelling.

Chapter 3 starts with a review in wind turbine aerodynamics. In addition to discussing the relevant effects for FWTs, a linearized model for the thrust and torque, suitable for control system design, is presented. Then, the main concepts on floating wind turbine control, for different operational regions, are introduced. The "detuned" strategy is compared with two motion-compensation approaches, based on feedback and feedforward of the nacelle velocity to the control law. State-space models of the coupled nacelle-rotor system are devised, including states for a 2^{nd}-order low-pass filter for the nacelle velocity, for stability analysis purposes. The method is adopted in practice to study the stability of a 20 MW spar FWT, considering the three control approaches.

In Chapter 4, the wave and wind models adopted in the thesis are described. Coupled analysis is then discussed, including the most important coupling effects for FWTs, aero-hydro-servo-elastic programs for FWT simulations, and modelling considerations. The chapter is finalized with methods for structural assessment of FWTs, including load case selection based on metocean data, and procedures for fatigue and extreme loads analyses.

Chapter 5 discusses the methodology and main findings of each publication. Selected results are reproduced, while the complete papers are available in Appendix A.

Conclusions and suggestions for future work are provided in Chapter 6.

Chapter 2

Hydrodynamic and structural modelling of floating wind turbines

Different modelling strategies and levels of accuracy can be adopted in numerical models for floating wind turbines. While a system with 2 or 3 rigid-body DOFs can be adequate for control design purposes, a formulation with hundreds of DOFs may be needed for a fully-flexible model used in structural analyses. The hydrodynamic and aerodynamic models can also vary in complexity, depending on the application.

This chapter describes modelling principles that affect FWT global motions, as well as those necessary for the structural analysis of the platform and tower.

2.1 Modelling principles

Floating wind turbine coupled analyses in time-domain demand a numerical model including the relevant load models and structural properties. Figure 2.1 shows examples of numerical FWT models in SIMA. A FWT can be divided in the following components:

- a floating platform, providing the buoyancy to support its own weight and the weight of tower and wind turbine, plus the mooring vertical pretension component;

- a tower, typically consisting of a hollow cylinder with varying diameter and thickness;

- a wind turbine, comprising nacelle, drivetrain, hub, and blades;
- a mooring system, which normally consists of catenary or taught lines (or tensioned tendons, in the case of TLPs), and anchors.

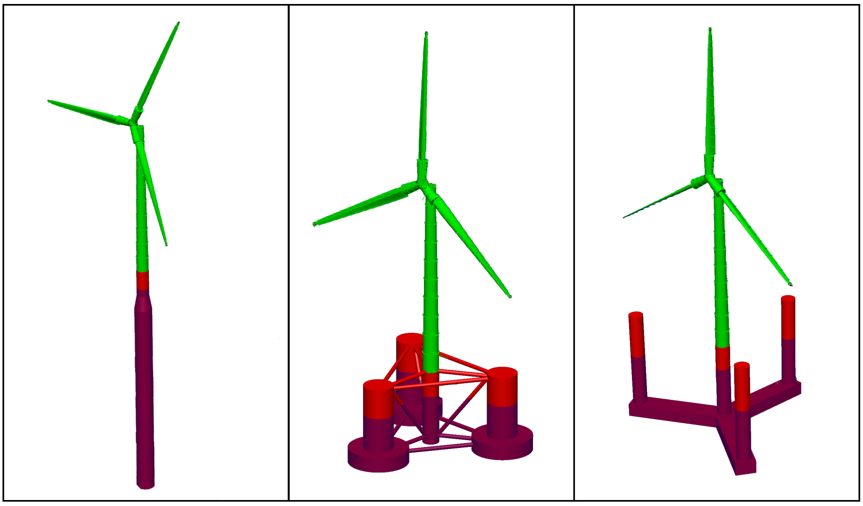

Figure 2.1: Examples of floating wind turbines modelled in SIMA (without mooring lines). From left to right: the OC3 Hywind 5 MW spar FWT [1]; the OC4 5 MW semi FWT [2]; and the CSC 5 MW semi FWT [3].

Platform

Platform modelling involves both the choice of adequate hydrodynamic load models, as well as the approaches to represent structural dynamics (i.e., motions and deformations under loads).

In many cases, a rigid-body assumption can be adequate for modelling the platform. Exceptions are when sectional loads in the platform's components are of interest, or when the platform flexible modes are expected to significantly affect the FWT global response. The latter case was shown in Publication J.2 to be true for a 5 MW TLPWT, and is also discussed in Chapter 5.

When platform elasticity is important, two main approaches can be adopted: a finite element (FE) model, or a model based on modal superposition. The latter case, adopted e.g. by Borg et al. [31], has the advantage of reducing the number of DOFs, lowering computational cost significantly compared with a FE approach. A FE model, on the other hand, benefits from modelling robustness and compatibility with off-the-shelf software dedicated to marine structures applications. Fully-flexible FWT platforms using FE modelling have been demonstrated by Svendsen [39], Luan [81], and in Publication J.3.

For some applications, a hybrid model can be adopted where some of the platform components are modelled as rigid, and others as flexible. This procedure was adopted e.g. by Kvittem [56] for a semi-submersible wind turbine, where columns were modelled as rigid bodies, while braces were treated as flexible beams.

Tower

A rigid tower can be adequate when tower sectional loads are not of interest, and when tower flexibility does not affect the global dynamics. This is the case for example in controller design/verification, mooring analysis, and analyses of platform motions.

Tower loads are, however, an important metric in the structural analysis of FWTs. Bending moments and axial/shear forces at the tower base and other intermediate sections are relevant in fatigue and extreme analysis. In addition, the gravitational loads associated with the RNA weight can be affected by tower deflection, which also impacts the sectional loads close to tower top [82].

Beam elements with axisymmetric cross sections are in most cases adequate to model a tower in a FE approach. The number of elements depends on the tower length, but 20-40 elements are typically used. Some software like OpenFAST offer the possibility of modelling the tower with modal superposition, where the user inputs the eigenfrequencies and mode shapes as polynomials. Assuming small deflections, modal superposition can provide accurate predictions of the sectional loads.

Wind turbine

Wind turbine blades are very flexible structures. Common deflections under operating conditions can significantly affect the angle of attack near the tip, with important differences in torque and thrust compared with a rigidly modelled rotor. The latter, in any case, will provide larger loads, such that the assumption provides conservative results [82].

Fairly detailed models are in general required for the blades. The blade is divided in segments spanwise, each of them with uniform chord length, airfoil coefficients, twist angle, and distance from the rotor cone (blade prebend). The number of segments should ensure a smooth profile, with better refinement where changes in geometry and structural properties are more relevant.

Modal superposition can be used for modelling blade elasticity, especially when a local structural analysis of the blade is not needed [83]. Finite element models can be more adequate if an accurate prediction of sectional loads is required. In this case beam elements with at least two planes of symmetry are indicated. One disadvantage of using a FE approach for the blades is that the tip speed can be relatively high, which can cause numerical problems due to large element rotations, depending on the integration method.

The blade roots are attached to the hub, whose inertia properties are normally significant for the rotor dynamics. At least the hub mass and moment of inertia around the shaft should be modelled. The nacelle and drivetrain inertia properties are also relevant. For wind turbines with large gear ratios, it may be important to consider the drivetrain moment of inertia around the shaft, while for direct drive machines the latter becomes negligible compared with the rotor inertia.

Mooring system

For catenary-moored FWTs, the most accurate model for the mooring lines is attained with a FE approach. Bar elements are in general appropriate, and sectional loads are available along the entire line. In addition, dynamic effects associated with inertia and drag are captured based on the actual elements' accelerations and velocities. A disadvantage with this approach is the high number of elements required for the model, since mooring line lengths are on the order of hundreds of meters.

Due to the large deflections and geometric effects, modal superposition is not adopted for modelling catenary mooring lines. Alternatives for a FE model are a quasi-static approach; or a linear restoring matrix modelled at the floater.

Quasi-static models adopt classic catenary equations, based on water depth, floater position, and the line's weight in water [84]. A linearized stiffness matrix is then obtained, and can be updated whenever the model moves significantly from the equilibrium position. Approximated dynamic effects can be included in the model. Tensions at the fairleads can be estimated, but are not as accurate as those obtained with a FE approach. Another drawback is that it can be complicated to model elements commonly used in real mooring systems, like clump weights and buoys.

The adoption of a linear restoring matrix is the simplest model, and also the most efficient in computational terms. One important disadvantage is that restoring in surge in catenary-moored systems can present important non-linearities for typical FWT displacements due to thrust. As shown in Publication J.1, this effect can affect the surge natural period significantly.

For TLPWTs, important couplings between tendons and other modes related to platform motions, tower vibrations, and 1p/3p cycles, can take place. One should then be careful in the use of simplified models, since important dynamic effects related to these couplings can be neglected using springs to model the tendons [85]. For a FE model, the use of beam elements is suggested [86]. Modal superposition can be considered if loss of tension is not expected to happen.

2.2 Hydrodynamic models for FWT platforms

2.2.1 Hydrostatics

Hydrostatic loads result from the integration of the pressure field, in the absence of fluid velocities/accelerations, over the hull wet area. Hydrostatic restoring normally refers to the balance between hydrostatic and gravity loads, such that it is common to also include terms related to the body weight in the restoring matrix. Assuming small displacements around the resting position, the linearized restoring forces/moments in heave, roll, and pitch are given by:

$$\mathbf{F}_{hs} = -\mathbf{C}_{hs}\xi \, , \tag{2.1}$$

where $\mathbf{F_{hs}}$ is the vector of restoring loads, $\xi = [\xi_1, \xi_2, \xi_3, \xi_4, \xi_5, \xi_6]^\top$ is the vector of displacements around the equilibrium position, and $\mathbf{C}_{hs}$ is the hydrostatic restoring matrix. For a body with symmetry about the xz-plane, and assuming small motions:

$$\mathbf{C}_{hs} = \begin{bmatrix} 0 & 0 & 0 & 0 & 0 & 0 \\ 0 & 0 & 0 & 0 & 0 & 0 \\ 0 & 0 & c_{33} & 0 & c_{35} & 0 \\ 0 & 0 & 0 & c_{44} & 0 & 0 \\ 0 & 0 & c_{53} & 0 & c_{55} & 0 \\ 0 & 0 & 0 & 0 & 0 & 0 \end{bmatrix} . \tag{2.2}$$

The restoring coefficients are given by [84]:

$$c_{33} = \rho_w g A_{wp} \tag{2.3}$$

$$c_{35} = c_{53} = -\iint\limits_{A_{wp}} x dx dy\,, \tag{2.4}$$

$$c_{44} = \rho_w g \forall z_B - mgz_G + \iint\limits_{A_{wp}} y^2 dx dy \tag{2.5}$$

$$c_{55} = \rho_w g \forall z_B - mgz_G + \iint\limits_{A_{wp}} x^2 dx dy\,, \tag{2.6}$$

where ρ_w is the water density, g is the acceleration of gravity, A_{wp} is the waterplane area, $\forall$ is the submerged volume in equilibrium position, m is the total mass of the FWT, and z_B and z_G are the vertical centers of buoyancy and gravity, respectively.

2.2.2 Potential theory

For a large body with non-zero relative velocity with respect to the surrounding fluid, hydrodynamic loads not related with viscous effects can in general be predicted with accuracy by potential theory. Under the assumption of incompressible and inviscid fluid, and irrotational flow, the fluid velocity field $\mathbf{v}$ can be obtained from the gradient of a potential function, Φ. The pressure field in the fluid domain, and thus loads on submerged structures, can then be obtained applying Bernoulli's equation [84].

The potential function is found by solving Laplace's equation, subjected to boundary conditions at the floating body surface, at the free surface, at the bottom, and at an infinite radial distance from the body. In practice, the problem is solved by expanding Φ as a series of functions with increasing order:

$$\Phi = \Phi_1 \epsilon + \Phi_2 \epsilon^2 + \dots\,. \tag{2.7}$$

In general, loads associated with Φ_1 and Φ_2 are the most relevant for problems involving large floating bodies. The solutions are normally found by assuming a distribution of source functions over the body surface, which is discretized in panels. Together with the boundary conditions, the potential functions associated with each panel form a system of equations. In this work, WAMIT [87] is used for calculating potential theory loads using this solution method.

First-order wave loads

Under the assumption of low wave amplitudes and small motions, loads obtained from Φ_1 are in general accurate for typical floating structures, when viscous effects are not important. The problem is normally divided into the radiation and the diffraction problem. Details of the solution are provided e.g. by Newman [88].

The radiation problem assumes that the body is forced to oscillate in calm waters, at a given frequency ω, radiating waves. As a reaction to these motions, the fluid exerts forces and moments at the body, with components proportional to the body's acceleration and velocity:

$$F_{r,i}(\omega) = -a_{ij}(\omega)\ddot{x}_j - b_{ij}(\omega)\dot{x}_j \, , \tag{2.8}$$

where a_{ij} and b_{ij} are the *added mass* and *radiation damping* coefficients, respectively. The indices ij indicate a load in DOF i due to a unitary acceleration/velocity in DOF j.

In the diffraction problem, the body is assumed as fixed, and subjected to incident waves. The potential function is assumed as the superposition of the undisturbed wave and the diffracted wave. The resulting pressure field integrated over the body surface provides the *wave excitation force* in each DOF, $F_{d,i}(\omega)$.

For large-volume bodies, fluid perturbations due to the body presence are important in the calculation of excitation loads. When the wave is long compared with the body's characteristic length[1], diffraction effects become negligible, and the excitation force can be found based on the incident wave potential, only – the so-called Froude-Krylov forces.

Second-order wave loads

The solution of the second-order problem (the one associated with Φ_2) results in loads with difference frequency ($\omega_i - \omega_j$) and sum frequency ($\omega_i + \omega_j$) components.The difference-frequency wave loads excite low-frequency motions in surge, sway, and yaw for typical floating structures, and are thus important in the analysis of mooring systems. For large FWTs, roll and pitch can also be excited, since their periods can become relatively long. Sum-frequency forces can excite heave motions of TLPWTs [58].

Quadratic transfer functions (QTFs) relate both difference- and sum-frequency forces to pair of waves with unitary amplitude. Their calculation, however, is time-consuming and requires detailed discretization of the hull and the surrounding free-surface. An useful approximation consists in neglecting the free-surface forcing terms in the evaluation of Φ_2, thus eliminating the need of meshing the free-surface – with significant reduction in

---

[1] According to Faltinsen [84], diffraction effects become less important for a ratio λ/D larger than 5, where λ is the wave length and D is the body characteristic length.

computational time and modelling efforts. This approximation was found to be very accurate in representing the full QTF for semi-submersible FWTs [89, 90], and was adopted in Publication J.3 for the calculation of QTFs for the 20 MW spar FWTs.

For the difference-frequency components, Newman's approximation [91] is another convenient alternative, which does not depend on the solution of the 2^{nd}-order potential. The method consists of using elements from the QTF's main diagonal to approximate the elements closer to the diagonal. The main diagonal terms, also known as mean drift coefficients, can be obtained from the 1^{st}-order solution.

Newman's approximation is more accurate for QTFs whose elements do not vary too quickly around the main diagonal. In addition, it is more appropriate for platforms with long (≈100 s) natural periods, since difference-frequencies resulting in loads with shorter periods are farther from the main diagonal.

2.2.3 Morison's equation

Morison's equation can be used to estimate the loads on a slender structure. For a moving cylinder with diameter D, the force on a section with length dz is given by [84]:

$$dF = \underbrace{\frac{1}{2}\rho_w C_d D dz(u-\dot{\eta}_1)\left|u-\dot{\eta}_1\right|}_{\text{viscous}} + \underbrace{\rho_w \frac{\pi D^2}{4} dz a_1}_{\text{Froude-Krylov}} - \underbrace{\rho_w (C_m - 1)\frac{\pi D^2}{4} dz\ddot{\eta}}_{\text{added mass}}, \tag{2.9}$$

where u and a_1 are the velocity and acceleration components of the undisturbed flow, transversal to the cylinder, at the middle of the section; $\dot{\eta}_1$ and $\ddot{\eta}_1$ are the section's velocity and acceleration, transversal to the cylinder; and C_d and C_m are the drag and mass coefficients, respectively. These coefficients should in principle be calibrated based on experiments, but reference values for typical cross sections are provided in DNV-RP-C203 [50].

As indicated in the equation, viscous drag loads are represented by the first term, which is of second-order in the relative fluid velocity. The second term is the Froude-Krylov force on a cylinder, while the third term accounts for the force due to added mass. The latter two form the Morison equation's inertial term. For applications where the long wave assumption is not valid, it is possible to combine the viscous drag term with loads based on potential theory, instead of using the inertial terms from Equation (2.9).

2.2.4 Viscous damping

For some structures, the viscous damping is better modelled as a combination of linear and quadratic terms – rather than the purely quadratic formulation obtained with Morison's equation. A global matrix of linear coefficients, b^v_{ij}, multiplied by the relative velocity between the body and the flow, can be adopted in this case. These coefficients are not simple to estimate theoretically, and are normally calibrated based on experiments.

When combined with Morison's equation, the linear viscous damping coefficients and the quadratic drag coefficient C_d should be determined together, to avoid double consideration of viscous effects.

2.3 Structural modeling of FWTs

Several levels of detail can be considered in the structural assessment of floating wind turbines. Nonlinearities associated with failure modes (including e.g. buckling or yielding of plates) can be explicitly modelled, but in the context of coupled analyses they are in general not included. Instead, the objective is to determine the sectional loads, and then indirectly evaluate fatigue and ultimate limit states. Material properties are often assumed as linear, also.

The scope of this thesis are the sectional loads at the platform and tower. This section describes the adopted models and assumptions for this purpose.

2.3.1 Rigid-body equation of motions in time domain

For a floating rigid body, the equation of motion in 6 DOF is given by [83]:

$$\left(\mathbf{M}_{RB} + \mathbf{A}_{\infty}\right)\ddot{\mathbf{x}} + \mathbf{B}^v\dot{\mathbf{x}} + \mathbf{C}_{hs}\mathbf{x} + \int_0^t \mathbf{H}(t-\tau)\dot{\mathbf{x}}(\tau)\mathrm{d}\tau = \mathbf{q}(t,\mathbf{x},\dot{\mathbf{x}})\,, \quad (2.10)$$

where $\mathbf{M}_{RB}$ is the rigid-body inertia matrix; $\mathbf{A}_{\infty}$ is the matrix of asymptotic added mass coefficients, for infinite frequency; B^v is the matrix of linear viscous damping coefficients; $\mathbf{C}_{hs}$ is the matrix of hydrostatic restoring; $\mathbf{H}$ is the matrix of retardation functions; and $\mathbf{q}$ is a vector of external loads, accounting for 1^{st}- and 2^{nd}-order wave loads, contributions from Morison-type viscous drag terms, and mooring system loads. For a floating wind turbine, $\mathbf{q}$ may also include the aerodynamic loads.

The retardation functions, $h_{ij}(t)$, represent the radiation loads in time-domain [92], and can be obtained from the radiation damping coefficients [93]:

$$h_{ij}(t) = \frac{2}{\pi}\int_0^{\infty} b_{ij}(\omega)\cos(\omega t)d\omega\,. \quad (2.11)$$

2.3.2 Nonlinear finite element method

The finite element method (FEM) is an analysis method for the numerical solution of field problems – i.e., problems which require the spatial distribution of dependent variables [94]. In structural analysis, FEM consists of representing the structure with discrete elements, each with a limited number of DOFs, for the solution of the displacement equation:

$$\mathbf{M}_s\ddot{\mathbf{r}} + \mathbf{B}_s\dot{\mathbf{r}} + \mathbf{K}_s(\mathbf{r})\mathbf{r} = \mathbf{R}^{ext}\,, \tag{2.12}$$

where $\mathbf{R}^{ext}$ is a vector of external loads; and $\mathbf{M}_s$, $\mathbf{B}_s$, and $\mathbf{K}_s$ are the structural inertia, damping, and stiffness matrices, respectively. The latter is assumed to depend on the displacement vector $\mathbf{r}$ itself, leading to a nonlinear formulation. For a FWT, this geometric dependence is relevant in the modelling of mooring lines and rotor blades stiffness [95].

Both bar and beam elements are used for the FE models in this work. Bar elements are adequate in cases were only the axial tensions are of interest, while a beam element should be adopted whenever bending/torsional loads are also relevant. In this case, assumptions regarding the sectional distribution of inertia and stiffness properties must be determined carefully.

Rayleigh damping

Structural damping in FE models are important to represent the actual energy dissipation in vibrating structures, avoiding artificial resonant vibration amplitudes. In addition, it improves numerical stability. The damping matrix $\mathbf{B}_s$ can be conveniently formulated in FE models using the *Rayleigh damping* formulation [94]:

$$\mathbf{B_s} = \alpha\mathbf{M_s} + \beta\mathbf{K_s}\,, \tag{2.13}$$

where α and β are non-negative constants. The formulation can be applied for individual DOFs or to the global system, in which case the vibration modes become orthogonal to $\mathbf{B_s}$, and the relative damping associated with each mode is given by:

$$\zeta_i = \frac{1}{2}\left(\frac{\alpha}{\omega_i} + \beta\omega_i\right)\,, \tag{2.14}$$

where ω_i is the modal frequency.

The first term inside the parenthesis in Equation (2.14) will provide more damping for vibrations with lower frequencies. For floating wind turbines, this can result in artificially over-damping the surge, sway, and yaw motions, as well as the rotor DOF. For this reason, it is recommended to set $\alpha = 0$ and use a stiffness-proportional damping model.

The choice for β should be such to provide the desired level of damping at the most relevant structural vibration modes. Typical values adopted for reference wind turbines fall in the range of 1.0-2.0% for the tower fore-aft and side-side modes; and 0.5-3.0% for the blade flap- and edgewise modes [44, 96, 97].

2.3.3 Modal superposition

One disadvantage with the FEM in time-domain dynamic analyses is the large number of DOFs, which for modelling marine structures can be of the order of thousands [83]. An alternative is to define generalized DOFs to represent the flexible modes, in addition to the 6 rigid DOFs. A FE model can be used to determine the free-vibration eigenmodes, $\mathbf{\Psi_i}$, representing the main vibration patterns – as well as the matrices of modal mass and stiffness. The modal vibration in time-domain is then given by:

$$r_i(x,t) = \mathbf{\Psi_i}(x) y_i(t)\,, \tag{2.15}$$

where $y_i(t)$ is a time-varying function.

The number of modes to represent the flexible behavior should be large enough to cover the range of frequencies of interest. In addition, it should take into account the spatial and temporal variation of the loads acting on the structure, since the modes obtained from the free vibration problem are not affected by external loads [83]. In this work, modal theory is used for the calculation of generalized added mass and radiation damping coefficients in Publication J.2.

2.3.4 Hydroelastic modelling

Hydroelasticity may be defined as the interaction between structural deflections and the hydrodynamic loads actuating on the body [98]. Structures like e.g. fish farms, floating airports, and floating solar panels present strong hydroelastic behavior, since the flow-induced deformations are large enough to affect the fluid flow significantly.

For a formulation based on modal superposition, hydroelastic effects can be taken into account by including the generalized modes representing structural flexibility in the potential theory problem, as proposed by Newman [99]. The solution will include the added mass/radiation damping, as well as wave force transfer functions, associated with the flexible modes – in addition to the rigid-body DOFs. Borg et al. [31] adopted this methodology for a 10 MW spar FWT.

In any case, the structural deflections on FWTs are small compared with the rigid-body motions, and it is shown in Publication J.2 that their influence on hydrodynamic loads is negligible for current designs. However, the elastic effects on the hull provoked by hydrodynamic loads is relevant in the assessment of sectional loads. A hydroelastic model for today's FWT platforms can thus be reduced to what Borg et al. [33] called a "0^{th}-order approach" – that is, structural deflections are affected by, but do not affect, the surrounding flow.

When the platform is modelled with finite elements, the hydrodynamic loads can be distributed over the hull by discretizing it into segments, over which the loads are applied as nodal forces. Morison's equation (Eq. 2.9) can be applied if a long-wave assumption is reasonable for the platform in question. However, even when this is the case, care should be taken to prevent the high-frequency end of the wave spectrum to artificially excite the structure. This was shown in Publication J.3 to increase fatigue damage considerably for a 20 MW Spar FWT. Also, Engebretsen et al. [42] found up to 96% higher fatigue damage when an 8 MW Spar FWT was modelled with a purely Morison formulation, compared with the case when potential theory was adopted, combined with the quadratic drag term from Eq. (2.9).

Distribution of loads from potential theory

The frequency dependency of hydrodynamic loads can be taken into account in a flexible structure by distributing potential theory based coefficients and force transfer functions over the platform surface [39–41]. This is done by first solving the radiation-diffraction problem for the entire body, assumed as rigid. Then, the platform is discretized into segments, to which the loads are mapped and applied. The quadratic term from Morison's equation (Eq. 2.9) can be combined with this formulation, for inclusion of viscous drag effects.

The number of segments adopted for the platform discretization is a compromise between accuracy and computational time. A too coarse discretization will produce unrealistic deflections, while too many segments may increase the processing time related with the solution of the convolution integral representing radiation effects (see Eq. (2.10). One alternative to improve efficiency is to approximate the convolution integral by a higher-order ordinary differential equation, which is integrated in the time domain using a state space representation. Taghipour et al. discuss different methods for identifying the coefficients of the differential equation. [100], as well as the application of the method for a flexible barge [101].

Chapter 3

Wind turbine aerodynamics and controls

The aerodynamic torque around the rotor shaft results from the distributed lift and drag forces along the blades, which are a function not only of the relative wind speed, but also of the rotor speed and airfoil angle of attack. There are, of course, additional aerodynamic forces acting on the rotor in addition to the torque.

One of these loads is the force perpendicular to the rotor plane, also known as thrust – the largest of the three force components. For a floating wind turbine, the thrust produces important structural loads, as well as global motions in surge and pitch.

The objectives of wind turbine control systems vary with the wind speed. Variable-speed-variable-pitch (VSVP) control systems adjust both generator torque and blade pitch angle in order to maximize power production below rated wind speed; and to limit power capture and rotor loads above rated wind speed. In both cases, the controller action influences the thrust, affecting the dynamics of floating wind turbines.

3.1 Aerodynamics

3.1.1 Blade element momentum method

The torque and thrust on a wind turbine result from the interaction between the incoming wind and the rotor. The *Blade Element Momentum* (BEM) method is a well-known formulation to calculate the rotor loads, considering the relative wind flow through the rotor and the latter's rotational speed [21, 102].

As the name indicates, BEM merges momentum theory with the blade element theory. Momentum theory is based on conservation of linear and angular momentum, and is applied over a control volume containing an annular section of the rotor. It is then assumed that the loss of momentum throughout the section is due to the work done by the wind on the blade, allowing the calculation of the *induction factors*. These indicate the fractional decrease in the wind velocity across the rotor plane, relative to the free stream [21].

Assuming that the blade may be divided into independent, non-interacting segments, the induction factors are used for evaluating the velocities over each 2-D blade section. The drag and lift can then be calculated and integrated along the blade span, resulting in the total aerodynamic load. A new induction factor is then obtained, and the process is iterated until convergence is attained.

Being a relatively simple model, BEM has its limitations. Standard corrections normally implemented in wind turbine software are the Glauert correction, for large (> 0.4) induction factors; and Prandtl's factors for hub and tip losses [21].

Other relevant effects not accounted for by the basic BEM formulation are dynamic wake and dynamic stall. The former, also known as "dynamic inflow", consists of the delayed induced velocity in the rotor plane due to shed vorticity. According to de Vaal [79], the effect is well captured by BEM combined with Stig Øye's model [102], when provoked by the horizontal motions experienced by a rotor on typical FWTs.

Dynamic stall refers to time-varying changes in the lift and drag coefficients of an airfoil, due to time variations in the angle of attack. It can be represented with Stig Øye's model or Beddoes-Leishmann model. Neglecting dynamic stall can result in spurious flapwise blade vibrations [102]. Its time constant is however too short for provoking interactions with FWT motions [79].

By distributing the lift and drag loads along the blades, it is also possible to obtain their sectional stresses directly from a global analyses, thus accounting for aeroelasticity.

3.1.2 Wind turbine linearization

In the design of wind turbine control systems, it is convenient to linearize the aerodynamic torque, Q_a, and thrust, T, around predetermined operation points of interest:

$$Q_a = Q_{a,0} + \frac{\partial Q}{\partial \Omega}\Delta\Omega + \frac{\partial Q}{\partial u}\Delta u + \frac{\partial Q}{\partial \beta}\Delta\beta \tag{3.1}$$

$$T = T_0 + \frac{\partial T}{\partial \Omega}\Delta\Omega + \frac{\partial T}{\partial u}\Delta u + \frac{\partial T}{\partial \beta}\Delta\beta\,, \tag{3.2}$$

where Ω is the rotor speed, u is the relative wind velocity through the rotor, and β is the blade pitch angle.

Despite the nonlinear character of wind turbine aerodynamics, the torque and thrust linearization as above are considered reasonable for controller tuning purposes [103].

3.1.3 Relevant non-dimensional coefficients

Some non-dimensional coefficients are normally used to describe a wind turbine's operation [62]. The tip-speed ratio, λ, is given by

$$\lambda = \frac{\Omega R}{U}\,, \tag{3.3}$$

where U is the incident wind speed and R is the rotor radius. The thrust, torque, and power coefficients are given by:

$$C_T(\lambda,\beta) = \frac{T}{\frac{1}{2}\rho_a \pi R^2 U^2} \tag{3.4}$$

$$C_Q(\lambda,\beta) = \frac{Q_a}{\frac{1}{2}\rho_a \pi R^3 U^2} \tag{3.5}$$

$$C_P(\lambda,\beta) = \frac{P}{\frac{1}{2}\rho_a \pi R^2 U^3}\,, \tag{3.6}$$

where P is the power and ρ_a is the air density.

3.1.4 Additional aerodynamic effects

Aerodynamic effects related to the tower can be relevant for FWTs. Tower drag can become the most important aerodynamic load for an idling turbine under high wind velocity, while the modified velocity field due to tower shadow induces thrust fluctuations at blade-passing frequencies. For the analyses in this work, aerodynamic drag on the tower is represented with a quadratic model, while tower shadow effects are modelled using potential theory.

Drag loads on the nacelle, as well as on the platform, can also be represented with wind drag coefficients.

3.2 Controls

Most wind turbines rely on automated mechanisms to optimize power production, improve power quality, and minimize loads on the rotor, generator, and tower/substructure. Large wind turbines mostly adopt VSVP control systems. Figure 3.1 shows the rotor speed and blade-pitch angle at different operating regions of such controller, configured for the NREL 5 MW wind turbine [43].

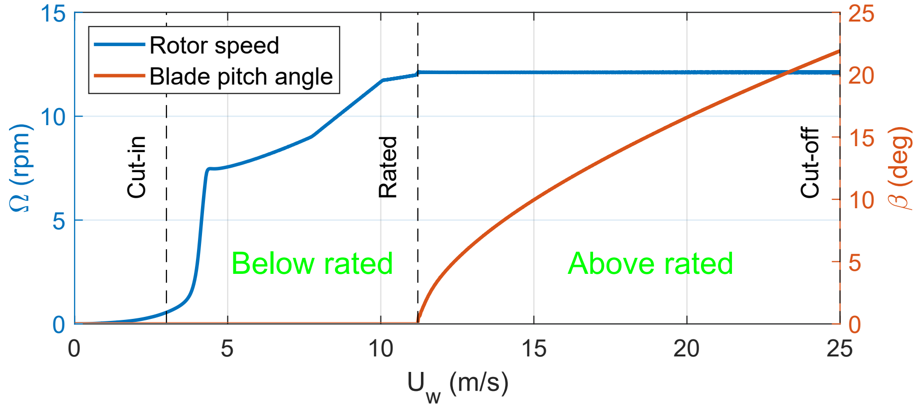

Figure 3.1: VSVP controller operating regions for the NREL 5 MW wind turbine.

This section describes the main characteristics of VSVP controllers, as well as their interactions with FWT dynamics. The focus is set on the general controller functionalities. Real wind turbines include a number of additional features, which are not in the scope of this thesis.

3.2.1 Below rated

Below rated wind speed, the main objective of the generator torque controller is to maximize power production. One way to achieve this goal is by expressing the torque as a quadratic function of the low-pass filtered generator speed, ω_g [64]:

$$Q_g = k_{br}\omega_g^2\,, \tag{3.7}$$

where k_{br} is a function of the maximum achievable power coefficient, $C_{p,max}$, and the associated tip speed ratio, λ':

$$k_{br} = \frac{\rho_a \pi R^5 C_{p,max}}{2\lambda'}\,, \tag{3.8}$$

with R being the rotor radius.

The maximum power coefficient $C_{p,max}$ depends on the rotor geometry, and is a function of wind speed, rotor speed, and blade pitch angle. It can be found for example by running time-domain simulations with different combinations of these variables. OpenFAST is a convenient tool for this purpose, due to its flexibility in enabling/disabling the generator DOF.

The generator torque operates as determined in Equation (3.7) between the cut-in and rated wind speeds. This range is normally called Region 2, in the literature. Region 1 refers to wind speeds below cut-in, where zero torque is applied by the generator. The transition between both regions can be as simple as a linear function, as adopted by Jonkman et al. [43]; or governed by a smoothing function, as proposed e.g. by Hansen et al. [104]. The same applies for the transition between Region 2 and Region 3, which comprises above rated wind operation.

3.2.2 Above rated

Above rated wind speed, the blade pitch controller will be activated in order to limit the aerodynamic torque, and thus rotor speed. It typically consists of a proportional-integral (PI) feedback of the rotor speed error:

$$\Delta\beta = K_p \Delta\Omega + K_i \int_0^t \Delta\Omega dt\,, \tag{3.9}$$

with K_p and K_i being the proportional and integral gains. The rotor speed error $\Delta\Omega$ is given by

$$\Delta\Omega = \Omega - \Omega_r\,, \tag{3.10}$$

where the constant reference $\Omega_r = \Omega_0$ is the rated rotor speed.

The controller gains are adjusted according to the desired rotor dynamics in closed loop:

$$I_d \dot{\Omega} = Q_a - Q_g = \Delta Q\,, \tag{3.11}$$

where I_d is the combined rotor and drivetrain moment of inertia about the rotor shaft. Above rated wind speed (Region 3), the generator torque Q_g can either be kept constant ($Q_g = Q_{g,r}$), or varied in order to keep the power constant. In the latter case, it can be expressed as:

$$Q_g = \frac{P_r}{N_g \Omega} \approx Q_{g,r} - \frac{P_r}{N_g \Omega_r^2} \Delta\Omega\,, \tag{3.12}$$

where P_r is the rated power and N_g is the drivetrain gear ratio.

Linearizing the aerodynamic torque Q_a as in Equation (3.1) and following Jonkman et al. [43], a second-order system can now be written by creating a new variable, $\dot{\phi} = \Delta\Omega$, and combining Equations (3.9-3.1):

$$I_d\ddot{\phi} + \left[-\frac{\partial Q_a}{\partial \Omega} - \frac{\partial Q_a}{\partial \beta}K_p - \frac{P_r}{N_g\Omega_r^2}\right]\dot{\phi} - \frac{\partial Q_a}{\partial \beta}K_i\phi = Q_{a,0} - Q_{g,r} = 0\,. \quad (3.13)$$

The controller gains can then be chosen according to the desired system natural frequency (ω_{ctr}) and damping (ζ_{ctr}):

$$K_i = -\frac{\omega_{ctr}^2 I_d}{\frac{\partial Q_a}{\partial \beta}} \quad (3.14)$$

$$K_p = -\frac{2I_d\omega_{ctr}\zeta_{ctr} + \frac{\partial Q_a}{\partial \Omega} + \frac{P_r}{N_g\Omega_r^2}}{\frac{\partial Q_a}{\partial \beta}} \approx -\frac{2I_d\omega_{ctr}\zeta_{ctr}}{\frac{\partial Q_a}{\partial \beta}}\,, \quad (3.15)$$

where the approximation assumes that the terms $\frac{\partial Q_a}{\partial \Omega}$ and $\frac{P_r}{N_g\Omega_r^2}$ are much smaller than $2I_d\omega_{ctr}\zeta_{ctr}$, which holds for typical large wind turbines.

The determination of the controller natural frequency is a compromise between satisfactory tracking of the rotor speed, and stability. While for the former objective it is desirable to have ω_{ctr} as high as possible, a too large value can result in interaction with structural modes, leading to resonant responses. For a floating wind turbine, one may also consider avoiding the typical wave frequency range, to prevent the rotor from responding to WF motions. A natural frequency around $2\pi/15 = 0.42$ rad/s or lower should be considered as a starting point. Typical values for ζ_{ctr} are normally 0.6 or larger [35, 43, 105].

Since the aerodynamic derivatives are themselves a function of the turbine operating point (u,Ω,β), a gain scheduling strategy is required to ensure that the desired control dynamics are kept through the entire operational range above rated wind. Typically, this is done with a look-up table relating the gains to the current collective blade pitch angle.

3.2.3 Motion-controller interactions and the detuned controller

Stability issues can arise when the blade-pitch controller responds to rotor speed variations caused by a FWT's motions in surge and pitch [18, 34, 106]. A negative damping effect is experienced by the nacelle, if the controller cannot distinguish the rotor speed fluctuations provoked by FWT motions from those arising from turbulence. As a result, resonant motions in pitch take place, leading to large tower loads and causing interruptions in production [107]. Surge motions are also amplified, with negative consequences to mooring fatigue.

Different measures are proposed in the literature to avoid the instability. The simplest of them is to “detune” the controller, i.e., to reduce the gains in order to achieve a controller natural frequency lower than the FWT pitch natural frequency [34]. Other methods rely on keeping ω_{ctr} at a higher level, while adding motion compensation strategies to the controller command based on measurements of the platform/nacelle motions [18, 69, 71, 106].

One justification for the adoption of a detuned controller is to claim that wind turbulence energy is mostly at a lower frequency range. Figure 3.2 shows the Kaimal spectrum for turbulent wind with mean speed $V_{hub} = 15.0$ m/s and turbulence intensity $I = 0.14$. Although most of the energy does lie below 0.01 Hz, the energy in the range 0.02-0.10 Hz is not negligible.

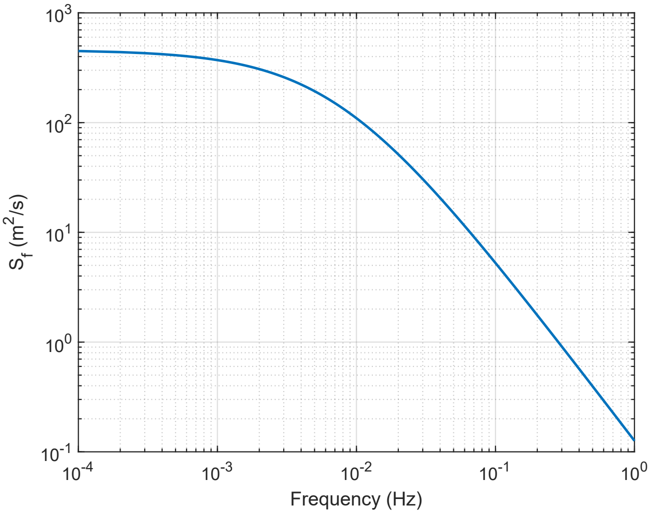

Figure 3.2: Theoretical Kaimal spectrum for $V_{hub} = 15.0$ m/s, $I = 0.14$.

The natural frequency of a detuned controller needs to be somewhat below the pitch natural frequency, which normally lies around 30-40 s for 10 MW FWTs and tends to increase for larger (15-20 MW) units. Thus, larger excursions of the rotor speed are expected when the detuned controller is adopted. This is illustrated in Figure 3.3, where rotor speed time series for a bottom-fixed DTU 10 MW [44] are shown using ω_{ctr} values of 0.42 rad/s (15.0 s) and 0.16 rad/s (40.0s). The latter, which corresponds to a detuned configuration, presents variations not observed when the quicker version of the controller is adopted. The increased rotor speed excursions negatively impact power quality, in addition to provoking larger variability of the rotor loads.

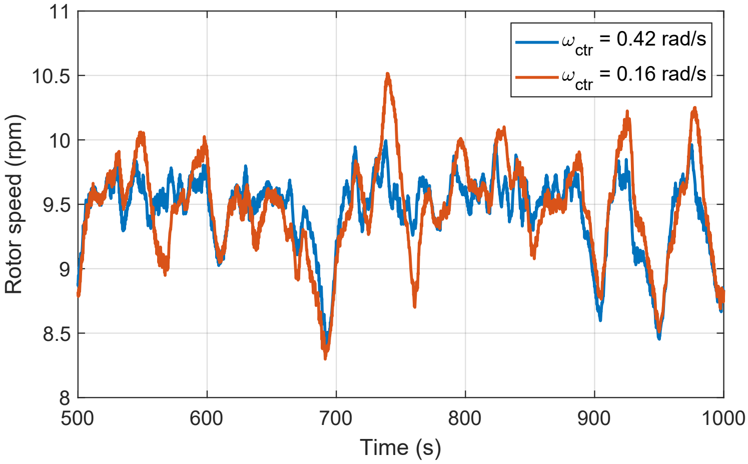

Figure 3.3: Rotor speed comparison for controllers with different natural frequencies.

Another drawback with the detuned controller is that it results in marginal aerodynamic damping of the FWT pitch motions. As discussed in Publications J.1 and C.1, the aerodynamic damping effect depends on the coupled rotor-platform dynamics, becoming lower as ω_{ctr} approaches the FWT pitch natural frequency – which is the case for detuned controllers. Even though the instability is avoided, pitch motions tend to persist for longer than they would in the presence of more aerodynamic damping, provided by the rotor when a non-detuned controller is adopted.

3.2.4 Motion compensation strategies

A controller with a higher natural frequency can be adopted for floating wind turbines if the baseline feedback law from Equation 3.9 is combined with a motion compensation strategy. This can be, for example, through direct feedback of the measured nacelle velocity, v_n, to the commanded blade pitch, as discussed by Jonkman [106]:

$$\Delta\beta = K_p \Delta\Omega + K_i \int_0^t \Delta\Omega dt + K_{fb} v_n \,. \tag{3.16}$$

This approach will be identified as the *nacelle velocity feedback* method.

Other methods rely on rejecting the rotor speed fluctuations caused by the FWT motions from the error $\Delta\Omega$, before the latter is fed into the controller. Skaare et al. [69] used an observer to separate the rotor speed components provoked by fluctuations in wind speed from those arising from the FWT motions – and then feeding only the former into the controller. A simpler approach, proposed by Lackner [71], modifies the reference rotor speed Ω_r based on v_n.

$$\Omega_r(t) = \Omega_0 + K_{ff} v_n \,, \quad K_{ff} < 0 \,, \tag{3.17}$$

The updated reference rotor speed Ω_r is used in the PI control law. By using the nacelle velocity for calculating the rotor speed reference, the controller is informed whether the turbine is pitching downwind or upwind, thus avoiding the rotor speed variations caused by nacelle motions to be fed into the controller. This approach will thus be identified as the *nacelle velocity feedforward* method.

Replacing Equation (3.17) in (3.9) the control law becomes:

$$\Delta\beta = K_p \Delta\Omega + K_i \int_0^t \Delta\Omega dt - K_p K_{ff} v_n - K_i K_{ff} x_n \,. \tag{3.18}$$

Comparing Equations (3.16) and (3.18), it is visible that the main difference between both approaches is the presence of a term proportional to the nacelle position. It will be clear below that this is equivalent to adding stiffness to the nacelle fore-aft displacement.

Floating wind turbines are subjected to waves, and thus the nacelle velocity will contain wave-frequency components. Although WF pitch motions are in general small, the resulting tangential velocity at the nacelle height may become a significant contribution, inducing non-negligible WF components to the blade pitch command. It is thus desirable to low-pass filter the nacelle velocity before using it in Equations (3.16) and (3.18).

Low-pass filtering can induce a significant phase lag to the filtered signal. This can affect stability of the controller, and should thus be included in the stability analysis.

3.2.5 Linear platform-rotor-filter coupled system

Stability of the platform-rotor-filter coupled system can be verified based on the eigenvalues of a linearized system of equations. Linear state-space systems are developed below for the controller without motion compensation, as well as when nacelle velocity feedback or feedforward are adopted.

In the latter two cases, the dynamics of a 2^{nd}-order Butterworth low-pass filter to the nacelle velocity are included in the equations. Other sources of phase lag into the system can be dynamic wake effects, low pass filtering of the rotor speed, and blade-pitch and generator torque actuator dynamics. These will be neglected in this analysis. Pedersen [68] provides a comprehensive stability analysis of a controller with nacelle velocity feedforward for a FWT, including dynamic wake effects.

The nacelle motion is affected by the platform surge and pitch motions. Only pitch, however, will be considered, since this is the mode for which the motion instability is more serious [106]. The uncoupled platform pitch equation is given by:

$$m_{55}\ddot{\theta} + b_{55}\dot{\theta} + c_{55}\theta = \Delta T L_h \,, \tag{3.19}$$

where m_{55} includes rigid body and added mass contributions to the inertia in pitch, b_{55} is hydrodynamic damping, c_{55} is the restoring coefficient, and L_h is the hub height w.r.t. the rotation center. c_{55} is adjusted for matching the same pitch natural period as obtained in a 2-DOF coupled system, thus also taking into account restoring effects induced by the mooring system.

The aerodynamic thrust variation $\Delta T = T - T_0$ can be linearized as in Equation (3.2). The variation in longitudinal wind speed, Δu, is a combination of turbulence and the nacelle motion:

$$\Delta u = u_t - v_n \,, \tag{3.20}$$

while the blade-pitch action $\Delta\beta$ is initially assumed not to include any of the stabilization strategies, being given as in Equation (3.9).

From now on, the notation $A_b = \frac{\partial A}{\partial b}$ is adopted. Combining the equations above, and noting that the nacelle position x_n may be related to the platform pitch angle as $x = L_h\theta$, the nacelle dynamics can be written according to:

$$\bar{m}_{55}\dot{v}_n + \left(\bar{b}_{55} + T_u\right) v_n + \bar{c}_{55}x_n - \left(K_pT_\beta + T_\Omega\right)\Omega - K_iT_\beta\phi = T_uu_t \,, \tag{3.21}$$

where the bar over m, b, c indicates division by L_h^2. Disregarding the term $\frac{P_r}{N_g\Omega_r^2}$, the rotor dynamics (Equation 3.13) can be rewritten:

$$I_d\dot{\Omega} - \left(K_pQ_\beta + Q_\Omega\right)\Omega - K_iQ_\beta\phi + Q_uv_n = Q_uu_t\,. \tag{3.22}$$

The coupled equations for the platform and rotor dynamics can now be represented in state-space form:

$$\dot{\mathbf{x}} = \mathbf{Ax} + \mathbf{Bu} \tag{3.23}$$

$$\mathbf{y} = \mathbf{Cx} + \mathbf{Du} \tag{3.24}$$

with $\mathbf{x} = [x_n \quad v_n \quad \phi \quad \Omega]^T$, $\mathbf{y} = [x_n \quad \Omega]^T$, and $\mathbf{u} = [u_t]^T$. In order to assemble the state matrix $\mathbf{A}$ and the input matrix $\mathbf{B}$, it can be helpful to rewrite the equations isolating the state derivatives:

$$\begin{aligned}
\dot{x}_n &= v_n \\
\dot{v}_n &= \frac{1}{\bar{m}_{55}}\left[-\bar{c}_{55}x_n - \left(\bar{b}_{55} + T_u\right)v_n + K_iT_\beta\phi + \left(K_pT_\beta + T_\Omega\right)\Omega + T_uu_t\right] \\
\dot{\phi} &= \Omega \\
\dot{\Omega} &= \frac{1}{I_d}\left[-Q_uv_n + K_iQ_\beta\phi + \left(K_pQ_\beta + Q_\Omega\right)\Omega + Q_uu_t\right]
\end{aligned} \tag{3.25}$$

Such that:

$$\mathbf{A} = \begin{bmatrix} 0 & 1 & 0 & 0 \\ -\frac{\bar{c}_{55}}{\bar{m}_{55}} & -\frac{\bar{b}_{55}+T_u}{\bar{m}_{55}} & \frac{K_iT_\beta}{\bar{m}_{55}} & \frac{K_pT_\beta+T_\Omega}{\bar{m}_{55}} \\ 0 & 0 & 0 & 1 \\ 0 & -\frac{Q_u}{I_d} & \frac{K_iQ_\beta}{I_d} & \frac{K_pQ_\beta+Q_\Omega}{I_d} \end{bmatrix}, \tag{3.26}$$

$$\mathbf{B} = \begin{bmatrix} \frac{T_u}{\bar{m}_{55}} \\ \frac{Q_u}{I_d} \end{bmatrix}. \tag{3.27}$$

Nacelle velocity feedback

The nacelle velocity is now included in the control law as given in Equation (3.16). Without low pass filtering, the nacelle and rotor dynamics equations now become:

$$\bar{m}_{55}\dot{v}_n + \left(\bar{b}_{55} + T_u - T_\beta K_{fb}\right)v_n + \bar{c}_{55}x_n - \left(K_pT_\beta + T_\Omega\right)\Omega - K_iT_\beta\phi = T_uu_t\,, \tag{3.28}$$

$$I_d\dot{\Omega} - \left(K_pQ_\beta + Q_\Omega\right)\Omega - K_iQ_\beta\phi + \left(Q_u - Q_\beta K_{fb}\right)v_n = Q_uu_t\,. \tag{3.29}$$

The system matrix then becomes

$$\mathbf{A} = \begin{bmatrix} 0 & 1 & 0 & 0 \\ -\frac{\bar{c}_{55}}{\bar{m}_{55}} & -\frac{\bar{b}_{55}+T_u-T_\beta K_{fb}}{\bar{m}_{55}} & \frac{K_i T_\beta}{\bar{m}_{55}} & \frac{K_p T_\beta + T_\Omega}{\bar{m}_{55}} \\ 0 & 0 & 0 & 1 \\ 0 & -\frac{Q_u - Q_\beta K_{fb}}{I_d} & \frac{K_i Q_\beta}{I_d} & \frac{K_p Q_\beta + Q_\Omega}{I_d} \end{bmatrix} . \tag{3.30}$$

If the filtered nacelle velocity, v_f, is used in the control law, the order of the system must be increased. Good filtering performance was found with a 2nd-order Butterworth low pass filter, which has the following transfer function:

$$H(s) = \frac{\omega_f}{s^2 + 2\zeta_f \omega_f s + \omega_f^2} , \tag{3.31}$$

where ω_f and ζ_f are the filter cut-off frequency and damping, respectively. The damping is commonly set to 0.707, which provides the steepest filtering action. The cut-off frequency is a compromise between filtering ability and the induced phase lag. The corresponding time-domain equations are then added to the system:

$$\begin{aligned} \dot{x}_f &= v_f \\ \dot{v}_f &= -2\zeta_f \omega_f v_f - \omega_f^2 x_f + \omega_f^2 x_n , \end{aligned} \qquad (3.32)\ (3.33)$$

and the dynamic equations become

$$\bar{m}_{55}\dot{v}_n + \left(\bar{b}_{55} + T_u\right) v_n + \bar{c}_{55} x_n - \left(K_p T_\beta + T_\Omega\right) \Omega - \\ K_i T_\beta \phi - T_\beta K_{fb} v_f = T_u u_t , \tag{3.34}$$

$$I_d \dot{\Omega} - \left(K_p Q_\beta + Q_\Omega\right) \Omega - K_i Q_\beta \phi + Q_u v_n - Q_\beta K_{fb} v_f = Q_u u_t . \tag{3.35}$$

The augmented state and output vectors become

$$\begin{aligned} \mathbf{x} &= \begin{bmatrix} x_n & v_n & \phi & \Omega & x_f & v_f \end{bmatrix}^T \\ \mathbf{y} &= \begin{bmatrix} x_n & \Omega & v_f \end{bmatrix}^T , \end{aligned} \qquad (3.36)\ (3.37)$$

and the system matrix is now 6x6:

$$\mathbf{A} = \begin{bmatrix} 0 & 1 & 0 & 0 & 0 & 0 \\ -\frac{\bar{c}_{55}}{\bar{m}_{55}} & -\frac{\bar{b}_{55}+T_u}{\bar{m}_{55}} & \frac{K_iT_\beta}{\bar{m}_{55}} & \frac{K_pT_\beta+T_\Omega}{\bar{m}_{55}} & 0 & \frac{T_\beta K_{fb}}{\bar{m}_{55}} \\ 0 & 0 & 0 & 1 & 0 & 0 \\ 0 & -\frac{Q_u}{I_d} & \frac{K_iQ_\beta}{I_d} & \frac{K_pQ_\beta+Q_\Omega}{I_d} & 0 & \frac{Q_\beta K_{fb}}{I_d} \\ 0 & 0 & 0 & 0 & 0 & 1 \\ \omega_f^2 & 0 & 0 & 0 & -\omega_f^2 & -2\zeta_f\omega_f \end{bmatrix} . \tag{3.38}$$

Nacelle velocity feedforward

Nacelle velocity feedforward is now taken into account in the controller by updating the reference rotor speed as in Eq. (3.10). Without the filter, the nacelle and rotor dynamics become

$$\begin{aligned} \bar{m}_{55}\dot{v}_n + \left(\bar{b}_{55} + T_u + T_\beta K_p K_{ff}\right) v_n + \left(\bar{c}_{55} + T_\beta K_i K_{ff}\right) x_n \\ - \left(K_pT_\beta + T_\Omega\right)\Omega - K_iT_\beta\phi = T_u u_t \, , \end{aligned} \tag{3.39}$$

$$\begin{aligned} I_d\dot{\Omega} - \left(K_pQ_\beta + Q_\Omega\right)\Omega - K_iQ_\beta\phi \\ + \left(Q_u + Q_\beta K_p K_{ff}\right) v_n + Q_\beta K_i K_{ff} x_n = Q_u u_t \, , \end{aligned} \tag{3.40}$$

while the system matrix becomes

$$\mathbf{A} = \begin{bmatrix} 0 & 1 & 0 & 0 \\ -\frac{\bar{c}_{55}+T_\beta K_i K_{ff}}{\bar{m}_{55}} & -\frac{\bar{b}_{55}+T_u+T_\beta K_p K_{ff}}{\bar{m}_{55}} & \frac{K_iT_\beta}{\bar{m}_{55}} & \frac{K_pT_\beta+T_\Omega}{\bar{m}_{55}} \\ 0 & 0 & 0 & 1 \\ -\frac{Q_\beta K_i K_{ff}}{I_d} & -\frac{Q_u+Q_\beta K_p K_{ff}}{I_d} & \frac{K_iQ_\beta}{I_d} & \frac{K_pQ_\beta+Q_\Omega}{I_d} \end{bmatrix} . \tag{3.41}$$

When the filter is included, the dynamics and system matrix are

$$\begin{aligned} \bar{m}_{55}\dot{v}_n + \left(\bar{b}_{55} + T_u\right) v_n + \bar{c}_{55}x_n - \left(K_pT_\beta + T_\Omega\right)\Omega - K_iT_\beta\phi \\ + T_\beta K_p K_{ff} v_f + T_\beta K_i K_{ff} x_f = T_u u_t \, , \end{aligned} \tag{3.42}$$

$$\begin{aligned} I_d\dot{\Omega} - \left(K_pQ_\beta + Q_\Omega\right)\Omega - K_iQ_\beta\phi + Q_u v_n \\ + Q_\beta K_p K_{ff} v_f + Q_\beta K_i K_{ff} x_f = Q_u u_t \, . \end{aligned} \tag{3.43}$$

$$\mathbf{A} = \begin{bmatrix} 0 & 1 & 0 & 0 & 0 & 0 \\ -\frac{\bar{c}_{55}}{\bar{m}_{55}} & -\frac{\bar{b}_{55}+T_u}{\bar{m}_{55}} & \frac{K_i T_\beta}{\bar{m}_{55}} & \frac{K_p T_\beta + T_\Omega}{\bar{m}_{55}} & -\frac{T_\beta K_i K_{ff}}{\bar{m}_{55}} & -\frac{T_\beta K_p K_{ff}}{\bar{m}_{55}} \\ 0 & 0 & 0 & 1 & 0 & 0 \\ 0 & -\frac{Q_u}{I_d} & \frac{K_i Q_\beta}{I_d} & \frac{K_p Q_\beta + Q_\Omega}{I_d} & -\frac{Q_\beta K_i K_{ff}}{I_d} & -\frac{Q_\beta K_p K_{ff}}{I_d} \\ 0 & 0 & 0 & 0 & 0 & 1 \\ \omega_f^2 & 0 & 0 & 0 & -\omega_f^2 & -2\zeta_f \omega_f \end{bmatrix} . \tag{3.44}$$

Filter cut-off frequency

The nacelle velocity filter is coupled to the system dynamics, as is evident from the system matrices for the different controllers. Its influence on the overall stability depends on the cut-off frequency, ω_f, which determines the filtering ability. Reducing ω_f will attenuate wave frequency components more effectively, but will also increase the phase lag at the platform pitch resonant frequency. Depending on this phase shift, feedback/feedforward of the filtered nacelle velocity may destabilize the system.

In addition, the cut-off frequency should be higher enough than the platform pitch natural frequency, such that the LF component of the nacelle velocity is not significantly attenuated by the filter. The choice of ω_f is then a compromise between removing as much as possible of the WF components from the nacelle velocity, but without affecting the LF components significantly, and avoiding excessive phase lag.

Assuming that the waves for a given site have most of their energy below 15.0 s, and that platform natural periods will typically be longer than 25.0 s, it would be reasonable in this case to set the cut-off frequency at $2\pi/20 \approx 0.31$ rad/s. Platforms with longer pitch natural periods will benefit from having lower cut-off frequencies, resulting in a more effective filtering action.

3.2.6 Stability analysis – case study

As a case study, a 20 MW spar FWT presented in Publication J.3 (Spar6) is used for a stability analysis considering the baseline controller (Equation 3.9), as well as the motion compensation strategies based on nacelle velocity feedback (Equation 3.16) and feedforward (Equation 3.18). The FWT and turbine main properties of interest used in the analysis are provided in Table 3.1.

The pitch natural period provided in the table is obtained from a coupled surge-pitch system. Since in the present analysis only pitch is considered,

Table 3.1: Spar6 20 MW FWT main properties for control stability analysis.

Property	**Value**
I_{55} (kg.m^2)	2.97×10^{11}
a_{55} (kg.m^2)	1.27×10^{11}
T_5 (s)	38.7
N_g (-)	164.0
Ω_0 (rpm)	7.15
V_r (m/s)	10.7
I_d (kg.m^2)	2.90×10^9
L_h (m)	160.20

an equivalent linear stiffness coefficient c_{55} is calculated to provide the same natural period based on a single-DOF system:

$$c_{55} = \frac{4\pi^2 m_{55}}{T_5^2} = 1.12 \times 10^{10}\,\text{N.m/rad}\,, \tag{3.45}$$

where $m_{55} = I_{55} + a_{55}$.

For a linear system, stability can be ensured when the real parts of all the eigenvalues are negative. For the baseline controller, this is verified with the $\mathbf{A}$ matrix in Equation 3.26. For the present analysis, m_{55} and c_{55} are determined as above, while the hydrodynamic damping coefficient b_{55} is disregarded. The aerodynamic derivatives are obtained with OpenFAST [108, 109]. The controller gains K_i and K_p are determined based on the required natural frequency ω_{ctr}, following Equations (3.14-3.15).

Two values for ω_{ctr} are adopted: $\omega_{ctr} = 0.31$ rad/s, corresponding to a period of 20.0 s; and $\omega_{ctr} = 0.11$ rad/s, which is the highest value possible to ensure stability for all hub wind speeds above rated, in the absence of hydrodynamic damping (detuned controller). $\zeta_{ctr} = 0.6$ is assumed for both cases. Figure 3.4 shows the real part of the eigenvalue associated with the least stable mode[1], as a function of the hub-height wind speed. It is noted that the highest values are always at rated wind speed, which thus governs the natural frequency for the detuned controller.

The eigenvalue associated with a given mode i can be related to the mode's natural frequency and damping according to:

$$\lambda_i = -\zeta_i \omega_{n,i} \pm j\omega_{n,i}\sqrt{1-\zeta_i^2}\,. \tag{3.46}$$

---

[1] The least stable mode is the one associated with the eigenvalue with least negative/-most positive real part.

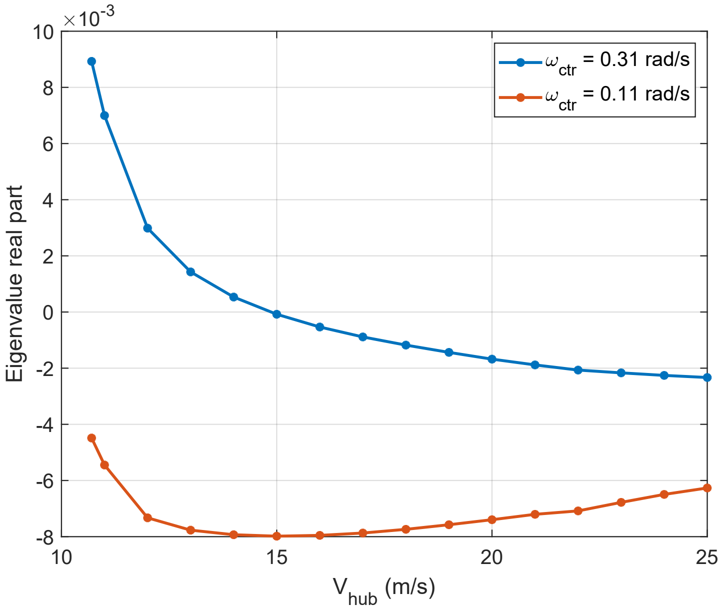

Figure 3.4: Highest eigenvalue real part for Spar6 with baseline PI controller.

For a coupled system, the eigenvalues will be associated with combinations of the modes represented by the system states. It is nevertheless possible to relate each eigenvalue with the rotor/pitch modes by comparing $\omega_{n,i}$ with the natural frequencies of the uncoupled systems – the pitch natural frequency, for the platform, and the rotor natural frequency, determined by the controller configuration. This assumption also allows the estimation of the damping associated with each mode.

Table 3.2 shows the resulting period and aerodynamic damping associated with the platform pitch motions, when the different values for ω_{ctr} are used for the baseline controller, and at rated wind speed. An aerodynamic damping coefficient of approx. -6% of the critical value is introduced to the platform motions with the higher ω_{ctr}, rendering the system unstable in pitch. It is also noted that the pitch period is increased with both controllers, but mostly for the detuned controller. This effect is further discussed in Publication J.1 and Chapter 5.

Hydrodynamic damping in pitch can be significant, especially for semi-submersible and barge platforms. In some cases it can compensate for the

Table 3.2: Period and damping associated with platform pitch motion with different controller natural frequencies – $V_{hub} = 10.7$ m/s.

ω_{ctr} (rad/s)	T_5 (s)	ζ_5 (-)
0.11	43.5	0.03
0.31	39.7	-0.06

negative aerodynamic damping, avoiding the instability. It is also possible to adjust the controller gain scheduling to obtain the largest possible gains ensuring stability at each wind speed, as proposed by Lemmer et al. [105]. Other platform concepts, like spars, may have a lower level of hydrodynamic damping, giving less room for such approach.

Figure 3.5 shows the real part of the eigenvalue associated with the least stable mode of the coupled system, when the nacelle velocity feedback approach (Equation 3.16) is adopted, as a function of the velocity gain K_{fb}. The controller natural frequency is 0.31 rad/s, and $\zeta_{ctr} = 0.6$. Two lines are shown: one without low-pass filtering of v_n; and another with the filter active, and a cut-off frequency $\omega_f = 2\pi/20.0 = 0.31$ rad/s. Without the filter, the system is stable for $K_{fb} \in [-0.191; -0.104]$. However, no range for K_{fb} rendering stability was found when the filter is present.

Lenfest et al. [35] adopted a similar approach for tuning K_{fb}, using the same controller for a 5 MW semi-submersible FWT. Values of K_{fb} ensuring stability were found, but the authors did not include the filter states in the stability analysis. In addition, hydrodynamic damping was accounted for.

Nacelle velocity feedforward (Equation 3.18), on the other hand, can provide a stable system even when the filter is present. This is shown in Figure 3.6, where the real part of the eigenvalue associated with the least stable mode is shown as a function of K_{ff}. A LP filter with $\omega_f = 0.31$ rad/s is included in the system. The three lines correspond to different controller natural frequencies, while $\zeta_{ctr} = 0.6$ is kept for all cases. The curves indicate that a gain $K_{ff} = -0.10$ rad/m is appropriate for all the ω_{ctr} considered.

Table 3.3 shows the period and damping associated with the platform pitch motions when nacelle velocity feedforward is adopted. The controller natural frequency and damping are set to 0.31 rad/s and 0.6, respectively, and $K_{ff} = 0.10$ rad/s. It is noted that the pitch period is significantly elongated, especially for wind velocities closer to rated. An aerodynamic damping coefficient of 0.17 is attained at rated wind speed, decreasing towards cut-off but no lower than 0.11.

The adoption of nacelle velocity feedforward to the baseline PI controller

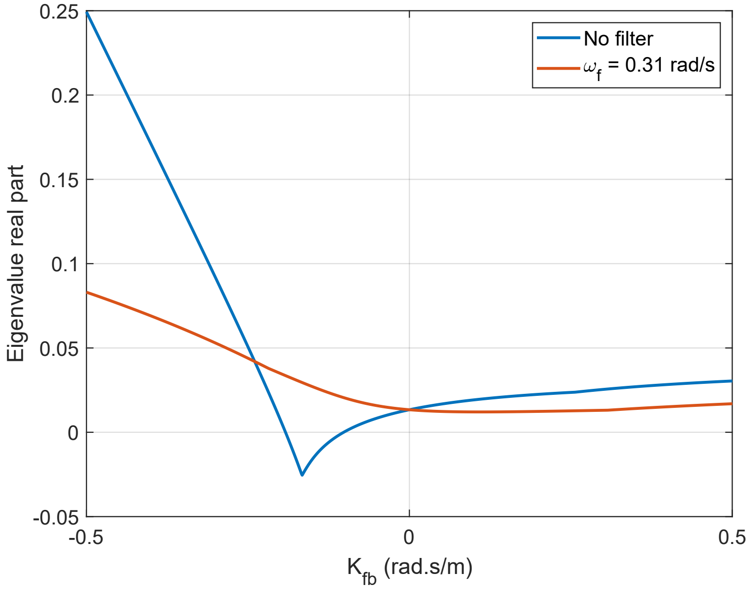

Figure 3.5: Highest eigenvalue real part for Spar6 with PI controller + nacelle velocity feedback, with and without low-pass filtering of v_n.

not only allows the choice of the desired ω_{ctr}, irrespective of the hydrodynamic damping, but also adds significant positive aerodynamic damping to the pitch motions. Section 6.2 of Publication J.3 compares time-domain simulation results adopting this strategy and the detuned controller, for Spar6, under a realistic loading condition. The performance with the former is evident not only in terms of rotor speed/power fluctuations, but also in tower bending moment at lower frequencies. Hegseth et al. [73] adopted the same motion compensation strategy in the design optimization of a 10 MW spar FWT, allowing for reduced tower dimensions than when a detuned controller was adopted.

3.2.7 Structural load mitigation

In addition to the primary purpose of regulating rotor speed, the wind turbine controller can also be configured to reduce structural loads related to the turbine operation. It is also possible to compensate for roll and yaw motions, thus reducing the associated substructure/mooring loads. This section focuses on two measures: individual pitch control, and thrust peak

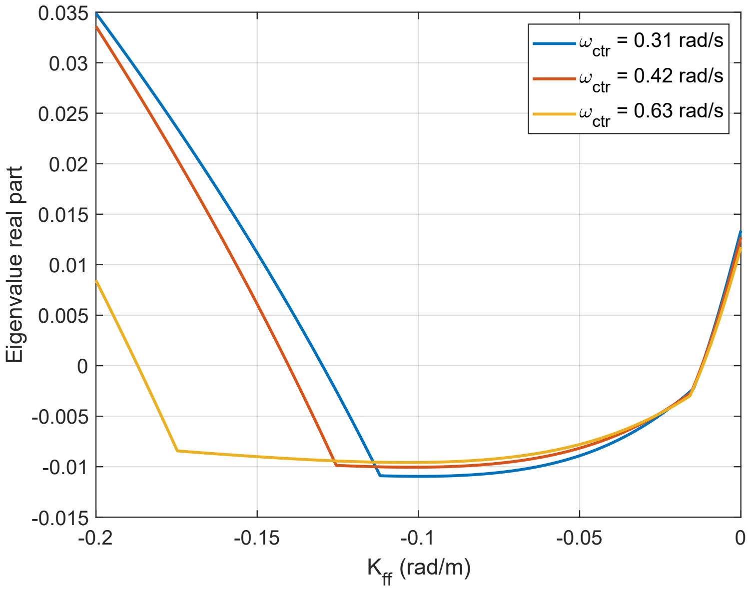

Figure 3.6: Highest eigenvalue real part for Spar6 with PI controller + nacelle velocity feedforward, for different controller natural frequencies. LP-filter on v_n active in all cases.

shaving.

Individual pitch control

The control techniques presented so far assume collective blade pitch control – that is, the controller commands the same pitch angle to all blades. Individual pitch control (IPC) consists of commanding specific increments to each blade, on top of the collective command. Although not used in this work, a short discussion about its uses is included here.

One of the main reasons to adopt IPC is to reduce excitation at blade passing frequencies. The individual blade pitch commands may be determined in order to compensate for the different wind velocity seen by each blade, caused by wind shear, tower shadow effects, and turbulence.

As pointed out by Bossanyi [103], however, effective reduction of blade-passing related loads with IPC is only possible if the asymmetric loading on the rotor can be measured with accuracy. This is because the wind speed variations through the rotor of large wind turbines are dominated by

Table 3.3: Period and damping associated with the platform pitch motion, for a controller with nacelle velocity feedforward. $\omega_{ctr} = 0.31$ rad/s, $\zeta_{ctr} = 0.60$, $K_{ff} = 0.10$ rad/s.

	V_{hub} (m/s)			
	10.7	15.0	20.0	25.0
T_5 (s)	65.4	55.6	51.7	49.7
ζ_5 (-)	0.17	0.17	0.14	0.11

stochastic turbulent components, rather than the deterministic ones due to wind shear and tower shadow. For these latter, IPC could be based on the rotor azimuth at each instant, which is easy to measure.

Individual pitch control can also be used to create aerodynamic moments around the rotor. Namik et al. [110] used this feature to compensate for roll and pitch motions of a 5 MW barge FWT, and time-domain simulations showed a significant reduction in both the motions rate and tower base fatigue damage. The moments to compensate for a FWT motion in roll/pitch are however of large magnitude, while the method relies on applying these loads exclusively at the rotor. Although not discussed in the paper, the associated structural costs for blades, shaft, drivetrain, and tower top are expected to be significant, if not prohibitive.

Thrust peak shaving

Rotor thrust peaks at rated wind speed. The force, applied at hub height, can result in high loading at the tower base. In addition, the mean platform pitch angle can produce a high mean gravitational load related to the RNA weight, which is shown in Publication J.3 to have an important contribution to extreme loads in large FWTs.

Thrust peak shaving consists of limiting the rotor thrust at a range near rated wind speed, by pitching the blades to a minimum angle [111]. A look-up table can be created, relating the blade pitch as a function of e.g. incoming wind speed at hub height, in order to achieve the desired thrust.

By increasing the blade pitch angle, while keeping rotor speed and wind speed constant, one should expect also a reduction in aerodynamic torque, and thus, power. This is illustrated in Figure 3.7, which shows rotor thrust and power for the 20 MW wind turbine presented by Ashuri et al.[4]. A 13% reduction in thrust is achieved at rated wind speed, with up to 8% loss of produced power just below rated wind speed.

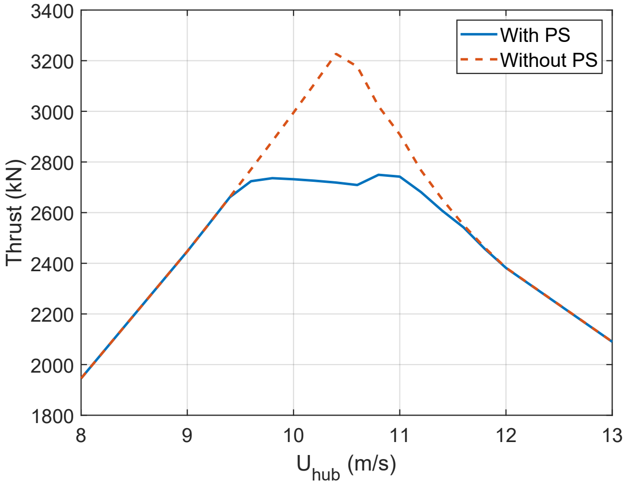

(a) Thrust

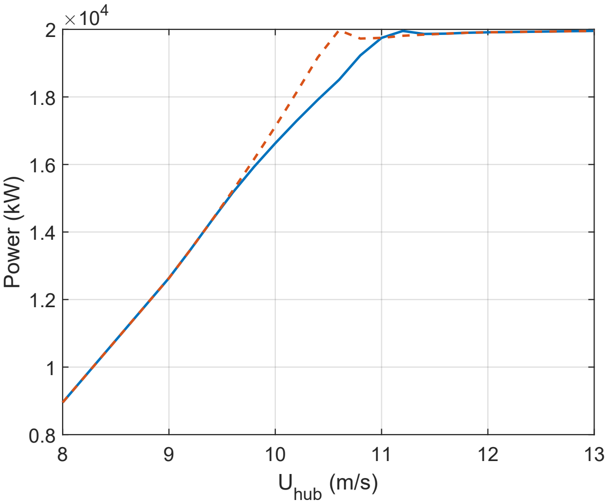

(b) Power

Figure 3.7: Thrust and power curves with and without peak shaving, for a 20 MW wind turbine [4].

Chapter 4

Floating wind turbine time-domain analysis

Numerical simulations are an important tool in the analysis of FWT global dynamics, structural integrity assessment, mooring system responses, and controller performance. This chapter describes models for environmental loads, procedures for FWT coupled analyses, and the methodology for fatigue and extreme analysis adopted in this work.

4.1 Environmental modeling

4.1.1 Waves

Linear wave theory, also known as Airy theory, assumes waves as harmonic and provides in general a good representation of ocean waves with limited height [112]. A realistic, irregular wave is then idealized as the superposition of regular (harmonic) waves, with varying amplitude and period.

A *sea state* can be characterized by parameters describing the typical height and period of the waves. The significant wave height, H_s, is defined as the average of the one-third highest waves in a sea state. The wave peak period, T_p, corresponds to the frequency associated with the most energetic waves in the same sea state. These parameters are normally assumed to remain stationary for a period of up to 3 hours, which is thus considered a typical duration of a short-term sea state [84].

A wave spectrum is a description of the energy density distribution of a sea state in the the frequency-domain. Wave time series can be obtained from the wave spectrum with an inverse Fourier transform. Some empirical formulations provide a wave spectrum as a function of H_s and T_p. The

JONSWAP spectrum is an appropriate formulation for developing seas[1], and is given by[112]:

$$S_w(\omega) = \left[1 - 0.287\ln(\gamma)\right]\frac{5}{16}H_s^2\omega_p^4\omega^{-5}\exp\left[-\frac{5}{4}\left(\frac{\omega}{\omega_p}\right)^{-4}\right]\gamma^{\exp\left[-0.5\left(\frac{\omega-\omega_p}{\sigma\omega_p}\right)^2\right]}, \tag{4.1}$$

with σ given by

$$\sigma = \begin{cases} 0.07 & \text{for } \omega \leq \omega_p \\ 0.09 & \text{for } \omega > \omega_p \end{cases},$$

while γ is the peak-shape parameter. If not provided, γ can be related to H_s and T_p according to:

$$\gamma = \begin{cases} 5.0 & \text{for } T_p/\sqrt{H_s} \leq 3.6 \\ \exp\left(5.75 - 1.15T_p/\sqrt{H_s}\right) & \text{for } 3.6 < T_p/\sqrt{H_s} < 5.0 \\ 1.0 & \text{for } T_p/\sqrt{H_s} \geq 5.0 \end{cases}. \tag{4.2}$$

The JONSWAP spectrum parameters above relate to North Sea conditions, and should be adapted to local data before being used for other regions. Figure 4.1 shows the spectrum calculated for two sea states, with same H_s and different T_p, with γ given by Eq. (4.2). For the sea state with shorter T_p, γ becomes higher, resulting in a spectrum with energy more concentrated around ω_p.

Long-crested (unidirectional) waves are directly represented by the wave spectrum. Short-crested waves can be obtained by multiplying the spectrum with a wave energy spreading function [84].

4.1.2 Wind

Time-domain analysis of FWTs requires a wind model that reasonably captures the temporal and spatial variations of the incident wind velocity field through the rotor. Although the wind propagates in three dimensions, it is normally the horizontal component, across the rotor plane, that is used to characterize the wind condition for a given load case.

For the purpose of wind turbine design, time variations in the wind velocity of up to hours are of interest, encompassing both turbulence and gusts [21]. Gusts are normally assumed as deterministic events in wind turbine analysis, and are not considered in this thesis. Turbulence has a

---

[1] Other standard wave spectrum formulations, like the Pierson-Moskowitz, Bretschneider, and Torsethaugen, can be more adequate to represent sea states for other conditions, including fully-developed seas or spectra with more than one peak [112]

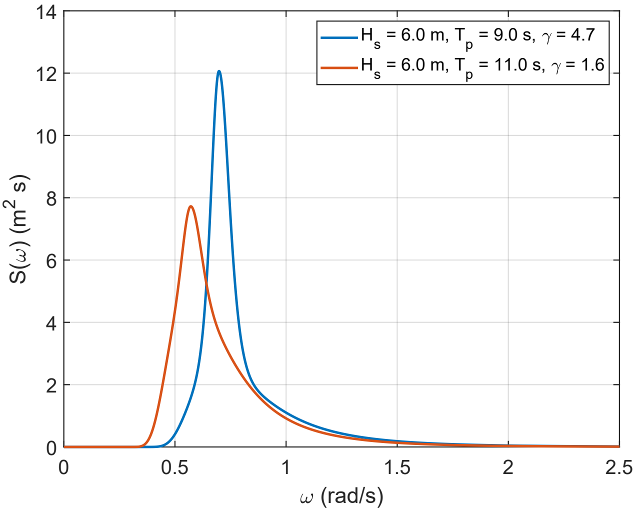

Figure 4.1: JONSWAP spectra for two different sea states. Although both have the same significant wave height, the different peak periods result in different γ, calculated according to Eq (4.2), affecting the energy distribution around ω_p.

stochastic nature, and it is usual to assume the total wind speed as the superposition of a mean and a turbulent component:

$$U = U_m + u_t \,. \tag{4.3}$$

The mean component, U_m, varies with height. Wind shear, as the variation is known, can be described with a power law profile:

$$U_m(z) = U_m(z_{ref})(z/z_{ref})^{\alpha} \,, \tag{4.4}$$

where the wind shear exponent α can be provided with metocean data, and is normally in the range 0.1-0.2.

The turbulent component, u_t, is commonly assumed as stochastic, following a zero-mean Gaussian distribution [113]. Turbulence intensity, I, is defined as the ratio between the standard deviation of u_t and the mean component:

$$I = \frac{\sigma_{u_t}}{U_m} \,. \tag{4.5}$$

While metocean data can provide typical values of I for specific sites, it is also common to adopt the turbulence characteristics recommended by IEC 61400-1 [113] in the structural analysis of FWTs. The *normal turbulence model* (NTM) applies for operational conditions, and prescribes the standard deviation of the turbulent component as:

$$\sigma_{u_t} = I_{ref}(0.75U_m(z_{hub}) + b)\,, \tag{4.6}$$

with $b = 5.6$ m/s, and the reference turbulence intensity I_{ref} corresponding to a hub wind speed of 15.0 m/s, defined according to the wind turbine class. Since turbulence is typically moderate at offshore sites, wind turbine class B (medium, $I_{ref} = 0.14$) or C (low, $I_{ref} = 0.12$) are reasonable choices for FWT analyses. For extreme conditions, the *extreme wind speed model* (EWM) can be adopted:

$$\sigma_{u_t} = 0.11U_m(z_{hub})\,. \tag{4.7}$$

The turbulent fluctuations in the wind speed are not uniform across the rotor plane. Although they are normally modelled with the same statistical properties, the wind speed measured at different points at a given instant will be different. A coherence function measures the dependence between turbulent wind speed time series at different points in space [102]. Together with wind shear, the spatial wind speed variations provoke important load fluctuations at the blade-passing frequencies.

Turbulent wind time series can be obtained based on turbulence models, of which the Kaimal spectrum associated with an exponential coherence model, and the Mann uniform shear model, are listed by IEC-61400-1. Bachynski and Eliassen [114] compared global responses for different FWT concepts using both models, finding non-negligible differences for low-frequency motions. Each model provided larger responses for specific DOFs, which is related by the authors to the different coherence models. Nybø et al. [115] found that, for a 15 MW spar FWT, both formulations produce lower surge and pitch motions, compared with another model that uses offshore wind field measurements into account. One of the explanations risen by the authors is the ability of this model to reproduce large scale wind speed fluctuations, thus exciting low-frequency FWT motions more realistically.

Three-dimensional turbulence time-series for the analyses in this thesis were generated based on the Kaimal model, using the software TurbSim [116]. The grid width and height were determined based on the rotor diameter, with a 32 x 32 grid for all the turbines analyzed.

4.1.3 Current

Current speed profiles can have complex variation with the water depth, but it is a common practice to model them with e.g. a power law formulation [50]. A current model can have significant impact on the integrity assessment of mooring lines and power cables, but current loads are normally negligible compared with wind and wave loads in the structural analysis of FWT platforms. For this reason, current loads are not considered in this thesis.

4.2 Floating wind turbine coupled analysis

A coupled system is, in the context of this thesis, a dynamic system composed of elements that interact significantly with each other. The term "coupled analysis", when used in this work, refers to a time-domain analysis of a coupled FWT system, where the most important interactions of a FWT's sub-systems are considered simultaneously with the overall system response.

Floating wind turbine global dynamics are mainly affected by three sources of loads: aerodynamic loads, at rotor, tower, and platform; hydrodynamic/hydrostatic loads, at the platform; and mooring positioning loads, also at the platform. The platform motions can affect the aerodynamic loads considerably[2]. These loads, conversely, induce displacements on the platform from its equilibrium position. The interactions between the platform motions and the control system, discussed in Chapter 3 and Publications J.1 and C.1, are another important source of coupling for FWTs – in simple terms, the pitch natural period, as well as the aerodynamic damping in surge and pitch, can be affected by the wind speed, motion frequency, and controller configuration. In addition, the mooring restoring loads can become nonlinear for large mean platform displacement due to winds and waves – which also affects the surge natural period.

Another important characteristic of FWTs is the variety of frequency ranges at which resonant structural responses can be excited. Significant tower vibrations may occur if the tower modal frequencies fall inside blade-passing ranges, increasing fatigue damage substantially [56]. Blades flexible modes can interact with the controller, if no proper filtering of rotor speed or other controller signals is implemented. Platform rigid-body motions are in general at frequency ranges with significant wind excitation. For spars,

---

[2] Hydrodynamic loads are also affected by the platform displacement, but this effect is not captured by first-order theory, which is the scope of this thesis – except for the slowly-varying wave loading in Publication J.3.

yaw can also be excited by 1p rotor loads.

Coupled analyses have been traditionally adopted in the assessment of marine structures comprising a floating body attached to slender elements (e.g. risers and mooring lines) [49]. The development of this approach, where the floating body and slender structures dynamics are evaluated simultaneously, represented a significant gain in the accuracy of predicted tensions on the latter, in comparison with a "de-coupled analysis" – where floater motions are obtained separately and then prescribed to the fairleads [117]. In short, a coupled analysis should be considered whenever resonant vibrations of different components can affect the system's global dynamics.

As described in Chapter 2, floating wind turbines are in many cases modelled as a combination of rigid bodies and slender structures. This, in addition to the highly coupled dynamics of FWTs, make coupled analyses fundamental for accurately computing motions and structural loads at the platform, tower, rotor blades, and mooring lines. Time-domain coupled analysis are required by both DNV-ST-0119 [46] and IEC61400-3-2 [45] in FWT structural assessment.

4.2.1 Numerical tools for coupled analyses of FWT

The term *aero-hydro-servo-elastic* refers to software which include the aerodynamic and hydrodynamic load models, control systems, and structural models needed for the analysis of offshore wind turbines [118]. Software for FWT simulations are often adapted from existing tools for onshore wind turbine analysis (e.g. HAWC2 [119], Bladed [120], OpenFAST [121]), or for offshore engineering (e.g. Sima [122], OrcaFlex [123]). It is thus to expect that the latter have more emphasis on hydrodynamic models, while the former have a larger emphasis on aerodynamics and drivetrain mechanisms.

Most of the research carried out in this thesis adopted Sima for the numerical simulations. OpenFAST was also used, but in a minor extent. In addition, NREL's Reference OpenSource Controller (ROSCO) [124] is used in part of the work.

Sima

Sima performs aero-hydro-servo-elastic simulations in the time domain, by combining Simo and Riflex – two programs originally developed for the analysis of marine structures.

Simo [125] is a simulator for complex marine operations, meaning that it can include multibody systems, with couplings. It includes models for hydrostatic restoring, 1^{st}- and 2^{nd}-order loads based on potential theory for large bodies, and load models for slender structures based on the Morison formulation. Mooring loads from catenary systems can be evaluated based on a quasi-static catenary model. A matrix of quadratic wind coefficients can be used for inclusion of wind loads.

Riflex [126] is a software based on a nonlinear finite element formulation, intended for the analysis of marine slender structures in the time domain. Both bar and beam elements can be used in the models, and hydrodynamic loads can be applied at nodes using different hydrodynamic models – including Morison formulation, potential theory, or the MacCamy-Fuchs formulation.

Wind turbine aerodynamic loads can be computed in Riflex using the blade element momentum (BEM) formulation. Glauert's correction is adopted for high induction factors, and Prandtl's correction factors for losses associated with the hub and blade tip can also be considered. Dynamic wake and dynamic stall are accounted for based on Øye's formulations [102]. A 2-D potential flow formulation around a circle is used for accounting for tower shadow effects. Control systems are supported for the generator torque, blade pitch angle, and nacelle yaw.

Details on Simo and Riflex implementations for FWT coupled analyses are provided by Ormberg et al. [127] and Luxcey et al. [82]. Simulations done with the package are compared against real-scale data of a 2.3 MW spar FWT by Skaare et al. [107]. A comparison with other programs in terms of hydrodynamic loads was done in the *Offshore Code Comparison Collaboration, Continuation* (OC4) project, where good agreement is observed with those codes using similar hydrodynamic models [118].

OpenFAST

OpenFAST is an open-source aero-hydro-servo-elastic software, based on multibody and modal superposition models. In contrast with Sima, OpenFAST was initially intended for onshore wind turbine simulations, but the main hydrodynamic models for FWTs have been implemented in the last years.

In addition to performing time-domain simulations, OpenFAST also includes the option of performing linearization of the system dynamics around user-defined operational points, based on a central-difference perturbation technique [108, 109]. This feature is particularly useful for obtaining the aerodynamic derivatives used in Chapter 3 for tuning the control system and evaluating the stability of the coupled control-rotor-platform system.

ROSCO

ROSCO is an open-source offshore wind turbine controller, featuring not only the algorithms for a VSVP controller but also wind speed estimators, nacelle yaw controller, individual pitch control, peak shaving, among other functionalities. It can be used in time-domain simulations as an external library, which is called at each time step by the aero-hydro-servo-elastic software. A modified version of ROSCO was adopted in Publication J.3.

4.2.2 Modelling considerations for FWT coupled analyses

Coupling between a rigid body and a FE model is normally done using a "master-slave" approach [49]. When the FWT platform is modelled as rigid, a common procedure is to set the tower base and mooring line fairleads as nodes slaved to a node fixed to the platform. The platform motions are then imposed to the tower base and mooring lines, which in turn also affect the floater dynamics.

In Sima, the rotor blades can be assumed either as rigid or flexible. In the latter case, a FE model with beam elements is adopted. The blade root is slaved to the shaft, which is free to rotate around its own axis but has the other extremity slaved to the tower top. A combination of bodies and beams can be used to model the hub and nacelle inertia properties.

A detailed model of the mooring lines, using finite elements, is only necessary if a structural assessment of the mooring system itself is to be done; or if details of the system are too complicated to be obtained with a quasi-static model. Otherwise, adoption of the latter can reduce computational time significantly. In this case, the mooring system loads are represented as a forces applied at a node at the fairleads positions.

The control system should be activated during all operational conditions. The controller receives the rotor speed and other signals of interest (e.g. nacelle velocity) from the simulator, and feeds back the demanded generator torque and blade pitch angle – which in Sima are imposed to the rotor shaft and blade root, respectively. Models for the generator torque and blade pitch actuator are not available, such that the associated dynamics, when relevant, must be evaluated inside the controller library. These effects are not considered in any of the analyses performed in this work, though.

Flexible platform modelling

When the platform is modelled as a flexible structure, it is necessary to distribute the hydrodynamic loads over the body surface, such that the correct structural deflections – and thus sectional loads – are obtained during the analysis. For the scope of this thesis, the interest is on sectional loads at the main components of a FWT platform (the cylinder of a spar, or columns/pontoons of semi-submersibles and TLPs). Figure 4.2 illustrates the distribution of wave excitation force on a spar FWT.

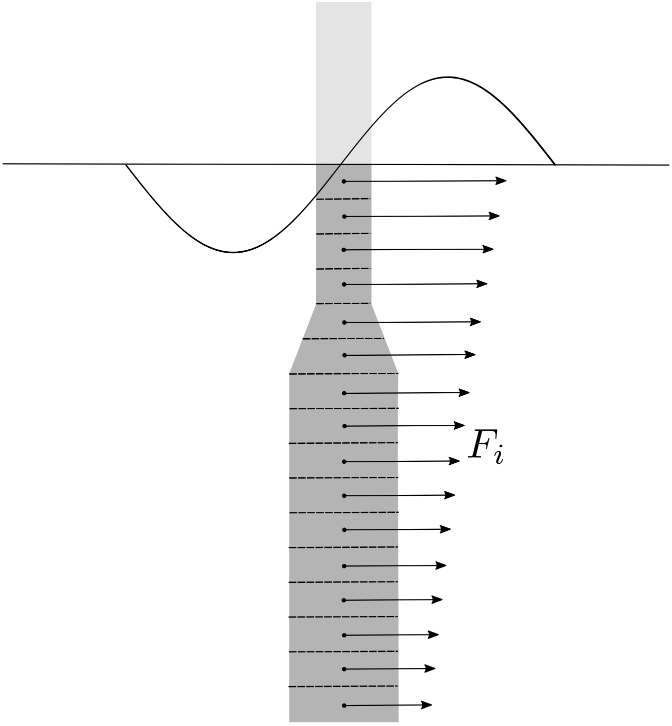

Figure 4.2: Discretization of a spar FWT platform for distribution of hydrodynamic loads. In the figure, the force vectors F_i represent the wave horizontal excitation force.

A first step to make a flexible platform model is then to decide upon the discretization to be used for the hydrodynamic load distribution. The number of segments should be large enough to provide a good representation of the mode shapes of interest, as well as the to ensure that added mass and radiation damping in the rotational DOFs are correctly represented.

Some potential-theory software can output not only the radiation and diffraction loads, but also the pressures associated with the panels obtained from the solution to each problem. These pressures can be used to compute the loads corresponding to each of the platform segments, after solving the problem assuming the body as rigid. It is recommended to adapt the mesh of the hull such that each segment contains an integer number of panels.

One concern with a FE model of a floating platform is to ensure that the buoyancy is properly accounted for in the calculation of the sectional loads. Depending on the modelling strategy, the buoyancy may be calculated based on the platform fraction below the section of interest only, which differs from the integrated pressure over the hull. A more detailed description of the problem, as well as a fix for a spar FWT, are presented in Publication J.3.

4.2.3 Simulation parameters

The simulated time for each load case realization is limited by stationarity of the environmental parameters. At the same time, floating wind turbines can have long natural periods, and a simulation should last long enough to allow a sufficient number of low-frequency vibrations.

Waves are commonly assumed as stationary over 3 hours [50]. The mean wind speed, on the other hand, is in general assumed to remain stationary over 10 minutes only [113]. Manwell et al. [21] however claim that a mean wind speed can be assumed stationary to up to 1 hour. In this work, 1-hour turbulent time series are adopted, since this assumption is conservative in terms of extremes [45] and avoids repeating 10-min wind time-series.

A consistent load and mass formulation was adopted for all the analyses involving a FE model. Material properties are assumed as linear. A Newmark integration procedure [94] was adopted, with $1/\beta = 3.9$ and $\gamma = 0.505$. The time step adopted was 5.0 ms in all analyses.

4.3 Structural assessment of FWTs

Structural integrity assessment consists of verifying the ability of a structure to withstand the expected environmental loads during a specified time span – typically longer than 20 years for FWTs. Accumulated structural damage due to cyclic loads can lead to fatigue failure, while extreme loads caused by harsh environmental conditions can exceed the material yielding limit, or provoke failure by buckling.

In this section, methods for evaluating fatigue damage and extreme loads in FWTs are presented. Failure by accident (e.g. control system faults, or collision with ships) can also affect the life of FWTs, but is not in the scope of this thesis.

4.3.1 Stochastic description of environmental conditions

The selection of an offshore wind park site is normally based on metocean data, obtained from measurements and numerical atmospheric models. Probability distributions of wind and waves are then adjusted to this data, providing the likelihood of occurrence of a given environmental condition.

For floating wind turbine analyses, a common procedure is to depart from a set of mean wind speeds, and then determine associated sea states based on a joint distribution of mean wind speed, wave significant height, and wave peak period. Although the directionality of wind and waves is also a stochastic parameter, it is in general conservative to assume co-linear wind and waves in FWT structural assessment [56, 59]. This assumption is adopted for all the analyses in this thesis [3].

Li et al. [128] used 10 years of environmental hindcast data to provide long-term joint distributions of wind and waves for five sites in the Atlantic and North Sea. The joint distribution of U, H_s, and T_p combines the marginal distribution of U; a conditional distribution of H_s, for a given U; and a conditional distribution of T_p, for a given pair (U, H_s):

$$f_{U,H_s,T_p}(u,h,t) = f_U(u) f_{H_s|U}(h|u) f_{T_p|U,H_s}(t|h,u)\,. \tag{4.8}$$

A two-parameter Weibull distribution is adopted to describe the marginal distribution of the one-hour mean wind speed at 10 m height, U_{10}. The probability density function (PDF) is given as follows:

$$f_{U_{10}}(u) = \frac{\alpha_U}{\beta_U}\left(\frac{u}{\beta_U}\right)^{\alpha_U - 1} \exp\left[-\left(\frac{u}{\beta_U}\right)^{\alpha_U}\right], \tag{4.9}$$

where α_U and β_U are the shape and scale parameters, respectively.

The conditional distribution of H_s for a given U is also assumed as a two-parameter Weibull distribution, with the following PDF:

$$f_{H_s|U}(h,u) = \frac{\alpha_{HU}}{\beta_{HU}}\left(\frac{h}{\beta_{HU}}\right)^{\alpha_{HU} - 1} \exp\left[-\left(\frac{h}{\beta_{HU}}\right)^{\alpha_{HU}}\right], \tag{4.10}$$

with the parameters α_{HU} and β_{HU} given by

$$\begin{aligned}\alpha_{HU} &= a_1 + a_2 u^{a_3}\\ \beta_{HU} &= b_1 + b_2 u^{b_3}\,.\end{aligned}$$

---

[3] Co-linear wind and waves may not be the most conservative configuration for some load cases not analyzed in this thesis, like emergency stops.

For the conditional distribution of T_p for a given pair (U, H_s), a log-normal distribution is adopted, with mean and standard deviation dependent on U and H_s. Due to limitations on the data relating both parameters, the authors propose an approximation for Eq. (4.8) where $f_{T_p|U,H_s}(t|h,u)$ is replaced by the conditional distribution of T_p on H_s only:

$$f_{U,H_s,T_p}(u,h,t) \approx f_U(u) f_{H_s|U}(h|u) f_{T_p|H_s}(t|h)\,, \tag{4.11}$$

with $f_{T_p|H_s}(t|h)$ following a log-normal distribution:

$$f_{T_p|H_s}(t|h) = \frac{1}{\sqrt{2\pi}\,\sigma_{TH} t} \exp\left[-\frac{1}{2}\left(\frac{\ln t - \mu_{TH}}{\sigma_{TH}}\right)^2\right]. \tag{4.12}$$

The distribution mean μ_{TH} and variance σ_{TH} are given by

$$\begin{aligned} \mu_{TH} &= c_1 + c_2 h^{c_3} \\ \sigma_{TH}^2 &= d_1 + d_2 \exp(d_3 h)\,. \end{aligned}$$

The site-dependent parameters in Eq. (4.9,4.10,4.12) are provided by Li et al. [128], and are not reproduced here.

4.3.2 Fatigue analysis

Cyclic loads provoke the appearance and growing of cracks at certain points of a structure. The fatigue limit state (FLS) is determined by the accumulated damage through the structure's operational life. For floating wind turbines, cyclic loads are mainly caused by the action of wind, waves, and the loads associated with rotation of the blades and drivetrain machinery [95].

Fatigue analysis in the scope of this work is limited to damage accumulation at steel welds. The axial stress at an azimuthal outer location θ of a circular cross section (Fig. 4.3) is computed from the axial force and bending moments, obtained from the time-domain FE simulations:

$$\sigma_x = \frac{N_x}{A} + \frac{M_y}{I_y} r\cos\theta - \frac{M_z}{I_z} r\sin\theta\,, \tag{4.13}$$

where N_x is the axial force; A is the annular section area; r is the section radius; M_y, M_z are the bending moments around the y and z axes; and I_y, I_z are the section moduli around the bending axes.

The axial stress time-series is an irregular, varying amplitude signal. Assuming that the effect of mean stress is negligible in crack growth, fatigue damage is then calculated with the varying part of the signal. The Rainflow

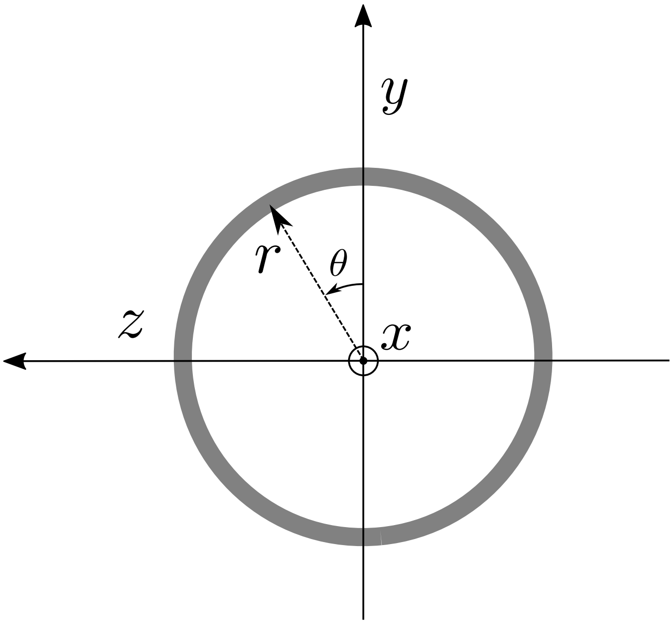

Figure 4.3: Circular cross section.

counting algorithm, as implemented in the MATLAB toolbox WAFO [129], is adopted for finding a sequence of equivalent load cycles with range S_i. Adopting a bi-linear S-N curve, combined with Palmgren-Miner's rule of linear damage accumulation, the damage is given by

$$D = \frac{1}{\bar{a}_1} \sum_{i=1}^{n_l} S_i^{m_1} + \frac{1}{\bar{a}_2} \sum_{j=1}^{n_h} S_j^{m_2} , \tag{4.14}$$

where the first summation accounts for the n_l cycles with $S_i > S_{lim}$ (low cycle region), while the second summation refers to the n_h cycles with $S_i < S_{lim}$ (high cycle region). The coefficients $\bar{a}_{1,2}$ are the intercept of each branch of the the S-N curve with the $\log N$ axis, while $m_{1,2}$ are the negative inverse slopes. S-N curves for welds typically found in marine structures are provided in the Recommend Practice DNV-RP-C203 [48], which is adopted for the analyses in this thesis.

Load case selection for fatigue analysis

Frequent, non-extreme wind and wave conditions contribute more significantly to fatigue damage of offshore structures [83]. A long-term analysis consists of determining relevant ranges of U, H_s, and T_p, and then running short-term simulations for all the combinations in this range with non-negligible joint probability of occurrence. The damages computed with Eq. (4.14) at different points of the structure are then weighted with Eq. (4.8 or 4.11). The inverse of the weighted damage provides the expected fatigue life.

This procedure can result in a large number of load cases to be analyzed. Assuming typical ranges and bin widths for the mean hub wind speed, wave significant height, and peak period, the number of combinations can easily reach the order of 1×10^3. In addition, due to the stochastic nature of turbulent wind and waves, several realizations of each combination are normally needed in a fatigue analysis. The total number of simulations can become prohibitive even for modern computers.

An appropriate selection of load cases can reduce the number of cases to be analyzed significantly. Lumping techniques consist of selecting few sea states representative of the H_s, T_p scatter diagram associated with a given U. In the present work, fatigue analysis was meant to compare between different modelling approaches, or the performance of different FWT designs.

Therefore, only the most probable sea state associated with each mean hub wind speed – defined as the H_s and T_p that, for a given U, maximize f_{U,H_s,T_p} – was considered. Although useful for comparing different models, it is remarked that the approach disregards other combinations of wind and waves that, although less likely to occur, could provoke higher structural damage than the most probable condition.

Kvittem and Moan [56] analyzed the sensitivity of fatigue estimate to simulation length, number of realizations, and bin size for the discretization of U, H_s, and T_p ranges, in the analysis of a 5 MW semi-submersible FWT. Based on their conclusions, four 1-hour realizations of each condition are assumed to be adequate for the analyses in this thesis.

4.3.3 Extreme value analysis

Extreme sectional loads in FWTs are relevant in the assessment of material yielding, as well as in buckling analysis. In general, they are provoked by combinations of harsh wind and wave conditions.

In contrast to fatigue analysis, extreme loads are not directly extracted from time-domain simulations. Instead, the simulations are used for determining an extreme value distribution, from which the extreme load is inferred. Again, a full long-term analysis would not be practical, due to the large number of environmental conditions (and realizations) to be evaluated.

In addition, only a limited set of conditions govern the tail of the extreme distribution – which is the region of interest in the context of extreme values.

In a short-term analysis, the mean wind speed and sea state parameters are assumed as stationary over a time span – assumed as one hour in this work. The extreme distribution is obtained from the extremes of a number of realizations of a given short-term condition. Typically, the Gumbel distribution fits satisfactorily to extreme loads in marine structures [83]. Figure 4.4 illustrates the definition of extreme values from short-term time series, as well as a Gumbel PDF.

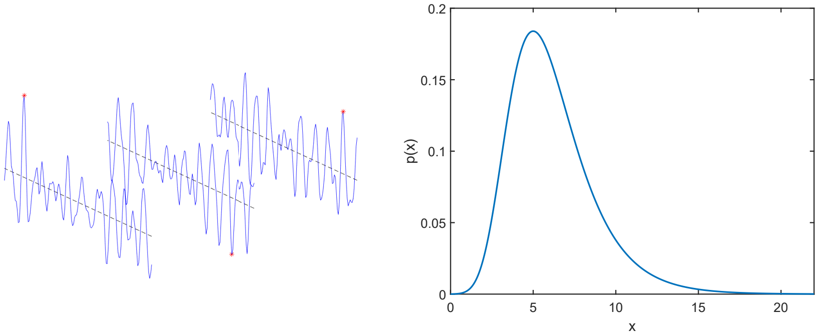

(a) Extreme value

(b) Gumbel distribution

Figure 4.4: Extreme values for different realizations, and Gumbel distribution.

Load case selection for extreme value analysis

Since only one value per realization is used for fitting the distribution, many simulations of each environmental condition may be needed for a good description of the distribution tail[4]. It is then desirable to select a reduced number of conditions, covering the relevant cases for obtaining the extreme distribution. One approach to select load cases is the FORM/IFORM method, which involves transformation of variables from the environment/response space to a normalized space [83].

An even simpler approach is the *environment contour method* (ECM), which is based on the environment only, without accounting for the response. The approach assumes that the largest responses will be caused by

---

[4] Alternative approaches, like the *peaks over threshold* (POT) method or the *Average Conditional Exceedance Rate* (ACER) method, use more data from each realization for the description of an extreme distribution [83].

wind/wave conditions associated with a given return period. For wind turbines, however, the largest mean wind loads are associated with operational conditions. The extreme response may thus not necessarily be associated with the extreme wind condition, which in general corresponds to an idling turbine.

Li et al. [61] proposed a *modified environmental contour method* (MECM), for the extreme analysis of FWTs. In this approach, not only the contour associated with an extreme wind, but also those corresponding to operational conditions, are taken into account in the analysis. By including the contour associated with the cut-off wind speed, in addition to the 50-year wind contour, the authors found that the extremes obtained with this method were within 10% of the results obtained with a full long-term analysis, for a 5 MW semi-submersible FWT.

For the extreme analyses in this work, the MECM is adopted including the contours associated with the rated and cut-off mean wind speeds, in addition to the 50-year wind speed. For each wind speed, infinite combinations of Hs and T_p yielding a return period of 50 years form the contour. A limited number of load cases are then selected along the contour domain. The contours are more easily determined by performing a transformation of variables, from the random environmental variables space (X-space), to a space where the variables follow a standard normal distribution (U-space):

$$F_X(x) = \Phi(u)\,, \tag{4.15}$$

where F and Φ are the CDFs in the respective spaces. Figure 4.5 shows the contours used in Publication J.3, in which 5 load cases are selected from the contours associated with the rated and cut-off wind speeds. For the 50-year wind speed, the H_s and T_p parameters forming the contour did not vary significantly, so only one pair was considered.

Extreme value estimation

For each load case from all the contours, a PDF for the 1-hour extreme sectional axial stress (Eq. 4.13) is obtained from the extremes of n realizations. The corresponding cumulative distribution function (CDF) is then obtained from integration of the PDF, and the extreme value associated to each load case is finally taken as the p-fractile of the CDF.

The overall extreme axial stress at each section is determined as the largest extreme value from all the load cases. In this work, $n = 20$ 1-hour realizations are considered for each load case. A fractile of 90% is assumed for all the contours.

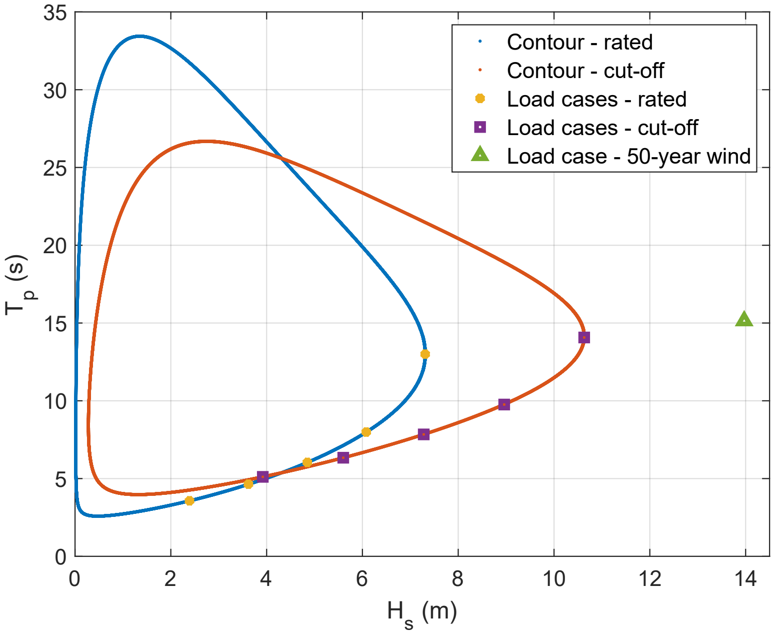

Figure 4.5: Environmental contours adopted in publication J.3.

Chapter 5

Results and discussion

This chapter relates some of the contributions to the publications. An extended description of the motivation, methods, and main results of each publication is provided, as well as a discussion on potential implications in the modelling, design, and analysis of floating wind turbines. The complete publications are found in Appendix A.

5.1 FWT global dynamics

Interactions between the platform dynamics, the rotor dynamics, and the wind turbine control system are assessed by Publications J.1 and C.1. In particular, variations in surge and pitch natural periods under operational conditions are explained, and the notion of frequency-dependent apparent inertia and damping effects is introduced.

5.1.1 Publication J.1

The starting point for Publication J.1 was the model test results reported by Bachynski et al. [29], with the CSC 5 MW semi-submersible FWT [3]. The surge and pitch decay periods for three wind speeds (8.0 m/s, 11.4 m/s, 15.0 m/s) were longer for the cases with non-zero wind speed, compared to the no-wind case, the highest variation being for the rated wind speed.

Another publication, by Goupee et al. [30], also reported an elongation in the pitch period during model tests with the 5 MW semi-submersible FWT used in the OC4 and OC5 projects [2, 130]. In this case, only one mean wind speed was tested (21.01 m/s), but with different set-ups for the generator and blade-pitch controllers. The platform pitch period was longer for all the decay tests with wind/active controller, compared with the tests without wind. In addition, the elongation in the period varied depending on the controller adopted.

Based on this information, it was not straightforward to determine what caused the period elongation in surge and pitch. First, the period variation was too large to be caused by negative damping occasionally induced by the controller (although this effect may be in place for the surge motions, as explained below). Another question was whether the effect had the same origin for both the surge and pitch DOFs.

Surge and pitch decay simulations, under constant wind speed, were performed in Sima. Three FWT concepts (Fig. 2.1) were considered: the two semi-submersible designs from the mentioned publications, and the OC3 Hywind 5 MW spar FWT [1]. The damped natural periods (in the absence of wind) are shown in Table 5.1. The three concepts were equipped with the NREL 5 MW reference wind turbine [43]. The entire wind turbine operational range (3.0-25.0 m/s) was considered, with one simulation per wind speed. The generator torque and blade-pitch controllers were active in all simulations, with a detuned strategy adopted for the latter – the same controller gains were used for the three platforms. The three concepts were moored with 3 catenary lines each.

Table 5.1: Surge and pitch damped natural periods for the three FWTs in Publication J.1.

	OC3-Hywind	**OC4 Semi**	**CSC5MW**
Surge (s)	125.2	114.1	83.5
Pitch (s)	30.0	25.8	32.2

The surge and pitch decay periods from the decay simulations are shown in Figure 5.1. For surge, it is highlighted that the curve for the OC4 Semi platform presents a different pattern compared with the other two: the shortest period happening at rated wind speed, and increasing towards cut-in and cut-off. The relevance of this observation is that, according to the definition by Robertson et al. [2], the mooring system for this FWT has one line extending towards the negative X direction, while for the other two FWTs the single line extends towards positive X (Fig. 5.2). This relation hinted at the fact that nonlinearities associated with the mooring system could be behind the period changes in surge.

For the pitch motions, the pattern of the curves is very similar for the three FWTs. A significant variation is seen, however, in the difference between the longest and shortest periods for each concept. Since the wind turbine (including controller configuration) was the same for all concepts,

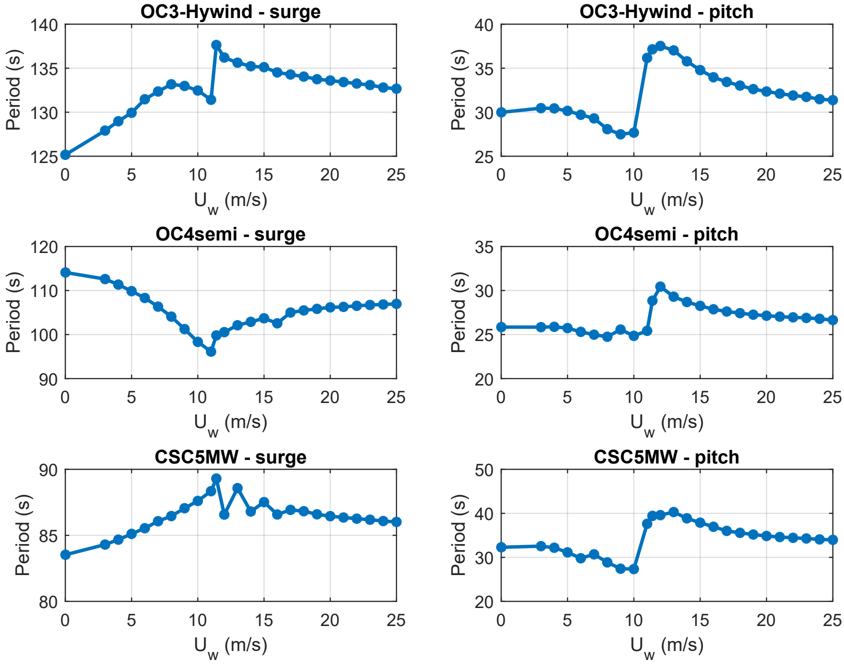

Figure 5.1: Surge and decay periods obtained from simulations with different incident wind speed (from Publication J.1).

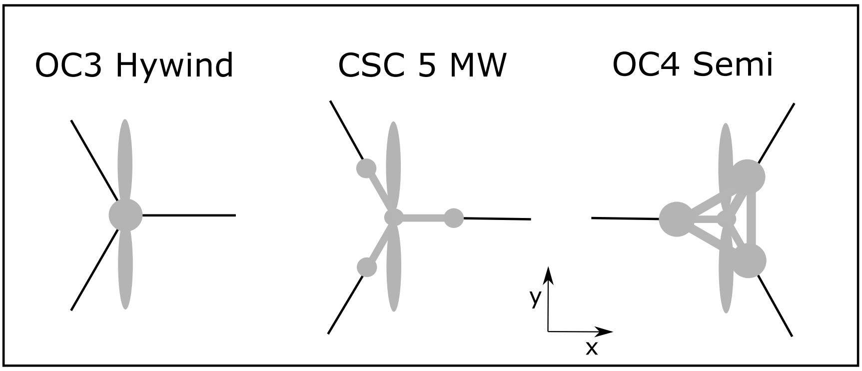

Figure 5.2: Bird's eye view of the mooring systems for the FWTs considered in Publication J.1.

the effect was then linked to the dynamic characteristics of each FWT. In particular, the damped natural periods (without wind) differed (Tab. 5.1). This suggested that the interaction between the motions and the controller could be behind the effect.

Another set of simulations was then carried out, where the turbine was forced to oscillate harmonically in the wind direction with constant amplitude, but varying frequency, and under different values for the (constant) incident wind speed. The purpose here was to measure the resulting thrust, and especially the phase between the thrust and the nacelle velocity.

For these simulations, a program was implemented coupling AeroDyn [131] with a 2-DOF system, consisting of the nacelle fore-aft motion and the rotor azimuth angle. A sinusoidal motion was imposed to the nacelle, while the rotor dynamics resulted from the equilibrium between the aerodynamic and the generator torque, as well as the rotor + drivetrain inertia. The same control system used in Sima was implemented, commanding the blade-pitch angle provided to AeroDyn, as well as the generator torque for the rotor.

The results showed that the fluctuations in the rotor thrust caused by the sinusoidal nacelle motions were also nearly sinusoidal, but with a phase ϕ relative to the thrust. In other words, assuming the nacelle velocity as $\dot{x}_{nac}(t) = x_0 \omega \cos(\omega t)$, the varying component of the thrust, F_{var}, becomes approximately:

$$F_{var} = f_0 x_0 \omega \cos(\omega t + \phi) \,, \tag{5.1}$$

where f_0 is a “velocity-to-thrust amplitude factor” (i.e., the ratio between the maximum steady-state values of F_{var} and $\dot{x}_{nac}$). Equation 5.1 is further developed in the paper, such that F_{var} can be written as a function of both the nacelle velocity and acceleration:

$$F_{var} = f_0 \left[\dot{x}_{nac} \cos(\phi) + \frac{\ddot{x}_{nac}}{\omega} \sin(\phi) \right] \,. \tag{5.2}$$

This formulation encouraged the definition of apparent damping and inertia effects, induced by the rotor thrust, to the nacelle dynamics. In particular, it is stressed the phase ϕ varied as a function of both the nacelle motion frequency and the incident wind velocity, and was also affected by the controller configuration and rotor dynamics. In other words, the varying component of the thrust will play a combination of damping and inertia roles on the nacelle; and the relative contribution from each of these effects will depend on those parameters.

It is noted that Eq. (5.2) can be equivalently expressed in terms of the nacelle displacement, x, instead of the acceleration:

$$F_{var} = f_0 \left[\dot{x}_{nac} \cos(\phi) - \omega x_{nac} \sin(\phi) \right] \,, \tag{5.3}$$

where now F_{var} is thought as a combination of damping and stiffness effects. In other words, part of the rotor thrust would have an effect of bringing the nacelle back to neutral position (or repelling it away, in the case of negative stiffness). Although this interpretation may be adequate in some contexts (e.g. in Eq. 3.18), the effect is treated as inertia in this thesis.

Simplified, 2-D models of each FWT were then created, where the surge and pitch inertia and damping coefficients are updated for each wind speed and decay period, based on Eq. (5.2). In addition, the mooring stiffness is linearized around the mean platform position for each incident mean wind speed. The eigenperiods obtained with these simplified models are compared with the periods shown in Fig. 5.1, with reasonable matching for most of the incident wind speed range. Reference is made to Fig. 9-14 in Publication J.1, which shows the comparisons for all FWTs.

5.1.2 Publication C.1

In this publication, the apparent inertia and damping effects identified in Publication J.1 were approached in the context of frequency-domain (FD) models for FWTs. In a number of publications, the interactions between FWT motions and the rotor loads are approximated in FD models using a damping coefficient, which is assumed as constant for a given incident wind speed [41, 57, 132]. This coefficient can be assumed as the derivative of the thrust with respect to the incident wind:

$$b_{aer} = T_u = \frac{\partial T}{\partial u} \,. \tag{5.4}$$

This approach may be a good approximation for bottom-fixed wind turbines, since for the latter these interactions do in fact provide mostly a damping effect. However, for floating wind turbines, this method disregards the frequency dependence of the damping, as well as the period changes in pitch due to the apparent inertia effect.

The paper compared this strategy with an extended approach, where both the frequency-dependent aerodynamic damping and inertia coefficients were obtained analytically from a 2-DOF system, considering both the platform pitch and rotor dynamics. A PI-controller (Eq. 3.9) was used for regulating the blade pitch. For this work, the DTU 10 MW reference wind turbine [44] was adopted. The coefficients were found to be given by:

$$a_{aer}(\omega) = -\frac{1}{\omega^2}\,\mathrm{Re}\left\{i\omega T_u - \left[\left(T_\Omega + K_p T_\beta\right) i\omega + K_i T_\beta\right] C(\omega)\right\} \tag{5.5}$$

$$b_{aer}(\omega) = \frac{1}{\omega}\,\mathrm{Im}\left\{i\omega T_u - \left[\left(T_\Omega + K_p T_\beta\right) i\omega + K_i T_\beta\right] C(\omega)\right\} \,, \tag{5.6}$$

with $C(\omega)$ defined as:

$$C(\omega) = \frac{i\omega Q_u}{I_d\omega^2 + (Q_\Omega + K_p Q_\beta)\, i\omega + K_i Q_\beta}\,. \tag{5.7}$$

The aerodynamic derivatives $T_{u,\beta,\Omega}, Q_{v,\beta,\Omega}$ were as defined in Chapter 3. These coefficients were compared with those obtained with forced nacelle oscillations, as used for Publication J.1, with very good agreement. It is highlighted in the paper that a constant damping coefficient is in general higher than the one obtained taking the rotor dynamics and controller into account.

Three FD models were then created of the OO-Star 10 MW semi-submersible FWT [133]: one using a constant damping coefficient; and two using frequency-dependent inertia and damping coefficients, obtained either with Eq. (5.5-5.6), or with forced nacelle oscillations under constant wind. Wind loads were included based on the turbulent wind spectrum, used as input in a transfer function from wind speed to thrust force. This transfer function is obtained for a bottom-fixed wind turbine.

The responses under combined wind and waves were compared with time-domain simulations in Sima. Figure 5.3 shows the power spectral density functions of the pitch motions with all models. For 13.0 m/s, all the FD methods over-predicted the response around the pitch natural frequency (0.03 Hz), but for higher wind speed, the FD model with constant damping coefficient provided lower resonant responses. The other FD models, conversely, overpredicted the resonant pitch motions.

5.1.3 Practical implications for the analysis of FWT dynamics

The objective with both publications is not to propose simplified models, based on the aerodynamic damping and inertia/stiffness coefficients, to represent the interactions between platform motions, rotor dynamics, and control system. Rather, the main contribution is a better understanding of these interactions.

To illustrate how this understanding can be helpful in practice, a table from Publication J.1 is reproduced below (Tab. 5.2), comparing the aerodynamic damping effect with the respective linear viscous damping coefficients adopted in the simulations. Another table (Tab. 5.3) is included here, showing the comparison against the critical modal damping ($b_{cr} = 2m\omega_n$)). As it is seen, above rated wind speed, a strong negative aerodynamic damping effect is observed in surge. This is as expected, considering that the

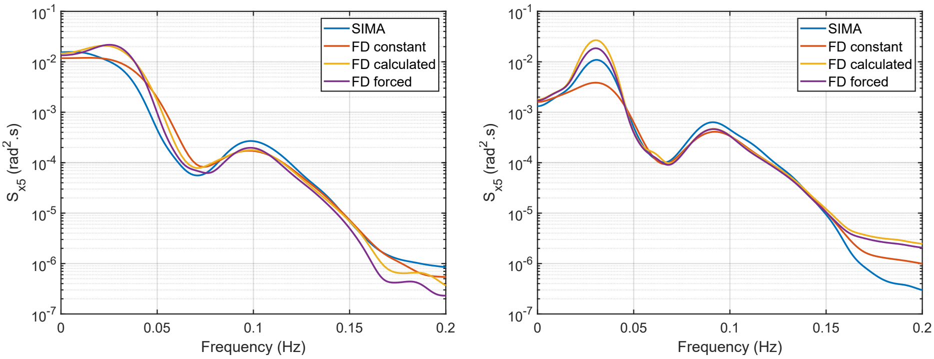

(a) $U_w = 13.0$ m/s. (b) $U_w = 19.0$ m/s.

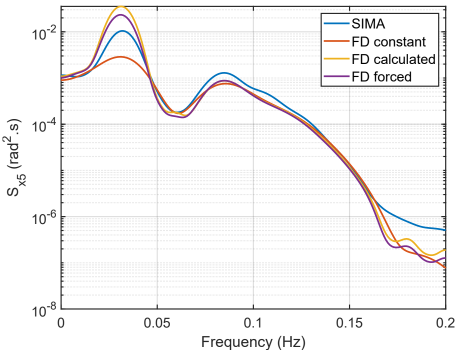

(c) $U_w = 25.0$ m/s.

Figure 5.3: Platform pitch response – comparison between **Sima** simulations and frequency-domain analyses with a **constant** damping coefficient for each wind speed; and with frequency-dependent inertia and damping coefficients, either **calculated** with Eq. (5.5-5.6) or with **forced** nacelle oscillations.

Table 5.2: Ratio (%) between aerodynamic apparent damping and linear viscous damping.

		$U_w = 7.0$ m/s	$U_w = 11.4$ m/s	$U_w = 18.0$ m/s
surge $\frac{b_{aer}}{b_{11}}$	OC3Hywind	21.80	−92.78	−13.95
	OC4semi	45.11	−140.43	−31.28
	CSC5MW	24.98	−62.49	−20.67
pitch $\frac{b_{aer}h_{hub}^2}{b_{55}}$	OC3Hywind	19.89	18.10	−5.37
	OC4semi	60.27	73.18	−11.65
	CSC5MW	83.47	45.12	−25.07

Table 5.3: Ratio (%) between aerodynamic apparent damping and critical modal damping.

		$U_w = 7.0$ m/s	$U_w = 11.4$ m/s	Uw = 18.0 m/s
surge $\frac{b_{aer}}{b_{cr,11}}$	OC3Hywind	1.96	-8.36	-1.26
	OC4semi	1.42	-4.43	-0.99
	CSC5MW	1.34	-3.36	-1.11
pitch $\frac{b_{aer}h_{hub}^2}{b_{cr,55}}$	OC3Hywind	0.60	0.54	-0.16
	OC4semi	2.88	3.50	-0.56
	CSC5MW	2.77	1.50	-0.83

controller gains used in the simulations are adjusted to prevent controller responses near the pitch natural frequency. Since the period in surge is longer, the controller will respond to wind fluctuations due to this motion, which results in the negative feedback, and thus negative damping effect.

Being aware of this possibility, a designer can be less prone to use an overly simplified model for the wind turbine loads during e.g. mooring design. By knowing beforehand that the damping effect in surge can be negative, frequency-dependent, and significant, it is more defensible to adopt a simulation model that properly accounts for the interaction, rather than e.g. prescribing a thrust time-series to the tower top.

In principle, the changes in the pitch period are not a reason of concern. It does not seem likely that the period will be shifted towards e.g. to the wave frequency range, resulting in resonant motion. One potential problem, however, may be the combination of the new period in pitch with the heave period, which for some platforms can result in Mathieu instability.

This phenomenon occurs due to variations in the waterplane area due to large heave motions, and/or high waves. These variations will affect the restoring coefficient, making it nonlinear. Haslum and Faltinsen [134] studied this effect for spar platforms, which typically have variations in the diameter towards the free surface. One particular combination of heave and pitch periods results from the case where the wave envelope matches the pitch natural period. This happens for waves with period given by:

$$T_{cri} = \frac{1}{\frac{1}{T_3} + \frac{1}{T_5}}, \tag{5.8}$$

where T_3 and T_5 are the heave and pitch natural periods, respectively.

Considering for example Spar6, one of the 20 MW spar FWTs from Publication J.3 (T_3 = 30.8 s, T_5 = 38.7 s), the critical period following Eq. (5.8) is 17.2 s. If the pitch period is reduced by 10% due to the rotor-motion interactions, T_{cri} would be reduced to 16.3 s. Although the reduction may not seem large, it is closer to typical wave peak periods.

It is noted that the possibility of Mathieu instability enhanced by the pitch period changes has not been verified in this research, and it is not certain that it would occur.

5.2 Platform flexibility and FWT dynamics

Publication J.2 extended the work performed by Svendsen [39], who wrote his Master's thesis on modelling of flexible structures for a 5 MW tension leg platform wind turbine. The properties of the flexible structural elements were obtained from his work, as well as the numerical model of the TLPWT. The scope of the article was to verify the consequences of adopting a flexible platform in terms of global dynamics and fatigue damage at tendons and tower base – in comparison with the more common assumption of a rigid platform. In addition, the paper also addressed hydroelastic effects associated with the pontoons' flexible modes.

Since the column was much stiffer than the pontoons, the latter governed the elastic response of the platform. The column was thus assumed as a rigid body, while the pontoons were modelled with beam elements, with one end connected to the column and another to the tendons (Fig. 5.4). Additional models with pontoons modelled with half and twice the original bending stiffness value were also considered.

Radiation and diffraction loads from potential theory were distributed over the pontoons, but some simplifications were adopted. First, since the added mass associated with the pontoons did not vary too much with respect to the frequency, constant coefficients were used – based on the integrated panels at each of the 21 sections used in the pontoons discretization. Radiation damping was negligible, and thus not included in the model. The wave excitation loads were also obtained from the panel pressures, and applied at each section.

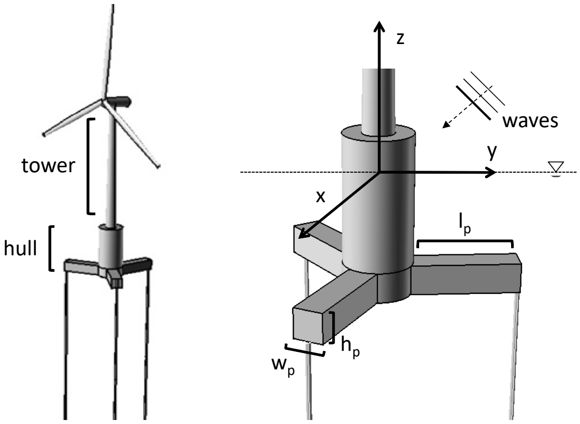

Figure 5.4: Tension leg platform wind turbine model used adopted in Publication J.2.

Hydroelasticty was taken into account by defining two more modes, in addition to the 6 rigid-body ones, related to the pontoon's' deflections: the seventh generalized mode was related to the first bending mode of pontoon 1, with pontoons 2 and 3 kept undeflected, as indicated in Fig 5.5. The eighth mode related to bending of pontoons 2 and 3, with pontoon 1 kept undeflected. The mode shapes were obtained with the eigenvalue analysis function in Riflex, and described as 3^{rd}-order polynomials, which were then used in WAMIT for the generation of hydrodynamic loads associated with the generalized modes.

The time-domain analyses consisted of decay simulations, simulations in regular waves, and fatigue analysis under irregular waves and turbulent wind. In addition, another set of regular waves simulations was performed to verify the effect of hydroelastic radiation loads on the platform global response.

According to the decay simulation results, the assumption of a flexible platform significantly increased the heave natural period, while the 1^{st} pitch/bending[1] period also became slightly longer. From the simulations

---

[1] For tension leg platform wind turbines, it is usual to consider the combined rigid-body pitch and 1^{st} tower bending mode together, since it may be difficult to distinguish between both.

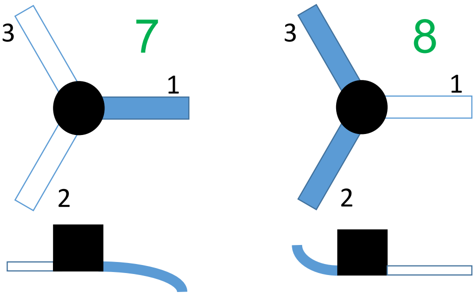

Figure 5.5: Pontoons' flexible modes adopted in the hydroelastic analysis.

with regular waves, the responses in heave and pitch were significantly amplified, depending on the period range. Force transfer functions between wave excitation and tower bending frequency/tendon axial tension were not significantly affected by platform flexibility, though.

The model with flexible pontoons presented less accumulated fatigue damage at the tower base and tendon connection to the pontoons. Spectral analysis of the stresses showed that the largest differences between the flexible and rigid models were close to the 1^{st} tower bending mode, above the wave frequency range. In addition, the load amplitude response was also lower for some of the load cases analyzed.

The results from the hydroelastic simulations confirmed that these effects are not important for the platform analyzed. The heave and pitch responses, as well as tower base and tendon loads, were indistinguishable from simulations not accounting for hydroelastic effects.

5.2.1 Implications on FWT modelling and analysis

Preliminary FWT design is often based on a rigid model for the platform. However, non-negligible errors in the estimated heave and 1^{st} pitch/bending natural frequencies were seen for a 5 MW TLPWT. A tower designed for a rigid floater could present a lower natural frequency due to elasticity in the platform, with potential interaction with loads at blade-passing frequencies. This effect, on the other hand, is expected to be less important for other platform concepts. A study with a flexible platform model should in any case be considered, especially for larger platforms of the next generation's FWTs.

Hydroelastic effects associated with the platform flexible modes do not seem to be important in FWT models. The results indicate that the order of magnitude of such effects are 2-3 times lower than other hydrodynamic loads, and it is not expected that their relative importance will increase significantly for other FWT concepts.

5.3 Design of large FWTs

Modelling the platform as a flexible structure can be necessary for large FWTs, as suggested in the previous section. In addition, in Chapter 3 a controller with a motion compensation strategy was shown to be more adequate than a detuning approach, as the pitch natural period becomes longer.

Both points are considered in Publication J.3, which discusses the design and analysis of spar platforms supporting a 20 MW wind turbine. The reference wind turbine designed by Ashuri et al. [4] was adopted. The tower base diameter and wall thickness were, however, increased, to avoid the 1st bending frequency being inside blade-passing ranges.

The spars were composed of two hollow cylinders with different diameters, with the cylinder at the bottom having the largest diameter. A tapered part connected both cylinders. A parametric design procedure was carried out, where the cylinders' diameters could vary inside given ranges. The draft was kept constant (90.0 m), as well as the length of the cylinder at the top (6.0 m). High-density (4000 kg/m^3) concrete [135] was assumed to fill a ballast column, starting from the bottom and extending towards a height h, varied until the weight-buoyancy equilibrium was reached[2]. The steel mass was calculated assuming a hull wall with 60 mm thickness, and density of 7850 kg/m^3. Additional constraints were imposed to keep the heave period away from typical waves range, as well as to avoid the heave and pitch natural periods being too close to each other. The mass of the mooring system, composed of 3 catenary lines, is accounted for in the design.

The procedure provided 660 solutions. For each of them, the static pitch angle at rated wind speed (θ_r) was calculated, based on the the rotor thrust and on a 2-DOF (surge-pitch) system including coupled restoring coefficients. The solutions were then divided into sub-sets with $\theta_r \leq 6°$, $8°$, and $10°$– FWT design standards do not establish strict requirements

---

[2] Normally, spar platforms also include fluid ballast (e.g. seawater) for adjusting the draft and stability during operations [136]. This strategy and the related consequences were however beyond the scope of Publication J.3, and have not been considered in the design.

Table 5.4: Main properties of the three spar FWT designs from Publication J.3.

	Spar6	Spar8	Spar10
Static pitch (deg)	6.0	8.0	10.0
Draft (m)	90.00	90.00	90.00
Diameter - top (m)	15.90	15.20	14.70
Diameter - bottom (m)	25.50	24.10	23.30
SWL to taper top (m)	6.00	6.00	6.00
SWL to taper bottom (m)	14.31	13.71	13.45
Ballast column height (m)	17.29	17.00	16.79
Ballast mass (kg)	3.53×10^7	3.10×10^7	2.86×10^7
Steel mass (kg)	3.77×10^6	3.55×10^6	3.43×10^6
GM (m)	11.89	9.82	8.40
Displacement (m^3)	4.26×10^4	3.82×10^4	3.58×10^4
Mooring system mass (kg)	6.27×10^5	6.10×10^5	6.01×10^5
r_{yy} (m)	82.46	82.80	83.04
T_{heave} (s)	30.8	30.3	30.3
T_{pitch} (s)	38.7	44.2	49.1

on this parameter. The solution with lowest steel mass from each of these sub-sets was considered in the study. Table 5.4 reproduces some of the main properties of the selected designs.

The three selected designs were then modelled in Sima. The platform, tower, and wind turbine blades were assumed as flexible, and were modelled with beam FE elements. Table 5.5 compares the 1st tower fore-aft bending frequencies for models adopting rigid and flexible platforms. A reduction of approximately 7% is noted when the fully flexible model is adopted.

Table 5.5: Comparison between 1st tower fore-aft bending frequencies for the 20 MW spars with rigid and flexible platforms.

	Frequency (Hz)		
	Spar6	Spar8	Spar10
Rigid model	0.44	0.45	0.45
Flexible model	0.41	0.42	0.42

The radiation and diffraction hydrodynamic loads were combined with quadratic viscous drag terms and distributed over the hull. Slowly-varying

2^{nd}-order wave loads in the 6 DOFs were considered with difference-frequency quadratic transfer functions. Mooring restoring loads were computed with a quasi-static model.

A VSVP control system was adopted for the generator torque and collective blade pitch angle. Above rated wind speed, the generator torque was adjusted to provide constant torque. The blade pitch controller consisted of a PI feedback on the rotor speed error, combined with feedforward of the nacelle velocity. The latter was low-pass filtered to avoid feeding of wave-frequency components to the control signal. The controller natural frequency and relative damping were set to 0.31 rad/s and 0.6, respectively, for the three FWTs. A peak shaving strategy was adopted to limit the thrust to 2800 kN near rated wind speed.

Fatigue and extreme analyses were carried out assuming combined wind and wave conditions, based on joint distributions provided by Li et al.[128] for a site at the Southwestern Norwegian coast. For fatigue, four time-domain realizations of 23 load cases were simulated for each spar. For the extreme analysis, 20 realizations of 11 load cases were considered. The latter were chosen from environmental contours associated with the rated, cut-off, and 50-year mean wind speed. The analyses were performed with time-series of the axial stresses at sections along the platform and tower. The fatigue analysis was also performed for two of the spars with a different hydrodynamic model, based on Morison's equation only.

Figure 5.6 shows the pitch motions and generator power for Spar6 (Tab. 5.4), for simulations adopting a controller with motion compensation, and with a detuned controller. The latter, despite stable, provides only a marginal level of damping, leading to large resonant pitch motions and power variations. The controller with motion compensation provides a higher level of aerodynamic damping, leading to reduced motions and better power quality.

Fatigue damage at the tower sections was larger for the spars with larger restoring in pitch (i.e., lower θ_r). Spectral analysis of the tower base axial stress indicates that this is due to larger inertial loads associated with wave-frequency RNA motions. For the platform, on the other hand, the damage was higher for platforms with higher θ_r. Modelling the hydrodynamic loads with Morison's equation resulted in significant overestimation of the platform fatigue damage, especially for Spar6, confirming the findings by Engebretsen et al. [42].

Extreme axial stresses were associated with load cases from contours at both rated and 50-year wind speeds. This was observed for sections at both the platform and tower, and for the three designs. In general, the largest extreme stresses were observed for platforms with lower restoring in pitch.

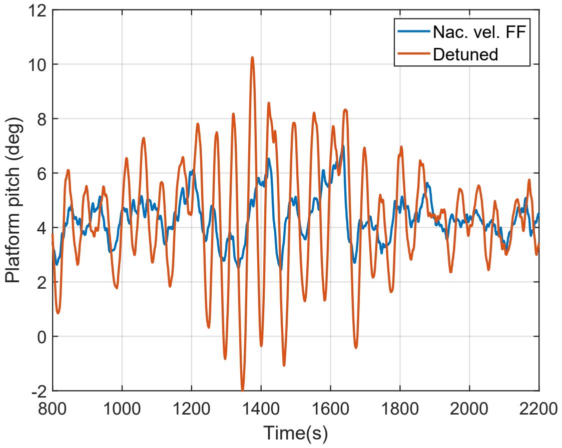

(a) Platform pitch

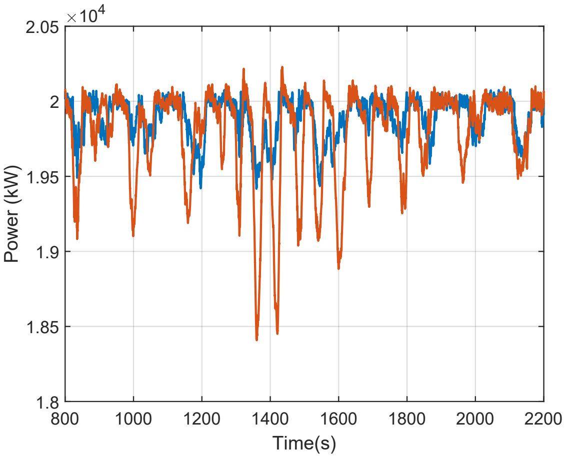

(b) Generator power

Figure 5.6: Platform pitch and generator power for Spar6, using a controller with nacelle velocity feedforward and a detuned controller. $U = 13.0$ m/s, $H_s = 2.51$ m, $T_p = 10.1$ s.

An analysis separating the contributions from inertial, gravity, and thrust loads showed that this difference was caused mainly by the gravitational components associated with the RNA weight.

Difference-frequency 2^{nd}-order wave loads had minor contribution both for fatigue damage and extreme loads. This was concluded by running additional analyses without the QTFs, and comparing the results with those obtained with a complete model. The difference was less than 1% for fatigue damage and less than 4% for extreme stresses.

5.3.1 Applications in the design and analysis of large FWTs

The results in this publication confirm in practice what is discussed also in Chapter 3: a detuned controller can be inadequate for larger FWTs. Due to the increased pitch natural periods, the reduction in the controller bandwidth to ensure stability can deteriorate the tracking of the rotor speed and produce excessive variations not only on power quality, but also thrust. In addition, the marginal level of aerodynamic damping when a detuned controller is used results in unrealistic resonant pitch motions.

Although real FWTs normally adopt more sophisticated controllers [107], the detuned controller is a very common approach in academic research, as well as during initial FWT design stages. The adoption of a motion compensation strategy, like the inclusion of nacelle velocity measurements to the controller, can improve the results without major complications regarding controller tuning.

Modelling of flexible platforms is also expected to become more important as FWT dimensions increase. In this respect, the choice of an appropriate method for distributing hydrodynamic loads over the hull becomes more relevant. The results in this publication show, for example, that the adoption of a model based on Morison's equation produced over-conservative fatigue damage. In this respect, it is recommended that loads from potential theory are adopted.

The static platform pitch angle under rated wind speed is a design parameter with implications not only on steel mass, but also in the structural performance of the analyzed FWTs. In this respect, performing similar analyses at initial stages of FWT design can help reducing the design space by e.g. setting upper boundaries to θ_r.

Gravity loads associated with the RNA are a major component in the extreme loads of the spar FWTs analyzed in this work. This trend is expected to hold also for other concepts. The consideration of load cases associated with the rated wind speed is essential in the analysis of extreme loads, since this wnd speed provides the largest mean platform pitch. Load cases associated with intermediate wind speeds (i.e., between rated and cut-off) should also be considered, since waves tend to become higher for higher wind speeds.

Chapter 6

Conclusions

The research presented in this thesis deals with topics on modelling, analysis, design, coupled dynamics, and control systems of floating wind turbines. The main conclusions are summarized below.

Coupled dynamics

Changes in surge and pitch natural periods are expected for floating wind turbines in operational conditions. However, the origin of the effect differs. For surge, the effect is associated with mooring stiffness nonlinearities, when large platform displacements result from the mean rotor thrust. For pitch, the phenomenon is associated with the oscillations in the rotor thrust due to the nacelle fore-aft motions. These thrust fluctuations can be decomposed as apparent inertia and damping effects – and the relative contribution from each of these effects is a function of incident wind, nacelle fore-aft motion frequency, and control system configuration.

In addition to explaining the different periods for different platforms and wind velocities, this result also expands the understanding of the aerodynamic damping effect. For detuned controllers, the aerodynamic damping in surge can be negative and have magnitude significantly larger than viscous damping. In practice, this finding discourages the adoption of overly simplified models for the thrust in analyses where the aerodynamic damping in surge can be relevant (e.g. mooring system design). The inclusion of the rotor-control dynamics in frequency-domain models is also recommended, instead of adopting constant aerodynamic damping coefficients.

Platform flexibility and hydroelasticity

Platform flexibility can have a significant impact on the global structural dynamics of TLPWTs, and large FWTs. An analysis with a 5 MW TLPWT showed that, in addition to affecting motion amplitudes and natural periods, the adoption of flexible pontoons reduced the estimated fatigue damage at the tower base and tendon top, compared with a rigid platform. The reduction was mostly related to stresses at the 1st pitch/bending frequency. For 20 MW spar-type FWTs, the 1st bending frequency was reduced in 7% when the platform was modelled as flexible, compared with a rigid platform model.

Hydroelastic effects associated with the pontoons' flexible modes, on the other hand, are negligible for the concept analyzed. Since the related loads are 2-3 orders of magnitude lower than radiation effects associated to the rigid-body modes, it is unlikely that hydroelasticity will become important even for larger FWTs.

FWT control systems

Wind turbine control systems must be adapted to operate on FWTs. In particular, control-motion interactions may cause instability and must be avoided. The detuning strategy, popular in academic works, is effective in preventing the instability, but reduces the controller performance in tracking the rotor speed, impairing power quality and increasing thrust variability.

Motion compensation strategies can avoid the instability without detuning the controller. Nacelle velocity feedback can improve the system performance, but stability issues can arise when a 2nd-order low-pass filter is applied on the nacelle velocity. Nacelle velocity feedforward seems to provide a better performance in terms of stability, even when the filter is included. A significant level of aerodynamic damping is added when this strategy is adopted, leading to substantial attenuation of the pitch motions – and thus tower and platform loads.

A tuning method was introduced for these approaches, based on the eigenvalues of state-space representations of the linearized platform-rotor-controller coupled system, and can be applied for FWTs other than the 20 MW spar used in the case study.

Design considerations for large FWTs

The static platform pitch under rated thrust (θ_r) is an important constraint in the design of 20 MW spar FWTs. In addition to impacting the design cost and natural periods, the parameter also influences the balance between inertial, gravitational, and thrust loads – thus affecting fatigue damage and extreme loads. The latter tend to be governed by the RNA weight, and thus is increased for larger θ_r. Fatigue, on the other hand, can increase or diminish with θ_r, depending on the location of the section analyzed.

Extreme loads for the analyzed FWTs are not necessarily associated with the harshest environmental conditions. Since gravity loads have a major role, conditions associated with the rated wind speed can provoke the extreme sectional stresses, due to the large main pitch angle.

Distribution of hydrodynamic loads based on Morison's equation resulted in increased fatigue damage, compared with an approach based on potential theory. Since the former does not take wave diffraction effects into account, it can over-excite the structure at frequencies close to the 1st tower bending natural frequency – which tends to be reduced for larger FWTs

The pitch natural period for a 20 MW FWTs can become significantly longer than typical values for 5-10 MW FWTs. One consequence is that a detuned controller for large FWTs needs unrealistically low bandwidths, resulting in unacceptable power quality and platform motions even at initial design stages. A motion compensation strategy should be adopted instead.

Slowly-varying 2nd-order wave loads seem to have negligible impact on fatigue damage for large FWTs. The influence on extreme loads is somewhat larger, but still limited.

Suggestions for future work

Some of the topics studied in this thesis merit further investigation. The following topics are directly related to the findings from this research:

- The effects of platform flexibility on global dynamics are expected to be more evident for larger platforms. For platform concepts like semi-submersibles and TLPs, torsional modes can be of special importance if their natural frequencies fall in the range of blade-passing loads. An investigation taking this possibility into account should be carried out, and the consequences for FWT design if these interactions are to be avoided should be assessed.

- In Chapter 5, triggering of Mathieu instability by waves of shorter wavelength was mentioned as a possible consequence of the changes in the pitch natural period. This possibility should be verified for FWT concepts susceptible to instability, using numerical models able to represent nonlinear hydrostatic restoring, or model tests.

- The 20 MW wind turbine model [4] adopted in Publication J.3 has an RNA mass (1975 t) which, considering the advances in drivetrain and blade material technology, may be heavier than in the real scenario [25]. In fact, scaling up the RNA mass of the IEA 15 MW reference wind turbine (1016 t) to 20 MW results in 1540 t, representing a 22 % reduction relative to the value obtained by Ashuri et al. [4]. A lighter RNA can affect some of the conclusions from Publication J.3 regarding the relative importance of gravitational loads on the extreme sectional stresses, as well as platform natural periods. Further investigation is needed.

- It is also relevant to extend the work in Publication J.3 for other FWT platform concepts. Musial et al. [23] point out that 75% of the installed and announced floating wind projects (as of 2020) adopt semi-submersible platforms, due to their relatively shallow draft and more convenient transportation/installation processes. The limited pitch motions of TLPs can be an advantage in reducing the tower bending loads associated with RNA accelerations and weight. New concepts like the TetraSpar [137] can also have advantages for larger structures, by merging the benefits of increased hydrostatic stability, lower draft, and a tubular structure that can be manufactured by existing shipyards.

- For increasingly large FWTs, it may also be important to assess possible limitations in the controller performance due to increased rotor inertia, combined with limited blade-pitch actuator dynamics for larger blades. High-fidelity aerodynamic load models can also be more relevant in the design of control approaches for larger FWTs, due to the increased spatial variability of the wind flow through the rotor.

The limited scope of the research inevitably translates into limitations, which also make relevant research gaps. Some of them are:

- Veers et al. [74] described challenges related with the aerodynamics of larger wind turbine rotors. In particular, effects related to steady aerodynamics associated with the larger blade deformations are listed as one phenomenon poorly described by standard aerodynamic models, like the ones adopted in this work. Although these effects may be more relevant for blade loads, it may also be interesting to check their importance for FWT global dynamics.

- More realistic wind turbulence models, as discussed by Nybø et al. [115], are even more likely to affect global dynamics and platform/tower loads. An approach to allow their systematic adoption in the analysis of large FWTs would be beneficial.

- The coupled analysis methods discussed in the thesis can provide accurate predictions of the sectional loads at the platform and tower. Methods for efficiently using these results in detailed local analyses are needed, for a comprehensive integrity assessment of welded components.

- Further benefits to the platform and tower structural life using the control system, other than those discussed in Publication J.3, must be explored. Individual pitch control may be fundamental in avoiding blade-passing excitation, should the tower bending frequency be further reduced. For spar-type concepts, IPC can also be tuned to reduce yaw loads, alleviating the mooring system loads. Thrust peak shaving can also be combined with an adaptive approach, using additional information of e.g. sea state to predict possible occurrence of extreme events, thus limiting even more the thrust (and thus gravitational loads) in advance.

References

[1] J. Jonkman, Definition of the floating system for phase IV of OC3, Tech. Rep. NREL/TP-500-47535, National Renewable Energy Laboratory, Golden, United States (2010).

[2] A. Robertson, J. Jonkman, M. Masciola, H. Song, A. Goupee, A. Coulling, C. Luan, Definition of the semisubmersible floating system for phase II of OC4, Technical Report NREL/TP-5000-60601, NREL, Denver, United States (2014).

[3] C. Luan, Z. Gao, T. Moan, Design and analysis of a braceless steel 5-MW semi-submersible wind turbine, in: Proocedings of the ASME 2016 35th International Conference on Offshore Mechanics and Arctic Engineering, 2016.

[4] T. Ashuri, J. R. R. A. Martins, M. B. Zaaijer, G. A. M. van Kuik, G. J. W. van Bussel, Aeroservoelastic design definition of a 20 MW common research wind turbine model, Wind Energy 19 (11) (2016) 2071–2087, we.1970. `doi:10.1002/we.1970`.

[5] Equinor, Floating offshore wind in Equinor, online; accessed 05-May-2021 (2022).
URL `https://www.equinor.com/en/what-we-do/floating-wind.html`

[6] TODA, Decarbonizing business, `https://www.toda.co.jp/english/tech/cop24.html/`, accessed: 2022-02-08 (2022).

[7] Principle Power, The WindFloat., [Online; accessed 12-February-2022] (2021).
URL `https://www.principlepower.com/windfloat`

[8] University of Maine, Volturnus – advanced structures and composites center, [Online; accessed 08-February-2022] (2020).
URL `https://composites.umaine.edu/research/volturnus/`

[9] Glosten, Glosten PelaStar floating wind turbine, [Online; accessed 08-February-2022] (2022).
URL `https://glosten.com/sectors/pelastar-tension-leg-platform-floating-offshore-wind/`

[10] Saitec Offshore Technologies, SATH – Saitec Offshore Technologies, [Online; accessed 08-February-2022] (2022).
URL `https://saitec-offshore.com/sath/`

[11] BW Ideol, Floating platform – offshore wind power, [Online; accessed 08-February-2022] (2022).
URL `https://www.bw-ideol.com/en/floatgen-demonstrator`

[12] General Electrics, Haliade-X offshore wind turbine - the world's most powerful offshore turbine built today, online; accessed 2021-09-05 (2021).
URL `https://www.ge.com/renewableenergy/wind-energy/offshore-wind/haliade-x-offshore-turbine`

[13] MingYang Smart Electric, Leading innovation: MingYang Smart Energy launches MySE 16.0-242, the world's largest offshore hybrid drive wind turbine, online; accessed 2021-09-05 (2021).
URL `http://www.myse.com.cn/en/jtxw/info.aspx?itemid=825`

[14] Vestas, V236-15.0 MW, [Online; accessed 08-February-2022] (2021).
URL `https://www.vestas.com/en/products/offshore/V236-15MW`

[15] Equinor, Hywind Scotland, the World's first floating wind farm, operated by Equinor, online; accessed 12-February-2022 (2021).
URL `https://communicationtoolbox.equinor.com/brandcenter/en/equinor/component/default/42130`

[16] J. Nichols, K. O. Ronold, A. L. Hopstad, Key Design Considerations, Springer International Publishing, Cham, 2016, pp. 241–269. `doi:10.1007/978-3-319-29398-1_5`.
URL `https://doi.org/10.1007/978-3-319-29398-1_5`

[17] A. R. Nejad, J. Keller, Y. Guo, S. Sheng, H. Polinder, S. Watson, J. Dong, Z. Qin, A. Ebrahimi, R. Schelenz, F. Gutiérrez Guzmán, D. Cornel, R. Golafshan, G. Jacobs, B. Blockmans, J. Bosmans, B. Pluymers, J. Carroll, S. Koukoura, E. Hart, A. McDonald,

A. Natarajan, J. Torsvik, F. K. Moghadam, P.-J. Daems, T. Verstraeten, C. Peeters, J. Helsen, Wind turbine drivetrains: state-of-the-art technologies and future development trends, Wind Energy Science 7 (1) (2022) 387–411. `doi:10.5194/wes-7-387-2022`.
URL `https://wes.copernicus.org/articles/7/387/2022/`

[18] F. Nielsen, T. Hanson, B. Skaare, Integrated dynamic analysis of floating offshore wind turbines, in: Proceedings of the ASME 2016 25th International Conference on Offshore Mechanics and Arctic Engineering, 2006.

[19] IEA, Net zero by 2050, Tech. rep., International Energy Agency, Paris (2021).
URL `https://www.iea.org/reports/net-zero-by-2050`

[20] NREL, Floating wind turbines on the rise – NREL offshore wind expert discusses future powered by floating offshore wind, online; accessed 12-February-2022 (2020).
URL `https://www.nrel.gov/news/program/2020/floating-offshore-wind-rises.html`

[21] J. F. Manwell, J. G. McGowan, A. L. Rogers, Wind Energy Explained: Theory, Design and Application, John Wiley & Sons, Ltd, 2009.

[22] A. Smith, UK offshore wind capacity factors – Energy Numbers, online; accessed 12-February-2022 (2021).
URL `https://energynumbers.info/uk-offshore-wind-capacity-factors`

[23] W. Musial, P. Spitsen, P. Beiter, P. Duffy, M. Marquis, A. Cooperman, R. Hammond, M. Shields, Offshore wind market report: 2021 edition, Tech. rep., U. S. Department of Energy, USA (2021).

[24] M. Jansen, I. Staffell, L. Kitzing, S. Quoilin, E. Wiggelinkhuizen, B. Bulder, I. Riepin, F. Müsgens, Offshore wind competitiveness in mature markets without subsidy, Nature Energy 5 (2020). `doi:https://doi.org/10.1038/s41560-020-0661-2`.

[25] K. Dykes, P. Veers, E. Lantz, H. Holttinen, O. Carlson, A. Tuohy, A. M. Sempreviva, A. Clifton, J. S. Rodrigo, D. Berry, D. Laird, S. Carron, P. Moriarty, M. Marquis, C. Meneveau, J. Peinke, J. Paquette, N. Johnson, L. Pao, P. Fleming, C. Bottasso, V. Lehtomaki, A. Robertson, M. Muskulus, J. Manwell, J. O. Tande, L. Sethuraman, O. Roberts, J. F. and, Results of IEA wind TCP workshop on

a grand vision for wind energy technology, Tech. rep., International Energy Agency (2019).
URL `https://www.nrel.gov/docs/fy19osti/72437.pdf`

[26] Equinor, Hywind Tampen – floating wind power project, online; accessed 13-February-2022 (2022).
URL `https://www.equinor.com/en/what-we-do/hywind-tampen.html`

[27] Principle Power, Project: Les éoliennes flottantes du Golfe de Lion, [Online; accessed 13-February-2022] (2021).
URL `https://www.principlepower.com/projects/les-eoliennes-flottantes-du-golfe-du-lion`

[28] C. Allen, A. Viselli, H. Dagher, A. Goupee, E. Gaertner, N. Abbas, M. Hall, , G. Barter, Definition of the UMaine VolturnUS-S reference platform developed for the IEA wind 15-megawatt offshore reference wind turbine, Tech. Rep. NREL/TP-5000-76773, National Renewable Energy Laboratory, Golden, United States (2020).

[29] E. E. Bachynski, M. Thys, T. Sauder, V. Chabaud, L. O. Saether, Real-time hybrid model testing of a braceless semi-submersible wind turbine. Part II: Experimental results, in: Proceedings of the ASME 2016 35th International Conference on Ocean, Offshore and Arctic Engineering, Busan, Korea, 2016.

[30] A. J. Goupee, R. W. Kimball, H. J. Dagher, Experimental observations of active blade pitch and generator control influence on floating wind turbine response, Renewable Energy 104 (2017) 9 – 19. `doi:http://dx.doi.org/10.1016/j.renene.2016.11.062`.

[31] M. Borg, A. M. Hansen, H. Bredmose, Floating substructure flexibility of large-volume 10MW offshore wind turbine platforms in dynamic calculations, Journal of Physics: Conference Series 753 (8) (2016).
URL `http://stacks.iop.org/1742-6596/753/i=8/a=082024`

[32] M. Borg, H. Bredmose, A. M. Hansen, Elastic deformations of floaters for offshore wind turbines: dynamic modelling and sectional load calculations, in: Proceedings of the ASME 2017 36th International Conference on Ocean, Offshore and Arctic Engineering, 2017.

[33] M. Borg, A. Pegalajar-Jurado, H. Sarlak, F. J. Madsen, H. Bredmose, F. Lemmer, F. Borisade, M. Kretschmer, Y. Wei, LIFES50+ - D4.7

models for advanced load effects and loads at component level, Tech. rep., Technical University of Denmark (2018).

[34] T. J. Larsen, T. D. Hanson, A method to avoid negative damped low frequent tower vibrations for a floating, pitch controlled wind turbine, Journal of Physics: Conference Series 75 (2007) 012073. `doi:10.1088/1742-6596/75/1/012073`.
URL `https://doi.org/10.1088%2F1742-6596%2F75%2F1%2F012073`

[35] E. Lenfest, A. Goupee, A. Wright, N. Abbas, Tuning of nacelle feedback gains for floating wind turbine controllers using a two-dof model, in: Proocedings of the ASME 2020 39th International Conference on Ocean, Offshore and Arctic Engineering, 2020.

[36] N. J. Abbas, D. S. Zalkind, L. Pao, A. Wright, A reference open-source controller for fixed and floating offshore wind turbines, Wind Energy Science 7 (1) (2022) 53–73. `doi:10.5194/wes-7-53-2022`.
URL `https://wes.copernicus.org/articles/7/53/2022/`

[37] D. Matha, J. Cruz, M. Masciola, E. E. Bachynski, M. Atcheson, A. J. Goupee, S. M. H. Gueydon, A. N. Robertson, Modelling of Floating Offshore Wind Technologies, Springer International Publishing, Cham, 2016, pp. 133–240. `doi:10.1007/978-3-319-29398-1_4`.
URL `https://doi.org/10.1007/978-3-319-29398-1_4`

[38] J. M. Jonkman, Dynamics modeling and loads analysis of an offshore floating wind turbine, Ph.d. thesis, University of Colorado, Denver, United States (2007).

[39] K. Svendsen, Structural design and dynamic analysis of a tension leg platform wind turbine, considering elasticity in the hull, Master's thesis, Norwegian University of Science and Technology / TU Delft (2016).

[40] C. Luan, Z. Gao, T. Moan, Development and verification of a time-domain approach for determining forces and moments in structural components of floaters with an application to floating wind turbines, Marine Structures 51 (2017) 87 – 109. `doi:http://dx.doi.org/10.1016/j.marstruc.2016.10.002`.
URL `http://www.sciencedirect.com/science/article/pii/S095183391630082X`

[41] J. M. Hegseth, E. E. Bachynski, M. Karimirad, Comparison and validation of hydrodynamic load models for a semi-submersible floating wind turbine, in: Proocedings of the ASME 2018 37th International Conference on Ocean, Offshore and Arctic Engineering, 2018. `doi:10.1115/OMAE2018-77676`.

[42] E. Engebretsen, H. Haslum, O. Aagaard, Distributed Potential Theory and its Application for Spar-Type Floating Offshore Wind Turbines, in: Proceedings of the ASME 2020 39th International Conference on Ocean, Offshore and Arctic Engineering, Virtual conference, 2020. `doi:10.1115/OMAE2020-18284`.
URL `https://doi.org/10.1115/OMAE2020-18284`

[43] J. Jonkman, S. Butterfield, W. Musial, G. Scott, Definition of a 5-MW reference wind turbine for offshore system development, Tech. Rep. NREL/TP-500-38060, National Renewable Energy Laboratory, Golden, United States (2009).

[44] C. Bak, F. Zahle, R. Bitsche, T. Kim, A. Yde, L. C. Henriksen, A. Natarajan, M. H. Hansen, Description of the DTU 10 MW reference wind turbine, Tech. Rep. DTU Wind Energy Report-I-0092, DTU Wind Energy (2013).

[45] IEC, Wind energy generation systems – part 3-2 design requirements for floating offshore wind turbines (IEC 61400-3-2) (2019).

[46] DNV-GL, Design of floating wind turbine structures (DNVGL-ST-0119) (2018).

[47] ABS, Guide for building and classing – floating offshore wind turbines (2020).

[48] DNV, Fatigue design of offshore steel structures (DNV-RP-C203) (2011).

[49] DNV, Global performance analysis of deepwater floating structures (DNV-RP-F205) (2010).

[50] DNV, Environmental conditions and environmental loads (DNV-RP-C205) (2010).

[51] E. E. Bachynski, T. Moan, Design considerations for tension leg platform wind turbines, Marine Structures 29 (1) (2012) 89 – 114. `doi:http://dx.doi.org/10.1016/j.marstruc.2012.09.001`.

URL `http://www.sciencedirect.com/science/article/pii/S0951833912000627`

[52] F. Lemmer, K. Müller, W. Yu, R. F. Guzman, M. Kretschmer, LIFES50+ - D4.3 optimization framework and methodology for optimized floater design, Tech. rep., University of Stuttgart (2016).

[53] I. Fylling, P. A. Berthelsen, Windopt - an optimization tool for floating support structures for deep water wind turbines, in: Proceedings of the ASME 2011 30th International Conference on Ocean, Offshore and Arctic Engineering, 2011.

[54] J. M. Hegseth, E. E. Bachynski, J. R. Martins, Integrated design optimization of spar floating wind turbines, Marine Structures 72 (2020) 102771. `doi:https://doi.org/10.1016/j.marstruc.2020.102771`.
URL `https://www.sciencedirect.com/science/article/pii/S0951833920300654`

[55] J. M. Jonkman, D. Matha, Dynamics of offshore floating wind turbines—analysis of three concepts, Wind Energy 14 (4) (2011) 557–569. `doi:10.1002/we.442`.
URL `http:https://doi.org/10.1002/we.442`

[56] M. I. Kvittem, T. Moan, Time domain analysis procedures for fatigue assessment of a semi-submersible wind turbine, Marine Structures 40 (Supplement C) (2015) 38 – 59. `doi:https://doi.org/10.1016/j.marstruc.2014.10.009`.
URL `http://www.sciencedirect.com/science/article/pii/S0951833914000756`

[57] M. I. Kvittem, T. Moan, Frequency versus time domain fatigue analysis of a semisubmersible wind turbine tower, Journal of Offshore Mechanics and Arctic Engineering 137 (1) (2015) 011901–011901–11. `doi:10.1115/1.4028340`.

[58] E. E. Bachynski, Design and dynamic analysis of tension leg platform wind turbines, Ph.d. thesis, Norwegian University of Science and Technology, Trondheim, Norway (2014).

[59] E. E. Bachynski, M. I. Kvittem, C. Luan, T. Moan, Wind-wave misalignment effects on floating wind turbines: Motions and tower load effects, Journal of Offshore Mechanics and Arctic Engineering 136 (2014). `doi:10.1115/1.4028028`.

[60] M. Karimirad, T. Moan, Extreme dynamic structural response analysis of catenary moored spar wind turbine in harsh environmental conditions, Journal of Offshore Mechanics and Arctic Engineering 133 (4), 041103 (04 2011). `arXiv:https://asmedigitalcollection.asme.org/offshoremechanics/article-pdf/133/4/041103/5756926/041103\_1.pdf`, `doi:10.1115/1.4003393`.
URL `https://doi.org/10.1115/1.4003393`

[61] Q. Li, Z. Gao, T. Moan, Modified environmental contour method to determine the long-term extreme responses of a semi-submersible wind turbine, Ocean Engineering 142 (2017) 563 – 576. `doi:https://doi.org/10.1016/j.oceaneng.2017.07.038`.
URL `http://www.sciencedirect.com/science/article/pii/S0029801817304109`

[62] F. Bianchi, H. de Battista, R. Mantz, Wind Turbine Control Systems: Principles, Modelling and Gain Scheduling Design, Advances in Industrial Control, Springer London, 2007.
URL `https://books.google.no/books?id=WeVSAAAAMAAJ`

[63] R. C. Dorf, R. H. Bishop, Modern Control Systems, 13th Edition, Pearson, USA, 2017.

[64] L. Y. Pao, K. E. Johnson, A tutorial on the dynamics and control of wind turbines and wind farms, in: 2009 American Control Conference, 2009.

[65] P. Fleming, I. Pineda, A. Wright, D. Arora, Evaluating methods for control of an offshore floating turbine, in: Proocedings of the ASME 2014 33rd International Conference on Ocean, Offshore and Arctic Engineering, 2014.

[66] M. Lackner, Controlling platform motions and reducing blade loads for floating wind turbines, Wind Engineering 33 (6) (2009).

[67] B. Skaare, F. G. Nielsen, Blade pitch control in a wind turbine installation (2013).

[68] M. D. Pedersen, Stabilization of floating wind turbines, Ph.d. thesis, Norwegian University of Science and Technology, Trondheim, Norway (2017).

[69] B. Skaare, T. D. Hanson, F. G. Nielsen, Importance of Control Strategies on Fatigue Life of Floating Wind Turbines, in: Proceedings of the

ASME 2007 26th International Conference on Ocean, Offshore and Arctic Engineering, 2007, pp. 493–500.

[70] F. Savenije, J. Peeringa, Control development for floating wind, Journal of Physics: Conference Series 524 (2014) 012090. `doi:10.1088/1742-6596/524/1/012090`.
URL `https://doi.org/10.1088/1742-6596/524/1/012090`

[71] M. A. Lackner, An investigation of variable power collective pitch control for load mitigation of floating offshore wind turbines, Wind Energy 16 (4) (2013) 519–528. `doi:10.1002/we.1500`.
URL `http://dx.doi.org/10.1002/we.1500`

[72] P. A. Fleming, A. Peiffer, D. Schlipf, Wind turbine controller to mitigate structural loads on a floating wind turbine platform, Journal of Offshore Mechanics and Arctic Engineering 141 (2019). `doi:10.1115/1.4042938`.

[73] J. M. Hegseth, E. E. Bachynski, J. R. R. A. Martins, Design optimization of spar floating wind turbines considering different control strategies, Journal of Physics: Conference Series 1669 (2020) 012010. `doi:10.1088/1742-6596/1669/1/012010`.
URL `https://doi.org/10.1088/1742-6596/1669/1/012010`

[74] P. Veers, K. Dykes, E. Lantz, S. Barth, C. L. Bottasso, O. Carlson, A. Clifton, J. Green, P. Green, H. Holttinen, D. Laird, V. Lehtomäki, J. K. Lundquist, J. Manwell, M. Marquis, C. Meneveau, P. Moriarty, X. Munduate, M. Muskulus, J. Naughton, L. Pao, J. Paquette, J. Peinke, A. Robertson, J. S. Rodrigo, A. M. Sempreviva, J. C. Smith, A. Tuohy, R. Wiser, Grand challenges in the science of wind energy, Science 366 (6464) (2019) eaau2027. `arXiv:https://www.science.org/doi/pdf/10.1126/science.aau2027`, `doi:10.1126/science.aau2027`.
URL `https://www.science.org/doi/abs/10.1126/science.aau2027`

[75] H. Haslum, M. Marley, S. T. Navalkar, B. Skaare, N. Maljaars, H. S. Andersen, Roll-Yaw lock: Aerodynamic motion instabilities of Floating Offshore Wind Turbines, Journal of Offshore Mechanics and Arctic Engineering (2022) 1–13`arXiv:https://asmedigitalcollection.asme.org/offshoremechanics/article-pdf/doi/10.1115/1.4053697/6830229/omae-21-1108.pdf`, `doi:10.1115/1.4053697`.
URL `https://doi.org/10.1115/1.4053697`

[76] Y. Zhao, J. Yang, Y. He, Preliminary design of a multi-column TLP foundation for a 5-MW offshore wind turbine, Energies 5 (10) (2012). URL `http://www.mdpi.com/1996-1073/5/10/3874`

[77] C.-G. Hsu, Substructure models for dynamic analysis of floating wind turbines and the effect of hull flexibility, Master's thesis, Norwegian University of Science and Technology / TU Delft (2019).

[78] J. B. de Vaal, M. O. L. Hansen, T. Moan, Influence of rigid body motions on rotor induced velocities and aerodynamic loads of a floating horizontal axis wind turbine, in: Proocedings of the ASME 2014 33rd International Conference on Ocean, Offshore and Arctic Engineering, 2014.

[79] J. Vaal, M. L. Hansen, T. Moan, Effect of wind turbine surge motion on rotor thrust and induced velocity, Wind Energy 17 (1) (2014) 105–121. `doi:10.1002/we.1562`.

[80] M. Thys, C. Souza, T. Sauder, N. Fonseca, P. A. Berthelsen, E. Engebretsen, H. Haslum, Experimental Investigation of the Coupling Between Aero- and Hydrodynamical Loads On A 12 MW Semi-Submersible Floating Wind Turbine, in: Proceedings of the ASME 2021 40th International Conference on Ocean, Offshore and Arctic Engineering, 2021. `arXiv:https://asmedigitalcollection.asme.org/OMAE/proceedings-pdf/OMAE2021/85192/V009T09A030/6780789/v009t09a030-omae2021-62980.pdf`, `doi:10.1115/OMAE2021-62980`.
URL `https://doi.org/10.1115/OMAE2021-62980`

[81] C. Luan, V. Chabaud, E. E. Bachynski, Z. Gao, T. Moan, Experimental validation of a time-domain approach for determining sectional loads in a floating wind turbine hull subjected to moderate waves, Energy Procedia 137 (2017) 366 – 381, 14th Deep Sea Offshore Wind R&D Conference, EERA DeepWind'2017. `doi:https://doi.org/10.1016/j.egypro.2017.10.361`.

[82] N. Luxcey, H. Ormberg, E. Passano, Global analysis of a floating wind turbine using an aero-hydro-elastic model. Part 2: benchmark study, in: Proceedings of the ASME 2011 30th International Conference on Ocean, Offshore and Arctic Engineering, 2011.

[83] A. Næss, T. Moan, Stochastic Dynamics of Marine Structures, Cambridge University Press, 2013.

[84] O. Faltinsen, Sea Loads on Ships and Offshore Structures, Cambridge Ocean Technology Series, Cambridge University Press, 1993.

[85] S. Bhattacharyya, S. Sreekumar, V. Idichandy, Coupled dynamics of seastar mini tension leg platform, Ocean Engineering 30 (6) (2003) 709–737. `doi:https://doi.org/10.1016/S0029-8018(02)00061-6`. URL `https://www.sciencedirect.com/science/article/pii/S0029801802000616`

[86] R. Adrezin, H. Benaroya, Non-linear stochastic dynamics of tension leg platforms, Journal of Sound and Vibration 220 (1) (1999) 27–65. `doi:10.1002/we.1562`.

[87] WAMIT, WAMIT User Manual, Chestnut Hill, United States (2006).

[88] J. Newman, Marine Hydrodynamics, The Massachusetts Institute of Technology, 1977.

[89] A. N. Simos, F. Ruggeri, R. A. Watai, A. Souto-Iglesias, C. Lopez-Pavon, Slow-drift of a floating wind turbine: An assessment of frequency-domain methods based on model tests, Renewable Energy 116 (Part A) (2018) 133 – 154. `doi:https://doi.org/10.1016/j.renene.2017.09.059`. URL `http://www.sciencedirect.com/science/article/pii/S0960148117309229`

[90] L. H. S. do Carmo, A slender-body approach for computing second-order wave forces in seakeeping simulations of floating offshore wind turbines, Ph.D. thesis, University of São Paulo, São Paulo, Brazil (2021).

[91] J. Newman, Second-order, slowly-varying forces on vessels in irregular waves, Tech. Rep. MIT Paper 19, Massachusetts Institute of Technology, Cambridge, United States (1974).

[92] W. E. Cummins, The impulse response and ship motions, in: Symposium on Ship Theory, 1962.

[93] T. F. Ogilvie, Recent progress toward the understanding and prediction of ship motions, Tech. rep., David W. Taylor Model Basin, Washington D.C., USA (1964).

[94] R. Cook, Concepts and applications of finite element analysis, 4th Edition, Wiley, 2001.

[95] M. I. Kvittem, Modelling and response analysis for fatigue design of a semi-submersible wind turbine, Ph.d. thesis, Norwegian University of Science and Technology, Trondheim, Norway (2014).

[96] J. Jonkman, M. Buhl Jr., FAST User's Guide (2005).

[97] E. Gaertner, J. Rinker, L. Sethuraman, F. Zahle, B. Anderson, G. Barter, N. Abbas, F. Meng, P. Bortolotti, W. Skrzypinski, G. Scott, R. Feil, H. Bredmose, K. Dykes, M. Sheilds, C. Allen, A. Viselli, Definition of the IEA 15-megawatt offshore reference wind turbine, Tech. rep., International Energy Agency (2020).
URL `https://www.nrel.gov/docs/fy20osti/75698.pdf`

[98] O. M. Faltinsen, Hydrodynamics of High-Speed Marine Vehicles, Cambridge University Press, 2006. `doi:10.1017/CBO9780511546068`.

[99] J. Newman, Wave effects on deformable bodies, Applied Ocean Research 16 (1) (1994) 47 – 59. `doi:http://dx.doi.org/10.1016/0141-1187(94)90013-2`.
URL `http://www.sciencedirect.com/science/article/pii/0141118794900132`

[100] R. Taghipour, T. Perez, T. Moan, Hybrid frequency–time domain models for dynamic response analysis of marine structures, Ocean Engineering 35 (7) (2008) 685 – 705. `doi:http://dx.doi.org/10.1016/j.oceaneng.2007.11.002`.
URL `http://www.sciencedirect.com/science/article/pii/S0029801807002363`

[101] R. Taghipour, T. Perez, T. Moan, Time domain hydroelastic analysis of a flexible marine structure using state-space models, Journal of Offshore Mechanics and Arctic Engineering 131 (2009).

[102] M. Hansen, Aerodynamics of Wind Turbines, Earthscan, 2013.

[103] E. A. Bossanyi, Wind turbine control for load reduction, Wind Energy 6 (3) (2003) 229–244. `doi:https://doi.org/10.1002/we.95`.
URL `https://onlinelibrary.wiley.com/doi/abs/10.1002/we.95`

[104] M. H. Hansen, L. C. Henriksen, Basic DTU wind energy controller, Tech. Rep. DTU Wind Energy E No. 0028, Technical University of Denmark (2019).

[105] F. Lemmer (né Sandner), W. Yu, D. Schlipf, P. W. Cheng, Robust gain scheduling baseline controller for floating offshore wind turbines, Wind Energy 23 (1) (2020) 17–30. `doi:https://doi.org/10.1002/we.2408`.
URL `https://onlinelibrary.wiley.com/doi/abs/10.1002/we.2408`

[106] J. M. Jonkman, Influence of control on the pitch damping of a floating wind turbine, in: Proceedings of the ASME Wind Energy Symposium, 2008.

[107] B. Skaare, F. G. Nielsen, T. D. Hanson, R. Yttervik, O. Havmøller, A. Rekdal, Analysis of measurements and simulations from the hywind demo floating wind turbine, Wind Energy 18 (6) (2015) 1105–1122. `arXiv:https://onlinelibrary.wiley.com/doi/pdf/10.1002/we.1750`, `doi:https://doi.org/10.1002/we.1750`.
URL `https://onlinelibrary.wiley.com/doi/abs/10.1002/we.1750`

[108] J. Jonkman, B. Jonkman, FAST modularization framework for wind turbine simulation: full-system linearization, in: The Science of Making Torque from Wind (TORQUE2016), 2016.

[109] J. M. Jonkman, A. D. Wright, G. J. Hayman, A. N. Robertson, Full-System Linearization for Floating Offshore Wind Turbines in OpenFAST, in: ASME 2018 1st International Offshore Wind Technical Conference, 2018. `doi:10.1115/IOWTC2018-1025`.

[110] H. Namik, K. Stol, Individual blade pitch control of floating offshore wind turbines, Wind Energy 13 (1) (2010) 74–85. `doi:https://doi.org/10.1002/we.332`.
URL `https://onlinelibrary.wiley.com/doi/abs/10.1002/we.332`

[111] B. Fischer, M. Shan, A survey on control methods for the mitigation of tower loads, Tech. Rep. Project report 01/104256, Fraunhofer-institute for wind energy and energy systems technology, IWES, Kassel, Germany (2013).

[112] S. Chakrabarti, Chapter 3 – Ocean Environment, in: S. K. CHAKRABARTI (Ed.), Handbook of Offshore Engineering, Elsevier, London, 2005, pp. 79 – 131. `doi:https://doi.org/10.1016/B978-008044381-2.50006-0`.

[113] IEC, Wind turbines – part 1: design requirements (iec 61400-1) (2005).

[114] E. E. Bachynski, L. Eliassen, The effects of coherent structures on the global response of floating offshore wind turbines, Wind Energy 22 (2) (2019) 219–238. `doi:https://doi.org/10.1002/we.2280`.

[115] A. Nybø, F. Gunnar Nielsen, M. Godvik, Sensitivity of the dynamic response of a multimegawatt floating wind turbine to the choice of turbulence model, Wind Energy n/a (n/a). `arXiv:https://onlinelibrary.wiley.com/doi/pdf/10.1002/we.2712`, `doi:https://doi.org/10.1002/we.2712`.
URL `https://onlinelibrary.wiley.com/doi/abs/10.1002/we.2712`

[116] B. J. Jonkman, L. Kilcher, Turbsim user's guide: version 1.06.00, Tech. rep., National Renewable Energy Laboratory (2012).

[117] H. Ormberg, K. Larsen, Coupled analysis of floater motion and mooring dynamics for a turret-moored ship, Applied Ocean Research 20 (1) (1998) 55 – 67. `doi:https://doi.org/10.1016/S0141-1187(98)00012-1`.

[118] A. Robertson, J. Jonkman, F. Vorpahl, W. Popko, J. Qvist, L. Frøyd, X. Chen, J. Azcona, E. Uzunoglu, C. Guedes Soares, C. Luan, H. Yutong, F. Pengcheng, A. Yde, T. Larsen, J. Nichols, R. Buils, L. Lei, T. A. Nygard, D. Manolas, A. Heege, S. R. Vatne, H. Ormberg, T. Duarte, C. Godreau, H. F. Hansen, A. W. Nielsen, H. Riber, C. L. Cunff, R. Abele, F. Beyer, A. Yamaguchi, K. J. Jung, H. Shin, W. Shi, H. Park, M. Alves, M. Guérinel, Offshore code comparison collaboration continuation within IEA wind task 30: Phase II results regarding a floating semisubmersible wind system, in: Proceedings of the ASME 2014 33rd International Conference on Ocean, Offshore and Arctic Engineering, 2014.

[119] DTU Wind Energy, HAWC2 aeroelastic simulation of wind turbines, online; accessed 2022-01-23 (2021).
URL `https://www.hawc2.dk/`

[120] DNV, Wind turbine design software - Bladed, online; accessed 2022-01-23 (2021).
URL `https://www.dnv.com/services/wind-turbine-design-software-bladed-3775/`

[121] NREL, OpenFAST - Wind research - NREL, online; accessed 2022-01-23 (2021).
URL https://www.nrel.gov/wind/nwtc/openfast.html/

[122] SINTEF Ocean, Sima - SINTEF, online; accessed 2022-01-23 (2021).
URL https://www.sintef.no/en/software/sima/

[123] Orcina, OrcaFlex, online; accessed 2022-01-23 (2021).
URL https://www.orcina.com/orcaflex/

[124] NREL, ROSCO. Version 2.4.1 (2021).
URL https://github.com/NREL/ROSCO

[125] SINTEF OCEAN, SIMO - Theory manual (2016).

[126] SINTEF OCEAN, RIFLEX - Theory manual (2016).

[127] H. Ormberg, E. Passano, N. Luxcey, Global analysis of a floating wind turbine using an aero-hydro-elastic model. Part 1: code development and case study, in: Proceedings of the ASME 2011 30th International Conference on Ocean, Offshore and Arctic Engineering, 2011.

[128] L. Li, Z. Gao, T. Moan, Joint environmental data at five European offshore sites for design of combined wind and wave energy devices, in: Proceedings of the ASME 2013 32nd International Conference on Ocean, Offshore and Arctic Engineering, 2013.

[129] WAFO-group, WAFO - A Matlab Toolbox for Analysis of Random Waves and Loads - A Tutorial for version 2017, Math. Stat., Center for Math. Sci., Lund Univ., Lund, Sweden (2017).
URL http://www.maths.lth.se/matstat/wafo

[130] A. N. Robertson, F. Wendt, J. M. Jonkman, W. Popko, H. Dagher, S. Gueydon, J. Qvist, F. Vittori, J. Azcona, E. Uzunoglu, C. Guedes Soares, R. Harries, A. Yde, C. Galinos, K. Hermans, J. B. de Vaal, P. Bozonnet, L. Bouy, I. Bayati, R. Bergua, J. Galvan, I. Mendikoa, C. B. Sanchez, H. Shin, S. Oh, C. Molins, Y. Debruyne, OC5 project phase II: Validation of global loads of the DeepCwind floating semisubmersible wind turbine, Energy Procedia 137 (2017) 38 – 57, 14th Deep Sea Offshore Wind R&D Conference, EERA DeepWind'2017. doi:https://doi.org/10.1016/j.egypro.2017.10.333.
URL http://www.sciencedirect.com/science/article/pii/S1876610217352931

[131] P. J. Moriarty, A. C. Hansen, AeroDyn theory manual, Tech. Rep. NREL/EL-500-36881, National Renewable Energy Laboratory, Denver, United States (2005).

[132] A. Pegalajar-Jurado, M. Borg, H. Bredmose, An efficient frequency-domain model for quick load analysis of floating offshore wind turbines, Wind Energy Science Discussions 2018 (2018) 1–30. `doi:10.5194/wes-2018-25`.

[133] K. Müller, F. Lemmer, W. Yu, LIFES50+ - D4.2 public definition of the two LIFES50+ 10MW floater concepts, Tech. rep., University of Stuttgart (2018).

[134] H. Haslum, O. Faltinsen, Alternative Shape of Spar Platforms for Use in Hostile Areas, in: OTC Offshore Technology Conference 99, Houston, USA, 1999. `doi:10.4043/10953-MS`.
URL `https://doi.org/10.4043/10953-MS`

[135] LKAB Minerals AB, High density concrete, `https://www.lkabminerals.com/en/industry-uses/building-construction/heavy-weight-concrete/`, accessed: 2022-02-08 (2019).

[136] A. Henderson, M. Collu, M. Masciola, Overview of Floating Offshore Wind Technologies, Springer International Publishing, Cham, 2016, pp. 87–132. `doi:10.1007/978-3-319-29398-1_3`.
URL `https://doi.org/10.1007/978-3-319-29398-1_3`

[137] RWE, Floating offshore wind - TetraSpar demonstrator, online; accessed 2022-03-05 (2022).
URL `https://www.rwe.com/en/our-portfolio/innovation-and-technology/floating-offshore-wind/tetraspar`

Appendix A

Publications

Publication J.1

Changes in surge and pitch decay periods of floating wind turbines for varying wind speed

Carlos Eduardo Silva de Souza, Erin E. Bachynski

Ocean Engineering (2019), Vol. 180, pp. 223-237.

Ocean Engineering 180 (2019) 223–237

Contents lists available at ScienceDirect

Ocean Engineering

journal homepage: www.elsevier.com/locate/oceaneng

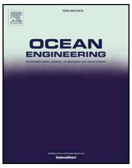

Changes in surge and pitch decay periods of floating wind turbines for varying wind speed

Carlos Eduardo S. Souza*, Erin E. Bachynski

Department of Marine Technology, NTNU, 7491, Trondheim, Norway

ARTICLE INFO

Keywords:
Floating wind turbines
Mooring systems
Coupled dynamics

ABSTRACT

Recently published experimental results show variations in surge and pitch decay periods of floating wind turbines (FWTs) subjected to different incident wind velocities. This paper explores the external loads acting on a FWT, with special attention to nonlinearities which affect its low-frequency global motions. The period variations in surge and pitch are found to have different sources. In surge, the mooring system nonlinearities dominate, while for pitch the relative phase between the nacelle velocity and the thrust induced in the rotor leads to an "apparent inertia/damping" effect. Simplified 2-DOF models using linearized stiffness coefficients for surge and modified inertia and damping matrices for pitch are developed. Comparisons with state-of-the-art aero-hydro-servo-elastic time-domain simulations show excellent agreement for three distinct catenary-moored FWT designs.

1. Introduction

Floating wind turbines (FWTs) have been proposed as the next generation of offshore wind energy harvesting systems. Some prototypes have already been deployed with power varying between 2 and 6 MW (PrinciplePower, 2014; Fukushima Forward, 2016; Equinor, 2018), while the generous wind resources at deeper waters and the more relaxed constraints in tower and rotor dimensions have resulted in ambitious concepts for supporting 10 MW turbines (LIFES50 + , 2015; Lemmer et al., 2016). Still, several challenges are to be overcome before FWTs become technically and commercially feasible. In particular, the platform construction costs have to be reduced.

A good understanding of FWT dynamics is necessary for optimal structural design and accurate power production estimates. However, FWTs are complex systems, subjected to nonlinear, coupled aerodynamic, hydrodynamic, mooring and controller-induced loads. Prediction of the system responses to different environmental conditions may be complicated, and unexpected behavior may be observed depending on the combination of loads.

One such behavior has been recently observed in FWT model tests, first reported in (Bachynski et al., 2016). The natural periods measured in surge and pitch decay tests varied when a scale-model FWT was subjected to different incident wind velocities. The effect was noticed in both the below- and above-rated wind velocity regimes. Another model test campaign (Goupee et al., 2017) reported the same phenomenon, but the tests were limited to pitch decay in above-rated wind velocities. The authors propose a qualitative explanation for the effect based on Taylor expansion of the thrust, considering the blade-pitch control action, but do not provide a prediction for the changes – nor do they discuss the effect for surge motions. In both publications, the model FWTs corresponded to catenary-moored semi-submersible platforms.

Low-frequency motions are of great importance in the design of a FWT. The low-frequency components of the aerodynamic thrust, second-order wave loads and the mooring system loads may excite rigid-body responses. The observed variations in natural period are therefore particularly important for the mooring system design and tuning of rotor controller gains.

In addition, there is a growing interest in the development of simplified models (e.g. frequency-domain approaches) that can reproduce FWT dynamics with an acceptable level of accuracy, for efficient application in early design iterations (Lupton, 2014; Pegalajar-Jurado et al., 2018). An accurate estimation of the decay periods for different operational conditions is necessary for proper tuning of such models, ensuring a fair prediction of the rigid-body response to linear loads.

1.1. Background

Previous expertise and tools from the offshore industry have been adapted for the analysis of FWTs dynamics – in particular, the technology and software for platform structural analysis, wave-structure

---

* Corresponding author.
E-mail address: carlos.souza@ntnu.no (C.E.S. Souza).

https://doi.org/10.1016/j.oceaneng.2019.02.075
Received 20 August 2018; Received in revised form 27 February 2019; Accepted 27 February 2019

interaction and mooring system design. Ormberg and Larsen (1998) introduced a method for simultaneously evaluating the floater motions and FEM-modelled mooring dynamics of a floating platform, in time-domain. The model was later updated (Ormberg et al., 2011; Luxcey et al., 2011) for inclusion of flexible tower and blades, and wind turbine aerodynamics and control. A different approach was taken by Jonkman (2007), who extended a land-based wind turbine analysis software for applications with floating substructures. The hydrodynamics and mooring models were nevertheless also borrowed from established knowledge of offshore engineering disciplines.

Brown (2005) summarizes the fundamental theory and practical design aspects of catenary mooring systems, highlighting the intrinsic nonlinear relation between platform excursion and the horizontal restoring component. Mooring systems for FWTs normally consist of 3–4 lines, which may combine chain and polyester segments. For simulation purposes, it may be convenient to assume simpler configurations with a uniform cross-section (Jonkman, 2010; Robertson et al., 2014; Luan et al., 2016).

Wind turbine aerodynamics can be reproduced with fairly simple models, like the Blade Element Momentum (BEM) method which is based on the equilibrium between aerodynamic loads on elements of the blade and the changes in fluid momentum through the rotor plane (Manwell et al., 2009). Corrections for large induction factors and tip/hub losses, respectively, are normally considered with simple multipliers, and additional accuracy may be obtained by adopting Øye's models for dynamic stall and dynamic wake effects (Hansen, 2013). Though developed for ground-fixed wind turbines, these models are also suitable for FWTs, especially in terms of thrust prediction (Vaal et al., 2014). Pedersen (2017) proposed a different approach for finding thrust and torque, based on circulation theory, arriving to a convenient model where the interconnected nature of both loads becomes evident through a compact matrix representation.

A wind turbine model comprises the main aerodynamic characteristics of the blades (i.e., lift/drag coefficients and geometric parameters); rotor and drivetrain mechanical properties; and control system strategies and parameters. The NREL 5 MW reference wind turbine (Jonkman et al., 2009) provides realistic parameters for the turbine subsystems. A *Variable Speed Variable Pitch* (VSVP) control system is adopted, actuating both on the generator torque and on the collective-blade pitch angle in order to regulate power production under different operating regimes.

The adoption of a blade-pitch controller for FWTs results in the instabilities reported in e.g. (Nielsen et al., 2006; Larsen and Hanson, 2007; Jonkman, 2008), leading to amplification of the platform surge and pitch motions. This effect may be attenuated by proper detuning of the controller gains, by placing the controller frequency away from the FWT surge/pitch natural rigid-body modes.

1.2. Scope and text organization

This paper explores the phenomenon of surge and pitch decay period variation when the FWT is subjected to different incident wind velocities. In Section 2, three different platform concepts are considered. Surge and pitch decay simulations are performed for each, under steady incident wind velocities covering the entire operational range, and the period variations are highlighted. Section 3 discusses FWT dynamics and introduces a simplified 2-DOF model to be used in the prediction of the periods. In Section 4, the period variation is related to the mooring system nonlinearities and to an "apparent" inertia and damping effect, and a strategy to consider these effects in the simplified model is developed. The predicted periods are compared with the simulations in Section 5, and conclusions and final considerations are presented in Section 6.

2. The decay period changing phenomenon

In order to illustrate the effect of changing surge/pitch decay periods for FWTs under varying incident velocities, time-domain simulations with three platform concepts are presented.

2.1. FWT concepts considered

The FWT models considered have all been published previously, and support the NREL 5 MW wind turbine (Jonkman et al., 2009). The platforms and mooring systems are briefly described below:

OC3-Hywind (Jonkman, 2010) A spar platform originally developed by the Norwegian company Equinor (formerly Statoil) and adapted as a concept design for the Offshore Code Comparison Collaboration (OC3). The mooring system is composed of 3 catenary homogeneous lines, with one of them aligned with the positive x-axis and forming an angle of 120°with the other two.

OC4semi (Robertson et al., 2014) A semi-submersible platform, comprising a central column connected through thin braces to three side columns. At the bottom of each column there is a "heave column", that is, a segment with larger diameter with the purpose of increasing the heave added mass and damping. The mooring system is also a 3-lines catenary configuration, but with two lines in the fore and another aligned with the negative x-axis.

CSC5MW (Luan et al., 2016, 2017) Another semi-submersible platform, differing from the former in that the three side columns are connected to the central column with pontoons, instead of braces. The pontoons contribute significantly to the buoyancy and are symmetrically distributed. The mooring system also consists of three homogeneous catenary lines, arranged similarly to the OC3Hywind.

Fig. 1 shows the three FWT concepts, and Table 1 presents their main dimensions. The tower model has also been obtained from (Jonkman et al., 2009), and consists of a 77.6 m long tubular structure, with a base diameter of 6.50 m and top diameter of 3.87 m. The tower base lies at 10.0 m above SWL on all platforms, such that the top is 87.6 m high. The resulting hub height is 90.0 m.

2.2. Simulation tool and procedure

The decay simulations are carried out with SIMA, which combines RIFLEX (SINTEF OCEAN, 2016a) and SIMO (SINTEF OCEAN, 2016b) in coupled time-domain simulations.[1] SIMO is a simulator of marine operations, and is responsible for computing the hydrodynamic loads on the platform. RIFLEX is a FEM based software for analysis of slender marine structures, and is used for the analysis of structural loads and displacements of the tower, rotor blades (beam elements) and mooring lines (bar elements). In addition, it calculates the aerodynamic loads, based on the BEM method (Manwell et al., 2009) with corrections for dynamic wake and dynamic stall effects; and rotor dynamics, including control.

Structural damping is included in the FE model by means of Rayleigh damping. Since moored floating platforms have compliant low-frequency modes, only the stiffness-proportional term is considered (Cook, 2001). Then, the damping model attenuates higher frequency structural vibrations and numerical noise, while the platform motions are damped by hydrodynamic and aerodynamic effects only.

The simulations consisted in applying an initial displacement in the

---

[1] The adopted simulation tool has been compared to other codes and experimental results. For example, decay simulations results (without wind) had excellent agreement with similar software in the context of OC3 (Jonkman and Musial, 2010) and OC4 (Robertson et al., 2017). The aerodynamic module was compared with other codes and experimental results within OC5 (Popko et al., 2018), also providing very satisfactory matching with the results obtained by the other participants.

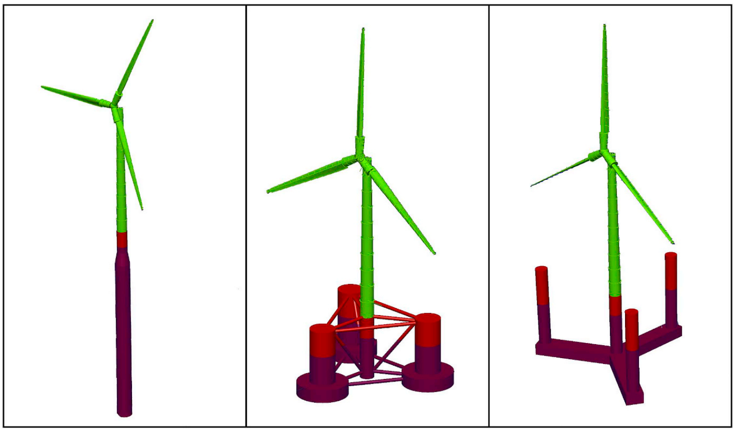

Fig. 1. FWT concepts considered in the simulations. From left to right: OC3-Hywind, OC4semi and CSC5MW.

Table 1
FWTs' main properties. Δ is the displacement, I_{yy} is the moment of inertia around a transversal axis at still water level (SWL), D is the draft, z_{CG} is the vertical coordinate of the center of gravity with respect to the SWL, z_{fl} is the vertical position of the mooring lines fairleads and d_w is the water depth.

	Δ (10^3 kg)	I_{yy} (10^6 kg.m^2)	D (m)	z_{CG} (m)	z_{fl} (m)	d_w (m)
OC3-Hywind	8066.0	68017.7	120.0	−77.99	− 70.0	320.0
OC4semi	14069.7	12692.7	20.0	− 9.88	− 14.0	200.0
CSC5MW	10215.7	13807.7	30.0	− 18.92	− 27.0	200.0

positive x direction, for the decay in surge, or a positive angle θ, for the decay in pitch. The platform was then released to oscillate, under the action of the rotor thrust. It is noted that the initial displacements were applied in addition to the loads imposed by the incident wind – i.e., the platforms oscillated around the static displacements caused by the thrust.

Surge and pitch decay tests were simulated for each of the wind velocities (U_w) of Table 2, which cover the entire operational range of the NREL 5 MW wind turbine (in addition to the free decay condition, i.e., U_w= 0).

2.3. Decay simulation results

For each simulation, the decay period was determined as the average period between oscillation peaks, using the statistical tool WAFO (WAFO-group, 2017). For wind velocities near rated, the limit-cycle behavior arising from the control-induced negative damping effect (Nielsen et al., 2006; Jonkman, 2008) is noticed, as illustrated in Fig. 2. It is then important to constrain the analysis to a limited time window after the platform is released, in order to ensure that the cycles considered for the period measurement are dominated by the decay motion. Nonetheless, the measured periods close to rated wind velocity are expected to be less accurate than those for which the limit-cycle effect is minor or non-existent.

The decay periods for surge and pitch as a function of incident wind velocity are shown in Fig. 3. For the surge decay periods (left-hand column), the pattern is similar for both the OC3-Hywind and the CSC5MW concepts: the period increases in the below-rated region, reaching a maximum at the rated wind speed (U_w= 11.4 m/s); and then decreases slowly for increasing velocities in the above-rated region, but always lying above the free-decay[2] period. For the OC4semi concept, however, the pattern is somewhat the opposite: the period decreases for increasing velocities in the below-rated region, has a minimum near rated wind velocity, and then increases moderately in the above-rated regime.

Table 2
Wind velocities considered for the decay simulations.

U_w (m/s)								
0.0	3.0	4.0	5.0	6.0	7.0	8.0	9.0	10.0
11.0	11.4	12.0	13.0	14.0	15.0	16.0	17.0	18.0
19.0	20.0	21.0	22.0	23.0	24.0	25.0		

For pitch decay, as shown in the right-hand column, the pattern is similar for the three concepts: the period is roughly constant until U_w = 5.0 m/s, and then decreases until near-rated wind velocity. It is then suddenly increased, reaching its maximum for $U_w \approx$ 12.0 m/s – and decreasing from then on. The variations in pitch period may vary in range according to the FWT considered. The OC4semi pitch periods lie inside a range of about 5.0 s; this interval varies more than 10.0 s for the OC3Hywind and CSC5MW.

3. Floating wind turbine dynamics

The simulations presented in the previous section are based on a complete model, including elastic effects and multibody dynamics. Now, a simplified approach is introduced, in which the rigid-body motions of a floating, catenary-moored body are the object of the analysis. The corresponding natural periods are distant from structural flexible modes, while the amplitudes may be 2–3 orders of magnitude higher than those associated with e.g. bending of the tower. Consequently, the following single-rigid-body system can be used for representing the dynamic effects of interest (Næss and Moan, 2013):

$$[\mathbf{M}_{RB} + \mathbf{A}_{rad}(\infty)]\ddot{\boldsymbol{\eta}} + \int_0^t \mathbf{K}(t-\tau)\dot{\boldsymbol{\eta}}(\tau)d\tau + \mathbf{D}_v(\dot{\boldsymbol{\eta}})\dot{\boldsymbol{\eta}} + [\mathbf{C}_{hs}(\boldsymbol{\eta}) + \mathbf{C}_{mr}(\boldsymbol{\eta})]\boldsymbol{\eta} = \mathbf{F}_{ext}\,, \quad (1)$$

where $\mathbf{M}_{RB}$ is the rigid-body inertia matrix, $\mathbf{A}_{rad}(\infty)$ is the infinite-frequency added mass matrix, $\mathbf{K}$ is a matrix of retardation functions, is the viscous damping matrix, $\mathbf{C}_{hs}$ and $\mathbf{C}_{mr}$ are the hydrostatic and mooring stiffness matrices, respectively, $\mathbf{F}_{ext}$ is a vector of external loads, and $\boldsymbol{\eta}$ is a vector with the body coordinates in an Earth-fixed coordinate system which has its origin on the water free-surface, with the z-axis pointing upwards (Fig. 4).

---

[2] I.e., the decay for U_w= 0 m/s.

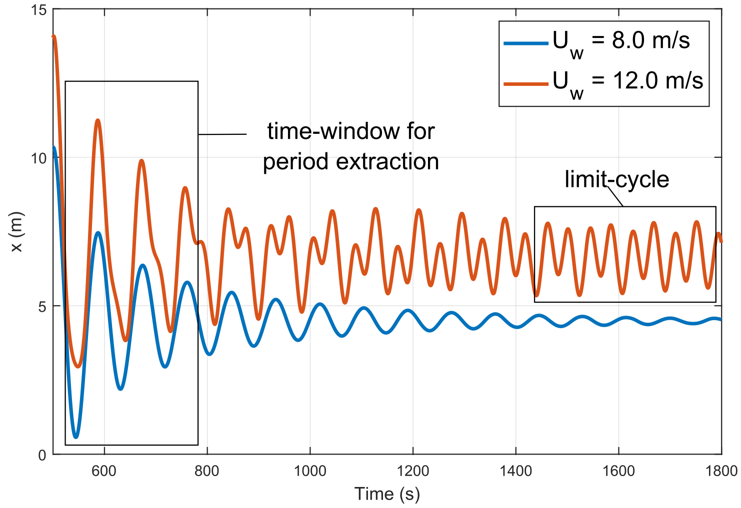

Fig. 2. Surge decay time-series for the CSC5MW, under U_w= 8.0 m/s and U_w= 12.0 m/s.

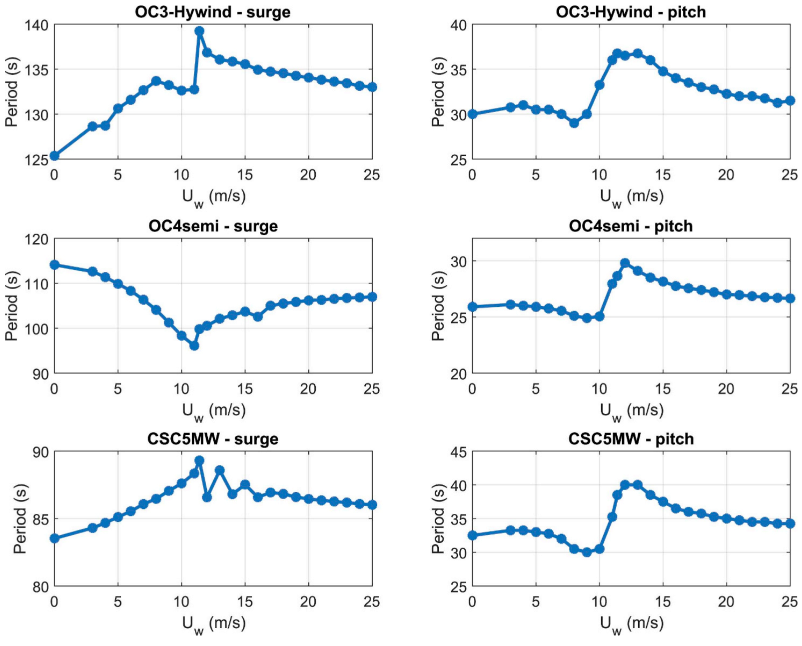

Fig. 3. Surge and pitch decay periods for three FWTs considered, under the incident wind velocities of Table 2.

3.1. Simplified 2-DOF model

The present study considers 0°-winds only – i.e., travelling along the positive x direction. Rotor gyroscopic effects are disregarded, and heave motions are assumed to be entirely decoupled from the other degrees of freedom. Therefore, only surge and pitch dynamics are of interest. Besides, a few assumptions can be proposed to simplify Equation (1) in the analysis of surge and pitch decay:

1. *The platform motions have very low-frequency ($\omega \approx 0$), such that* $\mathbf{K}$ *can be disregarded and the radiation effects can be approximated by replacing* $\mathbf{A}_{rad}(\infty)$ *for* $\mathbf{A}_{rad}(0)$. The reason behind this assumption is the absence of waves and the long natural periods of the floating system's rigid-body motions, corresponding to negligible radiation damping.
2. *The viscous damping can be represented by linear damping only.* This is a reasonable statement considering the low velocities involved.
3. *The hydrostatic and mooring stiffness matrices are independent of the body position.* For the hydrostatic restoring stiffness, this assumption may be justified based on the small changes in volume due to the floater motion, and also on the fairly wall-sided platforms considered in the analysis. With regards to mooring, the matrix has to be linearized around points of interest, since nonlinear effects become important far from the equilibrium position (see Fig. 5).
4. *The only external load is the rotor thrust.* This follows from the fact

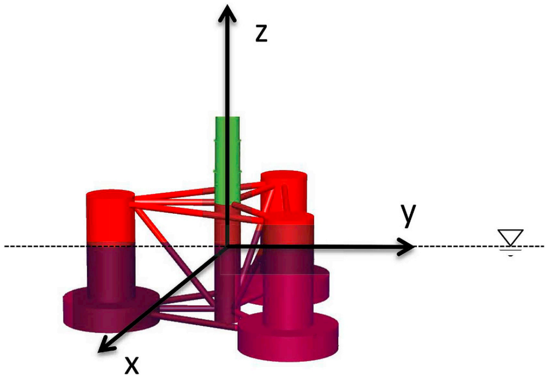

Fig. 4. Coordinate system adopted, placed over the OC4semi platform for reference.

that radiation loads, viscous hydrodynamic forces and mooring/hydrostatic stiffness are already considered in the l.h.s. of the equation, and no waves are present. Besides, wind drag loads on the tower are disregarded.

Equation (1) then reduces to

$$\mathbf{M}\ddot{\eta} + \mathbf{B}_v^l\dot{\eta} + \mathbf{C}\eta = \mathbf{F}_{wind}\,. \tag{2}$$

For a 2-DOF (surge-pitch) system, the matrices in (2) become:

$$\mathbf{M} = \mathbf{M}_{RB} + \mathbf{A}_{rad}(0),\;\; \mathbf{M}_{RB} = \begin{bmatrix} m & mz_g \\ mz_g & I_{yy} \end{bmatrix},\;\; \mathbf{A}_{rad}(0) = \begin{bmatrix} a_{11} & a_{15} \\ a_{51} & a_{55} \end{bmatrix},$$

$$\mathbf{B}_v^l = \begin{bmatrix} b_{11} & 0 \\ 0 & b_{55} \end{bmatrix},$$

$$\mathbf{C} = \mathbf{C}_{hs} + \mathbf{C}_{mr},\;\; \mathbf{C}_{hs} = \begin{bmatrix} 0 & 0 \\ 0 & C_{55}^{hs} \end{bmatrix},\;\; \mathbf{C}_{mr} = \begin{bmatrix} C_{11}^{mr} & C_{15}^{mr} \\ C_{51}^{mr} & C_{55}^{mr} \end{bmatrix},$$

$$\eta = \begin{bmatrix} x \\ \theta \end{bmatrix},$$

$$\mathbf{F}_{wind} = \begin{bmatrix} F_{aer}\cos\theta \\ F_{aer}z_{hub}\cos^2\theta \end{bmatrix},$$

where m is the total mass of the platform, tower, hub and nacelle; z_g is the system's vertical coordinate of the center of gravity; I_{yy} is the total moment of inertia in pitch; a_{ij} are the zero-frequency added mass coefficients; b_{ii} are the linearized viscous damping coefficients in surge and pitch; C_{55}^{hs} is the linear hydrostatic restoring coefficient in pitch, already accounting for gravitational effects; C_{ij}^{mr} are the linear mooring restoring coefficients; x is the displacement in surge; θ is the pitch angle; F_{aer} is the turbine thrust; and z_{hub} is the hub height.

3.2. Control system

Wind turbines are normally equipped with a control system, in order to optimize power production and interrupt the operation under unfavourable conditions. The NREL 5 MW wind turbine controller actuates on the generator torque (Q_{gen}) and collective blade pitch angle (β), depending on the operational regime.

The generator torque is based on the filtered shaft velocity, ω. In the below-rated regime ($3.0\,\text{m/s} \leq U_w < 11.4\,\text{m/s}$), the torque is proportional to the squared shaft velocity, such as to optimize power production; in the above-rated region ($11.4\,\text{m/s} \leq U_w \leq 25.0\,\text{m/s}$), it is inversely proportional to the shaft velocity, such as to keep the power constant.

In the above-rated regime, the rotor speed is regulated through changes in the blade-pitch angle (which lead to changes in the aerodynamic torque load). The change in blade pitch angle is determined by a gain-scheduled proportional-integral (PI) controller:

$$\Delta\beta = K_p(\beta)\Delta\omega + K_i(\beta)\int_0^t \Delta\omega dt\,, \tag{3}$$

where the proportional (K_p) and integral (K_i) gains are calculated as a function of the blades' current pitch angle, β; see Table 3 for the gains adopted for $\beta = 0$. The input to the controller ($\Delta\omega$) is the difference between the rotor speed and the reference rotor speed. A more detailed description of the control strategy, including the gain scheduling procedure, is provided by Jonkman et al (2009).

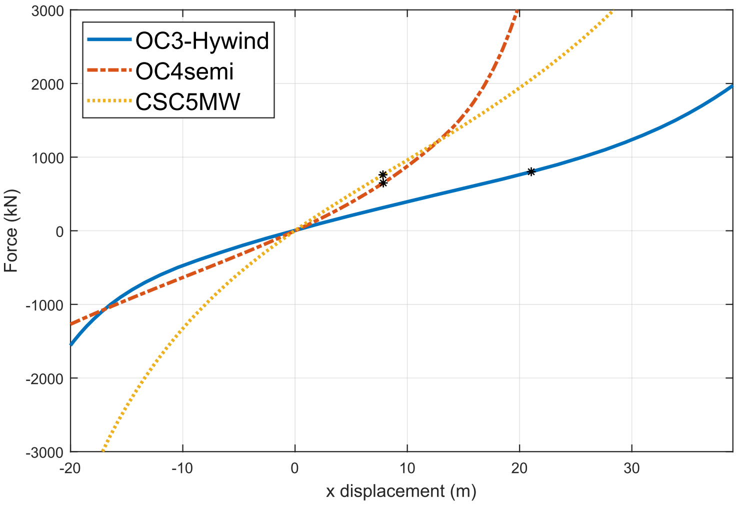

Fig. 5. Force-displacement curves obtained from pullout simulations in surge. The asterisks indicate platform displacement for U_w= 11.4 m/s. The different offsets in platform pitch explain the slightly different horizontal components of the thrust indicated in the y-axis.

Table 3
Blade-pitch controller gains for zero pitch angle.

$K_p(\beta = 0)$	$K_i(\beta = 0)$
0.6087 s^{-1}	0.0870

3.3. External loads

When a FWT oscillates under the action of wind, it is subjected to three main sources of loads: the aerodynamic thrust, induced on the rotor[3]; the hydrodynamic loads, acting on the submerged portion of the platform; and the mooring loads, applied on the fairleads, which normally are also underwater.

The aerodynamic thrust is a function of the relative flow velocity in the rotor, which is a combination of the incident wind velocity, the nacelle velocity and the inflow velocity. When the turbine oscillates, the nacelle velocity is also oscillatory and so is the thrust. A phase shift, however, is observed between thrust and nacelle velocity. This effect may be worked out and treated as a modification in the nacelle's inertia and damping, therefore influencing the FWT decay periods.

In the absence of waves, hydrodynamic loads may be divided into two groups: the radiation loads, related to the waves produced by the body's motion; and the viscous loads, which are a function of the body's velocity. For typical surge/pitch decay periods ($\omega \approx 0$), radiation loads reduce to acceleration-proportional terms, commonly known as added mass. The added mass influences the natural periods, but there is no reason to relate it to the period *changes* for different wind velocities.[4] Viscous damping also affects natural periods, but cannot be used to explain the period variations, either.

Catenary mooring systems normally provide fairly linear stiffness when the platform is close to the neutral position. For surge, however, the stiffness gets nonlinear as the platform is displaced along the x-axis. Therefore, when subjected to a mean wind loading, the platform may oscillate around a mean position which lies in the nonlinear range, leading to a natural period different from when the system oscillates around the neutral position.

It is then expected that the nonlinearities induced by aerodynamic thrust and catenary mooring system should play prevailing roles behind the period variation phenomenon, as discussed below.

4. Prediction of the decay period changes for varying U_w

Simplified representations for the nonlinear effects discussed in the previous section are now developed, providing means to estimate the decay periods based on Equation (2).

4.1. Mooring system nonlinearities

Catenary mooring systems are meant to position a floating body using the mooring lines' own weight-in-water. When the platform is displaced away from the anchor, a portion of the line resting on the seabed is lifted, increasing the weight to be supported by the floater. In addition, due to the change in angle, the horizontal component of the tension increases, also contributing nonlinearly to the horizontal restoring force (Brown, 2005). The nonlinearity is evident in Fig. 5, where the mooring stiffness curves for the three platforms are shown. When subjected to a mean wind force, the platform will oscillate around the corresponding offset, with different stiffnesses – and therefore periods – for varying wind velocities.

Loads induced by catenary mooring systems may be estimated analytically (Faltinsen, 1993). Here, expressions for the mooring stiffness are instead determined through polynomial fitting of the data in Fig. 5. Since the wind displaces the FWT towards the positive x direction, the fitting is made for $x > 0$ only. 3rd-order polynomials are found to fit the data with excellent agreement, such that the following nonlinear stiffness model is applied:

$$F_r(x) = -k_1x - k_2x^2 - k_3x^3 = -k(x)x \; , \tag{4}$$

where k_1, k_2 and k_3 are obtained from the data fitting procedure, and the x-dependent stiffness coefficient is given by:

$$k(x) = k_1 + k_2x + k_3x^2 \; . \tag{5}$$

Time-domain simulations can be performed by replacing the C_{11}^{mr} element of the stiffness matrix with $k(x)$, calculated according to the procedure above, in Equation (2). Alternatively, the nonlinear model of Equation (4) can be linearized around a given offset x_0. Keeping up to first-order terms in a Taylor expansion, it becomes:

$$F_r(x) \approx (k_2x_0^2 + 2k_3x_0^3) - (k_1 + 2k_2x_0 + 3k_3x_0^2)x \; , \tag{6}$$

such that the linearized stiffness coefficient k_{11}^{lin} is given by

$$k_{11}^{lin}(x_0) = k_1 + 2k_2x_0 + 3k_3x_0^2 \; . \tag{7}$$

Typical platform rotations in pitch do not produce important geometric changes in the mooring lines, resulting in a fairly linear behavior for the mooring stiffness in this DOF. Therefore, the main source of nonlinear mooring restoring for pitch comes from the surge-pitch coupling, which depends on the vertical distance from the fairleads to the platform's center of gravity.

Still, restoring in pitch for catenary-moored FWTs is dominated by hydrostatic effects – which, for typical pitch angles, have linear behavior. Therefore, mooring stiffness should not be behind the observed changes in the pitch decay period for varying incident wind velocities. The pitch period changes must then be related to the r.h.s. of Equation (2).

4.2. Prediction of the surge decay periods with a linearized stiffness matrix

A simple way to estimate the surge decay periods is to linearize the stiffness around the offset associated to a given U_w, using the x_0 values obtained from the SIMA simulations in Equation (7). The coefficients k_1, k_2 and k_3 for each curve in Figure (5) are presented in Table 4. The cross terms of the mooring stiffness matrix are obtained from the linear stiffness in surge, multiplied by the fairleads vertical position relative to the SWL, z_{fl}, and the term for pitch is kept unchanged. The matrix for a given offset, $\mathbf{C}_{mr}(x_0)$, is then given by:

$$\mathbf{C}_{mr}(x_0) = \begin{bmatrix} k_{11}^{lin}(x_0) & k_{11}^{lin}(x_0)z_{fl} \\ k_{11}^{lin}(x_0)z_{fl} & C_{55}^{mr} \end{bmatrix} . \tag{8}$$

The period for each U_w can then be calculated from the eigenvalues of Equation (2), with the stiffness matrix defined as above.

Table 4
Coefficients for the linearized mooring stiffness in surge, as given by Equation (7).

	k_1 (Nm^{-2})	k_2 (Nm^{-3})	k_3 (Nm^{-4})
OC3Hywind	5.37×10^4	-1.44×10^3	3.52×10^1
OC4semi	7.13×10^4	7.52×10^2	8.98×10^1
CSC5MW	1.05×10^5	-1.39×10^3	5.00×10^1

---

[3] The drag on tower and hull should also be classified as an aerodynamic effect, but is of secondary importance and therefore disregarded.

[4] Actually, geometric changes due to variations in the mean pitch offset can affect the radiation loads. This effect is however disregarded in the benchmark simulations presented in Section 2, and therefore are also neglected here.

4.3. Aerodynamic apparent inertia/stiffness and damping effects

Let a FWT be subjected to steady, non-turbulent wind. The airflow velocity $w(t)$ is the relative axial flow velocity "felt" by the rotor, and is given by:

$$w(t) = w_0 - w_i(t) - \dot{x}_{nac} \, , \tag{9}$$

where w_0 is the incident wind velocity; $\dot{x}_{nac}$ is the nacelle horizontal velocity; and the inflow velocity, w_i, is a flow induced in the rotor by the vorticity shed by the blades, as stated by the Biot-Savart law.

Platform oscillations affect $w(t)$ through variations in, $\dot{x}_{nac}$[5] provoking fluctuations in the rotor torque and thrust. A thorough discussion about this effect is provided by Pedersen (2017) – Appendix A summarizes the most relevant formulations from that work for the purposes of this paper. Particularly, important insight is obtained from a combination of equations (A.5) and (A.6), leading to the following expression for the thrust[6]:

$$F = \kappa\,[\,\cos(u)w - \sin(u)\Omega\ell\,]\Omega \, , \tag{10}$$

where u is the blade-pitch control action, Ω is the rotor angular velocity and κ, ℓ are constants. Noting that $u = 0$ in the below-rated regime (no blade-pitch action), Equation (10) reduces to

$$F = \kappa w \Omega \, . \tag{11}$$

Replacing w as given by (9), and writing the rotor velocity as a mean plus a varying term, $\Omega(t) = \Omega_0 + \Omega'(t)$, the following expression is obtained for the thrust in the below-rated regime:

$$F = \kappa\Omega_0(w_0 - w_i) + \kappa(w_0 - w_i)\Omega' - \kappa\Omega_0\dot{x}_{nac} \, , \tag{12}$$

where only linear terms were kept. Assuming small variations in w_i, the first term in the r.h.s. of Equation (12) may be seen as a constant, while the second term depends essentially on the rotor dynamics. The last term oscillates proportionally to $\dot{x}_{nac}$, and since κ and Ω_0 are both positive, the negative sign implies that the thrust, in the below-rated region, will always induce a damping effect into the nacelle dynamics.

When the turbine operates in the above-rated regime, the blade-pitch control system results in non-zero values for u, and Equation (11) may be rewritten according to:

$$F = \kappa\Omega[\cos(u)(w_0 - w_i) - \sin(u)\Omega\ell] - \kappa\Omega_0\cos(u)\dot{x}_{nac} \, . \tag{13}$$

The second term now depends on $\cos(u)$, which is a function of the generator angular velocity through a PI-controller. Therefore, it is no longer possible to affirm that the oscillating term is proportional to $-\dot{x}_{nac}$. While an analytical development of this relation is not in the scope of this paper, it is of interest to understand how F varies as a function of $\dot{x}_{nac}$ in the above-rated regime, and the consequent effects on the system global dynamics.

For this purpose, a series of simulations were executed in which the NREL 5 MW turbine (including controller) oscillated horizontally, with rotor aerodynamics calculated with AeroDyn (Moriarty and Hansen, 2005). It was decided to adopt the BEM formulation with dynamic stall correction, and the blades were kept rigid. The oscillation amplitude was 10.0 m and the period varied from 20.0 s to 160.0 s, with increments of 1.0 s. The incident wind velocities are the same as those presented in Table 2.

Fig. 6 shows the aerodynamic thrust and nacelle velocity for an oscillation period of 30.0 s and incident wind velocities of 9.0 m/s, 11.4 m/s and 18.0 m/s. It is suggested that the thrust F can be written as a sum of a mean term, $F_{mean}(U_w)$, and a varying term, $F_{var}(U_w, \dot{x}_{nac})$:

$$F_{aer} = F_{mean}(U_w) + F_{var}(U_w, \dot{x}_{nac}) \, . \tag{14}$$

For U_w= 9.0 m/s, the phase difference between F_{var} and $\dot{x}_{nac}$ is close to π rad, which is in agreement with the discussion above. Defining a *velocity-to-thrust amplitude factor* f_0, $F_{var}(U_w, \dot{x}_{nac})$ may be rewritten as follows:

$$F_{var}(U_w, \dot{x}_{nac}) \approx -f_0\dot{x}_{nac} \, . \tag{15}$$

The 1-DOF motion of the nacelle, with mass m, stiffness k and damping c, and forced by F, is driven by:

$$m\ddot{x} + c\dot{x} + kx = F_{mean} - f_0\dot{x} \Rightarrow m\ddot{x} + (c + f_0)\dot{x} + kx = F_{mean} \, , \tag{16}$$

where the *nac* indicator on x was suppressed for conciseness.

The discussed damping effect of the thrust is now more visible. This is a well-known effect for FWTs, explained e.g. in (Jonkman, 2008; Goupee et al., 2017). The second and third plots of Fig. 6, however, show that the controller action results in the thrust oscillating with a phase ϕ relative to the nacelle velocity. This effect, also reported in (Lennie et al., 2016), is not fully understood yet, but dynamic wake effects, actuator dynamics and delays induced by signal filtering may possibly contribute to it.

Assuming that the nacelle motion may be described as $x(t) = x_0\sin(\omega t)$, the velocity is given by $\dot{x}(t) = x_0\omega\cos(\omega t)$, and F_{var} becomes

$$\begin{aligned} F_{var} &= f_0 x_0\omega\cos(\omega t + \phi) \\ &= f_0\,[x_0\omega\cos(\omega t)\cos(\phi) - x_0\omega\sin(\omega t)\sin(\phi)] \\ &= f_0\,[\dot{x}\cos(\phi) - \omega x\sin(\phi)] \, . \end{aligned} \tag{17}$$

Noting that

$$\omega x = \frac{\omega^2}{\omega}x = -\frac{\ddot{x}}{\omega} \, ,$$

the last term of Equation (17) can then alternatively be written as:

$$F_{var} = f_0\left[\dot{x}\cos(\phi) + \frac{\ddot{x}}{\omega}\sin(\phi)\right] . \tag{18}$$

In the above-rated regime the thrust is thus no longer proportional to the nacelle velocity only, but rather to a combination of nacelle velocity and position/acceleration. In the latter case, the effect may be interpreted as an "apparent inertia":

$$\left[m - \frac{f_0}{\omega}\sin(\phi)\right]\ddot{x} + [c - f_0\cos(\phi)]\dot{x} + kx = F_{mean} \, . \tag{19}$$

Variations in the system's natural period can now be related to f_0 and ϕ. When the phase is such that $|\sin(\phi)|$ increases, the thrust effect on the system's damping is reduced and the apparent changes in inertia become more important. A quantification of this influence demands a better understanding on how f_0 and ϕ vary with the incident wind velocity, the nacelle's period of oscillation and the motion amplitude.

4.4. Quantification of the apparent inertia and damping effects induced by the thrust

The above-mentioned simulations with AeroDyn provided a total of 3384 pairs of rotor thrust and nacelle velocity time-series. For each pair, a *fast Fourier transform* (FFT) was performed for both time-series, yielding their discrete frequency domain representations. The phase ϕ between the time-series could then be determined as the angle of the ratio between the thrust and nacelle velocity representations in the frequency domain, at the frequency of oscillation. The velocity-to-thrust amplitude factor, f_0, is obtained directly from the time-series, by considering the ratio of their maximum amplitudes.

Fig. 7 shows the values of ϕ calculated as explained above. One can clearly distinguish the below-rated region by the nearly uniform phase values – close to π rad, as discussed previously. Close to U_w= 11.4 m/s, the phase values change smoothly for shorter oscillation periods, lying between $\pi/6$ rad and $2\pi/3$ rad as the wind velocity increases. When the

---

[5] The inflow velocity w_i is also affected, but in a much lower degree.

[6] Note that equation (A.6) actually refers to the *circulatory thrust* only – i.e., the drag portion (A.7) is disregarded in this discussion, due to its relatively lower importance.

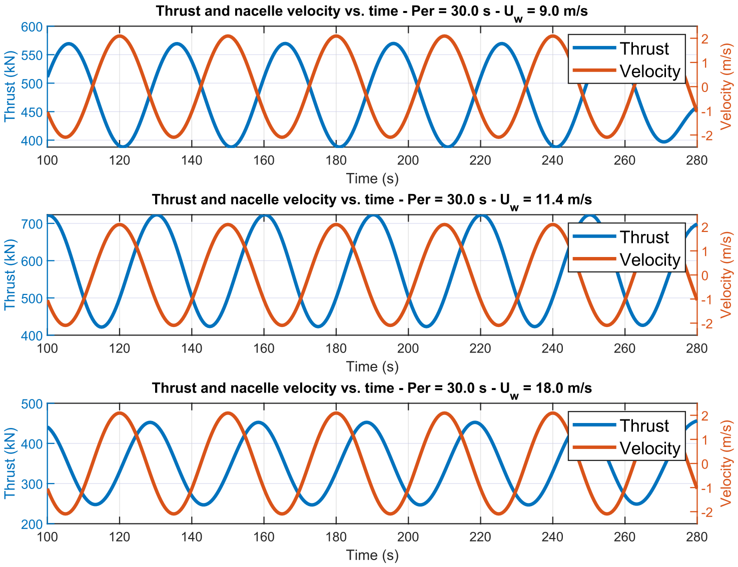

Fig. 6. Aerodynamic thrust and nacelle velocity from forced oscillations of the NREL 5 MW reference wind turbine, with amplitude of 10.0 m, oscillation period of 30.0 s and U_w= 9.0 m/s, 11.4 m/s and 18.0 m/s.

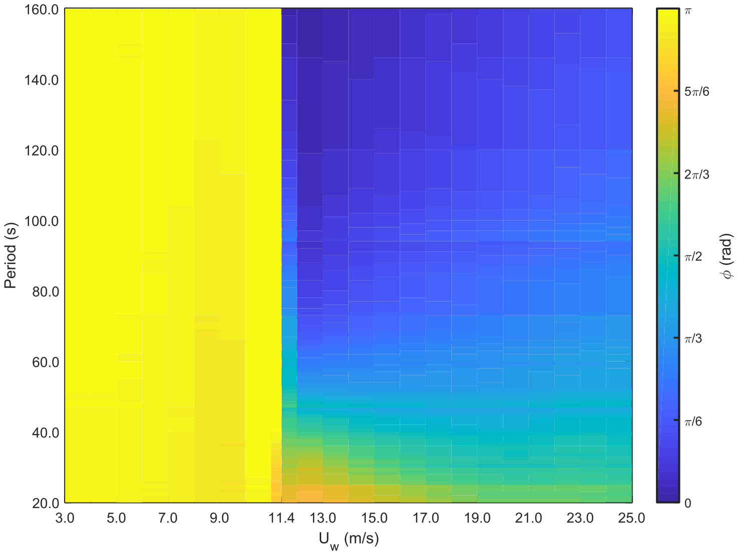

Fig. 7. Phases between rotor thrust and nacelle velocity (ϕ) as a function of incident wind velocity and oscillation period.

period is longer, the change is more abrupt and the phase tends to be smaller, lying between 0 rad and $\pi/6$ rad. This indicates that, when the system dynamics are slower, the thrust tends to follow the velocity more closely.

Another important feature of the plot is that it helps to visualize the operating conditions when, according to Equation (19), the thrust results in a negative damping effect – i.e., when the phase lies between 0 rad and $\pi/2$ rad. This is observed for most of the above-rated region, but for shorter periods and wind velocities closer to rated, the phase may be slightly higher than $\pi/2$ rad. This may be useful e.g. during the design of a controller.

The f_0 factor values are presented in a similar scheme, in Fig. 8. In general, the factor changes more intensely near rated wind velocity, where it is highly amplified in comparison to other operational regions.

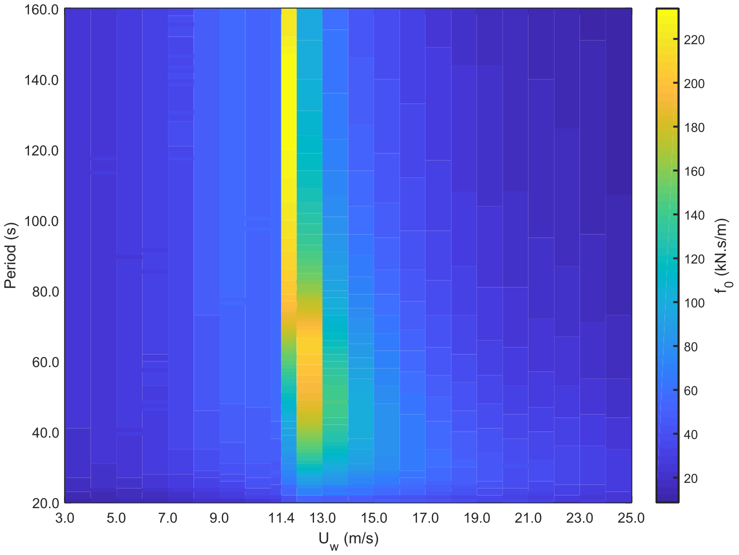

Fig. 8. Velocity-to-thrust amplitude factor (f_0) as a function of incident wind velocity and oscillation period.

The thrust amplitude changes much faster from below rated to rated when the periods are longer, while this transition is smoother for shorter periods.

Once ϕ and f_0 are known, the apparent inertia and damping from thrust can be quantified. From Equation (19), the aerodynamic apparent inertia and damping coefficients, a_{aer} and b_{aer}, are defined according to:

$$a_{aer} = -\frac{f_0}{\omega}\sin(\phi)\,, \quad b_{aer} = -f_0\cos(\phi)\,. \tag{20}$$

The matrices of aerodynamic apparent inertia and damping can then be written as:

$$\mathbf{A}_{aer} = \begin{bmatrix} a_{aer} & a_{aer}h_{nac} \\ a_{aer}h_{nac} & a_{aer}h_{nac}^2 \end{bmatrix}, \tag{21}$$

$$\mathbf{B}_{aer} = \begin{bmatrix} b_{aer} & b_{aer}h_{nac} \\ b_{aer}h_{nac} & b_{aer}h_{nac}^2 \end{bmatrix}, \tag{22}$$

where h_{nac} is the height of the nacelle with respect to SWL.

One should note that Figs. 7 and 8 are based on *imposed* nacelle oscillations – i.e., the motions are not affected by the thrust. This is in contrast with the decay simulations, in which the motions are not only influenced by the thrust but also indirectly modify it through the changes in flow velocity and varying rotor speed. Indeed, the second term on the r.h.s. of Equation (12) depends on Ω', whose dynamics are given by:

$$\dot{\Omega}' = \frac{Q_{aer} - Q_{gen}}{I_{rot}}\,, \tag{23}$$

where Q_{aer} and Q_{gen} are the aerodynamic and generator torque, respectively, and I_{rot} is the rotor moment of inertia around the shaft. From Equation (A.6) and the discussions in section 3.2, the dependence of Ω' on both $\dot{x}_{nac}$ and Ω become evident, but this is not captured by the proposed model. Inaccuracies on the period predictions are therefore expected especially in the below-rated regime. Above-rated, the torque regulation through blade-pitch control reduces the importance of the rotor dynamics, leading to more accurate period predictions.

4.5. Prediction of the pitch decay periods based on the apparent inertia and damping effects

The aerodynamic effects on inertia and damping can be accounted for in the FWT dynamics by adding $\mathbf{A}_{aer}$ and $\mathbf{B}_{aer}$ to the inertia and damping matrices:

$$\mathbf{M}' = \mathbf{M}_{RB} + \mathbf{A}_{rad}(0) + \mathbf{A}_{aer}\,, \tag{24}$$

$$\mathbf{B}' = \mathbf{B}_v^l + \mathbf{B}_{aer}\,, \tag{25}$$

such that Equation (2) can now be rewritten as follows:

$$\mathbf{M}'\ddot{\boldsymbol{\eta}} + \mathbf{B}'\dot{\boldsymbol{\eta}} + \mathbf{C}\boldsymbol{\eta} = \bar{\mathbf{F}}_{wind}\,, \tag{26}$$

where $\bar{\mathbf{F}}_{wind}$ is formed by the mean thrust component, F_{mean}:

$$\bar{\mathbf{F}}_{wind} = \begin{bmatrix} F_{mean} \\ F_{mean}z_{hub} \end{bmatrix}. \tag{27}$$

It is assumed in Equation (27) that the pitch angle is small enough for the dependence in θ to be neglected. As it is noted, the varying component of the thrust is now "absorbed" by the inertia and damping matrices, making it straightforward to relate its effects to changes in the decay periods for different incident wind velocities.

The pitch decay period for a given U_w can be calculated once the coefficients a_{aer} and b_{aer} are known. These coefficients, however, depend themselves on the period, such that an iterative procedure is adopted. Departing from an initial guess for the period, the phase ϕ and the amplitude factor f_0 are obtained by interpolation in the matrices presented in Figs. 7 and 8. A new value for the period is then obtained based on the corresponding a_{aer} and b_{aer}, and is compared to the previous guess. The process is repeated until the difference becomes lower than a given tolerance.

The relevance of the apparent inertia can now be assessed. Table 5 shows the ratio between the apparent inertia and the rigid-body plus zero-frequency added inertia, in surge (top) and pitch (bottom), for

Table 5
Ratio (%) between aerodynamic apparent mass and rigid-body + added mass.

		U_w= 7.0 m/s	U_w= 11.4 m/s	U_w= 18.0 m/s
surge $\frac{a_{aer}}{(m+a_{11})}$	OC3Hywind	0.04	2.60	1.57
	OC4semi	0.01	6.55	0.60
	CSC5MW	0.30	8.99	0.28
pitch $\frac{a_{aer}h_{hub}^2}{(I_{yy}+a_{55})}$	OC3Hywind	0.05	3.19	1.93
	OC4semi	0.22	10.02	8.22
	CSC5MW	0.53	18.81	10.77

Table 6
Ratio (%) between aerodynamic apparent damping and linear viscous damping.

		U_w= 7.0 m/s	U_w= 11.4 m/s	U_w= 18.0 m/s
surge $\frac{b_{aer}}{b_{11}}$	OC3Hywind	21.80	− 92.78	− 13.95
	OC4semi	45.11	− 140.43	− 31.28
	CSC5MW	24.98	− 62.49	− 20.67
pitch $\frac{b_{aer}h_{hub}^2}{b_{55}}$	OC3Hywind	19.89	18.10	− 5.37
	OC4semi	60.27	73.18	− 11.65
	CSC5MW	83.47	45.12	− 25.07

three values of U_w. For surge, the effect of apparent inertia is irrelevant for the below- and above-rated regimes, while near rated the value may have some importance.[7] For pitch, the apparent inertia is again negligible at the below-rated region. For above-rated, however, the nacelle apparent inertia assumes values that, when multiplied by the squared nacelle height, may result in an apparent moment of inertia effect with order of magnitude comparable to the FWT's rigid-body and added inertia, depending on the platform.

The apparent damping effect is relevant for both surge and pitch. As indicated in Table 6, for below-rated wind speeds it may significantly increase the viscous damping at both DOFs. For U_w= 11.4 m/s, however, the damping assumes a negative value in surge, even exceeding the equivalent linear viscous coefficient for the OC4semi. In the SIMA simulations (where the damping is a combination of linear and quadratic terms), this results in an effective zero-damping scenario, leading to the limit-cycle effect discussed in section 2.3. For pitch, however, the damping is still positive at rated, but becomes negative for all platforms as the wind velocity increases.

5. Results

The natural frequencies for each U_w are obtained from the eigenvalues of the undamped and homogeneous version of Equation (2):

$$\mathbf{M}\ddot{\eta} + \mathbf{C}\eta = 0\,, \tag{28}$$

where for surge the mooring stiffness matrix is written as in Equation (8), while for pitch the inertia matrix includes $\mathbf{A}_{aer}$, as given by Equation (24). The undamped natural frequency for a given DOF, $\omega_{0,i}$, is then corrected for accounting for damping, yielding the decay frequency $\omega_{d,i}$:

$$\omega_{d,i} = \omega_{0,i}\sqrt{1-\zeta_i^2}\,, \tag{29}$$

where ζ_i is the relative damping coefficient. While for surge it is based on the b_{11} coefficients from Section 3, for pitch it also accounts for the main diagonal elements of the matrix given in Equation (22).

5.1. Periods in surge

The predicted surge periods are presented in Figs. 9–11, which show the estimates for the three FWT concepts considered, under the range of incident wind velocities of Table 2. The bottom plots bring the relative error between estimated and simulated periods.

For the OC3-Hywind (Fig. 9), the estimated periods match the simulations with an error in general lower than 0.5% in the above-rated regime. For the below-rated region there is an increase in the relative error as the wind speed approaches the rated condition, notably for U_w= 8.0–11.0 m/s. At this range of wind speeds, the platform offsets in surge are not so different from what is observed for U_w= 12.0–16.0 m/s, where the discrepancy between simulations and estimates is much lower. This suggests that the discrepancies may hardly be attributed to the linearization method adopted.

The agreement between estimated and simulated periods is much better for the OC4semi (Fig. 10) and the CSC5MW (Fig. 11). Indeed, the relative error for both FWTs is lower than 1% for most U_w values, increasing only near rated wind velocity.

5.2. Periods in pitch

Figs. 12–14 show the estimated decay periods in pitch for the three FWT concepts considered, under the range of incident wind velocities of Table 2. For all three concepts, it is seen that the period variation from the SIMA simulations is very satisfactorily followed by the estimates in the rated and above-rated regime. For the OC3Hywind, the relative error for U_w= 11.4 m/s is around 4%, lying below 2% for higher velocities. For the OC4semi and CSC5MW the relative errors are even smaller, with simulated and estimated curves nearly coincident along the above-rated regime. In the below-rated region, however, the estimates for all concepts fail to predict a “depression” observed for the simulated periods in the range 6.0 m/s ≥ U_w≥ 10.0 m/s. A possible explanation may be the absence, in the simplified model, of the influence of the rotor dynamics – as discussed in section 4.4.

Even though all three FWT concepts are equipped with the same turbine, the magnitude of the period changes is not the same, as already pointed out in Section 2.3. This can be related to the fact that the natural periods (for U_w= 0) differ for each design, falling in different regions of Fig. 7. Indeed, Fig. 7 shows that at the range of periods between 20.0 s and 40.0 s the phases vary significantly in the above-rated regime, implying that modest changes in the FWT inertia properties may heavily influence the period variation phenomenon.

6. Conclusions

As previously reported in (Bachynski et al., 2016; Goupee et al., 2017), surge and pitch decay periods variations were observed for FWTs operating under different incident wind velocities. In this paper, the effect was reproduced in time-domain simulations performed with SIMA, and an investigation for its origins was carried out. It was found that the period variations in surge and pitch have distinct sources. While for the former the effect is mainly linked to the mooring system nonlinearities, for the latter it is induced by the thrust at the turbine, in combination with the nacelle motions.

A simplified model was then applied for predicting the period variations as a function of the incident wind velocity. For surge, the mooring stiffness coefficient was linearized around the offsets associated to each U_w, and then the periods were found from the eigenvalues of the linear 2-DOF equation of motion. The predictions closely agreed with the simulated periods, with relative errors of less than 1% along most of the range of U_w values. Higher (but still limited) discrepancies were observed close to rated regime.

For pitch, the relative phase between nacelle velocity and the thrust induced in the rotor could be related to apparent inertia and damping terms in the equations of motion. This effect was quantified for a

---

[7] Fig. 7 shows however that for periods higher than 90.0 s the change in phase at 11.4 m/s is quite sudden, such that one should be careful with the phases (and therefore inertia/damping effects) calculated for this wind speed.

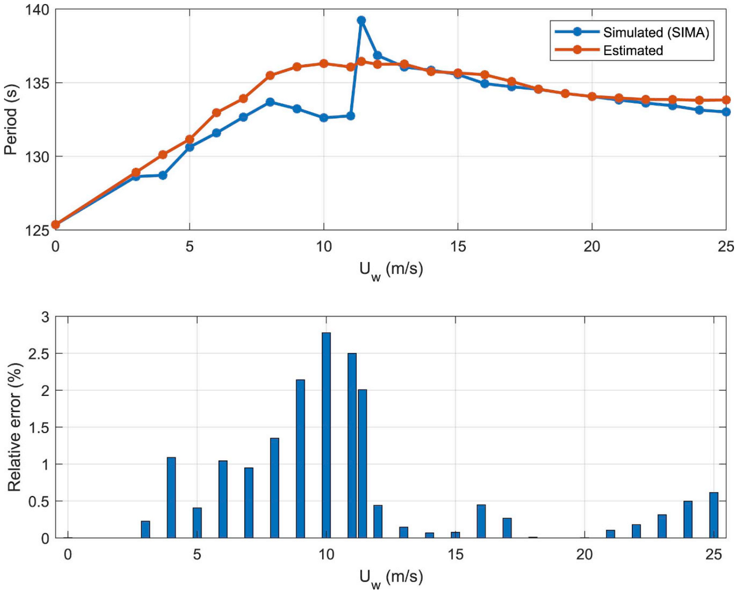

Fig. 9. Surge decay periods: simulations with SIMA and estimates based on Equation (2), with mooring stiffness matrix according to Equation (8) – OC3-Hywind.

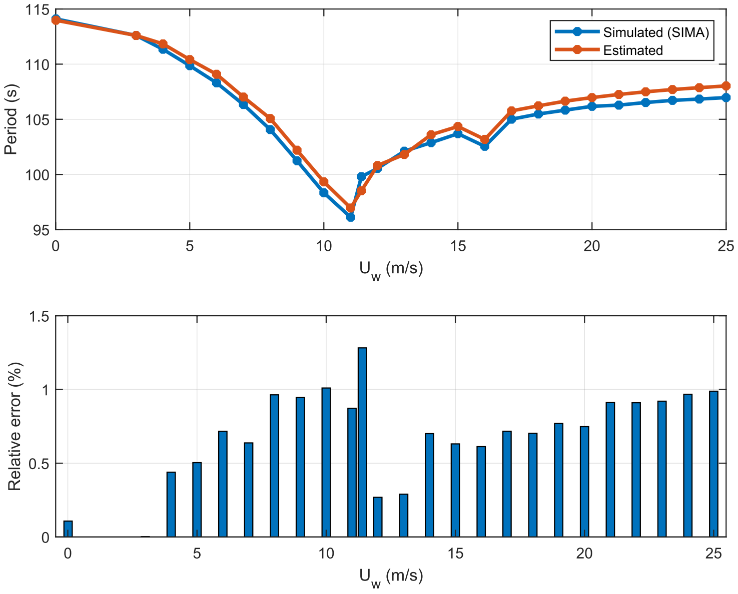

Fig. 10. Surge decay periods: simulations with SIMA and estimates based on Equation (2), with mooring stiffness matrix according to Equation (8) – OC4semi.

combination of wind velocities and oscillation periods, through simulations involving AeroDyn coupled to an 1-DOF system. Inertia and damping coefficients were then included in a linear model, from which the periods could be estimated. The method resulted in precise predictions of the period in comparison with the time-domain simulations, in the above-rated region. In the below-rated region, a "depression" was noticed for the simulated data which could not be replicated with the approximated method. The reasons for this discrepancy are unclear, but a possible explanation could be that the phases and amplitudes from Figs. 7 and 8 are based on imposed nacelle oscillations, which did not depend on the thrust – and rotor dynamics – in a coupled manner. A better understanding of this coupling effect and how to include it in the simplified model would represent important contributions to the method.

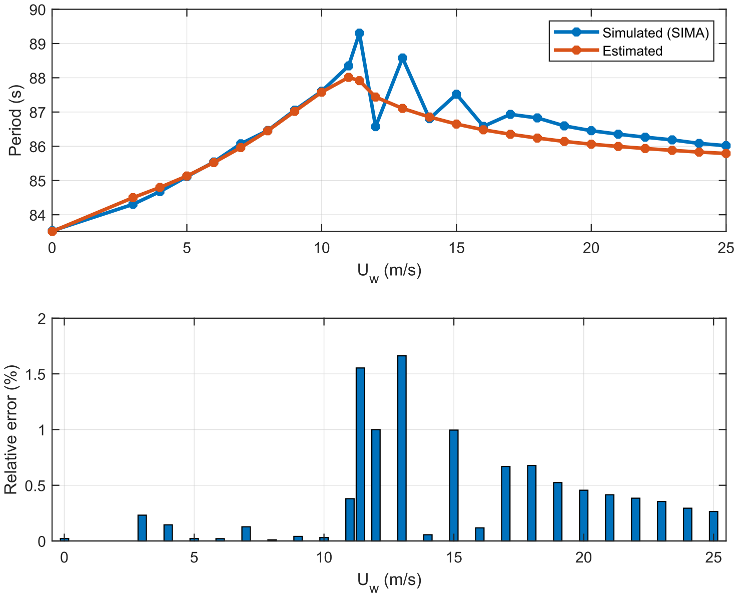

Fig. 11. Surge decay periods: simulations with SIMA and estimates based on Equation (2), with mooring stiffness matrix according to Equation (8) – CSC5MW.

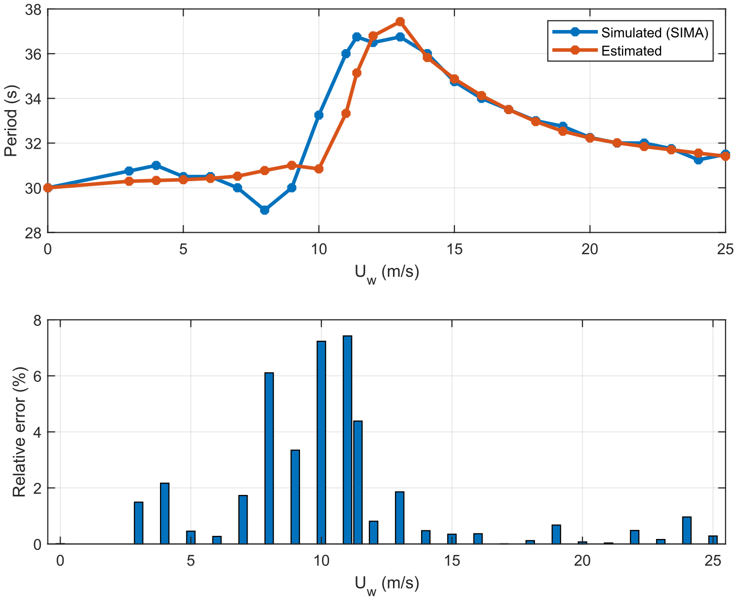

Fig. 12. Pitch decay periods: simulations with SIMA and estimates based on Equation (26) – OC3-Hywind.

The period variation in pitch depended on the height of the nacelle relative to SWL. The effect is expected to be more relevant for higher towers, and thus more important for turbines of higher capacity. On the other hand, the phenomenon can be attenuated by proper tuning of the FWT's own pitch natural period, by “placing” the oscillations in a range where the apparent inertia effect is less relevant.

The capability of predicting the period variation with a simplified method may be useful in different stages of the development of new FWT concepts. For example, the possibility of replacing full decay simulations (which took approximately 15 min, with an Intel® Core™i7

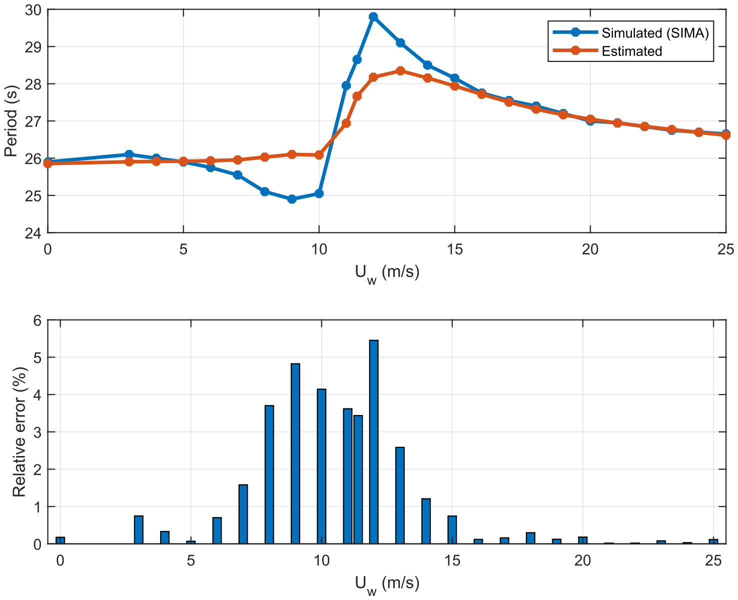

Fig. 13. Pitch decay periods: simulations with SIMA and estimates based on Equation (26) – OC4semi.

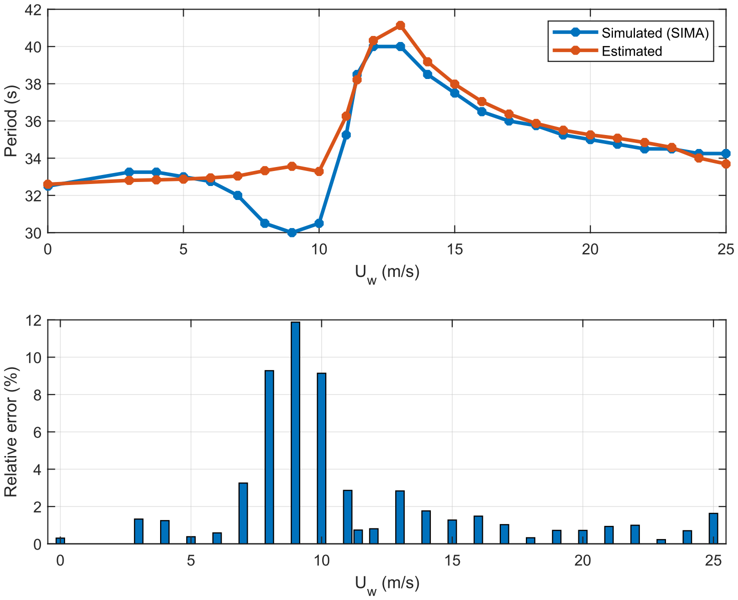

Fig. 14. Pitch decay periods: simulations with SIMA and estimates based on Equation (26) – CSC5MW.

6500U 2.50 GHz CPU, for each wind velocity) for eigenvalues calculations (0.8 s for the entire range of wind velocities) can be an advantage when different platform concepts are to be considered in early design phases. Further research may relate the proposed method to disciplines like structural integrity assessment, control system design, mooring systems and model testing. The method could also contribute in the development of new frequency-domain tools.

Acknowledgements

The authors are sincerely grateful to the financial support from NTNU/IMT and the Centre for Autonomous Marine Operations and Systems (Norwegian Research Council project 223254).

Appendix A. Parametric aerodynamics model based on Dynamic Vortex Theory

Pedersen (2017) devised a convenient model for the aerodynamic thrust and torque, where the interconnected nature of those loads are made evident through the so-defined *circulation function*. From the Kutta-Joukowsky theorem, the lift force $d\mathbf{f}$ on a line element $d\mathbf{l}$ is given by:

$$d\mathbf{f} = \rho \mathbf{u}_r \times \Gamma d\mathbf{l} \, , \tag{A.1}$$

where Γ is the circulation[8] and $\mathbf{u}_r$ is the relative flow velocity, which in a system of cylindrical coordinates (r, θ, z) fixed to the rotor is given by

$$\mathbf{u}_r(t) = \mathbf{e}_z w(t) - \mathbf{e}_\theta \Omega(t) r \, , \tag{A.2}$$

with w being the airflow and Ω the rotor angular velocity. Under the assumption of purely axial inflow, the normal component of $d\mathbf{f}$ is integrated over each of the blades, leading to the following expression for the circulatory thrust, F_c:

$$F_c(t) = \frac{\rho A N}{2\pi} \Gamma(t) \Omega(t) \, , \tag{A.3}$$

where ρ is the density of the air, A is the rotor swept area and N is the number of blades. Equivalently, the circulatory torque is found by integrating the tangential component of $d\mathbf{f}$ along each blade:

$$Q_c(t) = \frac{\rho A N}{2\pi} \Gamma(t) w(t) \, . \tag{A.4}$$

The author then proceeds with a series of simplifications for the circulation function, with the objective of devising an *engineering model* without significant losses in accuracy. Notably, by approximating Γ as an equivalent airfoil model, and assuming a flat-plate behavior for small angles of incidence, the circulation function $g(\Omega, w, u)$ is defined as:

$$g(\Omega, w, u) = \kappa [\cos(u) w - \sin(u) \Omega \ell] \, , \tag{A.5}$$

where $\kappa = 2\rho A_p R / 3\lambda_*$, with A_p being the swept area corrected for blade tip losses,[9] R the rotor radius, λ_* the tip speed ratio for maximum wind power extraction and ℓ a *length scale* factor. The parameter u is the controlled blade pitch angle, which is non-zero in the above-rated region only. The circulatory thrust and torque can then be rewritten as:

$$F_c = g(\Omega, w, u) \Omega, \quad Q_c = g(\Omega, w, u) w \, . \tag{A.6}$$

Drag may be relevant for the torque and, in a lesser degree, for the thrust. The drag thrust and torque are modelled according to

$$F_d = d_F |w| w, \quad Q_d = -d_Q \Omega^2 \, , \tag{A.7}$$

where the coefficients d_F and d_Q are determined in terms of losses in typical wind turbines. The following compact model in matrix form is then proposed:

$$\begin{bmatrix} F \\ Q \end{bmatrix} = \begin{bmatrix} d_F |w| & -g(\Omega, w, u) \\ g(\Omega, w, u) & d_Q \Omega \end{bmatrix} \begin{bmatrix} w \\ -\Omega \end{bmatrix} , \tag{A.8}$$

where the airflow w is given by Equation (9). Pedersen proposes that the low-frequency dynamics of the inflow, w_i, are driven by

$$\mu R_p \dot{w}_i + |w| w_i = \frac{F_c}{2\rho A_p} \, , \tag{A.9}$$

where $\mu = 8/3\pi$ is a *virtual inertia* parameter.

References

Bachynski, E.E., Thys, M., Sauder, T., Chabaud, V., Saether, L.O., 2016. Real-time hybrid model testing of a braceless semi-submersible wind turbine. Part II: experimental results. In: Proceedings of the ASME 2016 35th International Conference on Ocean, Offshore and Arctic Engineering, Busan, Korea.

Brown, D.T., 2005. Chapter 8-mooring systems. In: CHAKRABARTI, S.K. (Ed.), Handbook of Offshore Engineering. Elsevier, London, pp. 663–708. https://doi.org/10.1016/B978-0-08-044381-2.50015-1.

Cook, R., 2001. Concepts and Applications of Finite Element Analysis, fourth ed. Wiley.

Equinor, 2018. How Hywind Works. https://www.equinor.com/en/what-we-do/hywind-where-the-wind-takes-us/hywind-up-close-and-personal.html.

Faltinsen, O., 1993. Sea Loads on Ships and Offshore Structures. Cambridge Ocean Technology Series, Cambridge University Press.

Fukushima Forward, 2016. Fukushima Offshore Wind Consortium. http://www.fukushima-forward.jp/english/index.html.

Goupee, A.J., Kimball, R.W., Dagher, H.J., 2017. Experimental observations of active blade pitch and generator control influence on floating wind turbine response. Renew. Energy 104, 9–19. https://doi.org/10.1016/j.renene.2016.11.062.

Hansen, M., 2013. Aerodynamics of Wind Turbines. Earthscan.

Jonkman, J.M., 2007. Dynamics Modeling and Loads Analysis of an Offshore Floating Wind Turbine. Ph.D. thesis. University of Colorado, Denver, United States.

Jonkman, J.M., 2008. Influence of control on the pitch damping of a floating wind turbine. In: Proceedings of the ASME Wind Energy Symposium.

Jonkman, J., 2010. Definition of the Floating System for Phase IV of OC3, Tech. Rep. NREL/TP-500–47535. National Renewable Energy Laboratory, Colorado, United States.

Jonkman, J., Musial, W., 2010. Offshore Code Comparison Collaboration (OC3) for IEA - Task 23 Offshore Wind Technology and Deployment, Tech. Rep. NREL/TP-5000–48191. National Renewable Energy Laboratory.

Jonkman, J., Butterfield, S., Musial, W., Scott, G., 2009. Definition of a 5-MW Reference Wind Turbine for Offshore System Development, Tech. Rep. NREL/TP-500–38060. National Renewable Energy Laboratory, Denver, United States.

Larsen, T.J., Hanson, T.D., 2007. A method to avoid negative damped low frequent tower vibrations for a floating, pitch controlled wind turbine. J. Phys. Conf. Ser. 75, 012073. https://doi.org/10.1088/1742-6596/75/1/012073. https://doi.org/10.1088%2F1742-6596%2F75%2F1%2F012073.

Lemmer, F., Amann, F., Raach, S., Schlipf, D., 2016. Definition of the SWE-TripleSpar Floating Platform for the DTU 10MW Reference Wind Turbine, Tech. Rep. University of Stuttgart.

Lennie, M., Marten, D., Pechlivanoglou, G., Nayeri, C.N., Paschereit, C.O., 2016. Modern methods for investigating the stability of a pitching floating platform wind turbine. J. Phys. Conf. Ser. 753, 082012. https://doi.org/10.1088/1742-6596/753/8/082012. https://doi.org/10.1088%2F1742-6596%2F753%2F8%2F082012.

---

[8] The circulation is defined as the integral of the flow velocity field around any closed path C enclosing the airfoil, $\Gamma = \oint_C \mathbf{u} \cdot d\mathbf{l}'$.

[9] A common method for modelling tip loss effects is by reducing the effective rotor radius, through multiplication by a factor $0 < B < 1$. The corrected radius $R_p = BR$ then results in an effective swept area $A_p = B^2 A$.

LIFES50+, 2015. Innovative Floating Offshore Wind Energy. http://lifes50plus.eu/.

Luan, C., Gao, Z., Moan, T., 2016. Design and analysis of a braceless steel 5-MW semi-submersible wind turbine. In: Proocedings of the ASME 2016 35th International Conference on Offshore Mechanics and Arctic Engineering.

Luan, C., Chabaud, V., Bachynski, E.E., Gao, Z., Moan, T., 2017. Experimental validation of a time-domain approach for determining sectional loads in a floating wind turbine hull subjected to moderate waves. Energy Procedia 137, 366–381. 14th Deep Sea Offshore Wind R&D Conference, EERA DeepWind'2017. https://doi.org/10.1016/j.egypro.2017.10.361.

Lupton, R., 2014. Frequency-domain Modelling of Floating Wind Turbines. Ph.D. thesis. University of Cambridge, Cambridge, United Kingdom.

Luxcey, N., Ormberg, H., Passano, E., 2011. Global analysis of a floating wind turbine using an aero-hydro-elastic model. Part 2: benchmark study. In: Proceedings of the ASME 2011 30th International Conference on Ocean, Offshore and Arctic Engineering.

Manwell, J.F., McGowan, J.G., Rogers, A.L., 2009. Wind Energy Explained: Theory, Design and Application. John Wiley & Sons, Ltd.

Moriarty, P.J., Hansen, A.C., 2005. Aerodyn Theory Manual, Tech. Rep. NREL/EL-500–36881. National Renewable Energy Laboratory, Denver, Colorado.

Nielsen, F., Hanson, T., Skaare, B., 2006. Integrated dynamic analysis of floating offshore wind turbines. In: Proceedings of the 2006 25th International Conference on Offshore Mechanics and Arctic Engineering.

Næss, A., Moan, T., 2013. Stochastic Dynamics of Marine Structures. Cambridge University Press.

Ormberg, H., Larsen, K., 1998. Coupled analysis of floater motion and mooring dynamics for a turret-moored ship. Appl. Ocean Res. 20 (1), 55–67. https://doi.org/10.1016/S0141-1187(98)00012–1.

Ormberg, H., Passano, E., Luxcey, N., 2011. Global analysis of a floating wind turbine using an aero-hydro-elastic model. Part 1: code development and case study. In: Proceedings of the ASME 2011 30th International Conference on Ocean, Offshore and Arctic Engineering.

Pedersen, M.D., 2017. Stabilization of Floating Wind Turbines. Ph.D. thesis. Norwegian University of Science and Technology, Trondheim, Norway.

Pegalajar-Jurado, A., Borg, M., Bredmose, H., 2018. An efficient frequency-domain model for quick load analysis of floating offshore wind turbines. Wind Energy Science Discussions 2018, 1–30. https://doi.org/10.5194/wes-2018-25.

Popko, W., Huhn, M.L., Robertson, A., Jonkman, J., Wendt, F., Müller, K., Kretschmer, M., Vorpahl, F., Hagen, T.R., Galinos, C., Dreff, J.-B.L., Gilbert, P., Auriac, B., Víllora, F.N., Schünemann, P., Bayati, I., Belloli, M., Oh, S., Totsuka, Y., Qvist, J., Bachynski, E., Sørum, S.H., Thomassen, P.E., Shin, H., Vittori, F., Galván, J., Molins, C., Bonnet, P., van der Zee, T., Bergua, R., Wang, K., Fu, P., Cai, J., 2018. Verification of a numerical model of the offshore wind turbine from the alpha ventus wind farm within OC5 phase III. In: Proceedings of the ASME 2018 37th International Conference on Ocean, Offshore and Arctic Engineering.

PrinciplePower, 2014. Windfloat. http://www.principlepowerinc.com/en/windfloat.

Robertson, A., Jonkman, J., Masciola, M., Song, H., Goupee, A., Coulling, A., Luan, C., 2014. Definition of the Semisubmersible Floating System for Phase II of OC4, Technical Report NREL/TP-5000–60601. NREL, Denver, United States.

Robertson, A.N., Wendt, F., Jonkman, J.M., Popko, W., Dagher, H., Gueydon, S., Qvist, J., Vittori, F., Azcona, J., Uzunoglu, E., Guedes Soares, C., Harries, R., Yde, A., Galinos, C., Hermans, K., de Vaal, J.B., Bozonnet, P., Bouy, L., Bayati, I., Bergua, R., Galvan, J., Mendikoa, I., Sanchez, C.B., Shin, H., Oh, S., Molins, C., Debruyne, Y., 2017. OC5 project phase II: validation of global loads of the DeepCwind floating semi-submersible wind turbine. Energy Procedia 137, 38–57. 14th Deep Sea Offshore Wind R&D Conference, EERA DeepWind'2017. https://doi.org/10.1016/j.egypro.2017.10.333. http://www.sciencedirect.com/science/article/pii/S1876610217352931.

SINTEF OCEAN, 2016a. RIFLEX - Theory Manual.

SINTEF OCEAN, 2016b. SIMO - Theory Manual.

Vaal, J., Hansen, M.L., Moan, T., 2014. Effect of wind turbine surge motion on rotor thrust and induced velocity. Wind Energy 17 (1), 105–121. https://doi.org/10.1002/we.1562.

WAFO-group, 2017. WAFO - a Matlab Toolbox for analysis of random waves and loads - a Tutorial for version 2017. In: Math. Stat., Center for Math. Sci., Lund Univ., Lund, Sweden, . http://www.maths.lth.se/matstat/wafo.

Publication J.2

Effects of hull flexibility on the structural dynamics of a tension leg platform floating wind turbine

Carlos Eduardo Silva de Souza, Erin E. Bachynski

ASME Journal of Offshore Mechanics and Arctic Engineering (2020), Vol. 142: 011903.

Effects of hull flexibility on the structural dynamics of a TLP floating wind turbine

Carlos Eduardo Silva de Souza
Department of Marine Technology
Norwegian University of Science and Technology
Trondheim, Norway 7491
Email: carlos.souza@ntnu.no

Erin E. Bachynski
Department of Marine Technology
Norwegian University of Science and Technology
Trondheim, Norway 7491
Email: erin.bachynski@ntnu.no

ABSTRACT

Dynamic analysis of floating wind turbines often considers the hull as a rigid body. This paper explores the consequences of modeling the pontoons of a tension leg platform (TLP) wind turbine as flexible beams. The analysis is based on numerical simulations of free decays, structural response to wave excitation and short-term fatigue damage accumulation at tower base and tendons. In addition, the importance of hydroelastic effects due to the pontoons' vertical deformations is evaluated. Pontoon flexibility changed the platform natural periods and motion amplitude significantly, and the adoption of flexible pontoons reduced the predicted fatigue damage in the tower base and tendons. On the other hand, hydroelasticity had negligible consequences for motion and load responses considered here.

1 Introduction

Floating wind turbines (FWTs) have been considered the preferred solution for wind energy harvesting in deep water. Among the different platform concepts, the *tension leg platform* (TLP) is highlighted for significantly constraining the structure's vertical motions (heave, roll and pitch). Design methodology, hydrodynamics and dynamic analysis of TLP wind turbines are presented in e.g. [1–5]. As for other FWT concepts, however, the high costs associated with construction, installation, maintenance and decommissioning are challenges for TLP wind turbines, which have the additional risk of its stability being dependent on mooring lines integrity.

One of the strategies to reduce the Levelized Cost of Energy (LCOE) of FWTs consists in increasing the power generation of each turbine, which implies in the adoption of ever larger structures. The costs associated with installation/decommissioning and electrical infrastructure are mostly a function of the number of turbines installed [6]. Operation and maintenance (O&M) costs can also be expected to decrease for fewer (but more powerful) turbines. However, the costs not only of the turbine itself, but also of the floating substructure, tend to grow as the structural dimensions are increased.

Structural optimization is therefore fundamental in order to reduce the construction costs of larger floating platforms for wind turbines. A design solution with reduced sectional areas, however, results in less stiff structures. In this case, structural flexibility and its consequences for the global dynamics and internal loads can become an important design criterion.

In most published work, the global analysis of FWTs takes into account the flexibility of the tower and rotor blades only, while the hull is kept as a rigid-body. Only a few publications consider the consequences of an elastic hull in the structural mechanics. Henderson [3] considered modal deflections of the hull in a TLP model, observing different heave and pitch natural frequencies as compared to those obtained with a rigid model. The same conclusion was obtained by Zhao [7], by means of a free-vibration analysis of an entirely flexible TLP wind turbine, modeled with a finite element (FE) model. Svendsen [8] performed time-domain analyses with another TLP wind turbine considering a fully-flexible hull, noticing amplified responses in heave and pitch. In the context of the LIFES50+ project [9], a model for a semi-submersible 10 MW FWT, with the central column assumed as flexible, was proposed.

Hydroelasticity, i.e., the influence of structural deformations on the hydrodynamic loads, can be relevant for some marine structures, such as fishing farms [10] and very large floating structures (VLFS) [11]. Some researchers have evaluated the relevance of hydroelasticity for typical FWT hulls. Borg et al. [12] introduced a method for including hydroelastic effects in time-domain simulations with a spar platform designed to support a 10 MW turbine. The calculation of radiation and diffraction loads is extended to generalized degrees of freedom, and the time-domain formulation is augmented for inclusion of the additional modes. But, as the authors themselves point out, the first bending frequency of the spar is deliberately reduced in order to make the effect more visible. Therefore, it is not straightforward to conclude, from the results, whether the inclusion of hydroelasticity is relevant or not for real structures. The same method is applied in [13] in order to find the internal loads on a “triple-spar” floating platform. The authors conclude that the substructure flexible modes can excite tower bending moments, but it is not clear how much of this response comes from structural flexibility, and how much is due to hydroelastic effects.

The intended contribution of this paper is an assessment of the effect of hull flexibility and hydroelastic effects for a 5 MW TLP wind turbine. First, a model with a rigid hull and a model with flexible pontoons but rigid-body hydrodynamics are compared. The effect of structural flexibility is analyzed in terms of changes in natural periods, structural responses to regular waves, and short-term fatigue damage accumulation at the tower base and tendons, under realistic environmental conditions. Then, a separate analysis assesses the importance of hydroelasticity associated with the pontoons’ vertical deformation. For this purpose, a new tool is developed for considering the hydroelastic effect in the time domain.

The FWT model, simulation tool and the theoretical and procedural background behind the different analyses are described in Section 2. Results are shown and discussed in Section 3, and the main conclusions are presented in Section 4.

2 Methodology

2.1 Structural modeling

The substructure corresponds to the TLPWT3 defined in [4], a tension leg platform with three rectangular pontoons connected to the base of a central, cylindrical column (Fig. 1). The fore pontoon is parallel to the x-axis of the global coordinate system, which has its z-axis pointing upwards and is centered on the mean water level. The aft pontoons at port and starboard form an angle of 120°with the fore pontoon and each other.

Two different models are adopted for the platform. One of them assumes a fully rigid structure, meaning that there are no relative motions between the tower base and the tendon fairleads. This model will hereunder be named *rigid* model. The other model, based on stiffness properties obtained from [8], assumes the pontoons as flexible structures, modeled with nonlinear FE beam elements with double-symmetric cross sections. The hydrodynamic loads are distributed through the pontoons as explained in Section 2.2. The column is still regarded as rigid, since its bending stiffness is about 13 times as larger as for the pontoons. This model will be referred to as *flexible* model. The main properties of the platform are shown in Tab. 1.

The tower model is obtained from [14], with a base radius of 6.5 m, length of 77.6 m and mass equal to 249.7 t. Since the tower base is installed on the top of the platform, at 10.0 m above mean water level, the tower top lies at 87.6 m height, resulting in a hub height of 90.0 m. The turbine model adopted is the NREL 5 MW Reference Wind Turbine [15], which has a total mass for the nacelle-rotor assembly of 350.0 t. The tower and tendons are modeled with flexible axisymmetric beam elements. The tendons are designed to be neutrally buoyant and to provide a pretension of 8262 kN each. The water depth is 150.0 m.

Structural damping is modeled through stiffness-proportional Rayleigh damping. A stiffness-proportional constant of 0.001 s is adopted for the tower and tendons, while a constant of 0.005 s applies for the pontoons.

2.2 Hydrodynamic modeling

The radiation and diffraction hydrodynamic loads are calculated with the *boundary element method* (BEM)-based software WAMIT [16]. The same hydrodynamic calculations are used for both the rigid and the flexible model, but one must be careful in the way the loads are applied in the latter case.

Indeed, hydrodynamic loads result from the pressure field integrated over the body’s submerged surface. For a rigid body, the forces applied at any point can be directly transferred to e.g. the center of gravity (CG). When the pontoons are assumed as flexible, however, the excitation loads must be distributed along them. For this purpose, the pontoons were divided into 21 sections, each with 1.0 m length. The pressure values provided by WAMIT at each panel were then used for calculating the forces at the respective sections, in the frequency domain, such that the force time-series could be obtained for each sea state.

The added mass must also be distributed along the flexible pontoons. Besides the consequences to the global dynamics, the presence of added mass at the pontoons’ sections is fundamental for their flexible modes to be properly considered during the simulation. Also based on the pressures provided by WAMIT for each section, constant added mass coefficients are adopted, since the added mass at the pontoons do not vary significantly with frequency.

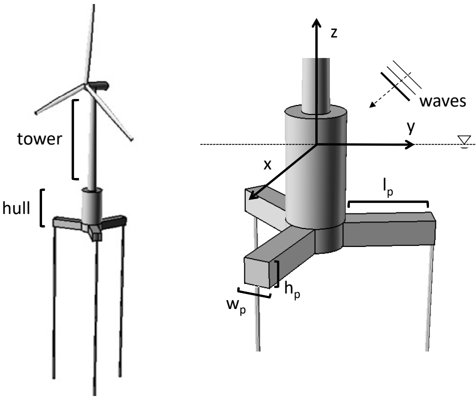

Fig. 1: Floating wind turbine TLPWT3 [4], and global coordinate system.

According to Ogilvie relations [17], a small variation of the added mass with frequency implies low radiation damping. Radiation damping was therefore considered negligible compared to added mass effects, and was not applied at the pontoon sections.

For the rigid TLP platform, and for the column of the flexible TLP, the frequency-dependent radiation coefficients are considered in the 6-DOF, rigid-body equations of motion based on Cummins equation [18]:

$$(m+A_\infty)\ddot{x}+D_1\dot{x}+Kx+\int_0^t h(t-\tau)\dot{x}(\tau)\mathrm{d}\tau = q(t,x,\dot{x}), \tag{1}$$

where m is the rigid-body mass matrix, A_∞ is the infinite-frequency added mass matrix, D_1 is the linear viscous damping matrix, K is the hydrostatic stiffness matrix, h is a matrix of retardation functions and q is a vector of external loads – which includes the wave excitation and the quadratic viscous damping terms, as detailed below. For the rigid model, q also includes the mooring system loads, while in the flexible model these are applied at the pontoons' tips. For the flexible model, the elements in A_∞ are calculated only with the pressures on the column panels, but considering the presence of pontoons and their effect on the fluid velocity field.

Second order wave loads may also be distributed along the pontoons, but this has not been done in the present work. Instead, mean- and slow-drift wave loads are calculated with Newman's approximation [19], and concentrated in the column for both models.

In addition to potential flow loads, viscous damping is considered by means of quadratic Morison drag terms, calculated for the column, pontoons and tendons. The quadratic drag coefficients C_D for cross and axial (skin friction) flows on circular cross-sections are taken as 0.7 and 0.07 [19], respectively, and the pontoon width is used in the formulation as an equivalent diameter. Since the pontoons are rectangular, these values may underpredict the drag when flow separation occurs. Since the same coefficients are applied in both the rigid and flexible models, this assumption should not influence the comparison of results. The linear viscous damping matrix D_1 ensures damping of low-frequency motions.

2.3 Simulation tool

All time-domain simulations were performed with SIMA, which combines RIFLEX [20], a finite element software for analysis of slender marine structures, with SIMO [21], a simulator for marine operations. RIFLEX is equipped with an aerodynamic model for wind turbine simulation based on the blade element momentum theory [22], with the Øye models for taking dynamic stall and dynamic wake effects into account [23]. Glauert's correction is adopted for high induction factors, and the Prantdl factor is used to account for hub and tip losses.

2.4 Decay simulations

The natural periods for both the rigid and flexible models were estimated by means of decay simulations. An initial offset in each of the degrees of freedom (DOFs) of interest – surge, heave and pitch – was imposed, and then the platform was released to oscillate freely, in the absence of waves and wind. The natural periods for each DOF were then obtained based on fast Fourier transform (FFT) analyses.

Table 1: Platform main structural properties

Symbol	Description	Value
V	Volume (m^3)	5655.0
m_b	Ballast mass (t)	1389.0
m_s	Steel mass (t)	1293.0
h_p	Pontoon height (m)	6.0
w_p	Pontoon width (m)	6.0
l_p	Pontoon length* (m)	21.0
h_c	Column height (m)	32.0
d_c	Column diameter (m)	14.0
D	TLP draft (m)	22.0
EA_t	Tendon axial stiffness (MN)	384.2
T_p	Tendon pretension (kN)	8262.0
EI_p	Pontoon bending stiffness† (GN.m^2)	551.0

*Measured from the column outer diameter. † For the flexible model.

2.5 Regular wave analysis

To assess the effect of pontoon flexibility on the platform wave response, time-domain simulations were performed considering regular waves, with incident direction of 0°, 1.0 m amplitude and period ranging from 3.0 s to 21.0 s, with increments of 1.0 s. Wind was not considered. For this analysis, two additional variations of the flexible model were included, with pontoon bending stiffness of $0.5EI_p$ and $2.0EI_p$ – with EI_p as given in Table 1.

The response amplitude operators (RAOs) for heave and pitch, as well as the force transfer functions (FTFs) for the tower-base bending moment and for the axial tension on the tendons, are then calculated based on the amplitudes of FFTs of the response time-series and the incident waves, at the frequency corresponding to the wave period in question.

2.6 Fatigue analysis

To assess how important the pontoons' flexibility can be for the fatigue life at the FWT tower base and tendons, a series of time-domain analyses was carried out, considering both the rigid and flexible models, and covering the entire range of wind velocities under which the NREL 5 MW turbine is operational, viz. 3.0 m/s to 25.0 m/s.

The probability of occurrence of each wind condition and the associated most probable sea states were determined based on the model proposed in [24], which provides combined distributions for wind and wave conditions for different locations in European waters. For this work, site 14 – corresponding to the southwestern coast of Norway – was selected.

Wind time-series were generated with the software *TurbSim* [25], with turbulence modeled using the IEC Kaimal spectral model. IEC turbulence category B is assumed, which corresponds to a moderate turbulence intensity I, decreasing for increasing mean wind velocities. For the waves, a 3-parameter JONSWAP wave spectrum was adopted, with a γ-factor value of 3.3. In all conditions, wind and waves were considered to be aligned with the positive x-axis.

Table 2 lists the combinations of wind and wave conditions, including the probability of occurrence of a bin centered on a given U_w (measured at hub height) and limited by a margin of ± 0.5 m/s. For a given U_w, the associated most probable H_s is the one that yields the maximum value of the conditional distribution. Similarly, the associated T_p corresponds to the maximum value of the conditional distribution of T_p given U_w and H_s. The range of operational wind velocities considered covers approximately 95% of the expected conditions for the chosen site.

In addition to the operational conditions, another case was considered with the turbine parked ($U_w = 30.0$ m/s) – shown in the bottom of Tab. 2. In spite of its low probability of occurrence, it is of interest to understand how the absence of aerodynamic damping affects the fatigue damage under the associated severe sea state, for both the rigid and flexible models.

One-hour time-domain simulations were performed for each of the conditions of Tab. 2, for the rigid and flexible models considered. Each condition was simulated using 6 different seeds for wind and waves, totaling $(23+1)\times 2\times 6 = 288$ simulations. The short-term fatigue damage D_{1h} at the outer radius of the tower base, aligned with the wind, is estimated from the axial stress time-series, which is obtained from the time-series of the tower axial force N_x and fore-aft bending

Table 2: Wind velocities at hub height and associated most probable sea states considered in the fatigue analysis – operational and parked-rotor conditions

Wind condition			Assoc. sea state	
U_w (m/s)	$P(U_w \pm 0.5)$ (%)	I (%)	H_s (m)	T_p (s)
3.0	3.14	36.6	1.4	9.2
4.0	4.68	30.1	1.5	9.3
5.0	4.91	26.2	1.6	9.4
6.0	5.53	23.6	1.7	9.5
7.0	6.87	21.7	1.8	9.6
8.0	6.32	20.3	1.9	9.7
9.0	6.43	19.2	2.0	9.7
10.0	7.30	18.3	2.2	9.9
11.0	6.20	17.6	2.3	10.0
12.0	5.91	17.0	2.5	10.1
13.0	6.28	16.5	2.7	10.3
14.0	5.02	16.1	2.9	10.4
15.0	4.53	15.7	3.1	10.6
16.0	4.55	15.4	3.3	10.7
17.0	3.45	15.1	3.5	10.8
18.0	3.35	14.9	3.8	11.0
19.0	2.45	14.6	4.0	11.1
20.0	2.04	14.4	4.3	11.3
21.0	1.89	14.2	4.6	11.5
22.0	1.32	14.1	4.8	11.6
23.0	1.06	13.9	5.1	11.8
24.0	0.93	13.8	5.4	11.9
25.0	0.62	13.6	5.8	12.1
30.0	0.15	13.1	7.5	12.9

moment M according to:

$$\sigma_{x,tower} = \frac{N_x}{A} - \frac{Mr}{I_y}, \tag{2}$$

where A is the annular section area, r is the section radius and I_y is its area moment of inertia around the bending axis, while the minus sign agrees with RIFLEX's conventions for output of stresses. For the tendon, it is assumed that the axial force is predominant in the axial stress $\sigma_{x,tendon}$, which is then given by:

$$\sigma_{x,tendon} = \frac{N_x}{A}, \tag{3}$$

Based on the resulting time-series for the axial stresses, a rainflow cycle counting procedure provided a series of cycles with stress range S_i, which, under assumption of a bi-linear S-N fatigue curve and linear damage accumulation, result in an

Table 3: S-N curve coefficients and stress limit for tower base and tendon axial stresses. The values correspond to curve D of Tab. 2-1 and curve F of Tab. 2-2 of [26], respectively.

	Tower	Tendon
$\bar{a}_1$	$1.0 \times 10^{12.164}$	$1.0 \times 10^{11.455}$
$\bar{a}_2$	$1.0 \times 10^{15.606}$	$1.0 \times 10^{15.091}$
m_1	3.0	3.0
m_2	5.0	5.0
S_{lim} (MPa)	52.63	41.52

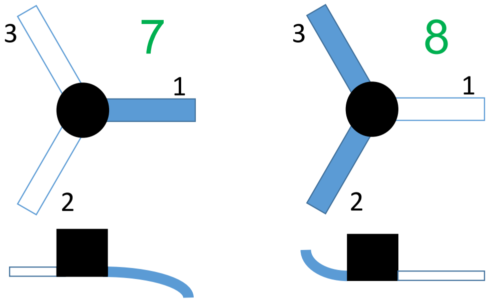

Fig. 2: Pontoons top and side views, and the associated generalized modes adopted in WAMIT

one-hour damage D_{1h} given by:

$$D_{1h} = \frac{1}{\bar{a}_1} \sum_{i=1}^{n_l} S_i^{m_1} + \frac{1}{\bar{a}_2} \sum_{j=1}^{n_h} S_j^{m_2}, \tag{4}$$

where the first summation refers to the n_l cycles with stress ranges higher than S_{lim} (low cycle region), while the second summation refers to the n_h cycles with stress ranges lower than S_{lim} (high cycle region). The stress limit S_{lim} and the coefficients $a_{1,2}$ and $m_{1,2}$ are obtained from [26], and are reproduced in Tab. 3.

2.7 Hydroelasticity analysis

Programs based on the boundary element method solve the wave-structure interaction problem by dividing the body geometry in panels, and then finding the source or dipole strength functions over each panel such that the pressure – and then the loads – can be calculated. For a rigid body, these potentials consist in a linear superposition of the diffraction potential and (up to) six radiation potentials, one for each DOF. The normal velocity for each panel is obtained from the coordinates of its vertices, given from the body geometry provided as input by the user.

In problems involving structural flexibility, this method is extended to additional DOFs, other than the rigid-body ones [27]. The user may define such *generalized* modes of motion, such that the normal velocities on each panel may be updated to represent the deformed condition. In WAMIT, the generalized modes can be implemented as algebraic functions (e.g., polynomials) describing the expected deformed configuration.

The hydroelastic effects analyzed in this work are those associated with the vertical bending of the TLP pontoons. It is assumed that the pontoon deflection resulting from the TLP motions can be satisfactorily represented by the first mode shape, which is fit to a 3$^{\text{rd}}$-order polynomial. This polynomial is then used for defining two generalized modes in WAMIT: one for the motion of the fore pontoon (pontoon 1) only, while the other two remain undeflected; and another for the two aft pontoons (pontoons 2 and 3) moving together, with the one in the fore kept undeflected. Figure 2 illustrates the pontoons' motions and the associated generalized modes (7 and 8).

For the present analysis, the mode shapes for the pontoons were found with the eigenvalue analysis tool of SIMA, based on an adapted model of the TLPWT3 where the hull (column and pontoons) was entirely described with beam-elements

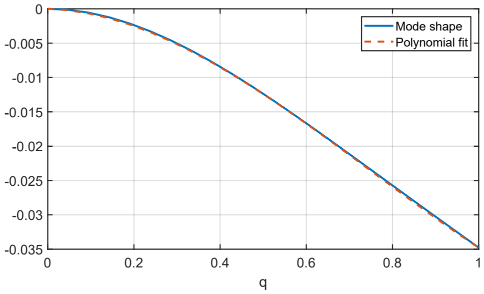

Fig. 3: Pontoon 1st mode shape and 3rd-order polynomial fit

with distributed mass and frequency-independent added mass. SIMA does not consider damping effects for the eigenvalue analysis, but these are negligible in the calculation of pontoon mode shapes. The first mode shape in the eigenvalue analysis is shown in Fig. 3, together with the following 3rd-order polynomial which was found to fit to the mode coordinates:

$$P(q) = 0.0264q^3 - 0.0595q^2 - 0.0016q\,, \tag{5}$$

where $q \in [0.0; 1.0]$ is a parameter along the length of each pontoon, from the column connection to the tip, normalized with the pontoon length. It is noted that the curve-fitting procedure results in a linear term, which in principle disagrees with the cantilever boundary-condition of zero-slope at the column. As observed in Fig. 3, however, this does not result in a significant discrepancy from the actual mode shape at $q = 0$.

3 Results and analysis

3.1 Decay simulations results

The natural periods obtained from the decay simulations are presented in Tab. 4. The decay time-series are shown in Fig. 4. For surge, the adoption of flexible pontoons does not induce a noticeable change in the natural period. For heave, however, the presence of the flexible pontoon reduces the overall system stiffness considerably, increasing the oscillation period by about 40%. This is confirmed by the first eigenmodes for the rigid and flexible models, shown in Fig. 5. As mentioned, the eigenvalue analysis does not include damping, which explains the slightly higher frequency shown in Fig. 5, when compared to the decay-based results of Tab. 4 (which include damping).

For the pitch decay, there is a slight increase in the periods, and a new mode is noticed. The higher modes, however, damp out for both the rigid and flexible models after about 30.0 s, after which the oscillation becomes fairly monochromatic. The persistent oscillation relates to the first bending mode of the tower – the so-called first pitch/bending periods in Tab. 4, for both the rigid and flexible models – and has considerably higher amplitude for the flexible model.

A discussion on modal damping ratio can be done by relating the periods on Tab. 4 to the stiffness-proportional damping constants presented in Section 2.1. For the tower and tendons, the relative damping factor remains below 1.0% for all the modes considered. For the pontoons, the damping factor related to the heave motion is below 2.0%, while for the 1st pitch/bending mode it is of 0.5 %.

3.2 Regular wave analysis results

Figure 6 shows the RAOs for heave and pitch, based on the regular wave analysis described in Section 2.5. For heave (Fig. 6a), the curves for the flexible model visibly deviate from the rigid, especially for the period range 6.0 s - 9.0 s, and also periods longer than 12.0 s. For pitch (Fig. 6b), the differences are larger in almost all periods, except in the interval 4.0 s–6.0 s. For the shortest periods, an explanation may be the proximity to the 1st pitch/tower bending frequency shown in Tab. 4.

The force transfer functions for the tower base and tendon 1 are shown in Fig. 7. The curves for tendons 2 and 3 are similar to tendon 1, and are therefore not shown. In spite of the larger motion responses, the difference between the curves is small, except for very short wave periods. This result may appear counter intuitive, but is actually a consequence of the presence of flexible structures transmitting the loads acting on the platform.

Table 4: Natural periods from decay simulations

	Rigid	Flexible
Surge (s)	40.96	40.96
Heave (s)	0.60	0.85
Pitch/bending, 1st (s)	2.77	2.93
Pitch, 2nd (s)	0.39	0.56
Pitch, 3rd (s)	-	0.46

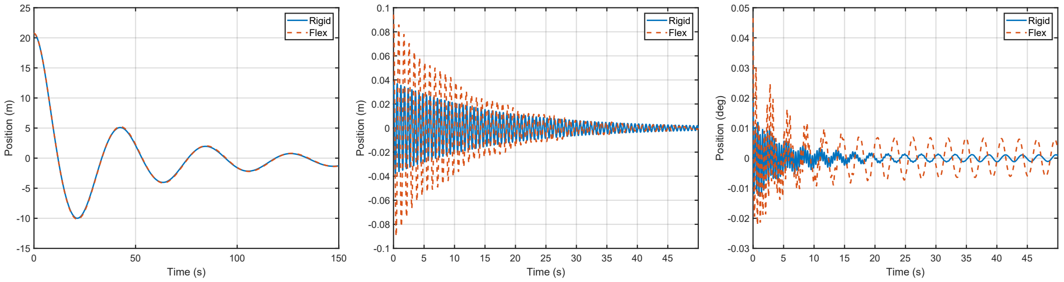

(a) Surge decay (b) Heave decay (c) Pitch decay

Fig. 4: Time-series of decay simulations with rigid and flexible models

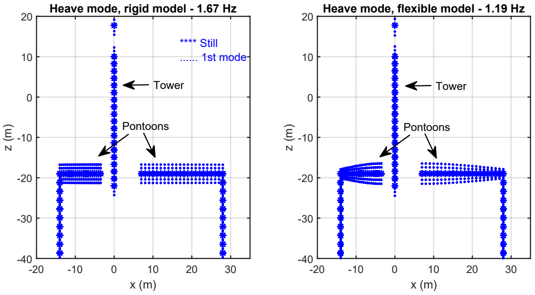

Fig. 5: Heave eigenmodes for the rigid (left) and flexible (right) models

In fact, when a rigid TLP platform pitches – i.e., rotates in the *xz*-plane, the resulting moment associated with the tower and turbine weight is compensated by not only hydrostatic restoration, but also strains in the tower base and, mainly, tendons. When flexible pontoons are present, they will also "contribute" to compensate for the moment.

The same rationale applies to the relation between the larger heave motions and almost unaltered tendon loads. If the increased motion is due to the pontoon deflection, it is to be expected that the pontoons themselves, and not the tendons, are loaded due to the strains resulting from the deflection.

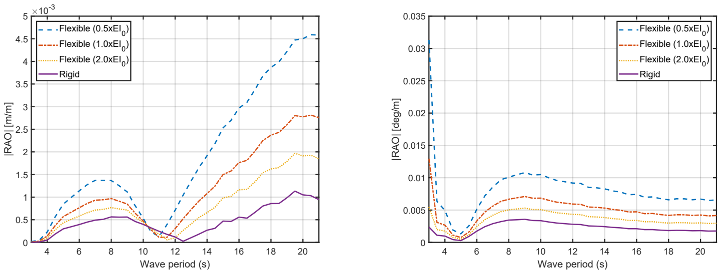

(a) Heave RAO

(b) Pitch RAO

Fig. 6: Response amplitude operators for heave and pitch

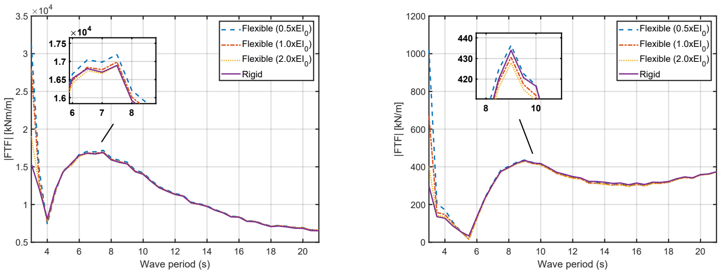

(a) Tower-base bending moment

(b) Axial tension on tendon 1

Fig. 7: Force transfer functions for the tower-base bending moment and tendon axial tension

Table 5: 1-hour accumulated damage at tower-base and tendon, for the rigid and flexible models

	Rigid	Flexible
Tower	3.37×10^{-5}	2.99×10^{-5}
Tendon	8.10×10^{-8}	7.55×10^{-8}

3.3 Fatigue analysis results

The axial forces and bending moments from the fatigue analysis were applied in Eq. (2) and (3), which, in combination with the rainflow counting algorithm from [28], were used for calculating the 1-hour accumulated damage at the tower base and tendon 1 according to Eq. (4). Table 5 shows the 1-h accumulated damage for both models, weighed with the probabilities associated to their corresponding environmental conditions as given in Tab. 2. The adoption of a model with flexible pontoons resulted in a 12.7% lower damage in the tower than for the fully-rigid hull model. For the tendon, the reduction was of 7.3%.

It is of interest to understand how the discrepancy between the calculated damages calculated changes according to the environmental condition. Figure 8 shows the accumulated damages at the tower base for each combination of wind and sea state, and the percent variation of the values for the flexible model w.r.t. the rigid model. In general, the rigid model provides higher fatigue damage – except for $U_w = 3.0$ m/s, where the 3p frequency (0.35 Hz) is nearly coincident with the 1st tower/bending frequency for the flexible model (0.34 Hz). For higher wind speeds, however, the damage is reduced when the flexible model is adopted. The largest difference between models occurs for wind velocities around 6.0 m/s. The damage at these conditions is relatively low, though. As the wind speed increases, the damage also grows, but for above-rated wind speed the difference between models is below 10% for both the tower base (Fig. 8) and tendon 1 (Fig. 9). For the parked condition ($U_w = 30.0$ m/s), where the wind loads are lower, the damage on tower base and tendon diminishes for both models. For the tower base, it is actually slightly (∼1%) larger for the flexible model, while for the tendon it is 9.6% higher for the rigid model.

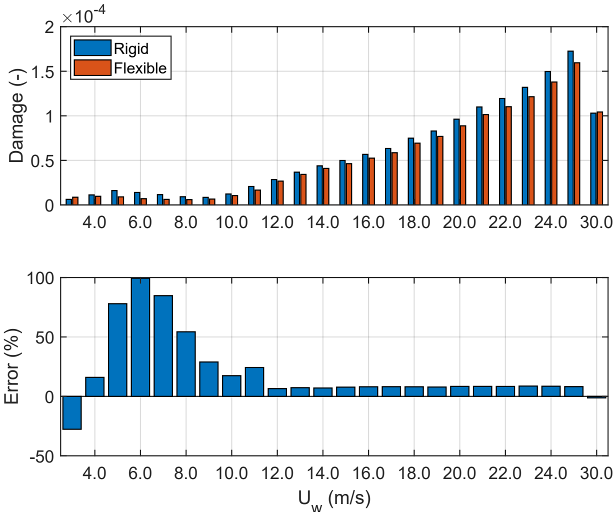

Fig. 8: One-hour fatigue damage at the tower base, for the rigid and flexible models (top), and percent error between flexible and rigid models (bottom)

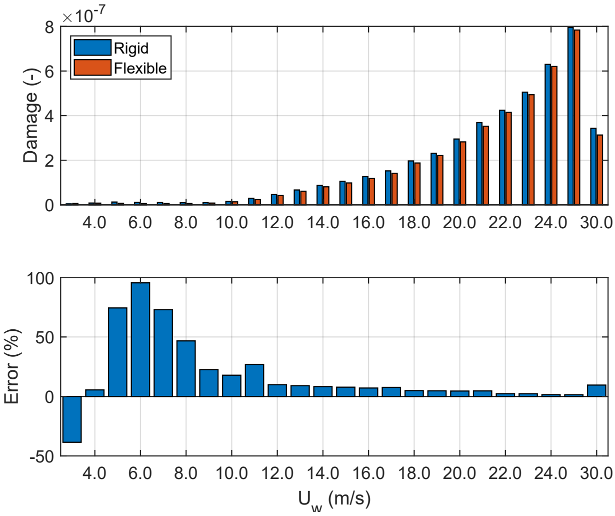

Fig. 9: One-hour fatigue damage at the top of tendon 1, for the rigid and flexible models (top), and percent error between flexible and rigid models (bottom)

Figures 10 and 11 show the load spectra for the tower base axial stress and tendon axial stress, respectively, for three wind speeds representing different operational conditions. For the three conditions, the “rigid” and “flexible” curves are nearly coincident for frequencies below 0.2 Hz for both the tower base and tendon. This indicates that the differences observed for the damage do not result from loads at the wave frequency – a result anticipated by the transfer functions shown in Fig. 7. Instead, from the plots it is clear that most of the discrepancy is actually at frequencies in the range (0.2 Hz – 0.7 Hz). This interval includes the 1st pitch/tower bending frequency shown in Tab. 4 and the 3p rotor frequencies, which for the cases in the plots lie into the range 0.48-0.60 Hz.

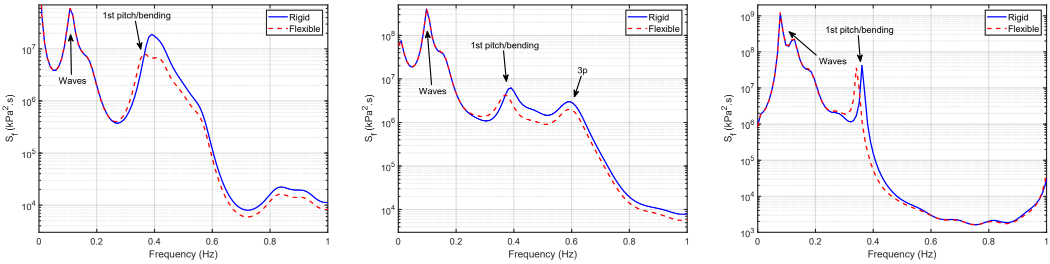

(a) $U_w = 8.0$ m/s (b) $U_w = 15.0$ m/s (c) $U_w = 30.0$ m/s

Fig. 10: Power spectral density of the tower-base axial stress, for the rigid and flexible models

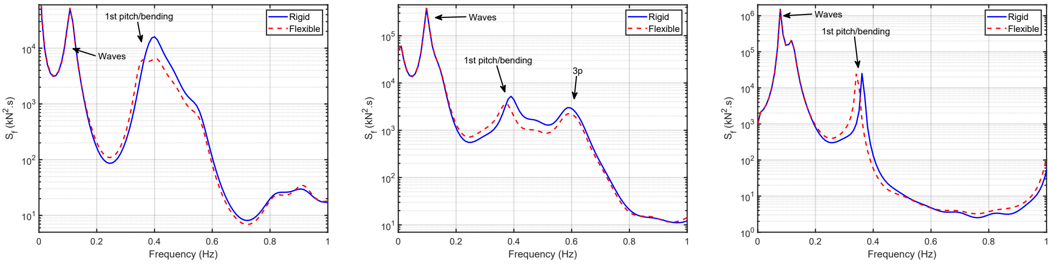

(a) $U_w = 8.0$ m/s (b) $U_w = 15.0$ m/s (c) $U_w = 30.0$ m/s

Fig. 11: Power spectral density of the tendon axial tension, for the rigid and flexible models

3.4 Hydroelasticity analysis results

The previous results compared the rigid and flexible models, but both with hydrodynamic loads based on a rigid-body assumption. The effects of considering hydroelasticity, as described in Section 2.7, are now analyzed. Figures 12 and 13 show the calculated added mass and radiation damping for heave[1] and pitch, together with the cross terms between each of those DOF's and the pontoon bending modes. For the latter, the coefficients for modes 7 and 8 are combined providing the highest result for each mode. It may be challenging to interpret these quantities for generalized modes. From the definition of added mass, the coefficient a_{ij} is *the force applied in DOF i due to a unit acceleration in DOF j*. In order to extend this definition to the context of generalized modes, it is necessary to first define a measurement for the deformation, based on the mode shape description provided to WAMIT.

In the present case, the deformation is quantified as the vertical motion at the tip of the pontoon, relative to the pontoon connection to the column. Therefore, the coefficient a_{37} corresponds to the force in heave when the vertical acceleration of the tip of pontoon 1, subtracted from the vertical acceleration of the column, equals 1.0 m/s^2. Equivalently, b_{58} corresponds to the moment in pitch when the vertical velocity of the tips of pontoons 2 and 3, subtracted from the vertical velocity of the column, equals 1.0 m/s.

While the coefficients presented in Fig. 12 and 13 provide a comparison between hydrodynamic *coefficients* for rigid and flexible modes, they should not be interpreted as a measure of hydrodynamic *loads*. Indeed, it is necessary to multiply each of the coefficients by the associated modes' velocities and accelerations. This is a trivial procedure for the rigid-body modes, but demands some additional calculations for the hydroelastic loads.

A special tool was developed for this purpose, consisting of measuring the pontoons' tips vertical accelerations and velocities, relative to the column, and multiplying them by the coefficients shown in Fig. 12 and 13. The resulting forces and moments are then included in SIMA's time-domain equations of motion as external loads, applied at the platform's center of gravity. The flexible model presented in section 2.2 was then updated with the method described above, resulting in the

---

[1] The curve for the heave rigid-body radiation damping (lower plot) may look inconsistent, since for longer periods it seems not to converge to zero. Convergence is observed, though, when the analysis is extended to higher periods than those shown in the plot.

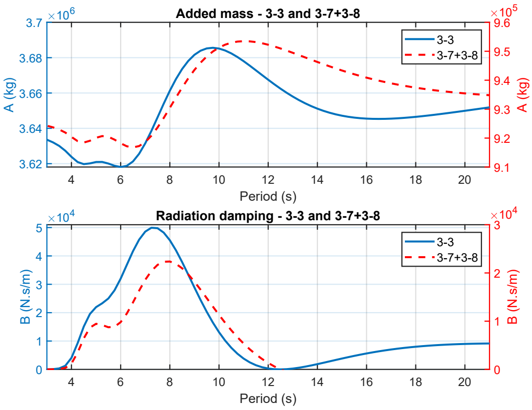

Fig. 12: Added mass and radiation damping for heave, for TLPWT3 with flexible pontoons

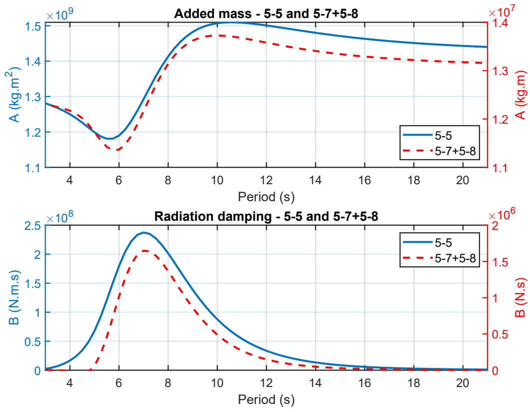

Fig. 13: Added mass and radiation damping for pitch, for TLPWT3 with flexible pontoons

hydroelastic model. Figure 14 shows the heave and pitch RAO amplitudes for the flexible and hydroelastic models, based on time-domain simulations with regular waves and absence of wind (in a similar procedure as presented in Section 2.5). For both responses, the curves for the flexible and hydroelastic cases are indistinguishable.

The same is observed for the force transfer functions for the tower base bending moment (in the xz-plane) and the tension on tendon 1 (Fig. 15), which are essentially unaffected by the consideration of hydroelasticity in the model. The curves are fairly coincident along the entire range of periods analyzed, suggesting that one shouldn't expect significant inaccuracies in neglecting hydroelastic effects during a structural analysis.

The loads applied at the column due to hydroelastic effects were 2-3 orders of magnitude lower than the wave excitation loads. This is consistent with the coefficients shown in Fig. 12 and 13, and considering the low amplitude of the pontoon deflection.

A remark should be made regarding the point of attack of the hydroelastic load, assumed to be concentrated at the TLP's center of gravity. It is not trivial to estimate in which extent this simplification affects the presented results, but in principle it should result in larger elastic deformations, leading to a conservative estimate of the motions and structural responses.

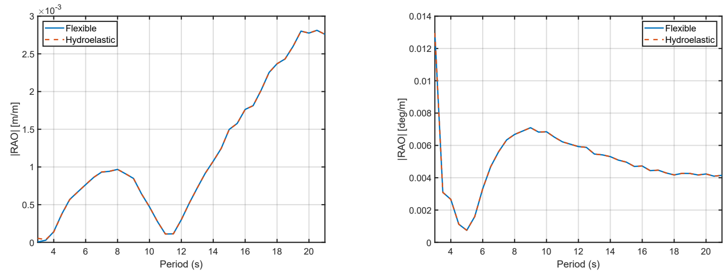

(a) Heave

(b) Pitch

Fig. 14: Response amplitude operators for heave and pitch – flexible and hydroelastic models

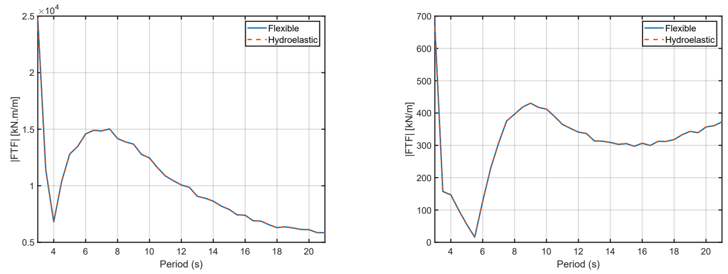

(a) Tower-base bending moment

(b) Tension on tendon 1

Fig. 15: Load transfer function for tower base bending moment and tension on tendon 1 – flexible and hydroelastic models

4 Conclusion

The consequences of considering flexible pontoons of a TLP wind turbine were analyzed. The study consisted of comparisons with a fully-rigid hull model, in numerical analyses of decay simulations; regular wave excitation; fatigue damage at tower base and tendon connection, under realistic operational conditions; and hydroelasticity associated with the pontoons' vertical deformation.

The decay simulations showed that, when the pontoons were modeled as flexible, the heave natural periods increased around 40%. In pitch, the first and second modal periods also increased for the flexible model, and an additional mode appeared. In other words, the design of a TLP wind turbine with a rigid hull may result in wrong estimation of the tower natural frequency and 3p resonance.

Response and load transfer functions, obtained with the regular wave analysis, showed that pontoon flexibility resulted in amplified heave and pitch responses, especially in the range of typical wave periods. The tower base and tendon load responses are however only slightly higher, except for very short wave periods, where the differences are more visible.

In terms of fatigue calculated for the tower base and one of the tendons, the adoption of a model with flexible pontoons resulted in lower accumulated damage, compared to the rigid model, leading to less conservative results. Spectral analysis showed that the discrepancy comes from loads at frequencies above the wave-frequency range, corresponding to the 1st pitch/tower-bending mode and the rotor 3p frequencies.

Although not analyzed here, sectional loads in the pontoons may be more accurately predicted with the flexible model. This may be especially useful in the design of the pontoons' internal structure, with consideration of the loads induced by the rotor.

Finally, the hydroelasticity analysis showed that the radiation loads due to pontoons deformation do not significantly affect the heave/pitch responses or the loads on the tower base and tendon connection. Even though this result is limited to the platform analyzed, it is expected that the effect may be even less relevant for structures not subjected to the same load distribution – which is the case of spars and semi-submersibles, for example. However, TLPs supporting larger turbines may present larger pontoon deflections and rotor excitations at other frequencies.

In addition, the tool developed for the hydroelastic analysis is restricted to regular waves, and it is therefore not appropriate for simulations with realistic sea states and wind. Also, validation through e.g. CFD analyses or experiments is still necessary, though the latter may be challenging due to the low magnitude of the forces involved.

5 Acknowledgments

The authors are sincerely grateful to the financial support from Equinor, NTNU/IMT and the Centre for Autonomous Marine Operations and Systems (AMOS).

References

[1] Tracy, C. H., 2007. "Parametric design of floating wind turbines". Master's thesis.

[2] Matha, D., 2009. "Model development and loads analysis of an offshore wind turbine on a tension leg platform, with a comparison to other floating turbine concepts". Master's thesis.

[3] Henderson, A. R., Argyriadis, K., Nichols, J., and Langston, D., 2010. "Offshore wind turbines on TLPs - assessment of floating support structures for offshore wind farms in German waters". In 10th German Wind Energy Conference.

[4] Bachynski, E. E., and Moan, T., 2012. "Design considerations for tension leg platform wind turbines". *Marine Structures,* **29**(1), pp. 89 – 114.

[5] Oguz, E., Clelland, D., Day, A. H., Incecik, A., López, J. A., Sánchez, G., and alez Almeria, G. G., 2018. "Experimental and numerical analysis of a TLP floating offshore wind turbine". *Ocean Engineering,* **147**, pp. 591 – 605.

[6] Hofmann, M., and Sperstad, I. B., 2014. "Will 10 MW wind turbines bring down the operation and maintenance cost of offshore wind farms?". *Energy Procedia,* **53**(Supplement C), pp. 231 – 238. EERA DeepWind' 2014, 11th Deep Sea Offshore Wind R&D Conference.

[7] Zhao, Y., Yang, J., and He, Y., 2012. "Preliminary design of a multi-column TLP foundation for a 5-MW offshore wind turbine". *Energies,* **5**(10).

[8] Svendsen, K., 2016. "Structural design and dynamic analysis of a tension leg platform wind turbine, considering elasticity in the hull". Master's thesis, Norwegian University of Science and Technology / TU Delft.

[9] Pegalajar-Jurado, A., Madsen, F., Borg, M., and Bredmose, H., 2018. LIFES50+ - D4.5 state-of-the-art models for the two LIFES50+ 10MW floater concepts. Tech. rep., Technical University of Denmark.

[10] Faltinsen, O., 2015. "Hydrodynamics of marine and offshore structures". pp. 835 – 847.

[11] Fujikubo, M., 2005. "Structural analysis for the design of VLFS". *Marine Structures,* **18**(2), pp. 201 – 226.

[12] Borg, M., Hansen, A. M., and Bredmose, H., 2016. "Floating substructure flexibility of large-volume 10MW offshore wind turbine platforms in dynamic calculations". *Journal of Physics: Conference Series,* **753**(8).

[13] Borg, M., Bredmose, H., and Hansen, A. M., 2017. "Elastic deformations of floaters for offshore wind turbines: dynamic modelling and sectional load calculations". In Proceedings of the ASME 2017 36th International Conference on Ocean, Offshore and Arctic Engineering.

[14] Jonkman, J., 2010. Definition of the floating system for phase IV of OC3. Tech. Rep. NREL/TP-500-47535, National Renewable Energy Laboratory, Colorado, United States.

[15] Jonkman, J., Butterfield, S., Musial, W., and Scott, G., 2009. Definition of a 5-MW reference wind turbine for offshore system development. Tech. Rep. NREL/TP-500-38060, National Renewable Energy Laboratory, Colorado, United States.

[16] WAMIT, I., 2006. *WAMIT User Manual*. Chestnut Hill, United States.

[17] Ogilvie, T. F., 1964. Recent progress toward the understanding and prediction of ship motions. Tech. rep., David W. Taylor Model Basin, Washington D.C., USA.

[18] Cummins, W. E., 1962. "The impulse response and ship motions". In Symposium on Ship Theory.

[19] Faltinsen, O., 1993. *Sea Loads on Ships and Offshore Structures*. Cambridge Ocean Technology Series. Cambridge University Press.

[20] SINTEF OCEAN, 2016. *RIFLEX - Theory manual*.

[21] SINTEF OCEAN, 2016. *SIMO - Theory manual*.

[22] Manwell, J. F., McGowan, J. G., and Rogers, A. L., 2009. *Wind Energy Explained: Theory, Design and Application*. John Wiley & Sons, Ltd.

[23] Hansen, M., 2013. *Aerodynamics of Wind Turbines*. Earthscan.

[24] Li, L., Gao, Z., and Moan, T., 2013. "Joint environmental data at five European offshore sites for design of combined wind and wave energy devices". In Proceedings of the ASME 2013 32nd International Conference on Ocean, Offshore and Arctic Engineering.

[25] Jonkman, B. J., and Kilcher, L., 2012. Turbsim user's guide: version 1.06.00. Tech. rep., National Renewable Energy Laboratory.

[26] DNV, 2011. Fatigue design of offshore steel structures (DNV-RP-C203).

[27] Newman, J., 1994. "Wave effects on deformable bodies". *Applied Ocean Research,* **16**(1), pp. 47 – 59.

[28] WAFO-group, 2017. *WAFO - A Matlab Toolbox for Analysis of Random Waves and Loads - A Tutorial for version 2017.* Math. Stat., Center for Math. Sci., Lund Univ., Lund, Sweden.

List of Figures

List of Tables

Publication J.3

Design, structural modeling, control, and performance of 20 MW spar floating wind turbines

Carlos Eduardo Silva de Souza, Erin E. Bachynski

Marine Structures (2022), Vol. 84: 103182.

Marine Structures 84 (2022) 103182

Contents lists available at ScienceDirect

Marine Structures

journal homepage: www.elsevier.com/locate/marstruc

Design, structural modeling, control, and performance of 20 MW spar floating wind turbines

Carlos Eduardo Silva de Souza [*], Erin E. Bachynski-Polić

Department of Marine Technology, Norwegian University of Science and Technology, Trondheim, Norway

ARTICLE INFO

Keywords:
Floating wind turbines
Fatigue analysis
Extreme analysis
Hydroelastic modeling
Wind turbine control systems

ABSTRACT

As floating wind turbines (FWTs) increase in size and power, the relative contribution of wave and wind loads to their global responses differs from what has been observed for 5–10 MW units. In addition, the larger deflections at the platform, increased natural period range for some degrees of freedom, and larger RNA weight at higher heights invite a review on structural modeling methods, design constraints, dynamic analysis, and control systems. This paper explores these topics through the design and structural analysis of three spar-type 20 MW FWTs, with different constraints on the static pitch angle at rated wind speed. Time-domain simulations are performed with a non-linear aero-hydro-servo-elastic software, and sectional fatigue damage and extreme motions and axial stresses for the three designs are compared. The platform is modeled as a flexible body, with hydrodynamic loads evaluated with potential theory and distributed over the hull. A control system with a motion compensation strategy is adopted, ensuring the same controller bandwidth for the three FWTs and showing significant performance improvements compared to detuning the controller gains. In addition to impacting steel and ballast mass, the static pitch angle at rated thrust affects the platform dynamics and fatigue damage/extreme loads significantly. The platforms with larger restoring in pitch present less fatigue damage at the platform, but more at the tower. Extreme stresses are largely affected by gravitational loads, such that the designs with larger pitch at rated thrust have the highest extreme stresses at the platform and most of the tower sections. Load cases associated with the rated wind speed often govern the extreme loads, unlike previous studies with 5 MW and 10 MW FWTs.

1. Introduction

Floating wind technology has been progressing towards increased power per unit. Current projects planned to be built in the next 5 years comprise wind parks with 8–13 MW floating wind turbines (FWTs) [1–3], while wind turbines with nominal power of 14 MW [4] and 16 MW [5] are reaching commercial maturity — and academic research has investigated the feasibility of 20 MW [6–8], 25 MW [9], and even 50 MW [10] machines.

The increased wind loads and heavier turbines challenge the design and performance of their supporting structures. The dynamic behavior and structural integrity of FWTs have been extensively investigated in the last decade, benefiting in a broad extent from the NREL 5 MW [11] and DTU 10 MW [12] reference wind turbines. Larger FWTs will, however, have different natural periods and response to wind and wave loads — the structural dynamics of large wind turbines were listed by Veers et al. as one of the "grand challenges in wind energy science" [13]. Thus, the conclusions obtained from 5–10 MW structures may not necessarily apply to

---

[*] Corresponding author.
E-mail address: carlos.souza@ntnu.no (C.E.S.d. Souza).

https://doi.org/10.1016/j.marstruc.2022.103182
Received 19 October 2021; Received in revised form 7 January 2022; Accepted 21 January 2022

those beyond 15 MW. In addition, appropriate methods to model and analyze the structural loads and coupled dynamics of large FWTs must be developed.

One point that needs further investigation relates to the modeling of FWTs as fully-flexible structures. While a significant volume of work models the platform as a rigid body, this assumption can be questionable when the dimensions increase and structural deflections become more important. Modeling the platform as a flexible body, on the other hand, requires the appropriate distribution of hydrodynamic loads over the structure [14–18]. The accuracy of the predicted sectional stresses on the platform can be compromised if radiation and diffraction loads are simplified, while computational time can increase significantly depending on how these loads are evaluated in time domain.

Cyclic loads in floating wind turbines are mainly caused by the action of wind, waves, and the loads associated with rotation of the blades and drivetrain machinery [19]. Kvittem and Moan [20] assessed fatigue damage calculation for a 5 MW semi-submersible FWT, considering bin size, simulation length, and number of realizations. Engebretsen et al. [18] compared fatigue damage for a 8 MW spar FWT when modeling hydrodynamic loads using Morison formulation and distributed potential theory (DPT), noting significant over-prediction when the former approach is adopted. Hegseth and Bachynski [21] assessed the distribution of fatigue damage over a 10 MW spar FWT platform and tower, in the context of design optimization.

Extreme axial stresses are important in the assessment of structural yielding and buckling. In addition, extreme platform pitch motions and nacelle fore-aft acceleration can cause large loads on the drivetrain and interruptions in production. For FWTs, extreme events result from the combination of harsh wave loads with the low-frequency motions induced by the wind. Karimirad and Moan [22] analyzed the extreme loads on a 5 MW spar FWT, finding extreme bending moments at the platform and tower to be associated with storm load cases – i.e., those corresponding to extreme wind conditions, when the turbine is idling. Li et al. [23] proposed to also consider the cut-off condition in the analysis for a 5 MW semi-submersible FWT, ensuring that load cases with an operating turbine are included — the rated condition, however, was found to be non-important for extreme loads for the platform considered.

Control systems play a significant role in the dynamic response of FWTs. Interaction with the FWT motions can provoke serious instabilities, resulting in large pitch motions and structural bending moments [24,25]. Controller "detuning" [26] is a common strategy to cope with this problem in academic research, but the method reduces the controller performance and can be unrealistic for larger FWTs, due to the increased pitch natural periods. Skaare et al. [27] used an observer to remove the influence of the FWT motions from the controller, avoiding the instability without needing to reduce the controller gains. A similar, but simpler method was proposed by Lackner [28], who used the FWT pitch velocity to modify the reference rotor speed. Hegseth et al. [29] used the latter method in the design optimization of 10 MW spar FWTs, obtaining reduced wall thickness for the tower compared with a design based on a detuned controller.

The objectives of this paper are to investigate the design, control system, and structural modeling considerations of 20 MW spar FWTs; and to perform a comprehensive dynamic and structural analysis, focusing on the relative importance of wind and wave loads on the fatigue life and extreme stresses at different locations of the platform and tower. Three spar FWTs supporting the 20 MW wind turbine from Ashuri et al. [6] are obtained from a parametric design process, with the diameters at the bottom and at sea water level (SWL) as design variables; the static pitch angle at rated wind speed constrained at 6°, 8°, and 10°; and the draft fixed at 90.0 m for all concepts. The entire structure is assumed as elastic, and modeled with finite elements. Hydrodynamic loads are evaluated with potential theory and distributed over the hull. A controller with motion compensation based on feedforward of the nacelle velocity is adopted, avoiding the instabilities related to controller-motion interactions. The analyses are based on fully-coupled, non-linear time-domain simulations, using an aero-hydro-servo-elastic software.

The parametric design of the platform, as well as adaptations to the original tower from Ashuri et al. [6] are presented in Section 2; the control system is introduced in Section 3, and the structural and hydrodynamic model is explained in Section 4; the dynamic analysis is described in Section 5, and results are presented and discussed in Section 6; conclusions are drawn in Section 7.

2. FWT design

2.1. 20 MW wind turbine model

Ashuri et al. [6] presented a 20 MW upwind, land-based wind turbine model, resulting from a multidisciplinary design optimization with constraints on structural life, modal frequencies, tip-speed ratio, and blade-tower clearance. The turbine is adopted in the present work, with some modifications related to its use on a floating platform.

One of the modifications is the tower design. The natural frequencies of the first tower bending modes of a bottom-fixed wind turbine are expected to increase when the same structure is installed on a floating platform [30]. Consequently, the shifted 1st fore-aft and side-side tower bending frequencies can lie within the 3p blade-passing range, rather than the soft-stiff range (Fig. 1), leading to resonant excitation and increased fatigue damage.

The tower is first shortened by 10 m, which is the desired height for the base above still water level (SWL). Then, the tower diameter and thickness are increased until the 1st bending frequency exceeds $3 \times \Omega_r = 0.36$ Hz when the tower is installed on a floating platform, where Ω_r is the rated rotor speed. By increasing the diameter of all the sections by a factor of 1.2, and keeping the diameter-to-thickness ratio of 160 [6], it is possible to obtain a 1st bending frequency ranging between 0.41–0.42 Hz (stiff-stiff), depending on the spar design. This solution is in line with the design optimization by Hegseth et al. [21], who found feasible solutions for stiff-stiff tower only, for a 10 MW FWT.

Although 6p excitation is not as critical as 3p, it is also desirable to avoid interactions at the 6p range. This is done by increasing the cut-in rotor speed to 4.2 rpm. This strategy avoids overlapping between the 3p and 6p ranges, allowing for the tower 1st bending frequency to be out of any blade-passing ranges. Table 1 shows the main properties of the wind turbine and tower, after the modifications. The mass and vertical centers of gravity (VCG)s (given with respect to SWL) are presented in Table 2.

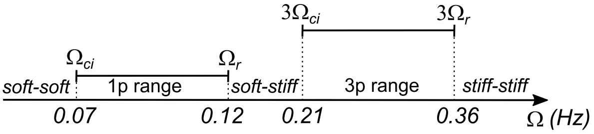

Fig. 1. Blade-passing frequency ranges for the 20 MW turbine.

Table 1
20 MW wind turbine properties [6].

Number of blades	3
Rotor diameter (m)	276.0
Hub height (m)	160.2
Cut-in, rated, cut-off wind speed (m/s)	3.0, 10.7, 25.0
Cut-in[a], rated rotor speed (rpm)	4.20, 7.15
Gear ratio	164.0
Generator efficiency (%)	94.4
Rated power (MW)	20.0
Tower base, top diameter[a] (m)	12.00, 7.44
Tower base, top thickness[a] (cm)	7.50, 5.58

[a]Indicates a modification from the original design.

Table 2
Mass and VCG (w.r.t. SWL) of wind turbine components and tower.

Component	Mass (kg)	VCG (m)
Tower	2.07×10^6	70.79
Blade × 3	7.77×10^5	160.59
Hub	2.53×10^5	160.20
Nacelle	9.45×10^5	157.18

2.2. Spar parametric design

The spar is assumed to be a cylindrical, hollow structure, with constant thickness along its length and at the bottom plate. The diameter, however, is variable, so the platform is divided in three parts: the bottom, the mid, and the top (Fig. 2). The smaller diameter at the top is intended to reduce wave loading near the surface, at the price of lower hydrostatic restoring in heave. The mid part is tapered, with the diameter varying from the larger radius at the bottom to the shorter one at the top. The tower begins 10.0 m above SWL.

The fundamental constraint for the spar design is the weight–buoyancy balance, expressed by

$$\left(m_{hull} + m_{bal} + m_{tow} + m_{rna} + m_{moor}\right) g = \rho g V_{sub} , \tag{1}$$

where m_{hull} is the hull steel mass; m_{bal} is the ballast mass; m_{tow} is the tower mass; m_{rna} is the rotor-nacelle assemble mass; m_{moor} is the mass-in-water of the mooring lines' hanging portion; and V_{sub} is the submerged volume of the platform. In addition, the following constraints are imposed for determining the solution space:

1. The draft (d) is always 90.0 m, to cope with limitations on typical shipyard capacity and transportation to the wind park.
2. The bounds on the diameter of the top section are 10.0 m to 16.0 m, allowing for a compromise between restoring in heave and wave loading.
3. The bounds on the diameter of the bottom section are 15.0 m to 26.0 m.
4. The tapered section starts 6.0 m below SWL. The length of the tapered section is determined from the fixed taper angle (30 deg) and the diameters.
5. The metacentric height must be larger than 1.0 m [31].
6. The heave natural period must be longer than 25 s. The pitch natural period must be always 5.0 s longer than the heave natural period, to avoid coupling effects (reducing the likelihood of Matthieu instability).

The hull steel mass is obtained from the volume of the spar wall and base, with steel density (ρ_{steel}) assumed as 7850.0 kg/m^3. The ballast consists of a cylindrical column of high-density concrete, extending from the base of the spar to a height h_{bal}. The ballast density ρ_{bal} is assumed as 4000.0 kg/m^3, which corresponds to commercially available high-density concrete [32].

The mooring system consists of 3 catenary chain lines. Despite the small contribution of the mooring system to the total FWT mass, disregarding it in Eq. (1) could result in significant miscalculation of the FWT draft, due to the low hydrostatic restoring in heave. The procedure for obtaining the mooring line length for a given required stiffness in surge follows the equations for quasi-static catenary mooring systems [33]. The necessary mooring stiffness in surge is normally dependent on the allowable platform excursion, and on the desired surge natural period. Only the latter is used as a constraint in this work, being specified as 120 s.

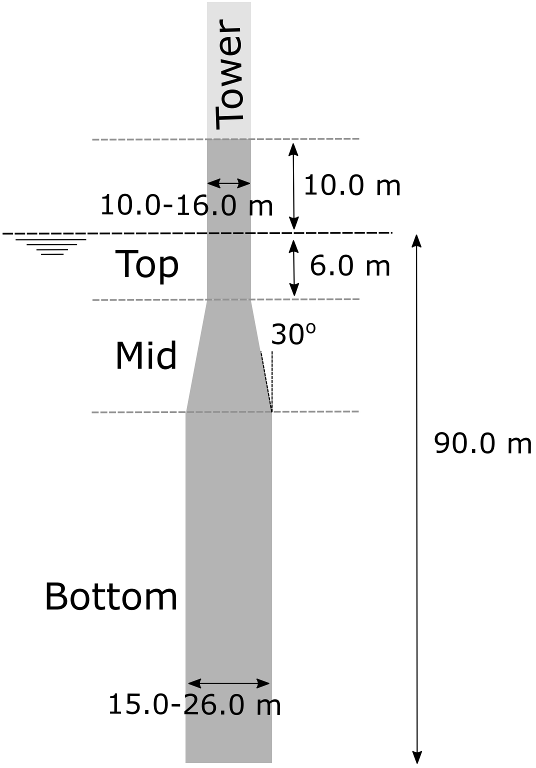

Fig. 2. Parts of the spar platform.

In order to estimate the natural periods during the parametric design stage, it is important to obtain a fair prediction of the added mass. The long-wave approximation for a cylinder is used to obtain the added mass coefficient in surge [34]:

$$a_{11} = \int_{-d}^{0} a_t dz = \rho\pi \int_{-d}^{0} r(z)^2 dz\,, \tag{2}$$

where the section radius r varies along the platform. The added mass coefficients in pitch (a_{55}) and coupled surge-pitch (a_{15}) are obtained as follows:

$$a_{55} = \int_{-d}^{0} a_t(r) z^2 dz = \rho\pi \int_{-d}^{0} r(z)^2 z^2 dz\,, \tag{3}$$

$$a_{15} = \int_{-d}^{0} a_t(r) z dz = \rho\pi \int_{-d}^{0} r(z)^2 z dz\,. \tag{4}$$

For heave, the added mass is assumed as half of the displaced mass of the volume of a sphere with the same radius as the bottom section.

The linear restoring terms in heave and pitch are directly obtained from the dimensions and metacentric height of each candidate solution, respectively. For heave, the natural period is estimated based on an 1-DOF system. For pitch, coupling with surge is taken into account in a 2-DOF system. The latter system is also used for determining the static platform pitch angle at rated thrust, θ_r. A MATLAB script is used for combining the platform dimensions and computing the corresponding inertia, volume, added mass, restoring coefficients, mooring properties, and natural periods — subjected to the constraints listed above.

3. Wind turbine control system

The control system consists of a variable speed, variable pitch (VSVP) approach, with a motion compensation strategy based on feedforward of the filtered nacelle velocity above rated wind speed. In addition, a peak shaving approach is adopted to limit thrust around rated wind speed. A modified version of the NREL ROSCO controller [35] is adopted, where the nacelle velocity feedforward approach is implemented.

Table 3
Wind turbine control parameters.

Controller natural frequency (rad/s)	0.31
Controller rel. damping (–)	0.7
Nac. velocity feedforward gain (rad/m)	−6.4
Nac.vel LP-filter cut-off frequency (rad/s)	0.18
Torque regime above rated	Constant power
Gen. torque const. in Region 2, HSS (N m s^2/rad^2)	11.99

3.1. *Below rated*

Following Ashuri et al. [6], the control strategy below rated rotor speed is based on the NREL 5 MW baseline controller, which combines an operational region for power optimization, with transitional regions near cut-in and rated rotor speeds. The corresponding parameters were obtained from the accompanying FAST model.

3.2. *Above rated*

Above rated wind speed, the original wind turbine model [6] adopted a proportional–integral (PI) controller to regulate the rotor speed error through the blade-pitch angle:

$$\Delta\beta = K_p \Delta\Omega + K_i \int_0^t \Delta\Omega dt\,, \tag{5}$$

with K_p and K_i being the proportional and integral gains. The rotor speed error $\Delta\Omega$ is given by

$$\Delta\Omega = \Omega - \Omega_r\,, \tag{6}$$

where the reference $\Omega_r = \Omega_0$ is the rated rotor speed.

Although this formulation provides satisfactory performance for a bottom-fixed turbine, its use in floating wind turbines can introduce resonant motions associated with controller-motion interaction [24–26]. Controller *detuning* is a common approach to deal with the problem. The idea is to reduce the gains, preventing the controller to respond to rotor speed variations caused by pitch motions.

Despite being widely used in academic research for FWTs, detuning reduces the controller's ability to cope with wind fluctuations on the order of the pitch natural period, leading to significant power fluctuations. In addition, excessive pitch motions can take place, leading to large structural loads and turbine shutdown [36]. Controller detuning is particularly problematic for the present work, since the pitch natural periods are relatively long compared with smaller FWTs. In addition, one of the main interests is to compare FWTs with different restoring – and thus natural periods – in pitch. A fair comparison between the different designs would then not be possible, since the controller bandwidths would vary for each FWT, affecting their dynamics significantly.

Lackner [28] avoided the instability associated with pitch motions by modifying the reference rotor speed as a function of the platform pitch velocity. In this work, an equivalent strategy is adopted, where the low-pass filtered nacelle velocity, $v_{n,f}$, is used to update Ω_r:

$$\Omega_r(t) = \Omega_0 + K_{ff} v_{n,f}\,, \quad K_{ff} < 0\,. \tag{7}$$

Including the time-varying $\Omega_r(t)$ in the rotor speed error (Eq. (6)) is equivalent to informing the controller whether the turbine is moving downwind or upwind, preventing it from responding to rotor speed fluctuations caused by the platform motions. This approach is thus known as feedforwarding of the nacelle velocity.

The platform pitch response to waves, although relatively low, can be amplified by the long arm from the center of rotation to the nacelle. Therefore, the nacelle velocity is low-pass filtered to avoid wave-frequency components being fed into the controller through $\Omega_r(t)$. A 2nd-order Butterworth filter was found to provide satisfactory filtering performance. Stability of the controller is verified based on a linearized system [37], including states from the nacelle motion, the rotor speed, and 2nd-order low pass filter. First-order aerodynamic derivatives were obtained using FAST's linearization module.

The PI controller with feedforward of the nacelle velocity allows the same controller natural frequency Ω_{ctr} to be used for all spar designs. Ω_{ctr} corresponding to 20 s, just longer than the typical wave frequency range, avoids interactions with wave responses. A gain-scheduling strategy is implemented in the form of a look-up table, to ensure that the required natural frequency is maintained for all blade pitch angles. The main parameters of the above-rated controller are provided in Table 3.

3.3. *Peak shaving*

Peak shaving is a strategy based on starting to pitch the blades just before rated wind speed, thus limiting the thrust and reducing structural loads [38]. The implementation in ROSCO consists of a look-up table where the minimum blade pitch angle is set as a function of the low-pass filtered wind speed. Instead of peaking at rated, the thrust then becomes flat at the range where peak shaving is active.

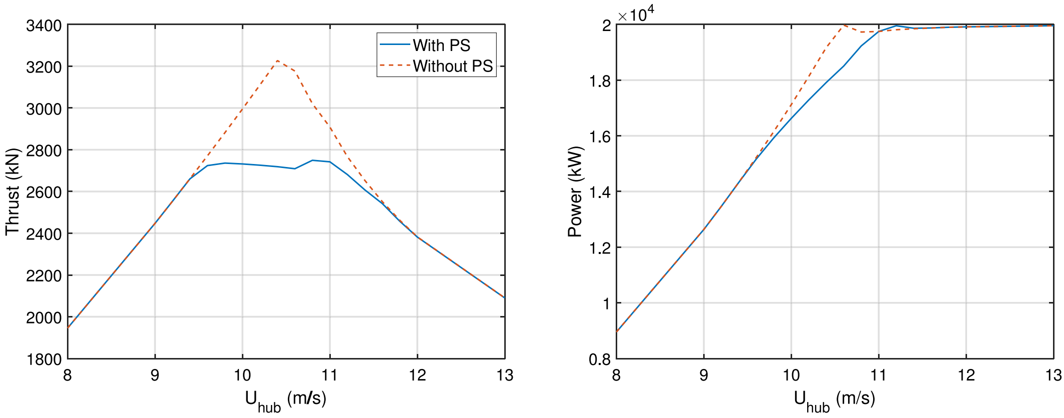

(a) Thrust (b) Power

Fig. 3. Thrust and power curves with and without peak shaving.

A consequence of peak shaving is a reduction of power capture just below the rated wind speed, which depends on the level of reduction in thrust required. In this work, the thrust is limited to 2.8×10^6 N, corresponding to ca. 87% of the original peak thrust at rated wind speed. Fig. 3 compares the thrust and power curves with and without peak shaving, for wind speeds close to rated. When peak shaving is active, a loss of power is observed for wind speeds between 9.5 m/s and 11.0 m/s, reaching up to 8% for $U = 10.6$ m/s.

4. Hydroelastic modeling

A consistent representation of the actual structural deflections, as well as of the hydrodynamic loads, is needed for accurately predicting the platform internal loads at the sections of interest. Two main approaches can be used for representing structural flexibility: a finite-element (FE) model, with the hydrodynamic loads distributed over the structure [14,16–18]; or a model based on modal superposition, with additional (generalized) degrees of freedom in order to represent flexible modes and the associated hydrodynamic loads [15,39,40].

The former approach is adopted in this work. The spar platforms are represented with FE beam elements, and divided in sections where the hydrodynamic loads are applied. Radiation and diffraction loads from 1st-order potential theory are applied at each section, combined with quadratic drag terms.

4.1. *Simulation tool*

The simulations are carried out using SIMA, which performs coupled time-domain analyses combining the software RIFLEX and SIMO [41]. RIFLEX [42] is a finite element (FE) software for structural analysis of slender marine structures, and is used in this work for modeling the platform, tower, and wind turbine blades. It also computes the wind turbine aerodynamic loads using a blade element momentum (BEM) formulation, with Glauert's correction for high induction factors and Prandtl's correction factors for losses associated with the hub and blade tip. Øye's formulations for dynamic wake and dynamic stall are also included in the code. Hansen [43] provides details on the BEM method, as well as the corrections mentioned above. Tower shadow is accounted for based on 2-D potential flow around a circle.

SIMO [44] is a simulator of marine operations for large bodies. In this work, it is used for modeling global linear damping, 2nd-order wave forces, the mooring system, and the nacelle inertia properties. Skaare et al. [36] presented a comparison between simulations using SIMA with measurements from a real 2.3 MW spar floating wind turbine.

All realizations were run for a total of 4000 s, where the initial 400 s were assumed as transient and removed from the analyses. A time-step of 0.005 s was used for all cases. In order to improve numerical stability of the FE model, a global stiffness-proportional Rayleigh damping factor of 2.5×10^{-3} was adopted in all simulations, while mass-proportional damping was not used to avoid artificially damping LF modes [45]. The inclusion of numerical damping results in an increase of about 0.3% in the global relative damping at the 3p frequency (0.40 Hz), which is the highest relevant frequency of excitation in the system.

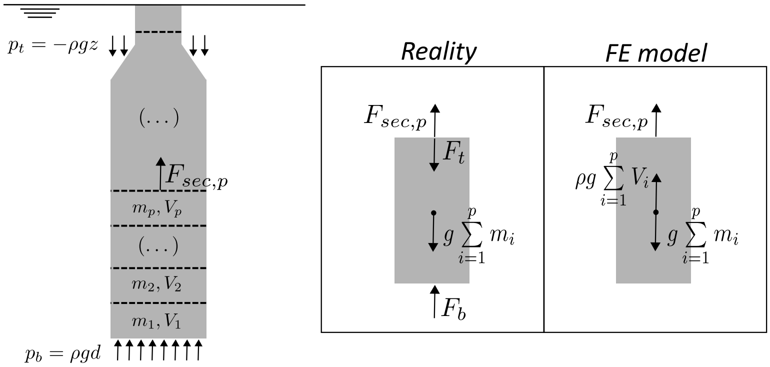

Fig. 4. Sectional axial force from hydrostatic equilibrium for an upright spar — the free-body diagrams illustrate the difference between the force obtained with the FE model and the analytical solution.

4.2. Structural model

4.2.1. Platform

The spar platform is modeled in RIFLEX using beam elements, with axisymmetric cross sections. The platform is subdivided in segments, on which the hydrodynamic loads are applied. The length of each segment varies according to its vertical position, but is limited to 5.0 m at the bottom and mid parts; and 3.0 m at the top part. Since the lower position of the mid part varies according to the design, the hull discretization varies slightly among the different spars.

The cross-sectional mass is determined based on the section diameter and thickness, and on the steel density given in Section 2. A steel modulus of elasticity $E = 2.0 \times 10^{11}$ Pa is assumed for calculating the axial and bending stiffness. Since the torsional mode is not of interest for this work, an excessively large value was assigned to the torsional stiffness. For the portion filled with ballast, the mass is correspondingly increased, but the stiffness is assumed to remain unchanged.

In RIFLEX, the buoyancy and weight are applied at the center of each section. From the static equilibrium of forces in Fig. 4, the mean axial force at the p-th section is given by

$$F_{sec,i}^{FE} = W_p - B_p = g \sum_{i=1}^{p} \left(m_i - \rho V_i \right) , \tag{8}$$

where m_i and V_i are the mass and volume of each section. For a real spar, however, the buoyancy in an undeflected position will be determined by the pressure distribution at the bottom and at the tapered segment. At the bottom, an upward force F_b is applied:

$$F_b = \rho g d \pi \frac{D_b^2}{4} , \tag{9}$$

where d is the draft and D_b is the base diameter. Thus, below the mid (tapered) section, the following correction must be considered for the axial force:

$$F_{sec,i}^{bot} = F_{sec,i}^{FE} + \rho g \left(\sum_{i=1}^{p} V_i - d \pi \frac{D_b^2}{4} \right) . \tag{10}$$

At the mid (tapered) part, the pressure integration of the hull results in a downward force with magnitude:

$$F_t = -\rho g z \pi \frac{D_b^2 - D_s^2}{4} , \tag{11}$$

where z is the vertical position of the section and D_s is the section diameter. The correction at this part of the platform becomes:

$$F_{sec,i}^{mid} = F_{sec,i}^{FE} + \rho g \left[\sum_{i=1}^{p} V_i - d \frac{\pi}{4} \left(d D_b^2 + z D_b^2 - z D_s^2 \right) \right] . \tag{12}$$

For the top part, the upward force corresponds to the platform buoyancy. The correction is then given by:

$$F_{sec,i}^{corr} = F_{sec,i}^{FE} + \rho g \left(\sum_{i=1}^{p} V_i - V \right) . \tag{13}$$

This correction is particularly important for the extreme analysis, especially for the sections closer to the spar bottom. For the fatigue analysis, on the other hand, it has a minor impact, since dynamic variations in the axial force have only minor contribution to the axial stresses, compared with the bending moments.

4.2.2. Wind turbine

The wind turbine blades are modeled with 19 beam elements, using double-symmetric cross sections. The structural and geometrical properties, as well as the airfoil coefficients, are obtained from the FAST model which accompanies the wind turbine definition [6]. The hub and nacelle inertia properties are also obtained from the same model.

The tower is modeled with 20 beam elements, using thin-walled cross sections. The inertia and stiffness properties are obtained similarly as for the platform.

4.3. Mooring system

The mooring system is modeled as a quasi-static system. An equivalent matrix of horizontal stiffness coefficients is found based on the mooring line mass and length, as well as fairlead and anchor positions, and based on catenary equations. Dynamic effects associated with velocity and acceleration of the line are not taken into account.

In order to increase the restoring arm in yaw, spar mooring systems typically include a “crow-foot” arrangement [36,46]. This configuration is not considered in the simplified mooring model adopted in this work. Instead, a linear stiffness coefficient in yaw is added at fairlead position to represent the crow-foot system, chosen to provide a natural period of 16.0 s in yaw for all designs. This is sufficiently longer than the cut-in 1p excitation period of 14.3 s, avoiding resonant yaw motions.

4.4. Hydrodynamic model

The 1st-order potential theory loads are obtained with WAMIT [47], with the spars assumed as rigid bodies. The mesh is created ensuring that panels are not intersected by the sections defining the segments, so that each segment contains whole panels only. The panel length is kept at approximately 1.0 m through the entire mesh. Wave periods from 3.0 s to 25.0 s, with steps of 1.0 s, were adopted in the computation of hydrodynamic loads.

WAMIT offers the option to output the complex panel pressures corresponding to the radiation and diffraction problems, separately. It is then possible to reconstruct the radiation coefficients and excitation transfer functions in 3 (translational) DOFs for each spar segment, using the pressures at the corresponding panels and the fundamental equations of potential theory (see e.g. Svendsen [14]). RIFLEX then evaluates the diffraction and radiation loads in the time domain simulations. The latter requires the solution of convolution integrals of the retardation functions [48,49], which can be time-consuming when the number of sections is large. These integrals are approximated by the software as series of exponential functions, to reduce computational time. See e.g. Taghipour et al. [50] for details on this approach. Viscous drag is added based on a quadratic model, with the non-dimensional transverse drag coefficient $C_d = 0.6$ for all the sections [51]. Drag loads in the longitudinal direction are not included.

The reconstruction of radiation coefficients from the distributed model does not result in a perfect representation for roll and pitch. For these DOFs, the method approximates the loads by the summation of lumped forces in surge and sway, respectively, multiplied by the squared distance from each segment to the origin – i.e., the fluid perturbation associated with the rotations are neglected. Fig. 5a compares the rigid-body and reconstructed pitch added mass for Spar8, whose dimensions are presented later in Table 8. The reconstructed coefficients are somewhat larger than their rigid-body counterparts. The difference is lower than 5% for the entire range of periods. Excitation loads are not affected by the same problem, but can be influenced by the hull discretization. Fig. 5b shows that the curves for excitation in pitch are nearly coincident, indicating that the hull discretization is satisfactory.

In addition to the distributed hydrodynamic loads over the body, the hydrodynamic model also includes a global linear damping matrix, in surge, sway, heave, and yaw. The damping coefficients are added to avoid unrealistic resonant responses at these DOFs. The criterion was to reach the same relative damping coefficients as obtained for the OC3Hywind spar [46].

4.4.1. Difference-frequency 2nd -order wave loads

Due to the large size and low natural frequencies of rigid body motions of the platforms, it is of interest to include the difference-frequency second order wave loads. This effect can be accounted for with quadratic transfer functions (QTFs), obtained from the solution of the second-order potential in addition to second-order terms of the first-order potential.

The QTFs were calculated for the spars using WAMIT, considering difference frequencies up to 0.28 rad/s. This range covers the natural periods of all DOFs except yaw (which is not excited by waves for a spar). In WAMIT, it is possible to approximate the computation of the second-order potential by neglecting the integration of the quadratic forcing over the free surface, avoiding the discretization of this area and reducing computational time significantly. Simos et al. [52] evaluated this approximation for a 5 MW semi-submersible FWT, finding very good agreement with the QTF computed with the complete second-order solution. Free-surface effects are expected to be even less important for a spar, due to its simpler geometry and larger draft, and the procedure is thus adopted in this work also.[1]

The difference-frequency 2nd-order wave loads are not distributed over the hull. Instead, they are applied as a nodal load on the center of the spar, at mean water line.

---

[1] The adoption of Newman’s approximation [53], on the other hand, is not recommended, due to the relatively short natural periods in heave, pitch, and roll.

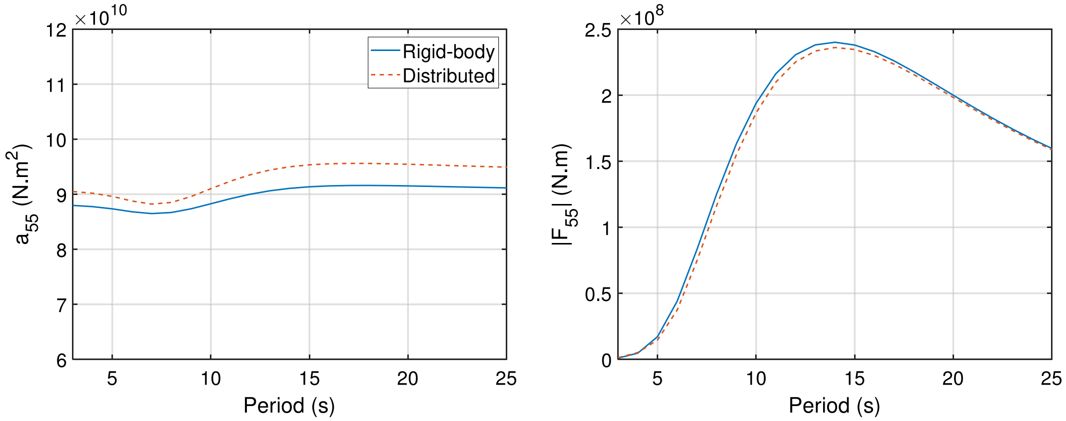

(a) Pitch added mass. (b) Pitch excitation moment.

Fig. 5. Pitch added mass and pitch excitation moment amplitude for 0° incident waves. Comparison between rigid-body and reconstructed from distributed model.

5. Dynamic analysis

5.1. Environmental conditions

The fatigue and extreme analyses are performed considering the environmental conditions for the Norwegian Sea, Site 14 from Li et al. [54]. The long-term joint probability distributions of hub mean wind speed (U), significant wave height (H_s), and wave peak period (T_p) are used for obtaining the most probable sea states associated with the wind turbine operational conditions, as well as the environmental contours corresponding to the 50-year cases. The distributions are obtained based on 10 years data from a numerical hindcast model. The water depth is set to 320.0 m.

The joint distribution of wind speed, wave significant height, and wave peak period, may be approximated by [54]

$$f_{U,H_s,T_p}(u,h,t) \approx f_U(u) f_{H_s|U}(h|u) f_{T_p|H_s}(t|h)\,, \tag{14}$$

where $f_U(u)$ is the marginal distribution of the mean wind speed; $f_{H_s|U}(h|u)$ is the conditional distribution of significant wave height, for a given mean wind speed; and $f_{T_p|H_s}(t|h)$ is the conditional distribution of wave peak period, for a given significant wave height.[2]

The marginal distribution of the one-hour mean wind speed at 10 m height, U_{10}, is assumed to follow a two-parameter Weibull distribution, with a probability density function (PDF) given as follows:

$$f_{U_{10}}(u) = \frac{\alpha_U}{\beta_U}\left(\frac{u}{\beta_U}\right)^{\alpha_U - 1} \exp\left[-\left(\frac{u}{\beta_U}\right)^{\alpha_U}\right], \tag{15}$$

where α_U and β_U are the shape and scale parameters, respectively, and are given in Table 4. Wind shear is assumed to follow a power law profile:

$$U(z) = U_{10}\left(\frac{z}{10}\right)^{\alpha_{PL}} \tag{16}$$

where the exponent α_{PL} is assumed as 0.14 for all wind speeds.

The PDF for the conditional distribution of the significant wave height, H_s, for a given U, is also given by a two-parameter Weibull distribution:

$$f_{H_s|U}(h,u) = \frac{\alpha_{HU}}{\beta_{HU}}\left(\frac{h}{\beta_{HU}}\right)^{\alpha_{HU} - 1} \exp\left[-\left(\frac{h}{\beta_{HU}}\right)^{\alpha_{HU}}\right], \tag{17}$$

with the parameters α_{HU} and β_{HU} given by

$$\begin{aligned} \alpha_{HU} &= a_1 + a_2 u^{a_3} \\ \beta_{HU} &= b_1 + b_2 u^{b_3}\,. \end{aligned}$$

The coefficients a_i, b_i are provided in Table 4.

---

[2] Rigorously, the conditional distribution of wave peak period for a given pair of mean wind speed and significant wave height, $f_{T_p|U,H_s}(t|h,u)$, should be used in Eq. (14). The simplification is proposed by Li et al. [54] and is not expected to affect the estimate of critical conditions significantly.

Table 4
Distribution parameters for site 14 of Li [54].

α_U	2.029
β_U	9.409
a_1	2.136
a_2	0.184
a_3	1.000
b_1	0.534
b_2	0.070
b_3	1.435
c_1	1.886
c_2	0.365
c_3	0.312
d_1	0.001
d_2	0.105
d_3	−0.264

The conditional distribution of wave peak period on the significant wave height is assumed to follow a log-normal distribution:

$$f_{T_p|H_s}(t|h) = \frac{1}{\sqrt{2\pi}\sigma_{TH} t} \exp\left[-\frac{1}{2}\left(\frac{\ln t - \mu_{TH}}{\sigma_{TH}}\right)^2\right], \tag{18}$$

where the distribution mean μ_{TH} and variance σ_{TH} are given by

$$\mu_{TH} = c_1 + c_2 h^{c_3}$$
$$\sigma^2_{TH} = d_1 + d_2 \exp(d_3 h),$$

with the coefficients c_i and d_i as provided in Table 4.

5.1.1. Environmental modeling

Waves are generated from time-domain realization of a three-parameter JONSWAP spectrum [33], with a γ-factor of 3.3 for all sea states. Long-crested waves are assumed.

Wind turbulence time series are generated using TurbSim [55], based on a Kaimal spectrum and with turbulence intensity following IEC Normal Turbulence Model category B [56] for all conditions. Wind shear is taken into account assuming a power law with exponent 0.14 for all wind speeds.

5.2. Fatigue analysis

A full long-term fatigue analysis includes all the possible combinations of mean wind speed, significant wave height, and wave peak period. As the present work focuses on the comparison between the different designs, the adopted fatigue analysis considers only the *most probable* sea state associated with each mean hub-height wind speed in the operational range.

Kvittem [20] showed that, for a 5 MW semi-submersible FWT, 4 realizations of 1h-simulations provide fatigue damage estimates within 5% of estimates based on 10 3-hour realizations. It is assumed that these conclusions are also valid for the FWTs of this work, such that the fatigue analyses are based on 4 realizations of 1h-simulations.

The most probable sea state associated with each mean hub wind speed corresponds to the H_s and T_p providing the highest value of the PDF's given by Eqs. (17) and (18), respectively. The mean hub wind speeds cover the turbine operational range from 4.0 m/s to 25.0 m/s with steps of 1.0 m/s. The probability of occurrence associated with bins centered at each mean wind speed, and bounded with ± 0.5 m/s, is obtained from Eq. (15).

5.2.1. Fatigue damage calculation

The fatigue analysis is based on DNV-RP-C203 [57], which recommends bi-linear S-N curves for offshore structures subjected to wind and wave loads. The accumulated damage is calculated at different sections of the platform and tower. All the conditions analyzed assume aligned wind and wave loads. The 1-hour fatigue damage accumulation D_{1h} is estimated from the average axial stress time-series of the 4 realizations, which are obtained from each section's axial force N_x and fore-aft bending moment M time-series according to:

$$\sigma_x = \frac{N_x}{A} + \frac{Mr}{I_y}, \tag{19}$$

where A is the annular section area, r is the section radius, and I_y is the section modulus around the bending axis.

A rainflow cycle counting procedure is then applied to the axial stress time series, providing a series of cycles with stress range S_i. The accumulated damage D_{1h} is obtained from:

$$D_{1h} = \frac{1}{\bar{a}_1}\sum_{i=1}^{n_l} S_i^{m_1} + \frac{1}{\bar{a}_2}\sum_{j=1}^{n_h} S_j^{m_2}, \tag{20}$$

Table 5
Load cases considered in the fatigue analysis — operational conditions.

V_{hub} (m/s)	$P(V_{hub} \pm 0.5)$ (%)	I (%)	H_s (m)	T_p (s)
4.0	3.75	30.1	1.49	9.3
5.0	4.51	26.2	1.56	9.4
6.0	5.14	23.6	1.64	9.4
7.0	5.63	21.7	1.73	9.5
8.0	5.98	20.3	1.83	9.6
9.0	6.18	19.2	1.95	9.7
10.0	6.23	18.3	2.07	9.8
11.0	6.17	17.6	2.21	9.9
12.0	5.97	17.0	2.35	10.1
13.0	5.69	16.5	2.51	10.1
14.0	5.33	16.1	2.68	10.3
15.0	4.91	15.7	2.85	10.4
16.0	4.46	15.4	3.04	10.5
17.0	3.98	15.1	3.24	10.6
18.0	3.51	14.9	3.44	10.8
19.0	3.05	14.6	3.66	11.0
20.0	2.61	14.4	3.89	11.1
21.0	2.21	14.2	4.12	11.2
22.0	1.84	14.1	4.37	11.4
23.0	1.51	13.9	4.62	11.5
24.0	1.23	13.8	4.88	11.7
25.0	0.99	13.6	5.15	11.8

Table 6
S-N curve coefficients and stress limit for spar and tower sections [57].

	Spar	Tower
$\bar{a}_1$	$1.0 \times 10^{11.764}$	$1.0 \times 10^{12.164}$
$\bar{a}_2$	$1.0 \times 10^{15.606}$	$1.0 \times 10^{15.606}$
m_1	3.0	3.0
m_2	5.0	5.0
S_{lim} (MPa)	52.63	52.63

where n_l and n_h are the number of cycles in the low and high cycles regions, respectively. The stress limit S_{lim} dividing the regions, as well as the coefficients $\bar{a}_{1,2}$ and $m_{1,2}$ defining the S-N curves, are obtained from DNV [57] and are reproduced in Table 6. For the platform sections, the curves in seawater with cathodic protection are adopted, while for the tower the curves in air are used. A circumferential butt weld made from both sides is assumed for the spar and tower sections. The thickness effect is accounted for by modifying the stress ranges as recommended by DNV [57]. Stress concentration factors due to misalignment and thickness in butt welds are not considered in the analyses.

The damage associated with each of the load cases in Table 5 is then weighted with the probability of occurrence of the respective bin, providing the averaged 1-hour accumulated fatigue $\bar{D}_{1h}$ at the platform and tower sections, for each spar.

5.3. Extreme analysis

A full long-term analysis (FLTA) is too time-consuming for practical prediction of extreme responses. In addition, usually a limited number of conditions govern the tail of the extremes distribution, such that methods for selection of these conditions are normally adopted in practice.

For floating wind turbines, Li et al. [23] proposed a *modified environmental contour method* (MECM), where the cut-off condition is also considered in addition to the 50-year environment. The idea is to account for cases where the turbine is not parked, as it is normally the case for the 50-year condition, such that loads related to thrust are also included in the analysis.

This approach is used for the analysis of extreme loads in this work, but the condition associated with the rated wind speed, which gives the largest mean thrust, is also added. Time-domain simulations are carried out for the 3 spars and considering each load case, with 20 realizations for waves and wind. For the case with 50-year hub wind speed, the turbine is set to idle with no generator torque and blades feathered to 88 degrees.

5.3.1. Load case selection for the extreme analysis

In the MECM, as adopted here, the sea states forming 50-year contours with three mean hub wind speeds (rated, cut-off, and 50-year wind) are selected. In other words, the 3-D surface formed by combinations of U, H_s, and T_p yielding a 50-year return period is “sliced” at the wind speeds of interest. The determination of the wind speed and sea state parameters is more easily done by transforming the random environmental variables (X-space) to a space where the variables follow a standard normal distribution (U-space):

$$F_{X_i}(x_i) = \Phi(u_i)\,, \tag{21}$$

Table 7
Hub mean wind speeds, turbulence intensity, and associated sea state parameters representing the environmental contours.

U (m/s)	I (%)	H_s (m)	T_p (s)	ID
		2.39	3.57	i-rt
		3.62	4.64	ii-rt
10.7	17.8	4.85	6.04	iii-rt
		6.08	7.99	iv-rt
		7.31	13.00	v-rt
		3.92	5.11	i-co
		5.60	6.34	ii-co
25.0	13.6	7.28	7.84	iii-co
		8.96	9.76	iv-co
		10.63	14.07	v-co
49.1	12.1	13.97	15.14	i-50

where $i = 1, 2, 3$ and F and Φ are the cumulative density functions in the respective spaces. The points in the U-space corresponding to a given return period form a sphere, which after transformation back to the X-space, provides the wind and sea state combinations with the required return period.

From the 50-year contour, the point providing the 50-year wind speed is associated with one combination of H_s and T_p only. For the rated and cut-off cases, there will be infinite combinations of H_s and T_p associated with the respective wind speeds, from which five are chosen for analysis according to the following wave height and steepness criteria:

- the combination with highest H_s;
- the combination with largest H_s/T_p ratio;
- three conditions at the lower half of the contour, equally spaced between the two previous ones.

The resulting load case combinations are provided in Table 7, and illustrated in Fig. 6.

5.3.2. Extreme response calculation

For the extreme response estimate, a Gumbel distribution is fit to the maxima from the 20 realizations using the MATLAB toolbox WAFO [58]. The 90% fractile of the corresponding cumulative density function (CDF) is then used to obtain the 50-year axial stresses. In addition to the axial stresses, extreme values are also obtained for the platform extreme pitch angle and for the nacelle acceleration, following the same procedure.

6. Results

6.1. Spar dimensions

A total of 660 feasible solutions resulted from the parametric design process. Fig. 7 shows the steel and ballast mass as a function of the static pitch angle at rated, for all the solutions. As noted, the requirement of larger restoring in pitch demands up to 30% larger ballast mass. An increase in steel mass of up to 10% is also observed, due to the larger platform diameter.

The solutions are divided in groups with $\theta_r \leq 6°$, $8°$, and $10°$. The solution with lowest steel mass is chosen from each group. Table 8 shows the main dimensions for each of the spars. In addition to having reduced steel and ballast mass, the solutions with lower restoring in pitch also have lower diameter at the top, and thus reduced wave loading. The displayed natural periods are obtained from decay simulations, thus accounting for radiation effects from potential theory, and viscous damping. The natural period in pitch is significantly affected, with a difference of 10.4 s between Spar6 and Spar10. The difference in mooring system mass is due to the requirement of same natural period in surge — platforms with lower mass require lower restoring, and thus lighter mooring lines. It is noted that the actual surge periods are slightly different than 120.0 s, due to the adoption of simplified added mass and disregarding damping in the parametric design process. The different platform designs do not affect the tower bending frequencies significantly.

Since the different designs have different FE meshes, the platform sections considered in the analysis are placed at slightly different distances from the keel. The exact positions of the sections for each platform are given in Table 9. For all spars, Sections 1–6 are located at the bottom part of the platform; Section 7 is at the tapered part; and section 8 is at the waterline (top part). For the tower (Table 10), the section positions are the same for all designs.

6.2. Control system performance

In addition to responding more promptly to changes in the wind speed, the controller with motion compensation also provides more aerodynamic damping to the pitch motions, compared with the detuned controller. This becomes clear when analyzing the closed-loop system eigenvalues, as shown in Fig. 8 for Spar6, under a mean wind speed of 13.0 m/s. The detuned controller gains

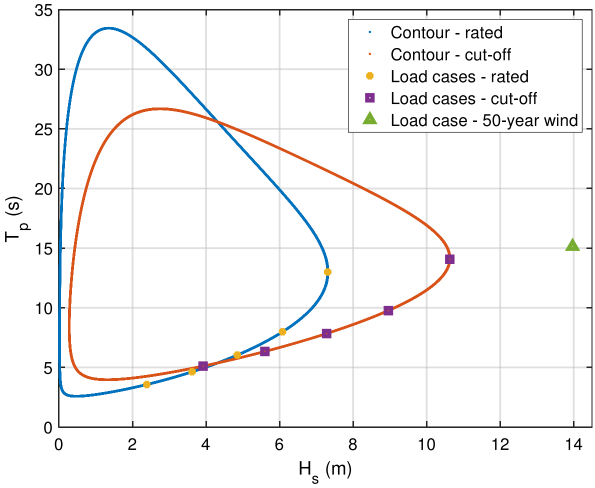

Fig. 6. Environmental contours and load cases for the extreme analysis.

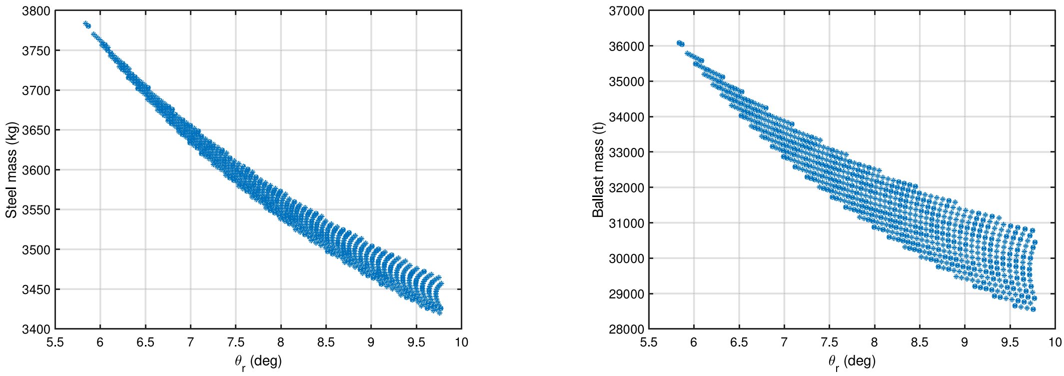

(a) Steel mass

(b) Ballast mass

Fig. 7. Steel and ballast mass as a function of static pitch at rated wind speed, for the feasible solutions.

correspond to rotor dynamics with natural period[3] of 59.0 s. The natural frequencies and damping corresponding to the eigenvalues mainly associated with the nacelle motion are shown in Table 11. While for the detuned controller the amount of damping is marginal, the motion compensation approach based on Eq. (7) introduces a relative damping of 25.2% into the system. The natural frequencies, on the other hand, are very similar.

Fig. 9 compares the controllers' performance with a time-window of the pitch motions and generator power, also for Spar6 and under turbulent wind with a mean speed of 13.0 m/s, and the associated wave conditions from Table 5. Although the instability due to controller-motion interactions is avoided by controller detuning, large resonant oscillations still are observed, due to the low level of aerodynamic damping. Large variations are also observed in the generated power. When motion compensation is used, the resonant pitch oscillations are damped out, and the variations in power are significantly reduced.

The power spectral density (PSD) of the tower base fore-aft bending moment, for the same case, is shown in Fig. 10. The pitch motions for the detuned case translate into more energy near the pitch natural frequency, as expected. The energy at the wave frequency range is similar in both cases, indicating good performance of the low-pass filter on the nacelle velocity in preventing feeding of wave-frequency components to the controller.

---

[3] With the detuned controller, the highest natural frequencies ensuring stability for Spar8 and Spar10 are 0.09 rad/s (68.0 s) and 0.08 rad/s (76.0 s), respectively.

Table 8
Main dimensions of the three spar FWT designs. Radii of gyration provided with respect to the origin of the body-fixed coordinate system.

	Spar6	Spar8	Spar10
Static pitch (deg)	6.0	8.0	10.0
Draft (m)	90.00	90.00	90.00
Diameter - top (m)	15.90	15.20	14.70
Diameter - bottom (m)	25.50	24.10	23.30
SWL to taper top (m)	6.00	6.00	6.00
SWL to taper bottom (m)	14.31	13.71	13.45
Ballast column height (m)	17.29	17.00	16.79
Ballast mass (kg)	3.53×10^7	3.10×10^7	2.86×10^7
Steel mass (kg)	3.77×10^6	3.55×10^6	3.43×10^6
GM (m)	11.89	9.82	8.40
KG (m)	30.09	32.30	33.75
KB (m)	41.91	42.05	42.09
Displacement (m^3)	4.26×10^4	3.82×10^4	3.58×10^4
C_{11} (N/m)	2.39×10^5	2.14×10^5	2.00×10^5
C_{33} (N/m)	1.99×10^6	1.82×10^6	1.70×10^6
C_{55} (N m/rad)	5.09×10^9	3.77×10^9	3.02×10^9
C_{66} (N m/rad)	8.21×10^8	7.13×10^8	6.59×10^8
Mooring system mass (kg)	6.27×10^5	6.10×10^5	6.01×10^5
r_{yy} (m)	82.46	82.80	83.04
r_{zz} (m)	11.04	10.87	10.80
T_{surge} (s)	124.4	121.0	119.0
T_{heave} (s)	30.8	30.3	30.3
T_{pitch} (s)	38.7	44.2	49.1
1st tower FA freq. (Hz)	0.41	0.42	0.42
2nd tower FA freq. (Hz)	1.55	1.54	1.53

Table 9
Distance of platform sections from the keel, for the different spars.

Section	Distance from keel (m)		
	Spar6	Spar8	Spar10
1	13.22	13.00	12.84
2	26.15	25.15	25.75
3	34.88	32.30	33.75
4	47.98	47.27	47.69
5	57.83	56.33	57.63
6	66.77	66.42	66.72
7	79.84	80.14	80.27
8	90.00	90.00	90.00

Table 10
Tower section positions and sectional dimensions.

Section	Diameter (m)	Thickness (mm)	Dist. from tower base (m)	Dist. from keel (m)
1	11.74	73.4	0.00	100.00
2	11.27	70.4	17.13	117.13
3	10.55	65.9	40.38	140.38
4	9.99	62.4	55.88	155.88
5	9.15	57.6	79.13	179.13
6	8.46	52.9	102.38	202.38
7	7.87	41.0	125.63	225.63
8	7.52	47.0	141.13	241.13

Table 11
Natural frequency and damping for the eigenvalues mainly associated with the nacelle motion, with both controllers.

	Detuned	Motion comp.
ω_n (rad/s)	0.1519	0.1487
ζ (–)	0.0153	0.2524

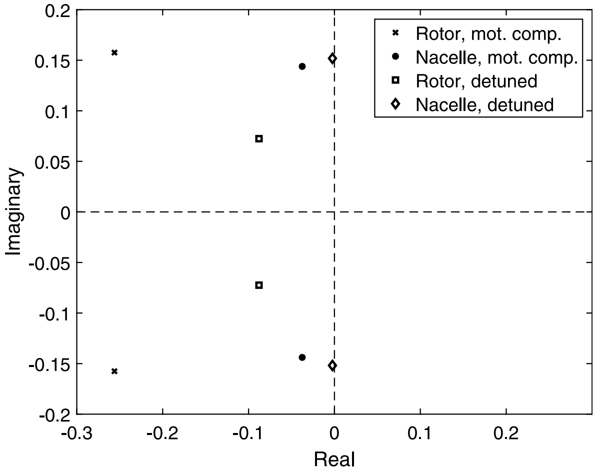

Fig. 8. Poles mainly associated with nacelle motion and rotor dynamics for the controller with motion compensation and the controller with detuned gains. $U = 13.0$ m/s.

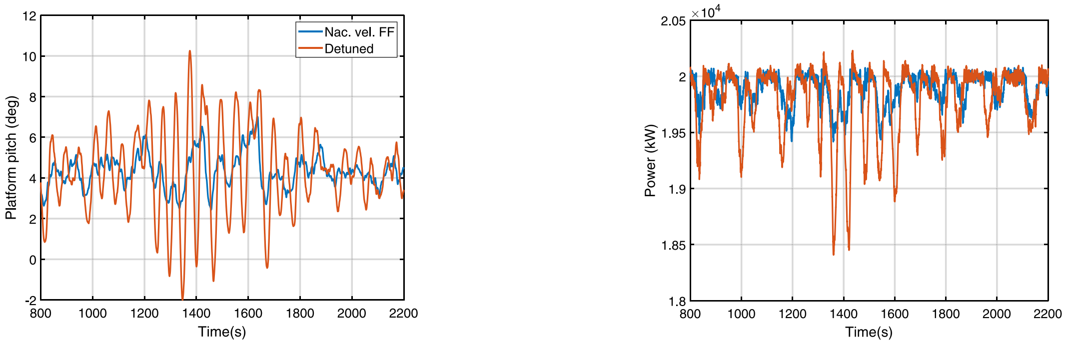

(a) Platform pitch (b) Generator power

Fig. 9. Platform pitch and generator power for Spar6, using a controller with nacelle velocity feedforward and a detuned controller. $U = 13.0$ m/s, $H_s = 2.51$ m, $T_p = 10.1$ s.

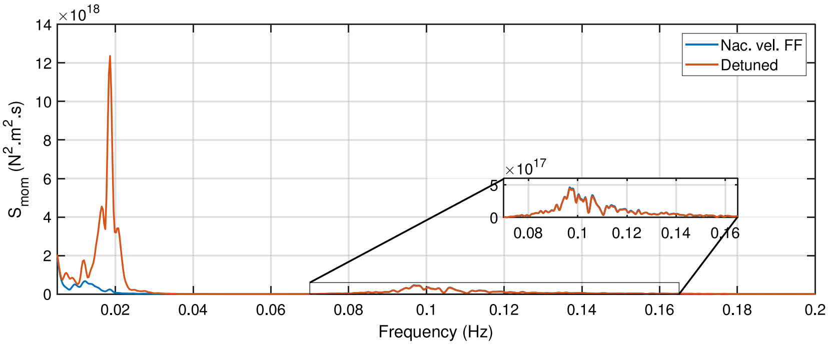

Fig. 10. Tower base fore-aft bending moment PSD for Spar6, using a controller with nacelle velocity feedforward and a detuned controller. $U = 13.0$ m/s, $H_s = 2.51$ m, $T_p = 10.1$ s.

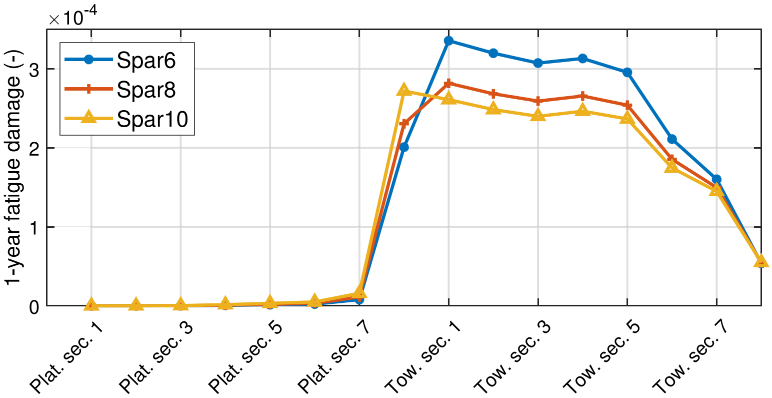

Fig. 11. Weighted sectional fatigue damage along the length of the spars.

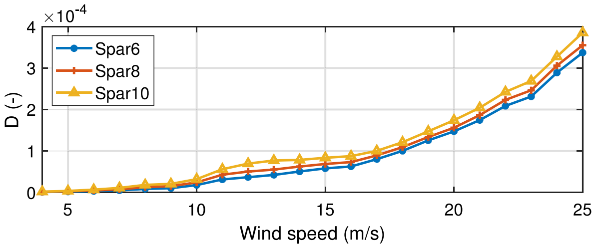

(a) Platform section 8

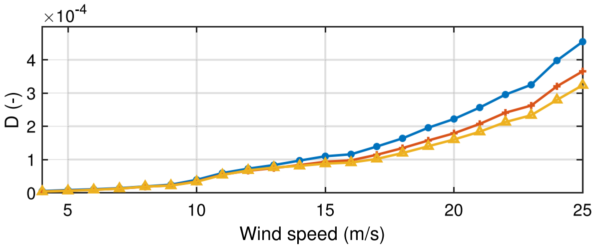

(b) Tower base

Fig. 12. One-hour fatigue damage at platform section 8 and tower base, for each of the load cases in Table 5.

6.3. *Fatigue analysis*

Fig. 11 shows the fatigue damage, weighted with the probabilities of occurrence in Table 5, at sections along the platform and tower. The damage for the platform sections closer to the bottom is several orders of magnitude lower than for locations near SWL. At the platform section 8, which coincides with SWL, the damage is larger for the designs with larger pitch at rated thrust (i.e., lower restoring in pitch). For the tower sections, however, the damage becomes larger for the designs with larger restoring in pitch.

The short-term damage associated with each load case is shown in Fig. 12. For the tower base, the discrepancy between the different designs is more relevant for higher wind speeds, which are associated with more severe waves. Fig. 13 shows the spectra of the axial stresses for one realization of the condition associated with $U = 20.0$ m/s, for Spar6 and Spar10. For platform section 8, the difference between both designs is more visible for low-frequency loads, but for the tower base, the WF response is significantly larger for Spar6. A possible explanation is that Spar6 has larger WF-related RNA accelerations, due to the larger restoring in pitch. Other sections at the platform and tower show similar trends, but with lower amplitudes.

The same load cases were also analyzed without including the QTFs, thus neglecting second-order wave loads. The difference in the weighted sectional fatigue damage shown in Fig. 11 was within 0.8% for the platform sections and 0.3% for the tower sections.

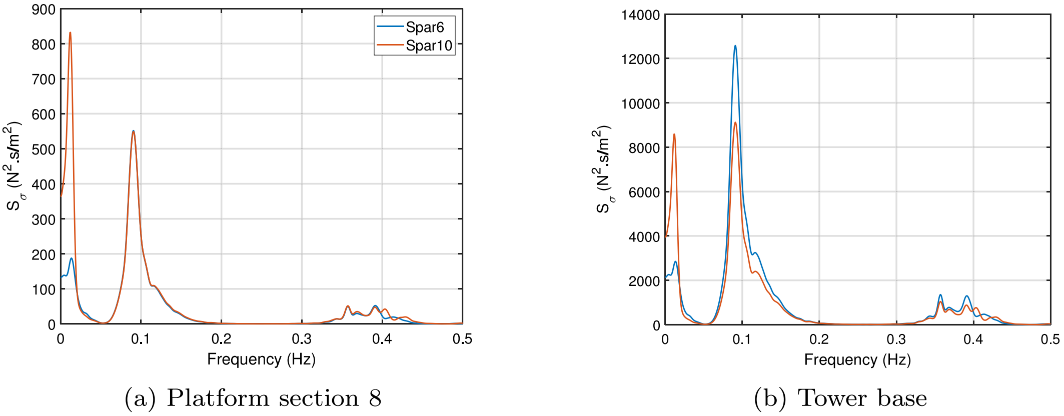

(a) Platform section 8

(b) Tower base

Fig. 13. Axial stress PSD for platform section 8 and tower base - U = 20.0 m/s, H_s = 3.4 m, T_p = 8.7 s.

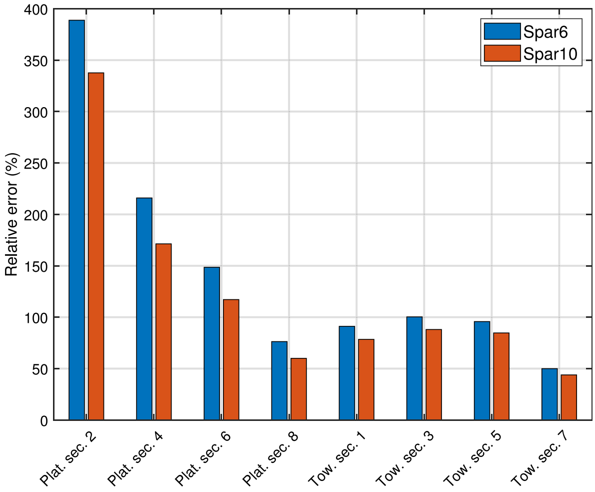

Fig. 14. Relative error in the fatigue damage obtained with the Morison formulation, compared with distributed potential theory, for Spar6 and Spar10.

6.3.1. Alternative hydrodynamic modeling with Morison formulation

Spar6 and Spar10 are also modeled with a pure Morison formulation [33], for comparison against distributed potential theory in the fatigue analysis. The same drag coefficient is used for the viscous term, while an added mass coefficient C_a = 1.0 is adopted for the inertial term. Compared to potential theory, this approach neglects near-field diffraction, resulting in overestimated loads for shorter wave lengths.

Fig. 14 shows the relative error in the weighted fatigue damage, when Morison formulation is adopted, compared with distributed potential theory. Morison formulation clearly overestimates the damage for both designs, for both the platform and tower. In Fig. 15 the power spectral density of the bending moment, at the platform section 8, is shown for Spar6 modeled with both methods. The load case corresponds to mean wind speed of 20.0 m/s, with H_s = 3.89 m and T_p = 11.1 s. Near the peak wave frequency the moment is just slightly overestimated by Morison formulation, while the excitation from the shortest waves is amplified close to the tower 1st fore-aft bending frequency, leading to the overestimation of the fatigue damage.

6.4. Extreme analysis

The different constraints in the static pitch angle under rated thrust have significant impact on the extreme dynamics, and thus sectional stresses. Fig. 16 shows the extreme platform pitch angle and nacelle acceleration, for the three spars. The extreme pitch for Spar6 is 3.0° above the static value, while for Spar10 the increase is 4.0°– resulting in a total of 14°. The extreme nacelle acceleration for Spar6, on the other hand, is only 18% larger than for Spar10.

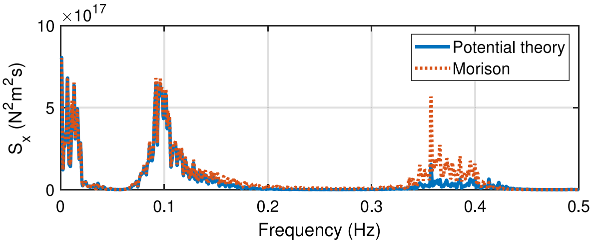

Fig. 15. Power density spectrum of bending moment at platform section 8, for Spar6, modeled with distributed potential theory and full Morison formulation. U = 20.0 m/s H_s = 3.89 m, T_p = 11.1 s.

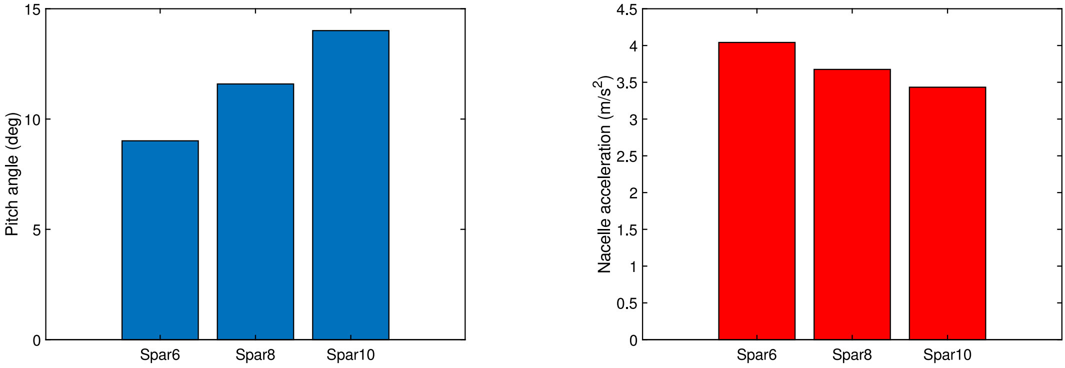

(a) Pitch angle (b) Nacelle acceleration

Fig. 16. Extreme platform pitch angle and nacelle acceleration.

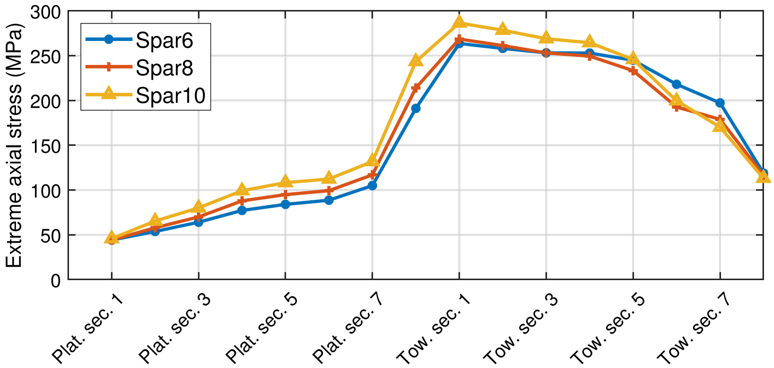

Fig. 17. Overall extreme sectional load along the length of the spars.

The extreme axial stresses along the platform and tower of all spars are shown in Fig. 17. The designs with largest static pitch angle are in general the ones with the largest extremes — except closer to the tower top, where Spar6 has the highest value. The largest differences between Spar6 and Spar10 are at the platform section 8 and at the tower base. When second-order wave loads were neglected, the difference in the extreme stresses was less than 1.3% for the platform, and less than 4.0% for the tower.

The load cases associated with the extreme stresses are shown in Table 12. For both the platform and tower, the extremes for all designs correspond to either the rated or the 50-year wind speeds — but never to conditions at the cut-off contour. For Spar6, the condition associated with 50-year wind governs the extremes at some platform sections, while for Spar8 and Spar10 all the platform extremes are associated with the rated wind speed. For the tower base, load cases at the 50-year contour govern the extremes for all designs, but for other sections along the tower the conditions associated with rated wind can be associated with the extreme loads.

Table 12
Load cases associated with extreme sectional stresses for each platform (ID as defined in Table 7).

		Spar6	Spar8	Spar10
Platform	Sec. 1	i-50	v-rt	v-rt
	Sec. 2	v-rt	v-rt	v-rt
	Sec. 3	v-rt	v-rt	v-rt
	Sec. 4	v-rt	v-rt	v-rt
	Sec. 5	i-50	v-rt	v-rt
	Sec. 6	i-50	v-rt	v-rt
	Sec. 7	i-50	iv-rt	iv-rt
	Sec. 8	i-50	iv-rt	iv-rt
Tower	Sec. 1	i-50	i-50	i-50
	Sec. 2	v-rt	i-50	i-50
	Sec. 3	v-rt	i-50	i-50
	Sec. 4	v-rt	i-50	i-50
	Sec. 5	i-50	i-50	i-50
	Sec. 6	i-50	i-50	i-50
	Sec. 7	i-50	i-50	i-50
	Sec. 8	i-50	iv-rt	iv-rt

The relative importance of each contour for the different designs is also illustrated in Fig. 18, which shows the extreme axial stresses obtained with rated, cut-off, and 50-year wind speed, and associated sea states. For the platform sections, the different designs affect extreme loads at rated more significantly, due to the mean stress associated with the pitch angle at rated. For the tower, the extreme loads associated with the 50-year contour are also significantly affected by the design.

For a better understanding of the dynamic effects leading to extreme events, the axial stress time-series can be approximated as follows:

$$\sigma_{tot} \approx \sigma_{ine} + \sigma_g + \sigma_{th} \,, \tag{22}$$

where σ_{ine} is the inertial component; σ_g is the gravitational component; and σ_{th} is the component associated with the thrust. σ_{ine} is obtained from the acceleration time-series multiplied by the structural mass above the sections considered, while for σ_g the time-varying compression force and bending moments due to the structural weight are used. The thrust multiplied by the distance to the section is considered for obtaining σ_{th}.

Fig. 19 shows the axial stress reconstructed according to Eq. (22), for Spar6 and Spar10. Good agreement is obtained with the actual stresses, which are indicated by the dotted lines in the top subfigures. The time window shown for the platform section 8 (Fig. 19a) is extracted from a rated condition, and it is seen that the main difference is on the LF-varying gravitational component — indicating that wind loads govern the extremes at this section. For the tower base (Fig. 19b), the time window relates to a condition associated with 50-year wind. In this case, the largest differences are also observed for the gravitational component, but due to variations at the wave frequency.

7. Conclusion

In this paper, three 20 MW spar FWTs are designed and compared in terms of global dynamics and structural loading along the platform and tower. The designs differ regarding the static platform pitch angle at rated wind speed, θ_r. The entire structure is modeled as elastic, and hydrodynamic loads are distributed over the platform with a combination of potential theory and quadratic drag terms. A control system with a motion compensation strategy is adopted, avoiding the use of detuned controllers. Structural performance is assessed in terms of fatigue damage and extreme axial stresses at sections over the platform and tower length.

The constraint in θ_r results in designs with distinct platform dynamics. This affects the relative contribution of inertial- and gravity-related structural loads due to the platform responses to wind and wave loads, resulting in different performance with respect to fatigue damage and extreme loads. The pitch natural periods, in general, are significantly longer than for published spar FWTs with 5 MW [46] and 10 MW [21] turbines — reaching 49.1 s for the design with $\theta_r = 10°$.

One of the consequences of the long natural period in pitch is the inadequacy of a detuned control system, which would require an excessively low controller bandwidth, leading to unrealistic motions, structural loads, and power quality. In addition, for large FWTs the relative importance of low-frequency motions to those associated with waves increases — which also favors the use of a controller with LF motion compensation. The adoption of a motion compensation strategy, based on modifying the reference rotor speed according to the nacelle velocity, proved to be a simple and effective solution for keeping a realistic controller bandwidth, while still providing aerodynamic damping to the pitch motions. Future research within structural analysis of large FWTs should avoid the use of detuned controllers. In addition, the adoption of peak shaving also showed to be beneficial, since the extreme loads are in general associated with rated wind speed.

Fatigue damage was largest for platform sections closer to SWL, and also to the tower base – a similar pattern to what was previously obtained for an optimized 10 MW spar [21]. For the platform, the largest damage was observed for designs with larger θ_r; for the tower, larger restoring in pitch (i.e., lower θ_r) resulted in increased fatigue damage, and the discrepancy in damage for

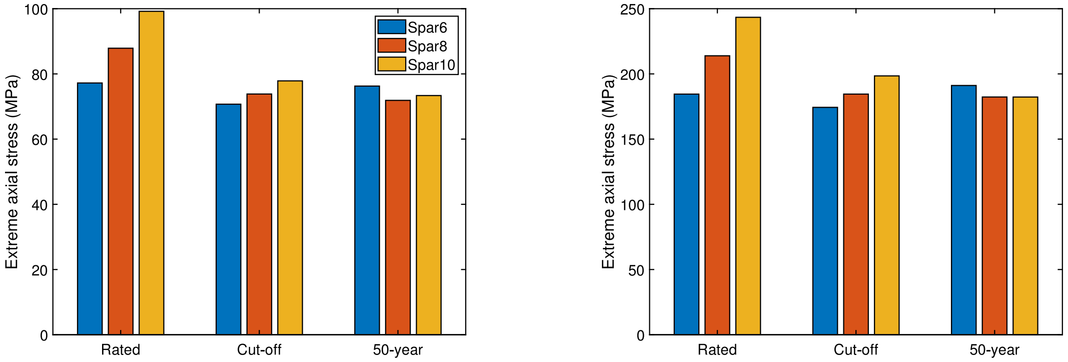

(a) Platform section 4 (b) Platform section 8

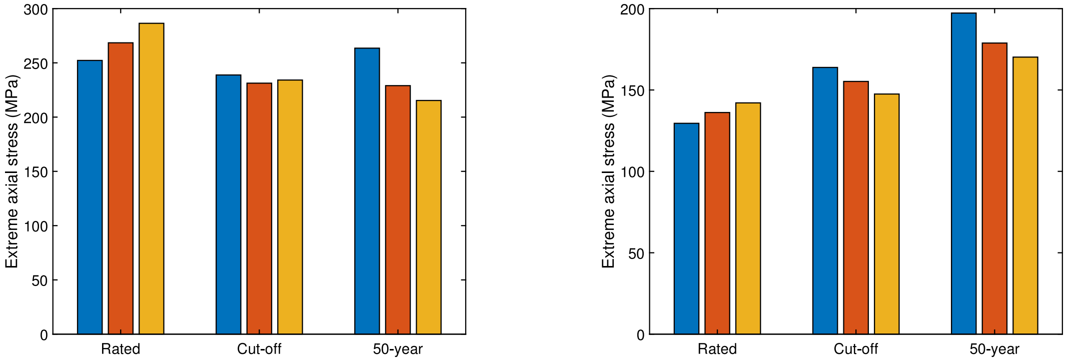

(c) Tower section 1 (base) (d) Tower section 7

Fig. 18. Extreme axial stresses at selected platform and tower sections.

the different designs increased with the wind speed. Spectral analysis of the axial stress at the tower base, for a load case near cut-off, showed increased response at wave-frequency range for Spar6 than for Spar10, suggesting larger influence of inertial loads associated with the tower top mass.

The comparison between distributed potential theory with Morison formulation confirms the results from Engebretsen et al. [18], in that Morison formulation over-predicts the fatigue damage significantly. The overestimation is higher for the design with larger restoring in pitch. The discrepancy is related to diffraction effects, and seems to be strongly associated with excitation of the 1st tower bending frequency by short-length waves. For a cylindrical structure like a spar, the MacCamy–Fuchs formulation is expected to provide similar results as those obtained with potential theory.

For the analyses of extreme responses and axial stresses, the modified environmental contour method (MECM) proposed by Li et al. [23] was adopted, including 50-year contours associated with rated and cut-off wind speeds, as well as the 50-year wind condition. An extreme dynamic pitch angle of 7° was obtained for Spar6, while for Spar10 it reached 14°. Nacelle acceleration, on the other hand, was 18% higher for Spar6 than for Spar10.

Regarding the axial stress, the largest extreme values were observed at the platform sections at SWL and at tower base, and for the designs with largest θ_r. The extreme axial stresses resulted from contours associated with both rated and 50-year wind speed, depending on the platform design and location of the platform/tower section. An analysis separating the relative contribution of inertial-, gravity-, and thrust-related loads showed that the difference in extreme loads between the different designs was mainly caused by the moments associated with RNA weight.

Difference-frequency second-order wave loads had limited effects on fatigue damage (0.3% for the platform and 0.8% for the tower), and small effects on the extreme stresses, (within 1.3% for the platform and 4.0% for the tower).

Previous research for 5 MW wind turbines [22,23] discarded the relevance of conditions at rated wind for extreme load analysis. The presented results confirm the need to include them in the extreme analysis of larger FWTs. The analysis also suggests that the static pitch angle under rated wind speed has large influence on fatigue damage and extreme motions and stresses. A similar study at the initial design phase of FWTs can be helpful in limiting the range of this variable, and thus reducing the design space.

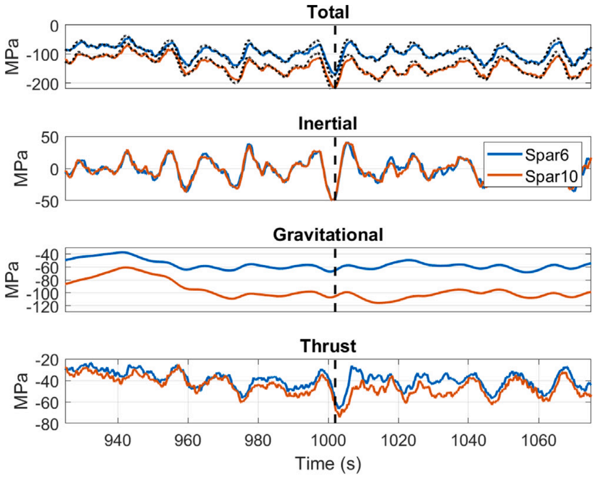

(a) Platform section 8 – $H_s = 7.3$ m, $T_p = 13.0$ s, $U = 10.7$ m/s

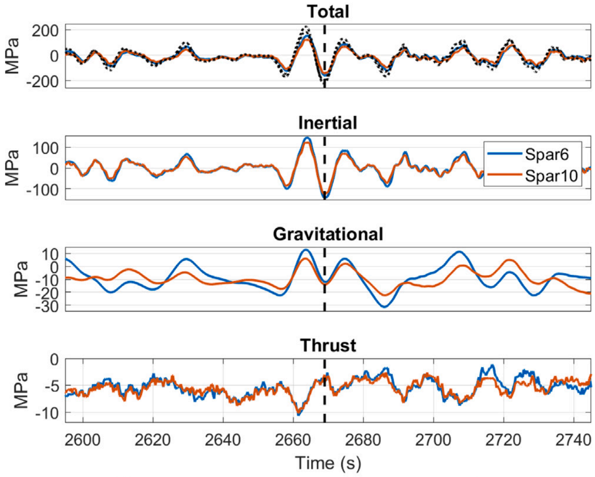

(b) Tower base – $H_s = 14.0$ m, $T_p = 15.1$ s, $U = 49.1$ m/s

Fig. 19. Axial stress components at spar section 8 (rated) and tower base (50-year condition), reconstructed according to Eq. (22). The dotted lines on the top plots represent the original stress time series, and the vertical dashed lines indicate the instant corresponding to the extreme stress.

Declaration of competing interest

One or more of the authors of this paper have disclosed potential or pertinent conflicts of interest, which may include receipt of payment, either direct or indirect, institutional support, or association with an entity in the biomedical field which may be perceived to have potential conflict of interest with this work. For full disclosure statements refer to https://doi.org/10.1016/j.marstruc.2022.103182. The first author, Carlos Eduardo Silva de Souza, is currently employed at the research institute that develops and maintains the software used for time-domain simulations (SIMA) in the paper.

Acknowledgments

The authors are sincerely grateful to the financial support from the Department of Marine Technology of the Norwegian University of Science and Technology, the Centre for Autonomous Marine Operations and Systems, Norway (Norwegian Research Council project 223254), and SFI BLUES, Norway (NFR project 309281).

References

[1] State of Maine. FAQs: Gulf of Maine floating offshore wind research array. 2020, [Online; accessed 17-September-2021].

[2] Equinor. Hywind Tampen: the world's first renewable power for offshore oil and gas. 2021, Online; accessed 2021-09-05.
[3] Principle Power. Projects - Principle Power, Inc.. 2021, [Online; accessed 17-September-2021].
[4] General Electrics. Haliade-X offshore wind turbine - The world's most powerful offshore turbine built today. 2021, Online; accessed 2021-09-05.
[5] MingYang Smart Electric. Leading innovation: MingYang Smart Energy launches MySE 16.0-242, the world's largest offshore Hybrid Drive wind turbine. 2021, Online; accessed 2021-09-05.
[6] Ashuri T, Martins JRRA, Zaaijer MB, van Kuik GAM, van Bussel GJW. Aeroservoelastic design definition of a 20 MW common research wind turbine model. Wind Energy 2016;19(11):2071–87, we.1970.
[7] Jensen PH, Chaviaropoulos T, Natarajan A, Rasmussen F, Madsen HA, Jamieseon P, Wingerden JW, Riziotis V, Barlas A, Polinder H, Abrahamsen AB, Powell D, Zinderen GJ, Kaufer D, Shirzadeh R, Armendariz JA, Voutsinas S, Manjock A, Paulsen US, DObbin J, Potestio S. LCOE reduction for the next generation offshore wind turbines - outcomes from the INNWIND.EU project. tech. rep., INNWIND.EU; 2017.
[8] Sartori L, Bellini F, Croce A, Bottasso C. Preliminary design and optimization of a 20MW reference wind turbine. J Phys Conf Ser 2018;1037:042003.
[9] Qin CC, Loth E, Zalkind DS, Pao LY, Yao S, Griffith DT, Selig MS, Damiani R. Downwind coning concept rotor for a 25 MW offshore wind turbine. Renew Energy 2020;156:314–27.
[10] Yao S, Chetan M, Griffith DT, Mendoza ASE, Selig MS, Martin D, Kianbakht S, Johnson K, Loth E. Aero-structural design and optimization of 50 MW wind turbine with over 250 m blades. Wind Eng 2021;July 2021:1–23.
[11] Jonkman J, Butterfield S, Musial W, Scott G. Definition of a 5-MW reference wind turbine for offshore system development. Tech. Rep. NREL/TP-500-38060, Colorado, United States: National Renewable Energy Laboratory; 2009.
[12] Bak C, Zahle F, Bitsche R, Kim T, Yde A, Henriksen LC, Natarajan A, Hansen MH. Description of the DTU 10 MW reference wind turbine. Tech. Rep. DTU Wind Energy Report-I-0092, DTU Wind Energy; 2013.
[13] Veers P, Dykes K, Lantz E, Barth S, Bottasso CL, Carlson O, Clifton A, Green J, Green P, Holttinen H, Laird D, Lehtomäki V, Lundquist JK, Manwell J, Marquis M, Meneveau C, Moriarty P, Munduate X, Muskulus M, Naughton J, Pao L, Paquette J, Peinke J, Robertson A, Rodrigo JS, Sempreviva AM, Smith JC, Tuohy A, Wiser R. Grand challenges in the science of wind energy. Science 2019;366(6464). eaau2027.
[14] Svendsen K. Structural design and dynamic analysis of a tension leg platform wind turbine, considering elasticity in the hull (Master's thesis), Norwegian University of Science and Technology / TU Delft; 2016.
[15] Borg M, Hansen AM, Bredmose H. Floating substructure flexibility of large-volume 10MW offshore wind turbine platforms in dynamic calculations. J Phys Conf Ser 2016;753(8).
[16] Luan C, Gao Z, Moan T. Development and verification of a time-domain approach for determining forces and moments in structural components of floaters with an application to floating wind turbines. Mar Struct 2017;51:87–109.
[17] Hegseth JM, Bachynski EE, Karimirad M. Comparison and validation of hydrodynamic load models for a semi-submersible floating wind turbine. In: Proocedings of the ASME 2018 37th international conference on ocean, offshore and arctic engineering. 2018.
[18] Engebretsen E, Haslum H, Aagaard O. Distributed potential theory and its application for spar-type floating offshore wind turbines. In: Proceedings of the ASME 2020 39th international conference on ocean, offshore and arctic engineering (Virtual conference), 2020.
[19] Kvittem MI. Modelling and response analysis for fatigue design of a semi-submersible wind turbine (Ph.D. thesis), Trondheim, Norway: Norwegian University of Science and Technology; 2014.
[20] Kvittem MI, Moan T. Time domain analysis procedures for fatigue assessment of a semi-submersible wind turbine. Mar Struct 2015;40(Supplement C):38–59.
[21] Hegseth JM, Bachynski EE, Martins JR. Integrated design optimization of spar floating wind turbines. Mar Struct 2020;72:102771.
[22] Karimirad M, Moan T. Extreme dynamic structural response analysis of catenary moored spar wind turbine in harsh environmental conditions. J Offshore Mech Arct Eng 2011;133(4):041103.
[23] Li Q, Gao Z, Moan T. Modified environmental contour method to determine the long-term extreme responses of a semi-submersible wind turbine. Ocean Eng 2017;142:563–76.
[24] Nielsen F, Hanson T, Skaare B. Integrated dynamic analysis of floating offshore wind turbines. In: Proceedings of the ASME 2016 25th international conference on offshore mechanics and arctic engineering. 2006.
[25] Larsen TJ, Hanson TD. A method to avoid negative damped low frequent tower vibrations for a floating, pitch controlled wind turbine. J Phys Conf Ser 2007;75:012073.
[26] Jonkman JM. Influence of control on the pitch damping of a floating wind turbine. In: Proceedings of the ASME wind energy symposium. 2008.
[27] Skaare B, Hanson TD, Nielsen FG. Importance of control strategies on fatigue life of floating wind turbines. In: Proceedings of the ASME 2007 26th international conference on ocean, offshore and arctic engineering. 2007, p. 493–500.
[28] Lackner MA. An investigation of variable power collective pitch control for load mitigation of floating offshore wind turbines. Wind Energy 2013;16(4):519–28.
[29] Hegseth JM, Bachynski EE, Martins JRRA. Design optimization of spar floating wind turbines considering different control strategies. J Phys Conf Ser 2020;1669:012010.
[30] Hsu C-G. Substructure models for dynamic analysis of floating wind turbines and the effect of hull flexibility (Master's thesis), Norwegian University of Science and Technology / TU Delft; 2019.
[31] DNV-GL. Design of floating wind turbine structures (DNVGL-ST-0119). DNV-GL AS; 2018.
[32] LKAB Minerals AB. High density concrete. 2019.
[33] Faltinsen O. Sea loads on ships and offshore structures. Cambridge ocean technology series, Cambridge University Press; 1993.
[34] Newman J. Marine hydrodynamics. The Massachusetts Institute of Technology; 1977.
[35] NREL. Rosco. Version 1.0.0. 2020.
[36] Skaare B, Nielsen FG, Hanson TD, Yttervik R, Havmøller O, Rekdal A. Analysis of measurements and simulations from the Hywind Demo floating wind turbine. Wind Energy 2015;18(6):1105–22.
[37] Lenfest E, Goupee A, Wright A, Abbas N. Tuning of nacelle feedback gains for floating wind turbine controllers using a two-dof model. In: Proocedings of the ASME 2020 39th international conference on ocean, offshore and arctic engineering. 2020.
[38] Fischer B, Shan M. A survey on control methods for the mitigation of tower loads. Tech. Rep. Project report 01/104256, Kassel, Germany: Fraunhofer-institute for wind energy and energy systems technology, IWES; 2013.
[39] Borg M, Bredmose H, Hansen AM. Elastic deformations of floaters for offshore wind turbines: dynamic modelling and sectional load calculations. In: Proceedings of the ASME 2017 36th international conference on ocean, offshore and arctic engineering. 2017.
[40] Hegseth JM, Bachynski EE. A semi-analytical frequency domain model for efficient design evaluation of spar floating wind turbines. Mar Struct 2019;64:186–210.
[41] Ormberg H, Larsen K. Coupled analysis of floater motion and mooring dynamics for a turret-moored ship. Appl Ocean Res 1998;20(1):55–67.
[42] SINTEF OCEAN. RIFLEX - Theory manual. 2016.
[43] Hansen M. Aerodynamics of wind turbines. Earthscan; 2013.
[44] SINTEF OCEAN. SIMO - Theory manual. 2016.
[45] Cook R. Concepts and applications of finite element analysis. 4th ed.. Wiley; 2001.
[46] Jonkman J. Definition of the floating system for phase IV of OC3. Tech. Rep. NREL/TP-500-47535, Colorado, United States: National Renewable Energy Laboratory; 2010.

[47] WAMIT. WAMIT user manual. Chestnut Hill, United States; 2006.
[48] Cummins WE. The impulse response and ship motions. In: Symposium on ship theory. 1962.
[49] Ogilvie TF. Recent progress toward the understanding and prediction of ship motions. tech. rep., Washington D.C., USA: David W. Taylor Model Basin; 1964.
[50] Taghipour R, Perez T, Moan T. Hybrid frequency–time domain models for dynamic response analysis of marine structures. Ocean Eng 2008;35(7):685–705.
[51] DNV. Environmental conditions and environmental loads (DNV-RP-C205). Det Norske Veritas; 2010.
[52] Simos AN, Ruggeri F, Watai RA, Souto-Iglesias A, Lopez-Pavon C. Slow-drift of a floating wind turbine: An assessment of frequency-domain methods based on model tests. Renew Energy 2018;116(Part A):133–54.
[53] Newman J. Second-order, slowly-varying forces on vessels in irregular waves. Tech. Rep. MIT Paper 19, Cambridge, United States: Massachusetts Institute of Technology; 1974.
[54] Li L, Gao Z, Moan T. Joint environmental data at five European offshore sites for design of combined wind and wave energy devices. In: Proceedings of the ASME 2013 32nd international conference on ocean, offshore and arctic engineering. 2013.
[55] Jonkman BJ, Kilcher L. TurbSim user's guide: version 1.06.00. tech. rep., National Renewable Energy Laboratory; 2012.
[56] IEC. Wind energy generation systems – Part 3-2 Design requirements for floating offshore wind turbines. International Electrotechnical Commission; 2019.
[57] DNV. Fatigue design of offshore steel structures (DNV-RP-C203). Det Norske Veritas; 2011.
[58] WAFO-group. WAFO - A matlab toolbox for analysis of random waves and loads - A tutorial for version 2017. Lund, Sweden: Math. Stat., Center for Math. Sci., Lund Univ.; 2017.

Publication C.1

Frequency-dependent aerodynamic damping and inertia in linearized dynamic analysis of floating wind turbines

Carlos Eduardo Silva de Souza, John Marius Hegseth, Erin E. Bachynski

Journal of Physics: Conference Series (2020), 1452: 012040. Presented at the NAWEA WindTech 2019 Conference (Amherst, USA).

Frequency-Dependent Aerodynamic Damping and Inertia in Linearized Dynamic Analysis of Floating Wind Turbines

Carlos Eduardo S Souza, John Marius Hegseth and Erin E Bachynski

Department of Marine Technology, Norwegian University of Science and Technology, 7491 Trondheim, Norway

E-mail: `carlos.souza@ntnu.no`

Abstract. In frequency-domain (FD) models of floating wind turbines (FWT), it is common to regard the interaction between nacelle motions and thrust by means of a constant aerodynamic damping coefficient. This approach is effective at higher motions frequencies, but does not consider interactions between nacelle motions and the blade pitch control system. As a result, the motions and loads at frequencies closer to the controller bandwidth may be underpredicted. A remedy for this problem is to include the linearized thrust expression in the FD model, such that the dynamic effects related to control are considered. In this paper, these dynamic effects are related to frequency-dependent damping and inertia terms. Expressions for damping and inertia coefficients are obtained with two different methods, and then included in the FD model. The resulting responses are compared to those obtained with the constant damping coefficient method, and also with coupled time-domain simulations of a semi-submersible 10 MW FWT. The better performance of the FD model with frequency-dependent inertia and damping coefficients encourages the adoption of the linearized thrust approach for representing the interaction between nacelle motions, thrust and control system.

1. Introduction

Frequency-domain (FD) methods can be helpful in the design of floating wind turbines (FWTs), providing responses for a large number of loading conditions with relatively low computational time. Previous work has indicated that the response of FWTs in moderate environmental conditions may be estimated reasonably well using FD models [1, 2, 3]. However, their reliability depends on an accurate prediction of loads and interactions with linearized models.

An especially interesting interaction takes place between nacelle motions and the rotor thrust. Fluctuations in the nacelle's horizontal velocity provoke changes in the flow through the rotor, leading to oscillations in the rotor speed and thrust. An aerodynamic damping effect results from this interaction, and is normally included in FD models by means of a constant aerodynamic damping coefficient. This coefficient may be obtained from the thrust derivative w.r.t. the relative wind speed [1, 3, 4], or by means of decay simulations of the FWT under different incident wind speeds [2].

This method is convenient to implement due to its relative simplicity, and is normally adopted in combination with the frequency-dependent thrust obtained for a fixed wind turbine, installed on the top of the tower. A disadvantage of this approach is that the interactions of the nacelle motions with the blade pitch control system are not considered, an effect that is known to reduce the damping or even render it negative [5, 6, 7], besides introducing an inertia effect [8]. As a consequence, the damping effect can be significantly overpredicted at frequencies close to the controller bandwidth, if the constant coefficient is used.

Control system effects can be included in an FD model by means of linearization of the thrust and torque. The rotor speed is then included as an additional degree of freedom, and the blade-pitch controller can be written in terms of the system states [9].

The objective of the present work is to relate the linearized thrust equations to the above-mentioned inertia and damping effects, providing a visualization of how those effects vary with wind speed and frequency for a given control system.

The aerodynamic inertia and damping coefficients are calculated both from the linearized thrust equations and from simulations where the nacelle is forced to oscillate with different frequencies, under uniform wind. The obtained coefficients are then included in an FD model of a semi-submersible 10 MW FWT. The responses predicted with the different methods for obtaining the coefficients are compared to coupled time-domain simulations, where the thrust is calculated with the blade element momentum (BEM) theory.

Section 2 presents the frequency domain model for the FWT; Section 3 introduces the thrust linearization procedure and provides formulations for the frequency-dependent aerodynamic inertia and damping coefficients; the time-domain simulations are explained in Section 4, and the results are presented in Section 5; final discussions and conclusions are provided in Section 6.

2. Frequency-domain analysis of FWT

The frequency domain model used in the present work consists of three degrees-of-freedom (DOFs), namely surge, heave, and pitch. The potential-theory hydrodynamic model is the same as the one adopted in the time-domain simulations, presented in Section 4. Viscous excitation is neglected, but viscous damping on the platform is added using stochastic linearization of the drag term in Morison's equation, where the standard deviation of the velocity along the length of the columns and pontoons is found using an iteration scheme.

The stiffness matrix includes both hydrostatic restoring and linearized mooring forces. The mooring stiffness matrix is a function of the mean offset, based on static equilibrium between mooring forces and mean thrust.

Transfer functions from wind speed to thrust force, $F_{UT}(\omega)$, are obtained for each mean wind speed as the squared root of the ratio between the spectrum of thrust time series, obtained from simulations with turbulent wind on a fixed turbine, and the incoming wind spectrum. The wind force vector is then found as

$$\mathbf{F}_U(\omega) = [F_{UT}(\omega) \quad 0 \quad z_{hub}F_{UT}(\omega)]^\top \ , \tag{1}$$

where z_{hub} is the hub height above still water level (SWL). Transfer functions from wave and wind input to platform response, $\mathbf{H}_{\zeta X}(\omega)$ and $\mathbf{H}_{UX}(\omega)$ respectively, are expressed as

$$\mathbf{H}_{\zeta X}(\omega) = \mathbf{H}_{FX}(\omega)\mathbf{F}_\zeta(\omega), \ \mathbf{H}_{UX}(\omega) = \mathbf{H}_{FX}(\omega)\mathbf{F}_U(\omega)\,, \tag{2}$$

where

$$\mathbf{H}_{FX}(\omega) = \left[-\omega^2(\mathbf{M} + \mathbf{A}(\omega)) + i\omega\mathbf{B}(\omega) + \mathbf{K}\right]^{-1} \tag{3}$$

is the frequency response function matrix. After solving for the platform motions, the tower base bending moment response is found by considering dynamic equilibrium.

Using the wind and wave spectra, the response spectrum for an arbitrary response parameter ξ is then expressed as

$$S_\xi(\omega) = |H_{\zeta\xi}(\omega)|^2 S_\zeta(\omega) + |H_{U\xi}(\omega)|^2 S_U(\omega)\,. \tag{4}$$

3. Aerodynamic damping and inertia effects

The FD model described in Section 2 neglects the variations in the thrust caused by the FWT motions. The interactions between thrust and FWT motions are often represented by a constant damping coefficient, which is added to the matrix $\mathbf{B}$ in equation (3). This approach neglects the controller action. When the controller is included, its effect results in frequency-dependent damping and inertia coefficients, as shown further below.

3.1. Thrust linearization without controller

A common way to calculate the aerodynamic damping in FD models [1, 4, 3] is to linearize the thrust with respect to the relative wind speed at hub height, v, at different mean incoming wind speeds, U_w, considering no change in the blade pitch angle or rotor speed. Using a first order Taylor series expansion, the thrust is then expressed as

$$T = T_0 + \frac{\partial T}{\partial v}\Delta v \,. \tag{5}$$

Let the nacelle dynamics be represented by an 1-DOF, 1^{st}-order system:

$$m\ddot{x} + c\dot{x} + kx = T \,. \tag{6}$$

Uniform, non-turbulent wind is assumed for now. Recalling that $v = U_w - \dot{x}$, it is noted that $\Delta v = v - U_w = -\dot{x}$. Replacing (5) in (6), the damping effect becomes clear:

$$m\ddot{x} + \left(c + \frac{\partial T}{\partial v}\right)\dot{x} + kx = T_0 \,, \tag{7}$$

and the coefficient, b_{aer}, can be expressed as

$$b_{aer} = \frac{\partial T}{\partial v} \,. \tag{8}$$

The damping effect estimated with this method considers the change in the steady-state thrust for a small perturbation in the uniform wind speed seen by the rotor, while neglecting the effect of the control system and rotor dynamics. Different coefficients are obtained for each incident wind velocity, but they are constant with respect to the nacelle frequency of oscillation. This method is relatively simple to use and normally provides satisfactory results when the turbine oscillates in a frequency range distant from the controller bandwidth. For lower frequencies of oscillation, interaction with the control system takes place and the damping coefficient dependence on frequency becomes more important.

3.2. Thrust linearization including controller

A more comprehensive method, which captures effects from the wind turbine controller, may be used by including the rotor speed DOF and control system in the FD model, and also linearizing the thrust with respect to rotor speed, Ω, and blade pitch angle, β:

$$T = T_0 + T_v\Delta v + T_\Omega\Delta\Omega + T_\beta\Delta\beta \,, \tag{9}$$

where the index indicates partial derivative w.r.t. the indicated variable, i.e., $A_B = \frac{\partial A}{\partial B}$. In order to find the damping coefficient, Equation (9) must be written in terms of $\dot{x}$ only. First, the aerodynamic torque, Q, is also given in its linearized version:

$$Q = Q_0 + Q_v\Delta v + Q_\Omega\Delta\Omega + Q_\beta\Delta\beta \,, \tag{10}$$

In addition, the rotor dynamics are given by

$$I_d \dot{\Omega} = Q - N_g E \,, \tag{11}$$

where I_d is the drivetrain inertia, N_g is the gear ratio and E is the electrical (generator) torque, here assumed as constant above rated wind speed. In equilibrium, $Q_0 = N_g E$, so replacing (10) in (11):

$$I_d \dot{\Omega} = Q_v \Delta v + Q_\Omega \Delta\Omega + Q_\beta \Delta\beta \,. \tag{12}$$

It is assumed that a PI controller commands the blade pitch angle, i.e.,

$$\Delta\beta = K_p \Delta\Omega + K_i \int \Delta\Omega dt \,, \tag{13}$$

where K_p and K_i are the proportional and integral controller gains. Equations (9) and (12) are now rewritten replacing $\Delta\beta$ as given in (13), and noting that $\Delta\Omega = \dot{\phi}$, where ϕ is the rotor azimuth angle:

$$T = T_0 - T_v \dot{x} + \left(T_\Omega + K_p T_\beta\right) \dot{\phi} + K_i T_\beta \phi \,, \tag{14}$$

$$I_d \ddot{\phi} - \left(Q_\Omega + K_p Q_\beta\right) \dot{\phi} - K_i Q_\beta \phi = -Q_v \dot{x} \,. \tag{15}$$

Assuming harmonic oscillation, Equation (15) can be written in the frequency domain, and the following transfer function between $x(\omega)$ and $\phi(\omega)$ is obtained:

$$\phi(\omega) = \frac{i\omega Q_v}{I_d \omega^2 + \left(Q_\Omega + K_p Q_\beta\right) i\omega + K_i Q_\beta} x(\omega) = C(\omega) x(\omega) \,. \tag{16}$$

The nacelle dynamics (Equation 6) are now written in terms of T as given in (14), and also expressed in the frequency domain, with $\phi(\omega)$ as given in (16):

$$\left\{ -m\omega^2 + i\omega c + k + \underbrace{i\omega T_v - \left[\left(T_\Omega + K_p T_\beta\right) i\omega + K_i T_\beta\right] C(\omega)}_{-\omega^2 a_{aer}(\omega) + i\omega b_{aer}(\omega)} \right\} x(\omega) = T_0 \,. \tag{17}$$

Based on the assumption that T responds harmonically to harmonic oscillations of the nacelle, the thrust can be written as a combination of terms proportional to the nacelle acceleration and velocity [8]. This assumption is further discussed in Section 3.3, but an immediate consequence is the definition of frequency-dependent, aerodynamic inertia and damping coefficients:

$$a_{aer}(\omega) = -\frac{1}{\omega^2} \operatorname{Re}\left\{ i\omega T_v - \left[\left(T_\Omega + K_p T_\beta\right) i\omega + K_i T_\beta\right] C(\omega) \right\} \tag{18}$$

$$b_{aer}(\omega) = \frac{1}{\omega} \operatorname{Im}\left\{ i\omega T_v - \left[\left(T_\Omega + K_p T_\beta\right) i\omega + K_i T_\beta\right] C(\omega) \right\} \tag{19}$$

3.3. Forced oscillations

The thrust and torque derivatives in Section 3 can be calculated analytically, based on the BEM equations, or numerically, using e.g. the central differences method. Both techniques assume that the thrust and torque respond immediately to changes in v, Ω and β, while in reality the time constants associated with rotor dynamics, aerodynamics, and control system, can be relevant when the nacelle moves at frequencies close to the controller bandwidth.

An alternative method to find the $a_{aer}(\omega)$ and $b_{aer}(\omega)$ coefficients is through simulations of forced nacelle oscillations, with aerodynamics calculated nonlinearly and under influence of

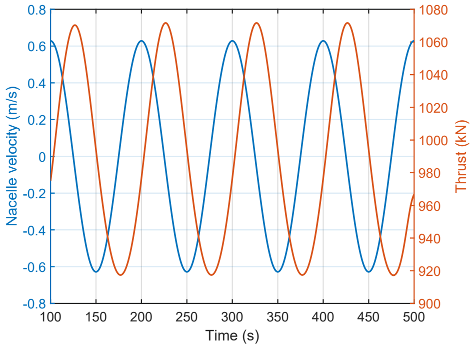

Figure 1: Thrust response to oscillations of the DTU 10 MW wind turbine, under constant incident wind speed of 13.0 m/s and period of oscillation of 100.0 s.

the control system. When the turbine oscillates harmonically, the thrust also oscillates nearly harmonically, but with a phase relative to the nacelle velocity. This can be seen in Figure 1, where the DTU 10 MW wind turbine is forced to oscillate with period 100.0 s and under constant incident wind speed of 13.0 m/s. The thrust can then be assumed to be composed of a mean plus an oscillating component:

$$T = T_0 + T_{osc}(U_w, \omega)\,. \tag{20}$$

Writing the nacelle velocity $\dot{x}$ as

$$\dot{x} = v_0 \cos(\omega t)\,, \tag{21}$$

the oscillating part of the thrust can then be assumed to be given by [8]

$$\begin{aligned} T_{osc} &= f_0 v_0 \cos(\omega t + \alpha) \\ &= f_0 \left[v_0 \cos(\omega t)\cos(\alpha) - v_0 \sin(\omega t)\sin(\alpha)\right] \\ &= f_0 \cos(\alpha)\dot{x} + \frac{f_0 \sin(\alpha)}{\omega}\ddot{x}\,. \end{aligned} \tag{22}$$

The amplifying factor f_0 and the phase α between nacelle velocity and thrust depend on the dynamic effects mentioned above, and are not straightforward to determine analytically. However, for a given turbine and control system they vary with the incident wind speed and frequency of oscillation, while motion amplitude does not seem to have a significant influence. They can therefore be obtained from forced oscillations covering the ranges of interest for both parameters. Fast Fourier transforms (FFTs) of the nacelle velocity and thrust are calculated, and f_0 and α can be directly obtained from the ratio between amplitudes or phases of both FFTs at the period of interest. Formulations for the aerodynamic inertia and damping coefficients are then directly determined from equation (23):

$$a_{aer}(U_w, \omega) = -\frac{f_0 \sin(\alpha)}{\omega}\,, \quad b_{aer}(U_w, \omega) = -f_0 \cos(\alpha)\,, \tag{23}$$

3.4. Coefficients calculation and comparison

The aerodynamic inertia and damping coefficients were obtained both from the linearized thrust and the forced oscillations method. For the former case, the thrust and torque derivatives were obtained from the linearized BEM equations. For the latter, forced oscillations of the DTU 10 MW wind turbine were performed with a simulator which obtains aerodynamic loads from AeroDyn [10], updates the blade pitch angle based on the same controller strategy presented in Section 4, and updates the rotor speed based on the rotor dynamics as in Equation (11). Oscillation periods varied from 20.0 s to 130.0 s, and uniform wind with the three velocities in Table 3 was considered. The BEM formulation with dynamic stall is adopted for the AeroDyn calculations.

The coefficients obtained with both approaches are shown in Figures 2 and 3. In spite of the oscillatory character of the curves obtained with the oscillation method, the agreement between both methods looks satisfactory, especially for higher wind velocities. The inertia effect is of the order of 1% of the mass of typical FWTs, resulting in negligible consequences for the surge dynamics. The contribution to the moment of inertia in pitch is however considerable, due to the nacelle height. Important changes in the pitch natural period can then result, as shown in [8]. The constant damping coefficients as obtained in equation (5) are also plotted in Fig. 3, showing that the discrepancy w.r.t. the frequency-dependent coefficients is larger for lower frequencies and higher wind velocities.

3.5. The aerodynamic inertia and damping effects on the FWT dynamics

It was already shown that the fluctuations in the aerodynamic thrust resulting from the nacelle motions may be treated as frequency-dependent inertia and damping effects. The derivation assumed non-turbulent wind, under the hypothesis that the fluctuations in the apparent wind flow in the rotor due to turbulence can be decoupled from those caused by the nacelle motions.

Under the same assumption, the fluctuations in the thrust due to nacelle oscillations can now be added to the FD model presented in Section 2. This is done by noting that, from Equations (22) and (23), the oscillating component of the thrust can be written as

$$T_{osc} = -a_{aer}\ddot{x} - b_{aer}\dot{x}\,. \tag{24}$$

The following aerodynamic and damping matrices, $\mathbf{A_{aer}}$ and $\mathbf{B_{aer}}$, are then defined:

$$\mathbf{A_{aer}}(\omega) = \begin{bmatrix} a_{aer}(\omega) & 0 & a_{aer}(\omega)z_{hub} \\ 0 & 0 & 0 \\ a_{aer}(\omega)z_{hub} & 0 & a_{aer}(\omega)z_{hub}^2 \end{bmatrix}, \quad \mathbf{B_{aer}}(\omega) = \begin{bmatrix} b_{aer}(\omega) & 0 & b_{aer}(\omega)z_{hub} \\ 0 & 0 & 0 \\ b_{aer}(\omega)z_{hub} & 0 & b_{aer}(\omega)z_{hub}^2 \end{bmatrix}. \tag{25}$$

$\mathbf{A_{aer}}$ and $\mathbf{B_{aer}}$ are now summed to $\mathbf{A}$ and $\mathbf{B}$ in equation (3), which includes the effect of nacelle motion in the FD analysis.

4. Simulations

The platform considered is the OO-Star 10 MW [11], a semi-submersible concept designed for the LIFES50+ project. The main properties are summarized in Table 1. The potential-theory hydrodynamic loads are generated with WADAM, and viscosity is added in form of the Morison drag term. The platform is installed at a water depth of 130.0 m, and the mooring system consists on a simplified 3-catenary line arrangement, which differs from the original of taut lines with clump weights.

The DTU 10 MW turbine (Table 2) is installed at the top of the tower, at a height of 118.4 m. The blade-pitch controller corresponds to the PI formulation of Equation (13), i.e., the power error contribution of the original controller [12] is not included. The controller gains are tuned such that its bandwidth is below the pitch natural period, and a gain scheduling strategy corrects the gains according to the current blade pitch angle.

The time-domain simulations were performed with SIMA, a workbench which allows for coupled analyses between floating bodies and slender elements [14, 15]. The platform, nacelle

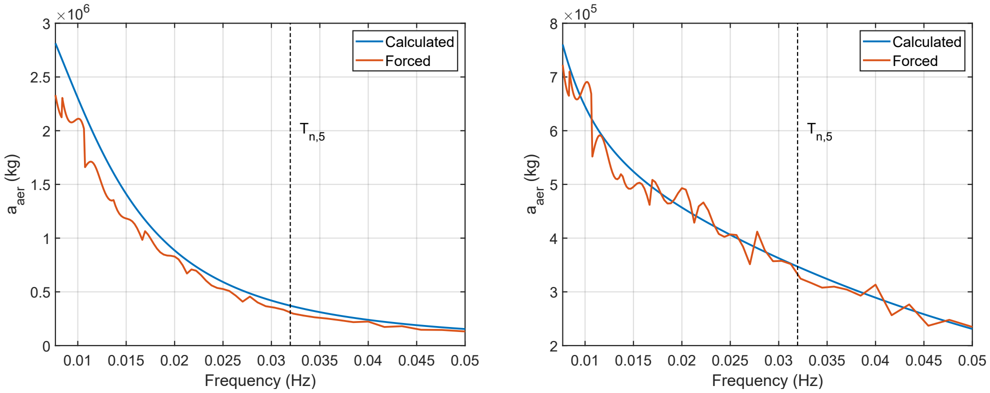

(a) $U_w = 13.0$ m/s.

(b) $U_w = 19.0$ m/s.

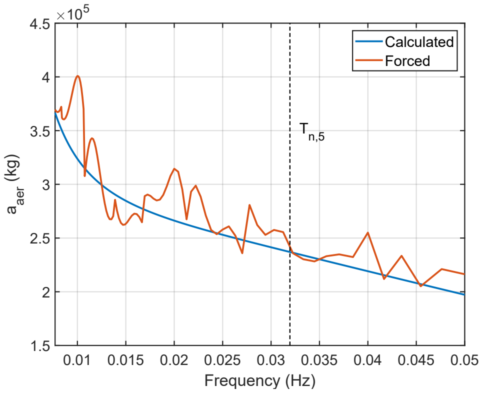

(c) $U_w = 25.0$ m/s.

Figure 2: Aerodynamic inertia coefficients, calculated with the linearized approach or obtained from the forced oscillations method.

Draft, D (m)	22.0
Total mass, m_{tot} (kg)	2.36×10^7
Center of gravity, VCG (m)	-7.9
Surge nat. per., T_1 (s)	181.8
Pitch nat. per., T_5 (s)	31.3

Table 1: Main properties of the OO-Star 10 MW FWT [11].

and hub are modeled as rigid bodies, while the blades, tower and mooring lines are modeled as flexible structures, with finite elements. The aerodynamics are based on the BEM theory, with dynamic stall and dynamic wake effects based on Øye's models [16]. Hub and tip losses are modeled with the Prandtl factor, and Glauerts correction is applied for high induction factors. The environmental conditions are listed in Table 3. Turbulent wind was generated with TurbSim [17], using the IEC Kaimal spectrum with turbulence characteristic B (moderate). A JONSWAP

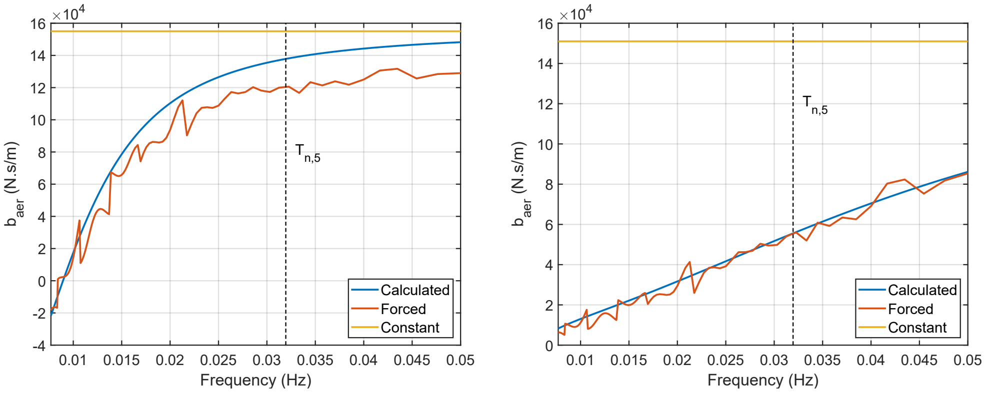

(a) $U_w = 13.0$ m/s.

(b) $U_w = 19.0$ m/s.

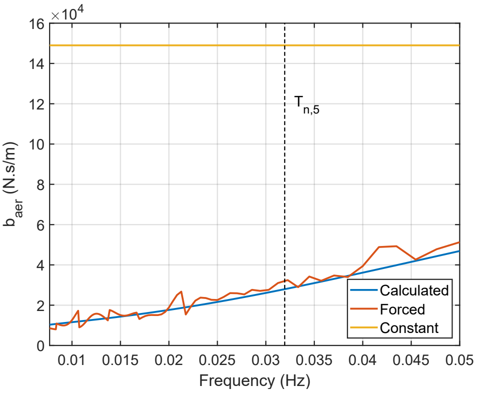

(c) $U_w = 25.0$ m/s.

Figure 3: Aerodynamic damping coefficients, calculated with the linearized approach (both constant and frequency-dependent) or obtained from the forced oscillations method.

Rotor radius, R (m)	89.2
Rated rotor speed, Ω_0 (rad/s)	1.0
Drivetrain inertia, I_d (kg.m^2)	1.6×10^8
Gear ratio, N_g (-)	50
Rotor-nacelle assemble mass, m_{RNA} (kg)	6.7×10^5
Proportional controller gain, K_p (s)	0.1794
Integral controller gain, K_i (-)	0.0165

Table 2: Main properties of the DTU 10MW wind turbine [13]. The controller gains refer to $\beta = 0°$.

wave spectrum with a γ factor of 3.3 was used to describe the sea state. The simulations lasted for one hour, which showed to provide a sufficient number of LF oscillations for the analysis. Only one realization of each condition was considered.

	U_w (m/s)	H_s (m)	T_p (s)
C1	13.0	2.7	10.3
C2	19.0	4.0	11.1
C3	25.0	5.8	12.1

Table 3: Environmental conditions.

5. Results

Figure 4 shows the frequency-domain pitch response for the three conditions in Table 3, obtained with time-domain simulations in SIMA; and with the FD model from Section 2, using the different approaches for including the aerodynamic damping and inertia effects, as presented in Section 3. When the constant damping coefficient from Equation (8) is adopted, the method is referred to as *FD constant*; with the frequency-dependent inertia and damping coefficients as given by Equations (18) and (19), the approach is named *FD calculated*; and when the coefficients are obtained from the forced harmonic oscillations, as in Equation (23), the *FD forced* identifier is adopted.

The curves indicate that the adoption of a constant damping coefficient overestimates the damping effect at lower frequencies, resulting in significantly underpredicted resonant response for frequencies below 0.05 Hz. When frequency-dependent coefficients are adopted, however, the situation is the opposite: the damping effect is underestimated, resulting in higher response for lower frequencies. Using the coefficients based on the forced oscillations leads to improved results in comparison with those obtained from the linearized thrust equations, in terms of the pitch motion standard deviation (Table 4). All three methods perform equivalently in the wave-frequency range (0.05-0.15 Hz), where the response is underpredicted due to the absence of viscous excitation in the FD model.

Similar conclusions can be obtained regarding the tower-base bending moment (Figure 5). The most remarkable difference in comparison with the plots for the pitch response is for $U_w = 13.0$ m/s (Figure 5a), which shows a persistent underprediction for all the three FD models for frequencies above 0.04 Hz. The errors in predicted tower base bending moment, shown in Table 4, are in general lower than for the pitch motion, since wave-frequency and 3p loads also influence the tower-base bending moment, and are less affected by the damping dependence of frequency. The accuracy is satisfactory for calculated and, especially, forced methods.

Figure 6 compares the low-frequency responses in pitch, for $U_w = 19.0$ m/s, when the inertia effect is included or disregarded. The FD model with damping coefficient obtained from forced oscillations is adopted, but only the blue curve includes the inertia coefficient – resulting in a peak period about 2.5 s longer then when the inertia effect is not considered.

6. Conclusion

A method was developed to illustrate the importance of including the interaction between the nacelle motions and thrust in the frequency-domain representation of a FWT. The thrust fluctuations resulting from nacelle motions can be interpreted as frequency-dependent inertia and damping effects, which challenges the traditional approach of adopting a constant aerodynamic damping coefficient.

Expressions were derived for the respective coefficients based both on a linearized expression for the thrust and on forced oscillations of a wind turbine in the time domain. The obtained coefficients were included in a 3 DOF FD model of the OOstar semi-submersible FWT. Comparisons were made between the models using a constant aerodynamic damping coefficient, the frequency-dependent inertia and damping coefficients obtained in two different ways, and

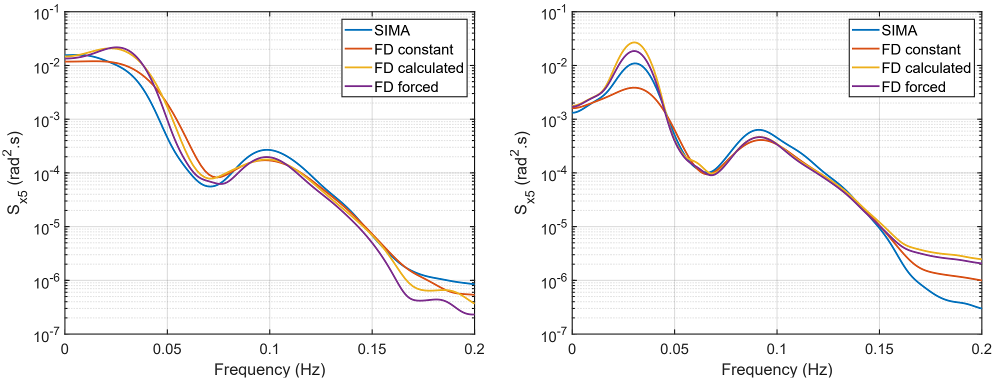

(a) $U_w = 13.0$ m/s.

(b) $U_w = 19.0$ m/s.

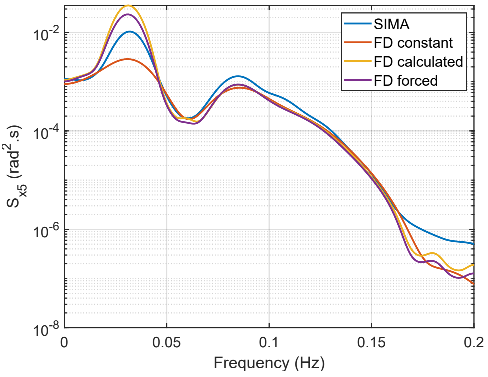

(c) $U_w = 25.0$ m/s.

Figure 4: Frequency-domain platform pitch response – comparison between SIMA simulations and frequency-domain analyses with different approaches for calculating the aerodynamic inertia and damping.

time-domain simulations. Both platform pitch motion and tower base bending moment were analyzed. It was observed that the constant damping coefficient underestimates the responses in the frequency range of the FWT surge and pitch natural frequencies.

The frequency-dependent coefficients, on the other hand, overestimated the response in the same frequency range, but are closer to the time-domain predictions. The aerodynamic inertia was shown to increase the pitch natural period by about 2.5 s, for a mean incident wind speed of 19.0 m/s. The differences between using coefficients based on the linearized thrust or on the forced oscillations were not very significant, but a slightly better agreement of the LF responses with the time-domain simulations was attained with the latter.

The introduction of inertia and damping coefficients was chosen for its didactic interest, but the adoption of a linearized thrust as in Equation (9) in a FD model is a simpler and equivalent approach to include the interaction between nacelle motion and thrust, with due consideration of controller and rotor dynamic effects.

In any case, a better agreement of the LF response should still be pursued. Other linearization

Condition	FD constant (%)	FD calculated (%)	FD forced (%)
C1	-0.2	+23.7	+21.8
C2	-24.8	+38.0	+20.0
C3	-29.6	+55.0	+30.6

Table 4: Error in pitch standard deviation compared to time domain simulations.

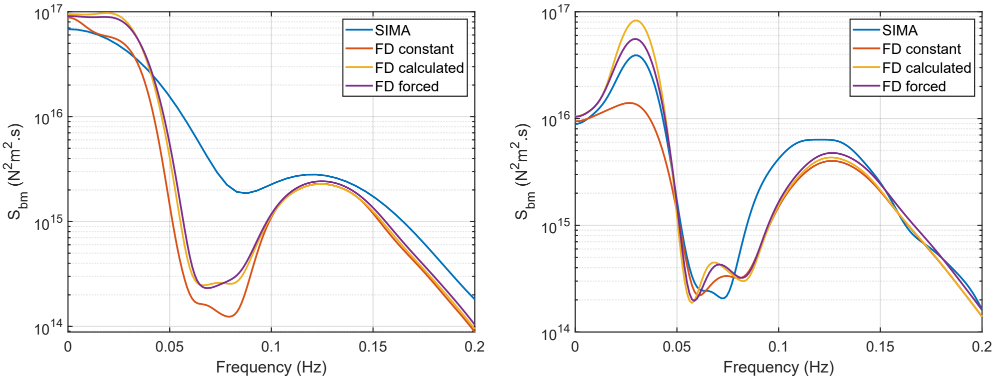

(a) $U_w = 13.0$ m/s. (b) $U_w = 19.0$ m/s.

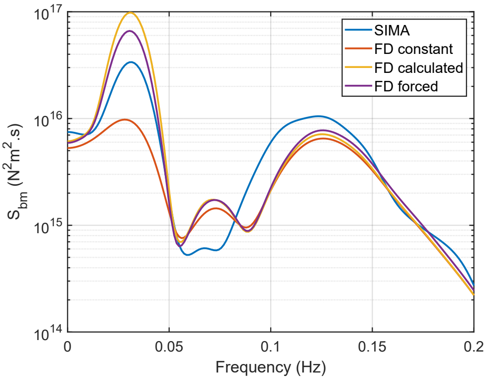

(c) $U_w = 25.0$ m/s.

Figure 5: Frequency-domain tower base bending moment – comparison between SIMA simulations and frequency-domain analyses with different approaches for calculating the aerodynamic inertia and damping.

methods could be attempted, trying to preserve effects other than those obtained with the partial derivatives of thrust and torque w.r.t. relative wind velocity, rotor speed and blade-pitch angle.

Condition	FD constant (%)	FD calculated (%)	FD forced (%)
C1	-7.1	+13.0	+10.7
C2	-29.8	+15.1	+2.9
C3	-33.0	+19.2	+5.3

Table 5: Error in tower base bending moment standard deviation compared to time domain simulations.

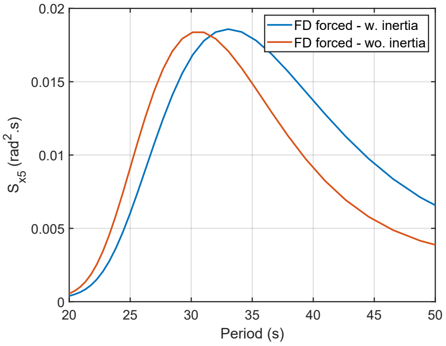

Figure 6: Pitch response estimated in the frequency domain for $U_w = 19.0$ m/s, with aerodynamic damping estimated using the forced oscillations method and with/without considering the aerodynamic inertia effect.

References

[1] Kvittem MI, Moan T. Frequency Versus Time Domain Fatigue Analysis of a Semisubmersible Wind Turbine Tower. Journal of Offshore Mechanics and Arctic Engineering. 2015 Feb;137(1):011901–011901–11. Available from: `http://dx.doi.org/10.1115/1.4028340`.

[2] Pegalajar-Jurado A, Borg M, Bredmose H. An efficient frequency-domain model for quick load analysis of floating offshore wind turbines. Wind Energy Science. 2018;3(2):693–712. Available from: `https://www.wind-energ-sci.net/3/693/2018/`.

[3] Hegseth JM, Bachynski EE. A semi-analytical frequency domain model for efficient design evaluation of spar floating wind turbines. Marine Structures. 2019;64:186 – 210. Available from: `http://www.sciencedirect.com/science/article/pii/S0951833918303149`.

[4] Bachynski EE. Design and dynamic analysis of tension leg platform wind turbines [Ph.D. thesis]. Norwegian University of Science and Technology. Trondheim, Norway; 2014.

[5] Nielsen F, Hanson T, Skaare B. Integrated dynamic analysis of floating offshore wind turbines. In: Proceedings of the ASME 2016 25th International Conference on Offshore Mechanics and Arctic Engineering; 2006. .

[6] Larsen TJ, Hanson TD. A method to avoid negative damped low frequent tower vibrations for a floating, pitch controlled wind turbine. Journal of Physics: Conference Series. 2007 jul;75:012073. Available from: `https://doi.org/10.1088%2F1742-6596%2F75%2F1%2F012073`.

[7] Jonkman JM. Influence of control on the pitch damping of a floating wind turbine. In: Proceedings of the ASME Wind Energy Symposium; 2008. .

[8] Souza CES, Bachynski EE. Changes in surge and pitch decay periods of floating wind turbines for varying wind speed. Ocean Engineering. 2019;180:223 – 237. Available from: `http://www.sciencedirect.com/science/article/pii/S0029801818315932`.

[9] Goupee AJ, Kimball RW, Dagher HJ. Experimental observations of active blade pitch and generator control influence on floating wind turbine response. Renewable Energy. 2017;104:9 – 19.

[10] Moriarty PJ, Hansen AC. AeroDyn Theory Manual. Denver, Colorado: National Renewable Energy

Laboratory; 2005. NREL/EL-500-36881.
[11] Müller K, Lemmer F, Yu W. LIFES50+ - D4.2 Public Definition of the Two LIFES50+ 10MW Floater Concepts. University of Stuttgart; 2018.
[12] Hansen MH, Henriksen LC. Basic DTU Wind Energy controller. Technical University of Denmark; 2019. DTU Wind Energy E No. 0028.
[13] Bak C, Zahle F, Bitsche R, Kim T, Yde A, Henriksen LC, et al. Description of the DTU 10 MW Reference Wind Turbine. DTU Wind Energy; 2013. DTU Wind Energy Report-I-0092.
[14] SINTEF OCEAN. RIFLEX - Theory manual; 2016.
[15] SINTEF OCEAN. SIMO - Theory manual; 2016.
[16] Hansen MOL. Aerodynamics of Wind Turbines. Earthscan; 2013.
[17] Jonkman BJ, Kilcher L. TurbSim User's Guide: version 1.06.00. National Renewable Energy Laboratory; 2012.

Appendix B

Previous PhD theses published at the Department of Marine Technology (earlier Faculty of Marine Technology)

Previous PhD theses published at the Department of Marine Technology (earlier: Faculty of Marine Technology)

NORWEGIAN UNIVERSITY OF SCIENCE AND TECHNOLOGY

Report No.	Author	Title
	Kavlie, Dag	Optimization of Plane Elastic Grillages, 1967
	Hansen, Hans R.	Man-Machine Communication and Data-Storage Methods in Ship Structural Design, 1971
	Gisvold, Kaare M.	A Method for non-linear mixed -integer programming and its Application to Design Problems, 1971
	Lund, Sverre	Tanker Frame Optimalization by means of SUMT-Transformation and Behaviour Models, 1971
	Vinje, Tor	On Vibration of Spherical Shells Interacting with Fluid, 1972
	Lorentz, Jan D.	Tank Arrangement for Crude Oil Carriers in Accordance with the new Anti-Pollution Regulations, 1975
	Carlsen, Carl A.	Computer-Aided Design of Tanker Structures, 1975
	Larsen, Carl M.	Static and Dynamic Analysis of Offshore Pipelines during Installation, 1976
UR-79-01	Brigt Hatlestad, MK	The finite element method used in a fatigue evaluation of fixed offshore platforms. (Dr.Ing. Thesis)
UR-79-02	Erik Pettersen, MK	Analysis and design of cellular structures. (Dr.Ing. Thesis)
UR-79-03	Sverre Valsgård, MK	Finite difference and finite element methods applied to nonlinear analysis of plated structures. (Dr.Ing. Thesis)
UR-79-04	Nils T. Nordsve, MK	Finite element collapse analysis of structural members considering imperfections and stresses due to fabrication. (Dr.Ing. Thesis)
UR-79-05	Ivar J. Fylling, MK	Analysis of towline forces in ocean towing systems. (Dr.Ing. Thesis)
UR-80-06	Nils Sandsmark, MM	Analysis of Stationary and Transient Heat Conduction by the Use of the Finite Element Method. (Dr.Ing. Thesis)
UR-80-09	Sverre Haver, MK	Analysis of uncertainties related to the stochastic modeling of ocean waves. (Dr.Ing. Thesis)
UR-81-15	Odland, Jonas	On the Strength of welded Ring stiffened cylindrical Shells primarily subjected to axial Compression
UR-82-17	Engesvik, Knut	Analysis of Uncertainties in the fatigue Capacity of

		Welded Joints
UR-82-18	Rye, Henrik	Ocean wave groups
UR-83-30	Eide, Oddvar Inge	On Cumulative Fatigue Damage in Steel Welded Joints
UR-83-33	Mo, Olav	Stochastic Time Domain Analysis of Slender Offshore Structures
UR-83-34	Amdahl, Jørgen	Energy absorption in Ship-platform impacts
UR-84-37	Mørch, Morten	Motions and mooring forces of semi submersibles as determined by full-scale measurements and theoretical analysis
UR-84-38	Soares, C. Guedes	Probabilistic models for load effects in ship structures
UR-84-39	Aarsnes, Jan V.	Current forces on ships
UR-84-40	Czujko, Jerzy	Collapse Analysis of Plates subjected to Biaxial Compression and Lateral Load
UR-85-46	Alf G. Engseth, MK	Finite element collapse analysis of tubular steel offshore structures. (Dr.Ing. Thesis)
UR-86-47	Dengody Sheshappa, MP	A Computer Design Model for Optimizing Fishing Vessel Designs Based on Techno-Economic Analysis. (Dr.Ing. Thesis)
UR-86-48	Vidar Aanesland, MH	A Theoretical and Numerical Study of Ship Wave Resistance. (Dr.Ing. Thesis)
UR-86-49	Heinz-Joachim Wessel, MK	Fracture Mechanics Analysis of Crack Growth in Plate Girders. (Dr.Ing. Thesis)
UR-86-50	Jon Taby, MK	Ultimate and Post-ultimate Strength of Dented Tubular Members. (Dr.Ing. Thesis)
UR-86-51	Walter Lian, MH	A Numerical Study of Two-Dimensional Separated Flow Past Bluff Bodies at Moderate KC-Numbers. (Dr.Ing. Thesis)
UR-86-52	Bjørn Sortland, MH	Force Measurements in Oscillating Flow on Ship Sections and Circular Cylinders in a U-Tube Water Tank. (Dr.Ing. Thesis)
UR-86-53	Kurt Strand, MM	A System Dynamic Approach to One-dimensional Fluid Flow. (Dr.Ing. Thesis)
UR-86-54	Arne Edvin Løken, MH	Three Dimensional Second Order Hydrodynamic Effects on Ocean Structures in Waves. (Dr.Ing. Thesis)
UR-86-55	Sigurd Falch, MH	A Numerical Study of Slamming of Two-Dimensional Bodies. (Dr.Ing. Thesis)
UR-87-56	Arne Braathen, MH	Application of a Vortex Tracking Method to the Prediction of Roll Damping of a Two-Dimension Floating Body. (Dr.Ing. Thesis)

UR-87-57	Bernt Leira, MK	Gaussian Vector Processes for Reliability Analysis involving Wave-Induced Load Effects. (Dr.Ing. Thesis)
UR-87-58	Magnus Småvik, MM	Thermal Load and Process Characteristics in a Two-Stroke Diesel Engine with Thermal Barriers (in Norwegian). (Dr.Ing. Thesis)
MTA-88-59	Bernt Arild Bremdal, MP	An Investigation of Marine Installation Processes – A Knowledge - Based Planning Approach. (Dr.Ing. Thesis)
MTA-88-60	Xu Jun, MK	Non-linear Dynamic Analysis of Space-framed Offshore Structures. (Dr.Ing. Thesis)
MTA-89-61	Gang Miao, MH	Hydrodynamic Forces and Dynamic Responses of Circular Cylinders in Wave Zones. (Dr.Ing. Thesis)
MTA-89-62	Martin Greenhow, MH	Linear and Non-Linear Studies of Waves and Floating Bodies. Part I and Part II. (Dr.Techn. Thesis)
MTA-89-63	Chang Li, MH	Force Coefficients of Spheres and Cubes in Oscillatory Flow with and without Current. (Dr.Ing. Thesis
MTA-89-64	Hu Ying, MP	A Study of Marketing and Design in Development of Marine Transport Systems. (Dr.Ing. Thesis)
MTA-89-65	Arild Jæger, MH	Seakeeping, Dynamic Stability and Performance of a Wedge Shaped Planing Hull. (Dr.Ing. Thesis)
MTA-89-66	Chan Siu Hung, MM	The dynamic characteristics of tilting-pad bearings
MTA-89-67	Kim Wikstrøm, MP	Analysis av projekteringen for ett offshore projekt. (Licenciat-avhandling)
MTA-89-68	Jiao Guoyang, MK	Reliability Analysis of Crack Growth under Random Loading, considering Model Updating. (Dr.Ing. Thesis)
MTA-89-69	Arnt Olufsen, MK	Uncertainty and Reliability Analysis of Fixed Offshore Structures. (Dr.Ing. Thesis)
MTA-89-70	Wu Yu-Lin, MR	System Reliability Analyses of Offshore Structures using improved Truss and Beam Models. (Dr.Ing. Thesis)
MTA-90-71	Jan Roger Hoff, MH	Three-dimensional Green function of a vessel with forward speed in waves. (Dr.Ing. Thesis)
MTA-90-72	Rong Zhao, MH	Slow-Drift Motions of a Moored Two-Dimensional Body in Irregular Waves. (Dr.Ing. Thesis)
MTA-90-73	Atle Minsaas, MP	Economical Risk Analysis. (Dr.Ing. Thesis)
MTA-90-74	Knut-Aril Farnes, MK	Long-term Statistics of Response in Non-linear Marine Structures. (Dr.Ing. Thesis)
MTA-90-75	Torbjørn Sotberg, MK	Application of Reliability Methods for Safety Assessment of Submarine Pipelines. (Dr.Ing.

		Thesis)
MTA-90-76	Zeuthen, Steffen, MP	SEAMAID. A computational model of the design process in a constraint-based logic programming environment. An example from the offshore domain. (Dr.Ing. Thesis)
MTA-91-77	Haagensen, Sven, MM	Fuel Dependant Cyclic Variability in a Spark Ignition Engine - An Optical Approach. (Dr.Ing. Thesis)
MTA-91-78	Løland, Geir, MH	Current forces on and flow through fish farms. (Dr.Ing. Thesis)
MTA-91-79	Hoen, Christopher, MK	System Identification of Structures Excited by Stochastic Load Processes. (Dr.Ing. Thesis)
MTA-91-80	Haugen, Stein, MK	Probabilistic Evaluation of Frequency of Collision between Ships and Offshore Platforms. (Dr.Ing. Thesis)
MTA-91-81	Sødahl, Nils, MK	Methods for Design and Analysis of Flexible Risers. (Dr.Ing. Thesis)
MTA-91-82	Ormberg, Harald, MK	Non-linear Response Analysis of Floating Fish Farm Systems. (Dr.Ing. Thesis)
MTA-91-83	Marley, Mark J., MK	Time Variant Reliability under Fatigue Degradation. (Dr.Ing. Thesis)
MTA-91-84	Krokstad, Jørgen R., MH	Second-order Loads in Multidirectional Seas. (Dr.Ing. Thesis)
MTA-91-85	Molteberg, Gunnar A., MM	The Application of System Identification Techniques to Performance Monitoring of Four Stroke Turbocharged Diesel Engines. (Dr.Ing. Thesis)
MTA-92-86	Mørch, Hans Jørgen Bjelke, MH	Aspects of Hydrofoil Design: with Emphasis on Hydrofoil Interaction in Calm Water. (Dr.Ing. Thesis)
MTA-92-87	Chan Siu Hung, MM	Nonlinear Analysis of Rotordynamic Instabilities in Highspeed Turbomachinery. (Dr.Ing. Thesis)
MTA-92-88	Bessason, Bjarni, MK	Assessment of Earthquake Loading and Response of Seismically Isolated Bridges. (Dr.Ing. Thesis)
MTA-92-89	Langli, Geir, MP	Improving Operational Safety through exploitation of Design Knowledge - an investigation of offshore platform safety. (Dr.Ing. Thesis)
MTA-92-90	Sævik, Svein, MK	On Stresses and Fatigue in Flexible Pipes. (Dr.Ing. Thesis)
MTA-92-91	Ask, Tor Ø., MM	Ignition and Flame Growth in Lean Gas-Air Mixtures. An Experimental Study with a Schlieren System. (Dr.Ing. Thesis)
MTA-86-92	Hessen, Gunnar, MK	Fracture Mechanics Analysis of Stiffened Tubular Members. (Dr.Ing. Thesis)

MTA-93-93	Steinebach, Christian, MM	Knowledge Based Systems for Diagnosis of Rotating Machinery. (Dr.Ing. Thesis)
MTA-93-94	Dalane, Jan Inge, MK	System Reliability in Design and Maintenance of Fixed Offshore Structures. (Dr.Ing. Thesis)
MTA-93-95	Steen, Sverre, MH	Cobblestone Effect on SES. (Dr.Ing. Thesis)
MTA-93-96	Karunakaran, Daniel, MK	Nonlinear Dynamic Response and Reliability Analysis of Drag-dominated Offshore Platforms. (Dr.Ing. Thesis)
MTA-93-97	Hagen, Arnulf, MP	The Framework of a Design Process Language. (Dr.Ing. Thesis)
MTA-93-98	Nordrik, Rune, MM	Investigation of Spark Ignition and Autoignition in Methane and Air Using Computational Fluid Dynamics and Chemical Reaction Kinetics. A Numerical Study of Ignition Processes in Internal Combustion Engines. (Dr.Ing. Thesis)
MTA-94-99	Passano, Elizabeth, MK	Efficient Analysis of Nonlinear Slender Marine Structures. (Dr.Ing. Thesis)
MTA-94-100	Kvålsvold, Jan, MH	Hydroelastic Modelling of Wetdeck Slamming on Multihull Vessels. (Dr.Ing. Thesis)
MTA-94-102	Bech, Sidsel M., MK	Experimental and Numerical Determination of Stiffness and Strength of GRP/PVC Sandwich Structures. (Dr.Ing. Thesis)
MTA-95-103	Paulsen, Hallvard, MM	A Study of Transient Jet and Spray using a Schlieren Method and Digital Image Processing. (Dr.Ing. Thesis)
MTA-95-104	Hovde, Geir Olav, MK	Fatigue and Overload Reliability of Offshore Structural Systems, Considering the Effect of Inspection and Repair. (Dr.Ing. Thesis)
MTA-95-105	Wang, Xiaozhi, MK	Reliability Analysis of Production Ships with Emphasis on Load Combination and Ultimate Strength. (Dr.Ing. Thesis)
MTA-95-106	Ulstein, Tore, MH	Nonlinear Effects of a Flexible Stern Seal Bag on Cobblestone Oscillations of an SES. (Dr.Ing. Thesis)
MTA-95-107	Solaas, Frøydis, MH	Analytical and Numerical Studies of Sloshing in Tanks. (Dr.Ing. Thesis)
MTA-95-108	Hellan, Øyvind, MK	Nonlinear Pushover and Cyclic Analyses in Ultimate Limit State Design and Reassessment of Tubular Steel Offshore Structures. (Dr.Ing. Thesis)
MTA-95-109	Hermundstad, Ole A., MK	Theoretical and Experimental Hydroelastic Analysis of High Speed Vessels. (Dr.Ing. Thesis)
MTA-96-110	Bratland, Anne K., MH	Wave-Current Interaction Effects on Large-Volume Bodies in Water of Finite Depth. (Dr.Ing. Thesis)
MTA-96-111	Herfjord, Kjell, MH	A Study of Two-dimensional Separated Flow by a Combination of the Finite Element Method and

		Navier-Stokes Equations. (Dr.Ing. Thesis)
MTA-96-112	Æsøy, Vilmar, MM	Hot Surface Assisted Compression Ignition in a Direct Injection Natural Gas Engine. (Dr.Ing. Thesis)
MTA-96-113	Eknes, Monika L., MK	Escalation Scenarios Initiated by Gas Explosions on Offshore Installations. (Dr.Ing. Thesis)
MTA-96-114	Erikstad, Stein O., MP	A Decision Support Model for Preliminary Ship Design. (Dr.Ing. Thesis)
MTA-96-115	Pedersen, Egil, MH	A Nautical Study of Towed Marine Seismic Streamer Cable Configurations. (Dr.Ing. Thesis)
MTA-97-116	Moksnes, Paul O., MM	Modelling Two-Phase Thermo-Fluid Systems Using Bond Graphs. (Dr.Ing. Thesis)
MTA-97-117	Halse, Karl H., MK	On Vortex Shedding and Prediction of Vortex-Induced Vibrations of Circular Cylinders. (Dr.Ing. Thesis)
MTA-97-118	Igland, Ragnar T., MK	Reliability Analysis of Pipelines during Laying, considering Ultimate Strength under Combined Loads. (Dr.Ing. Thesis)
MTA-97-119	Pedersen, Hans-P., MP	Levendefiskteknologi for fiskefartøy. (Dr.Ing. Thesis)
MTA-98-120	Vikestad, Kyrre, MK	Multi-Frequency Response of a Cylinder Subjected to Vortex Shedding and Support Motions. (Dr.Ing. Thesis)
MTA-98-121	Azadi, Mohammad R. E., MK	Analysis of Static and Dynamic Pile-Soil-Jacket Behaviour. (Dr.Ing. Thesis)
MTA-98-122	Ulltang, Terje, MP	A Communication Model for Product Information. (Dr.Ing. Thesis)
MTA-98-123	Torbergsen, Erik, MM	Impeller/Diffuser Interaction Forces in Centrifugal Pumps. (Dr.Ing. Thesis)
MTA-98-124	Hansen, Edmond, MH	A Discrete Element Model to Study Marginal Ice Zone Dynamics and the Behaviour of Vessels Moored in Broken Ice. (Dr.Ing. Thesis)
MTA-98-125	Videiro, Paulo M., MK	Reliability Based Design of Marine Structures. (Dr.Ing. Thesis)
MTA-99-126	Mainçon, Philippe, MK	Fatigue Reliability of Long Welds Application to Titanium Risers. (Dr.Ing. Thesis)
MTA-99-127	Haugen, Elin M., MH	Hydroelastic Analysis of Slamming on Stiffened Plates with Application to Catamaran Wetdecks. (Dr.Ing. Thesis)
MTA-99-128	Langhelle, Nina K., MK	Experimental Validation and Calibration of Nonlinear Finite Element Models for Use in Design of Aluminium Structures Exposed to Fire. (Dr.Ing. Thesis)
MTA-99-	Berstad, Are J., MK	Calculation of Fatigue Damage in Ship Structures.

129		(Dr.Ing. Thesis)
MTA-99-130	Andersen, Trond M., MM	Short Term Maintenance Planning. (Dr.Ing. Thesis)
MTA-99-131	Tveiten, Bård Wathne, MK	Fatigue Assessment of Welded Aluminium Ship Details. (Dr.Ing. Thesis)
MTA-99-132	Søreide, Fredrik, MP	Applications of underwater technology in deep water archaeology. Principles and practice. (Dr.Ing. Thesis)
MTA-99-133	Tønnessen, Rune, MH	A Finite Element Method Applied to Unsteady Viscous Flow Around 2D Blunt Bodies With Sharp Corners. (Dr.Ing. Thesis)
MTA-99-134	Elvekrok, Dag R., MP	Engineering Integration in Field Development Projects in the Norwegian Oil and Gas Industry. The Supplier Management of Norne. (Dr.Ing. Thesis)
MTA-99-135	Fagerholt, Kjetil, MP	Optimeringsbaserte Metoder for Ruteplanlegging innen skipsfart. (Dr.Ing. Thesis)
MTA-99-136	Bysveen, Marie, MM	Visualization in Two Directions on a Dynamic Combustion Rig for Studies of Fuel Quality. (Dr.Ing. Thesis)
MTA-2000-137	Storteig, Eskild, MM	Dynamic characteristics and leakage performance of liquid annular seals in centrifugal pumps. (Dr.Ing. Thesis)
MTA-2000-138	Sagli, Gro, MK	Model uncertainty and simplified estimates of long term extremes of hull girder loads in ships. (Dr.Ing. Thesis)
MTA-2000-139	Tronstad, Harald, MK	Nonlinear analysis and design of cable net structures like fishing gear based on the finite element method. (Dr.Ing. Thesis)
MTA-2000-140	Kroneberg, André, MP	Innovation in shipping by using scenarios. (Dr.Ing. Thesis)
MTA-2000-141	Haslum, Herbjørn Alf, MH	Simplified methods applied to nonlinear motion of spar platforms. (Dr.Ing. Thesis)
MTA-2001-142	Samdal, Ole Johan, MM	Modelling of Degradation Mechanisms and Stressor Interaction on Static Mechanical Equipment Residual Lifetime. (Dr.Ing. Thesis)
MTA-2001-143	Baarholm, Rolf Jarle, MH	Theoretical and experimental studies of wave impact underneath decks of offshore platforms. (Dr.Ing. Thesis)
MTA-2001-144	Wang, Lihua, MK	Probabilistic Analysis of Nonlinear Wave-induced Loads on Ships. (Dr.Ing. Thesis)
MTA-2001-145	Kristensen, Odd H. Holt, MK	Ultimate Capacity of Aluminium Plates under Multiple Loads, Considering HAZ Properties. (Dr.Ing. Thesis)
MTA-2001-146	Greco, Marilena, MH	A Two-Dimensional Study of Green-Water

		Loading. (Dr.Ing. Thesis)
MTA-2001-147	Heggelund, Svein E., MK	Calculation of Global Design Loads and Load Effects in Large High Speed Catamarans. (Dr.Ing. Thesis)
MTA-2001-148	Babalola, Olusegun T., MK	Fatigue Strength of Titanium Risers – Defect Sensitivity. (Dr.Ing. Thesis)
MTA-2001-149	Mohammed, Abuu K., MK	Nonlinear Shell Finite Elements for Ultimate Strength and Collapse Analysis of Ship Structures. (Dr.Ing. Thesis)
MTA-2002-150	Holmedal, Lars E., MH	Wave-current interactions in the vicinity of the sea bed. (Dr.Ing. Thesis)
MTA-2002-151	Rognebakke, Olav F., MH	Sloshing in rectangular tanks and interaction with ship motions. (Dr.Ing. Thesis)
MTA-2002-152	Lader, Pål Furset, MH	Geometry and Kinematics of Breaking Waves. (Dr.Ing. Thesis)
MTA-2002-153	Yang, Qinzheng, MH	Wash and wave resistance of ships in finite water depth. (Dr.Ing. Thesis)
MTA-2002-154	Melhus, Øyvin, MM	Utilization of VOC in Diesel Engines. Ignition and combustion of VOC released by crude oil tankers. (Dr.Ing. Thesis)
MTA-2002-155	Ronæss, Marit, MH	Wave Induced Motions of Two Ships Advancing on Parallel Course. (Dr.Ing. Thesis)
MTA-2002-156	Økland, Ole D., MK	Numerical and experimental investigation of whipping in twin hull vessels exposed to severe wet deck slamming. (Dr.Ing. Thesis)
MTA-2002-157	Ge, Chunhua, MK	Global Hydroelastic Response of Catamarans due to Wet Deck Slamming. (Dr.Ing. Thesis)
MTA-2002-158	Byklum, Eirik, MK	Nonlinear Shell Finite Elements for Ultimate Strength and Collapse Analysis of Ship Structures. (Dr.Ing. Thesis)
IMT-2003-1	Chen, Haibo, MK	Probabilistic Evaluation of FPSO-Tanker Collision in Tandem Offloading Operation. (Dr.Ing. Thesis)
IMT-2003-2	Skaugset, Kjetil Bjørn, MK	On the Suppression of Vortex Induced Vibrations of Circular Cylinders by Radial Water Jets. (Dr.Ing. Thesis)
IMT-2003-3	Chezhian, Muthu	Three-Dimensional Analysis of Slamming. (Dr.Ing. Thesis)
IMT-2003-4	Buhaug, Øyvind	Deposit Formation on Cylinder Liner Surfaces in Medium Speed Engines. (Dr.Ing. Thesis)
IMT-2003-5	Tregde, Vidar	Aspects of Ship Design: Optimization of Aft Hull with Inverse Geometry Design. (Dr.Ing. Thesis)
IMT-	Wist, Hanne Therese	Statistical Properties of Successive Ocean Wave

2003-6		Parameters. (Dr.Ing. Thesis)
IMT-2004-7	Ransau, Samuel	Numerical Methods for Flows with Evolving Interfaces. (Dr.Ing. Thesis)
IMT-2004-8	Soma, Torkel	Blue-Chip or Sub-Standard. A data interrogation approach of identity safety characteristics of shipping organization. (Dr.Ing. Thesis)
IMT-2004-9	Ersdal, Svein	An experimental study of hydrodynamic forces on cylinders and cables in near axial flow. (Dr.Ing. Thesis)
IMT-2005-10	Brodtkorb, Per Andreas	The Probability of Occurrence of Dangerous Wave Situations at Sea. (Dr.Ing. Thesis)
IMT-2005-11	Yttervik, Rune	Ocean current variability in relation to offshore engineering. (Dr.Ing. Thesis)
IMT-2005-12	Fredheim, Arne	Current Forces on Net-Structures. (Dr.Ing. Thesis)
IMT-2005-13	Heggernes, Kjetil	Flow around marine structures. (Dr.Ing. Thesis
IMT-2005-14	Fouques, Sebastien	Lagrangian Modelling of Ocean Surface Waves and Synthetic Aperture Radar Wave Measurements. (Dr.Ing. Thesis)
IMT-2006-15	Holm, Håvard	Numerical calculation of viscous free surface flow around marine structures. (Dr.Ing. Thesis)
IMT-2006-16	Bjørheim, Lars G.	Failure Assessment of Long Through Thickness Fatigue Cracks in Ship Hulls. (Dr.Ing. Thesis)
IMT-2006-17	Hansson, Lisbeth	Safety Management for Prevention of Occupational Accidents. (Dr.Ing. Thesis)
IMT-2006-18	Zhu, Xinying	Application of the CIP Method to Strongly Nonlinear Wave-Body Interaction Problems. (Dr.Ing. Thesis)
IMT-2006-19	Reite, Karl Johan	Modelling and Control of Trawl Systems. (Dr.Ing. Thesis)
IMT-2006-20	Smogeli, Øyvind Notland	Control of Marine Propellers. From Normal to Extreme Conditions. (Dr.Ing. Thesis)
IMT-2007-21	Storhaug, Gaute	Experimental Investigation of Wave Induced Vibrations and Their Effect on the Fatigue Loading of Ships. (Dr.Ing. Thesis)
IMT-2007-22	Sun, Hui	A Boundary Element Method Applied to Strongly Nonlinear Wave-Body Interaction Problems. (PhD Thesis, CeSOS)
IMT-2007-23	Rustad, Anne Marthine	Modelling and Control of Top Tensioned Risers. (PhD Thesis, CeSOS)
IMT-2007-24	Johansen, Vegar	Modelling flexible slender system for real-time simulations and control applications
IMT-2007-25	Wroldsen, Anders Sunde	Modelling and control of tensegrity structures.

		(PhD Thesis, CeSOS)
IMT-2007-26	Aronsen, Kristoffer Høye	An experimental investigation of in-line and combined inline and cross flow vortex induced vibrations. (Dr. avhandling, IMT)
IMT-2007-27	Gao, Zhen	Stochastic Response Analysis of Mooring Systems with Emphasis on Frequency-domain Analysis of Fatigue due to Wide-band Response Processes (PhD Thesis, CeSOS)
IMT-2007-28	Thorstensen, Tom Anders	Lifetime Profit Modelling of Ageing Systems Utilizing Information about Technical Condition. (Dr.ing. thesis, IMT)
IMT-2008-29	Refsnes, Jon Erling Gorset	Nonlinear Model-Based Control of Slender Body AUVs (PhD Thesis, IMT)
IMT-2008-30	Berntsen, Per Ivar B.	Structural Reliability Based Position Mooring. (PhD-Thesis, IMT)
IMT-2008-31	Ye, Naiquan	Fatigue Assessment of Aluminium Welded Box-stiffener Joints in Ships (Dr.ing. thesis, IMT)
IMT-2008-32	Radan, Damir	Integrated Control of Marine Electrical Power Systems. (PhD-Thesis, IMT)
IMT-2008-33	Thomassen, Paul	Methods for Dynamic Response Analysis and Fatigue Life Estimation of Floating Fish Cages. (Dr.ing. thesis, IMT)
IMT-2008-34	Pákozdi, Csaba	A Smoothed Particle Hydrodynamics Study of Two-dimensional Nonlinear Sloshing in Rectangular Tanks. (Dr.ing.thesis, IMT/ CeSOS)
IMT-2007-35	Grytøyr, Guttorm	A Higher-Order Boundary Element Method and Applications to Marine Hydrodynamics. (Dr.ing.thesis, IMT)
IMT-2008-36	Drummen, Ingo	Experimental and Numerical Investigation of Nonlinear Wave-Induced Load Effects in Containerships considering Hydroelasticity. (PhD thesis, CeSOS)
IMT-2008-37	Skejic, Renato	Maneuvering and Seakeeping of a Singel Ship and of Two Ships in Interaction. (PhD-Thesis, CeSOS)
IMT-2008-38	Harlem, Alf	An Age-Based Replacement Model for Repairable Systems with Attention to High-Speed Marine Diesel Engines. (PhD-Thesis, IMT)
IMT-2008-39	Alsos, Hagbart S.	Ship Grounding. Analysis of Ductile Fracture, Bottom Damage and Hull Girder Response. (PhD-thesis, IMT)
IMT-2008-40	Graczyk, Mateusz	Experimental Investigation of Sloshing Loading and Load Effects in Membrane LNG Tanks Subjected to Random Excitation. (PhD-thesis, CeSOS)
IMT-2008-41	Taghipour, Reza	Efficient Prediction of Dynamic Response for Flexible amd Multi-body Marine Structures. (PhD-

		thesis, CeSOS)
IMT-2008-42	Ruth, Eivind	Propulsion control and thrust allocation on marine vessels. (PhD thesis, CeSOS)
IMT-2008-43	Nystad, Bent Helge	Technical Condition Indexes and Remaining Useful Life of Aggregated Systems. PhD thesis, IMT
IMT-2008-44	Soni, Prashant Kumar	Hydrodynamic Coefficients for Vortex Induced Vibrations of Flexible Beams, PhD thesis, CeSOS
IMT-2009-45	Amlashi, Hadi K.K.	Ultimate Strength and Reliability-based Design of Ship Hulls with Emphasis on Combined Global and Local Loads. PhD Thesis, IMT
IMT-2009-46	Pedersen, Tom Arne	Bond Graph Modelling of Marine Power Systems. PhD Thesis, IMT
IMT-2009-47	Kristiansen, Trygve	Two-Dimensional Numerical and Experimental Studies of Piston-Mode Resonance. PhD-Thesis, CeSOS
IMT-2009-48	Ong, Muk Chen	Applications of a Standard High Reynolds Number Model and a Stochastic Scour Prediction Model for Marine Structures. PhD-thesis, IMT
IMT-2009-49	Hong, Lin	Simplified Analysis and Design of Ships subjected to Collision and Grounding. PhD-thesis, IMT
IMT-2009-50	Koushan, Kamran	Vortex Induced Vibrations of Free Span Pipelines, PhD thesis, IMT
IMT-2009-51	Korsvik, Jarl Eirik	Heuristic Methods for Ship Routing and Scheduling. PhD-thesis, IMT
IMT-2009-52	Lee, Jihoon	Experimental Investigation and Numerical in Analyzing the Ocean Current Displacement of Longlines. Ph.d.-Thesis, IMT.
IMT-2009-53	Vestbøstad, Tone Gran	A Numerical Study of Wave-in-Deck Impact usin a Two-Dimensional Constrained Interpolation Profile Method, Ph.d.thesis, CeSOS.
IMT-2009-54	Bruun, Kristine	Bond Graph Modelling of Fuel Cells for Marine Power Plants. Ph.d.-thesis, IMT
IMT 2009-55	Holstad, Anders	Numerical Investigation of Turbulence in a Sekwed Three-Dimensional Channel Flow, Ph.d.-thesis, IMT.
IMT 2009-56	Ayala-Uraga, Efren	Reliability-Based Assessment of Deteriorating Ship-shaped Offshore Structures, Ph.d.-thesis, IMT
IMT 2009-57	Kong, Xiangjun	A Numerical Study of a Damaged Ship in Beam Sea Waves. Ph.d.-thesis, IMT/CeSOS.
IMT 2010-58	Kristiansen, David	Wave Induced Effects on Floaters of Aquaculture Plants, Ph.d.-thesis, CeSOS.

IMT 2010-59	Ludvigsen, Martin	An ROV-Toolbox for Optical and Acoustic Scientific Seabed Investigation. Ph.d.-thesis IMT.
IMT 2010-60	Hals, Jørgen	Modelling and Phase Control of Wave-Energy Converters. Ph.d.thesis, CeSOS.
IMT 2010- 61	Shu, Zhi	Uncertainty Assessment of Wave Loads and Ultimate Strength of Tankers and Bulk Carriers in a Reliability Framework. Ph.d. Thesis, IMT/ CeSOS
IMT 2010-62	Shao, Yanlin	Numerical Potential-Flow Studies on Weakly-Nonlinear Wave-Body Interactions with/without Small Forward Speed, Ph.d.thesis,CeSOS.
IMT 2010-63	Califano, Andrea	Dynamic Loads on Marine Propellers due to Intermittent Ventilation. Ph.d.thesis, IMT.
IMT 2010-64	El Khoury, George	Numerical Simulations of Massively Separated Turbulent Flows, Ph.d.-thesis, IMT
IMT 2010-65	Seim, Knut Sponheim	Mixing Process in Dense Overflows with Emphasis on the Faroe Bank Channel Overflow. Ph.d.thesis, IMT
IMT 2010-66	Jia, Huirong	Structural Analysis of Intect and Damaged Ships in a Collission Risk Analysis Perspective. Ph.d.thesis CeSoS.
IMT 2010-67	Jiao, Linlin	Wave-Induced Effects on a Pontoon-type Very Large Floating Structures (VLFS). Ph.D.-thesis, CeSOS.
IMT 2010-68	Abrahamsen, Bjørn Christian	Sloshing Induced Tank Roof with Entrapped Air Pocket. Ph.d.thesis, CeSOS.
IMT 2011-69	Karimirad, Madjid	Stochastic Dynamic Response Analysis of Spar-Type Wind Turbines with Catenary or Taut Mooring Systems. Ph.d.-thesis, CeSOS.
IMT - 2011-70	Erlend Meland	Condition Monitoring of Safety Critical Valves. Ph.d.-thesis, IMT.
IMT – 2011-71	Yang, Limin	Stochastic Dynamic System Analysis of Wave Energy Converter with Hydraulic Power Take-Off, with Particular Reference to Wear Damage Analysis, Ph.d. Thesis, CeSOS.
IMT – 2011-72	Visscher, Jan	Application of Particla Image Velocimetry on Turbulent Marine Flows, Ph.d.Thesis, IMT.
IMT – 2011-73	Su, Biao	Numerical Predictions of Global and Local Ice Loads on Ships. Ph.d.Thesis, CeSOS.
IMT – 2011-74	Liu, Zhenhui	Analytical and Numerical Analysis of Iceberg Collision with Ship Structures. Ph.d.Thesis, IMT.
IMT – 2011-75	Aarsæther, Karl Gunnar	Modeling and Analysis of Ship Traffic by Observation and Numerical Simulation. Ph.d.Thesis, IMT.

Imt – 2011-76	Wu, Jie	Hydrodynamic Force Identification from Stochastic Vortex Induced Vibration Experiments with Slender Beams. Ph.d.Thesis, IMT.
Imt – 2011-77	Amini, Hamid	Azimuth Propulsors in Off-design Conditions. Ph.d.Thesis, IMT.
IMT – 2011-78	Nguyen, Tan-Hoi	Toward a System of Real-Time Prediction and Monitoring of Bottom Damage Conditions During Ship Grounding. Ph.d.thesis, IMT.
IMT- 2011-79	Tavakoli, Mohammad T.	Assessment of Oil Spill in Ship Collision and Grounding, Ph.d.thesis, IMT.
IMT- 2011-80	Guo, Bingjie	Numerical and Experimental Investigation of Added Resistance in Waves. Ph.d.Thesis, IMT.
IMT- 2011-81	Chen, Qiaofeng	Ultimate Strength of Aluminium Panels, considering HAZ Effects, IMT
IMT- 2012-82	Kota, Ravikiran S.	Wave Loads on Decks of Offshore Structures in Random Seas, CeSOS.
IMT- 2012-83	Sten, Ronny	Dynamic Simulation of Deep Water Drilling Risers with Heave Compensating System, IMT.
IMT- 2012-84	Berle, Øyvind	Risk and resilience in global maritime supply chains, IMT.
IMT- 2012-85	Fang, Shaoji	Fault Tolerant Position Mooring Control Based on Structural Reliability, CeSOS.
IMT- 2012-86	You, Jikun	Numerical studies on wave forces and moored ship motions in intermediate and shallow water, CeSOS.
IMT- 2012-87	Xiang ,Xu	Maneuvering of two interacting ships in waves, CeSOS
IMT- 2012-88	Dong, Wenbin	Time-domain fatigue response and reliability analysis of offshore wind turbines with emphasis on welded tubular joints and gear components, CeSOS
IMT- 2012-89	Zhu, Suji	Investigation of Wave-Induced Nonlinear Load Effects in Open Ships considering Hull Girder Vibrations in Bending and Torsion, CeSOS
IMT- 2012-90	Zhou, Li	Numerical and Experimental Investigation of Station-keeping in Level Ice, CeSOS
IMT- 2012-91	Ushakov, Sergey	Particulate matter emission characteristics from diesel enignes operating on conventional and alternative marine fuels, IMT
IMT- 2013-1	Yin, Decao	Experimental and Numerical Analysis of Combined In-line and Cross-flow Vortex Induced Vibrations, CeSOS

IMT-2013-2	Kurniawan, Adi	Modelling and geometry optimisation of wave energy converters, CeSOS
IMT-2013-3	Al Ryati, Nabil	Technical condition indexes doe auxiliary marine diesel engines, IMT
IMT-2013-4	Firoozkoohi, Reza	Experimental, numerical and analytical investigation of the effect of screens on sloshing, CeSOS
IMT-2013-5	Ommani, Babak	Potential-Flow Predictions of a Semi-Displacement Vessel Including Applications to Calm Water Broaching, CeSOS
IMT-2013-6	Xing, Yihan	Modelling and analysis of the gearbox in a floating spar-type wind turbine, CeSOS
IMT-7-2013	Balland, Océane	Optimization models for reducing air emissions from ships, IMT
IMT-8-2013	Yang, Dan	Transitional wake flow behind an inclined flat plate-----Computation and analysis, IMT
IMT-9-2013	Abdillah, Suyuthi	Prediction of Extreme Loads and Fatigue Damage for a Ship Hull due to Ice Action, IMT
IMT-10-2013	Ramìrez, Pedro Agustìn Pèrez	Ageing management and life extension of technical systems- Concepts and methods applied to oil and gas facilities, IMT
IMT-11-2013	Chuang, Zhenju	Experimental and Numerical Investigation of Speed Loss due to Seakeeping and Maneuvering. IMT
IMT-12-2013	Etemaddar, Mahmoud	Load and Response Analysis of Wind Turbines under Atmospheric Icing and Controller System Faults with Emphasis on Spar Type Floating Wind Turbines, IMT
IMT-13-2013	Lindstad, Haakon	Strategies and measures for reducing maritime CO2 emissons, IMT
IMT-14-2013	Haris, Sabril	Damage interaction analysis of ship collisions, IMT
IMT-15-2013	Shainee, Mohamed	Conceptual Design, Numerical and Experimental Investigation of a SPM Cage Concept for Offshore Mariculture, IMT
IMT-16-2013	Gansel, Lars	Flow past porous cylinders and effects of biofouling and fish behavior on the flow in and around Atlantic salmon net cages, IMT
IMT-17-2013	Gaspar, Henrique	Handling Aspects of Complexity in Conceptual Ship Design, IMT
IMT-18-2013	Thys, Maxime	Theoretical and Experimental Investigation of a Free Running Fishing Vessel at Small Frequency of Encounter, CeSOS
IMT-19-2013	Aglen, Ida	VIV in Free Spanning Pipelines, CeSOS

IMT-1-2014	Song, An	Theoretical and experimental studies of wave diffraction and radiation loads on a horizontally submerged perforated plate, CeSOS
IMT-2-2014	Rogne, Øyvind Ygre	Numerical and Experimental Investigation of a Hinged 5-body Wave Energy Converter, CeSOS
IMT-3-2014	Dai, Lijuan	Safe and efficient operation and maintenance of offshore wind farms ,IMT
IMT-4-2014	Bachynski, Erin Elizabeth	Design and Dynamic Analysis of Tension Leg Platform Wind Turbines, CeSOS
IMT-5-2014	Wang, Jingbo	Water Entry of Freefall Wedged – Wedge motions and Cavity Dynamics, CeSOS
IMT-6-2014	Kim, Ekaterina	Experimental and numerical studies related to the coupled behavior of ice mass and steel structures during accidental collisions, IMT
IMT-7-2014	Tan, Xiang	Numerical investigation of ship’s continuous- mode icebreaking in leverl ice, CeSOS
IMT-8-2014	Muliawan, Made Jaya	Design and Analysis of Combined Floating Wave and Wind Power Facilities, with Emphasis on Extreme Load Effects of the Mooring System, CeSOS
IMT-9-2014	Jiang, Zhiyu	Long-term response analysis of wind turbines with an emphasis on fault and shutdown conditions, IMT
IMT-10-2014	Dukan, Fredrik	ROV Motion Control Systems, IMT
IMT-11-2014	Grimsmo, Nils I.	Dynamic simulations of hydraulic cylinder for heave compensation of deep water drilling risers, IMT
IMT-12-2014	Kvittem, Marit I.	Modelling and response analysis for fatigue design of a semisubmersible wind turbine, CeSOS
IMT-13-2014	Akhtar, Juned	The Effects of Human Fatigue on Risk at Sea, IMT
IMT-14-2014	Syahroni, Nur	Fatigue Assessment of Welded Joints Taking into Account Effects of Residual Stress, IMT
IMT-1-2015	Bøckmann, Eirik	Wave Propulsion of ships, IMT
IMT-2-2015	Wang, Kai	Modelling and dynamic analysis of a semi-submersible floating vertical axis wind turbine, CeSOS
IMT-3-2015	Fredriksen, Arnt Gunvald	A numerical and experimental study of a two-dimensional body with moonpool in waves and current, CeSOS
IMT-4-2015	Jose Patricio Gallardo Canabes	Numerical studies of viscous flow around bluff bodies, IMT

IMT-5-2015	Vegard Longva	Formulation and application of finite element techniques for slender marine structures subjected to contact interactions, IMT
IMT-6-2015	Jacobus De Vaal	Aerodynamic modelling of floating wind turbines, CeSOS
IMT-7-2015	Fachri Nasution	Fatigue Performance of Copper Power Conductors, IMT
IMT-8-2015	Oleh I Karpa	Development of bivariate extreme value distributions for applications in marine technology,CeSOS
IMT-9-2015	Daniel de Almeida Fernandes	An output feedback motion control system for ROVs, AMOS
IMT-10-2015	Bo Zhao	Particle Filter for Fault Diagnosis: Application to Dynamic Positioning Vessel and Underwater Robotics, CeSOS
IMT-11-2015	Wenting Zhu	Impact of emission allocation in maritime transportation, IMT
IMT-12-2015	Amir Rasekhi Nejad	Dynamic Analysis and Design of Gearboxes in Offshore Wind Turbines in a Structural Reliability Perspective, CeSOS
IMT-13-2015	Arturo Jesùs Ortega Malca	Dynamic Response of Flexibles Risers due to Unsteady Slug Flow, CeSOS
IMT-14-2015	Dagfinn Husjord	Guidance and decision-support system for safe navigation of ships operating in close proximity, IMT
IMT-15-2015	Anirban Bhattacharyya	Ducted Propellers: Behaviour in Waves and Scale Effects, IMT
IMT-16-2015	Qin Zhang	Image Processing for Ice Parameter Identification in Ice Management, IMT
IMT-1-2016	Vincentius Rumawas	Human Factors in Ship Design and Operation: An Experiential Learning, IMT
IMT-2-2016	Martin Storheim	Structural response in ship-platform and ship-ice collisions, IMT
IMT-3-2016	Mia Abrahamsen Prsic	Numerical Simulations of the Flow around single and Tandem Circular Cylinders Close to a Plane Wall, IMT
IMT-4-2016	Tufan Arslan	Large-eddy simulations of cross-flow around ship sections, IMT

IMT-5-2016	Pierre Yves-Henry	Parametrisation of aquatic vegetation in hydraulic and coastal research,IMT
IMT-6-2016	Lin Li	Dynamic Analysis of the Instalation of Monopiles for Offshore Wind Turbines, CeSOS
IMT-7-2016	Øivind Kåre Kjerstad	Dynamic Positioning of Marine Vessels in Ice, IMT
IMT-8-2016	Xiaopeng Wu	Numerical Analysis of Anchor Handling and Fish Trawling Operations in a Safety Perspective, CeSOS
IMT-9-2016	Zhengshun Cheng	Integrated Dynamic Analysis of Floating Vertical Axis Wind Turbines, CeSOS
IMT-10-2016	Ling Wan	Experimental and Numerical Study of a Combined Offshore Wind and Wave Energy Converter Concept
IMT-11-2016	Wei Chai	Stochastic dynamic analysis and reliability evaluation of the roll motion for ships in random seas, CeSOS
IMT-12-2016	Øyvind Selnes Patricksson	Decision support for conceptual ship design with focus on a changing life cycle and future uncertainty, IMT
IMT-13-2016	Mats Jørgen Thorsen	Time domain analysis of vortex-induced vibrations, IMT
IMT-14-2016	Edgar McGuinness	Safety in the Norwegian Fishing Fleet – Analysis and measures for improvement, IMT
IMT-15-2016	Sepideh Jafarzadeh	Energy effiency and emission abatement in the fishing fleet, IMT
IMT-16-2016	Wilson Ivan Guachamin Acero	Assessment of marine operations for offshore wind turbine installation with emphasis on response-based operational limits, IMT
IMT-17-2016	Mauro Candeloro	Tools and Methods for Autonomous Operations on Seabed and Water Coumn using Underwater Vehicles, IMT
IMT-18-2016	Valentin Chabaud	Real-Time Hybrid Model Testing of Floating Wind Tubines, IMT
IMT-1-2017	Mohammad Saud Afzal	Three-dimensional streaming in a sea bed boundary layer
IMT-2-2017	Peng Li	A Theoretical and Experimental Study of Wave-induced Hydroelastic Response of a Circular Floating Collar
IMT-3-2017	Martin Bergström	A simulation-based design method for arctic maritime transport systems

IMT-4-2017	Bhushan Taskar	The effect of waves on marine propellers and propulsion
IMT-5-2017	Mohsen Bardestani	A two-dimensional numerical and experimental study of a floater with net and sinker tube in waves and current
IMT-6-2017	Fatemeh Hoseini Dadmarzi	Direct Numerical Simualtion of turbulent wakes behind different plate configurations
IMT-7-2017	Michel R. Miyazaki	Modeling and control of hybrid marine power plants
IMT-8-2017	Giri Rajasekhar Gunnu	Safety and effiency enhancement of anchor handling operations with particular emphasis on the stability of anchor handling vessels
IMT-9-2017	Kevin Koosup Yum	Transient Performance and Emissions of a Turbocharged Diesel Engine for Marine Power Plants
IMT-10-2017	Zhaolong Yu	Hydrodynamic and structural aspects of ship collisions
IMT-11-2017	Martin Hassel	Risk Analysis and Modelling of Allisions between Passing Vessels and Offshore Installations
IMT-12-2017	Astrid H. Brodtkorb	Hybrid Control of Marine Vessels – Dynamic Positioning in Varying Conditions
IMT-13-2017	Kjersti Bruserud	Simultaneous stochastic model of waves and current for prediction of structural design loads
IMT-14-2017	Finn-Idar Grøtta Giske	Long-Term Extreme Response Analysis of Marine Structures Using Inverse Reliability Methods
IMT-15-2017	Stian Skjong	Modeling and Simulation of Maritime Systems and Operations for Virtual Prototyping using co-Simulations
IMT-1-2018	Yingguang Chu	Virtual Prototyping for Marine Crane Design and Operations
IMT-2-2018	Sergey Gavrilin	Validation of ship manoeuvring simulation models
IMT-3-2018	Jeevith Hegde	Tools and methods to manage risk in autonomous subsea inspection,maintenance and repair operations
IMT-4-2018	Ida M. Strand	Sea Loads on Closed Flexible Fish Cages
IMT-5-2018	Erlend Kvinge Jørgensen	Navigation and Control of Underwater Robotic Vehicles

IMT-6-2018	Bård Stovner	Aided Intertial Navigation of Underwater Vehicles
IMT-7-2018	Erlend Liavåg Grotle	Thermodynamic Response Enhanced by Sloshing in Marine LNG Fuel Tanks
IMT-8-2018	Børge Rokseth	Safety and Verification of Advanced Maritime Vessels
IMT-9-2018	Jan Vidar Ulveseter	Advances in Semi-Empirical Time Domain Modelling of Vortex-Induced Vibrations
IMT-10-2018	Chenyu Luan	Design and analysis for a steel braceless semi-submersible hull for supporting a 5-MW horizontal axis wind turbine
IMT-11-2018	Carl Fredrik Rehn	Ship Design under Uncertainty
IMT-12-2018	Øyvind Ødegård	Towards Autonomous Operations and Systems in Marine Archaeology
IMT-13-2018	Stein Melvær Nornes	Guidance and Control of Marine Robotics for Ocean Mapping and Monitoring
IMT-14-2018	Petter Norgren	Autonomous Underwater Vehicles in Arctic Marine Operations: Arctic marine research and ice monitoring
IMT-15-2018	Minjoo Choi	Modular Adaptable Ship Design for Handling Uncertainty in the Future Operating Context
MT-16-2018	Ole Alexander Eidsvik	Dynamics of Remotely Operated Underwater Vehicle Systems
IMT-17-2018	Mahdi Ghane	Fault Diagnosis of Floating Wind Turbine Drivetrain- Methodologies and Applications
IMT-18-2018	Christoph Alexander Thieme	Risk Analysis and Modelling of Autonomous Marine Systems
IMT-19-2018	Yugao Shen	Operational limits for floating-collar fish farms in waves and current, without and with well-boat presence
IMT-20-2018	Tianjiao Dai	Investigations of Shear Interaction and Stresses in Flexible Pipes and Umbilicals
IMT-21-2018	Sigurd Solheim Pettersen	Resilience by Latent Capabilities in Marine Systems
IMT-22-2018	Thomas Sauder	Fidelity of Cyber-physical Empirical Methods. Application to the Active Truncation of Slender Marine Structures
IMT-23-2018	Jan-Tore Horn	Statistical and Modelling Uncertainties in the Design of Offshore Wind Turbines

IMT-24-2018	Anna Swider	Data Mining Methods for the Analysis of Power Systems of Vessels
IMT-1-2019	Zhao He	Hydrodynamic study of a moored fish farming cage with fish influence
IMT-2-2019	Isar Ghamari	Numerical and Experimental Study on the Ship Parametric Roll Resonance and the Effect of Anti-Roll Tank
IMT-3-2019	Håkon Strandenes	Turbulent Flow Simulations at Higher Reynolds Numbers
IMT-4-2019	Siri Mariane Holen	Safety in Norwegian Fish Farming – Concepts and Methods for Improvement
IMT-5-2019	Ping Fu	Reliability Analysis of Wake-Induced Riser Collision
IMT-6-2019	Vladimir Krivopolianskii	Experimental Investigation of Injection and Combustion Processes in Marine Gas Engines using Constant Volume Rig
IMT-7-2019	Anna Maria Kozlowska	Hydrodynamic Loads on Marine Propellers Subject to Ventilation and out of Water Condition.
IMT-8-2019	Hans-Martin Heyn	Motion Sensing on Vessels Operating in Sea Ice: A Local Ice Monitoring System for Transit and Stationkeeping Operations under the Influence of Sea Ice
IMT-9-2019	Stefan Vilsen	Method for Real-Time Hybrid Model Testing of Ocean Structures – Case on Slender Marine Systems
IMT-10-2019	Finn-Christian W. Hanssen	Non-Linear Wave-Body Interaction in Severe Waves
IMT-11-2019	Trygve Olav Fossum	Adaptive Sampling for Marine Robotics
IMT-12-2019	Jørgen Bremnes Nielsen	Modeling and Simulation for Design Evaluation
IMT-13-2019	Yuna Zhao	Numerical modelling and dyncamic analysis of offshore wind turbine blade installation
IMT-14-2019	Daniela Myland	Experimental and Theoretical Investigations on the Ship Resistance in Level Ice
IMT-15-2019	Zhengru Ren	Advanced control algorithms to support automated offshore wind turbine installation
IMT-16-2019	Drazen Polic	Ice-propeller impact analysis using an inverse propulsion machinery simulation approach
IMT-17-2019	Endre Sandvik	Sea passage scenario simulation for ship system performance evaluation

IMT-18-2019	Loup Suja-Thauvin	Response of Monopile Wind Turbines to Higher Order Wave Loads
IMT-19-2019	Emil Smilden	Structural control of offshore wind turbines – Increasing the role of control design in offshore wind farm development
IMT-20-2019	Aleksandar-Sasa Milakovic	On equivalent ice thickness and machine learning in ship ice transit simulations
IMT-1-2020	Amrit Shankar Verma	Modelling, Analysis and Response-based Operability Assessment of Offshore Wind Turbine Blade Installation with Emphasis on Impact Damages
IMT-2-2020	Bent Oddvar Arnesen Haugaløkken	Autonomous Technology for Inspection, Maintenance and Repair Operations in the Norwegian Aquaculture
IMT-3-2020	Seongpil Cho	Model-based fault detection and diagnosis of a blade pitch system in floating wind turbines
IMT-4-2020	Jose Jorge Garcia Agis	Effectiveness in Decision-Making in Ship Design under Uncertainty
IMT-5-2020	Thomas H. Viuff	Uncertainty Assessment of Wave-and Current-induced Global Response of Floating Bridges
IMT-6-2020	Fredrik Mentzoni	Hydrodynamic Loads on Complex Structures in the Wave Zone
IMT-7-2020	Senthuran Ravinthrakumar	Numerical and Experimental Studies of Resonant Flow in Moonpools in Operational Conditions
IMT-8-2020	Stian Skaalvik Sandøy	Acoustic-based Probabilistic Localization and Mapping using Unmanned Underwater Vehicles for Aquaculture Operations
IMT-9-2020	Kun Xu	Design and Analysis of Mooring System for Semi-submersible Floating Wind Turbine in Shallow Water
IMT-10-2020	Jianxun Zhu	Cavity Flows and Wake Behind an Elliptic Cylinder Translating Above the Wall
IMT-11-2020	Sandra Hogenboom	Decision-making within Dynamic Positioning Operations in the Offshore Industry – A Human Factors based Approach
IMT-12-2020	Woongshik Nam	Structural Resistance of Ship and Offshore Structures Exposed to the Risk of Brittle Failure
IMT-13-2020	Svenn Are Tutturen Værnø	Transient Performance in Dynamic Positioning of Ships: Investigation of Residual Load Models and Control Methods for Effective Compensation
IMT-14-2020	Mohd Atif Siddiqui	Experimental and Numerical Hydrodynamic Analysis of a Damaged Ship in Waves
IMT-15-2020	John Marius Hegseth	Efficient Modelling and Design Optimization of Large Floating Wind Turbines

IMT-16-2020	Asle Natskår	Reliability-based Assessment of Marine Operations with Emphasis on Sea Transport on Barges
IMT-17-2020	Shi Deng	Experimental and Numerical Study of Hydrodynamic Responses of a Twin-Tube Submerged Floating Tunnel Considering Vortex-Induced Vibration
IMT-18-2020	Jone Torsvik	Dynamic Analysis in Design and Operation of Large Floating Offshore Wind Turbine Drivetrains
IMT-1-2021	Ali Ebrahimi	Handling Complexity to Improve Ship Design Competitiveness
IMT-2-2021	Davide Proserpio	Isogeometric Phase-Field Methods for Modeling Fracture in Shell Structures
IMT-3-2021	Cai Tian	Numerical Studies of Viscous Flow Around Step Cylinders
IMT-4-2021	Farid Khazaeli Moghadam	Vibration-based Condition Monitoring of Large Offshore Wind Turbines in a Digital Twin Perspective
IMT-5-2021	Shuaishuai Wang	Design and Dynamic Analysis of a 10-MW Medium-Speed Drivetrain in Offshore Wind Turbines
IMT-6-2021	Sadi Tavakoli	Ship Propulsion Dynamics and Emissions
IMT-7-2021	Haoran Li	Nonlinear wave loads, and resulting global response statistics of a semi-submersible wind turbine platform with heave plates
IMT-8-2021	Einar Skiftestad Ueland	Load Control for Real-Time Hybrid Model Testing using Cable-Driven Parallel Robots
IMT-9-2021	Mengning Wu	Uncertainty of machine learning-based methods for wave forecast and its effect on installation of offshore wind turbines
IMT-10-2021	Xu Han	Onboard Tuning and Uncertainty Estimation of Vessel Seakeeping Model Parameters
IMT-01-2022	Ingunn Marie Holmen	Safety in Exposed Aquacultrue Operations
IMT-02-2022	Prateek Gupta	Ship Performance Monitoring using In-service Measurements and Big Data Analysis Methods
IMT-03-2022	Sangwoo Kim	Non-linear time domain analysis of deepwater riser vortex-induced vibrations
IMT-04-2022	Jarle Vinje Kramer	Hydrodynamic Aspects of Sail-Assisted Merchant Vessels
IMT-05-2022	Tiantian Zhu	Information and Decision-making for Accident Prevention

IMT-06-2022	Øyvind Rabliås	Numerical and Expermental Studies of Maneuvering in Regular and Irregular Waves
IMT-07-2022	Pramod Ghimire	Simulation-Based Ship Hybrid Power System Conspet Studies and Performance Analyses
IMT-08-2022	Carlos Eduardo Silva de Souza	Structural modelling, coupled dynamics, and design of large floating wind turbines